Analysis of Transport Phenomena in a Combusting Sulfide Particle Cloud: With Implications to the Flash Smelting of High-Grade Copper Concentrates

By

Grant A. Caffery

B.E., The University of Newcastle, 1996

A THESIS SUBMITTED IN PARTIAL FULFILMENT OF

THE REQUIREMENTS FOR THE DEGREE OF

DOCTOR OF PHILOSOPHY

in

THE FACULTY OF GRADUATE STUDIES

(Department of Metals and Materials Engineering)

We accept this thesis as conforming

to the required standard

THE UNIVERSITY OF BRITISH COLUMBIA

February, 2002

In presenting this thesis in partial fulfilment of the requirements for an advanced degree at the University of British Columbia, I agree that the Library shall make it freely available for reference and study. I further agree that permission for extensive copying of this thesis for scholarly purposes may be granted by the head of my department or by his or her representatives. It is understood that copying or publication of this thesis for financial gain shall not be allowed without my written permission.

Department of METALS & MATERIAL ENGINEERING

The University of British Columbia
Vancouver, Canada

Date 11/2/02

DE-6 (2/88)

Abstract

High-grade copper concentrates are becoming increasingly important as feed materials for flash smelting furnaces. Escondida concentrate from Chile is one of the most important of these high-grade concentrates. When smelting concentrate blends with Escondida loadings in excess of approximately 20 wt-%, BHP's San Manuel furnace observed unreacted concentrate accumulating at the bottom of the reaction shaft. This limited the quantity of Escondida concentrate that could be smelted by the furnace and therefore increased its treatment costs.

The objective of this project was to suggest operational improvements to optimise furnace performance at high Escondida loadings by gaining an understanding of the influence of high-grade concentrate on the flash smelting behaviour of concentrate blends. This objective was achieved by conducting experimental and Computational Fluid Dynamics (CFD) studies on the flash smelting process.

Results from the experimental study show that sulfide flash smelting can be described using group combustion theory. Furthermore results suggest addition of high-grade concentrate to the blend reduces the oxygen-to-concentrate ratio and increases the oxygen enrichment. This lowers the heat transfer effectiveness factor of the particles within the cloud and the burner exit velocity, in turn reducing the cloud heat transfer coefficient. The lower rate of heat transfer to the particles increases the distance required for them to reach their ignition temperature. At some Escondida loading, the heat-up

time of the particles becomes so large that there is insufficient residence time for particles to react with the available oxygen, leading to the observed operational problems.

To overcome these problems requires that the heat transfer characteristics of the concentrate burner be improved. Therefore experimental and CFD studies were conducted to compare the performance of a swirl burner to a bluff-body burner. The bluff-body burner was used to approximate the concentrate burner used in industry. Some differences between the bluff-body burner investigated in this study and the industrial concentrate burner may cause the observed results for the bluff-body burner to differ from those of the industrial concentrate burners. It was found that the swirl burner gives superior performance to the bluff body burner due to two effects:

1) formation of an internal re-circulation zone which transfers heat from the combustion zone to the fresh mixture, increasing the heat transfer rate to the concentrate particles; and

2) reduction of the volume of the stagnant zone within the shaft, increasing the average particle residence time.

Table of Contents

List of Tables

List of Figures

Nomenclature

Symbol	Definition	Units
A	Pre-exponential factor	$m.s^{-1}$
A_1	Primary stream flow area	m^2
A_2	Secondary stream flow area	m^2
A_f	Furnace operating diagram constant	$(m.s).kg^{-1}$
A_p	Particle surface area	m^2
a_j	Jet fitting parameter	m
amg	Aim matte grade	-
B_f	Furnace operating diagram constant	$s.kg^{-1}$
B_R	Blockage ratio	-
B_{SO2}	Kinetic parameter	-
B_w	Wall transfer number	$kg_{char}.kg_{gas}^{-1}$
B_∞	Far field transfer number	$kg_{char}.kg_{gas}^{-1}$
b	Age distribution constant	-
C	Gas phase concentration	$kmol.m^{-3}$
$C_{1\varepsilon}$	k-ε Model constant	-
$C_{2\varepsilon}$	k-ε Model constant	-
$C_{3\varepsilon}$	k-ε Model Constant	-
C_A	Gas phase concentration of species A	$kmol.m^{-3}$
C_D	Particle drag coefficient	-
C_L	Lagrangian time scale constant	-
C_{O2}	Oxygen concentration	$kmol.m^{-3}$
C_p	Mixture specific heat	$J.(kg.K)^{-1}$
C_s	Concentration at the particle surface	$kmol.m^{-3}$
D	Diffusivity	$m^2.s^{-1}$
D_{AB}	Diffusivity of A in B	$m^2.s^{-1}$
D_c	Chamber diameter	m
Da_{crit}	Critical Damkohler number	-
D_e	Effective diffusivity	$m^2.s^{-1}$
D_{eff}	Effective diffusivity	$m^2.s^{-1}$
D_{ij}	Diffusive term in the RSM	$m^2.s^{-3}$
D_k	Knudsen diffusivity	$m^2.s^{-1}$
D_o	Diffusivity at T_o	$m^2.s^{-1}$
D_{pore}	Pore diffusivity	$m^2.s^{-1}$
D_s	Characteristic length of solids sampler	m
d_b	Burner diameter	m
d_{bb}	Bluff body diameter	m
d_c	Cloud diameter	m
d_h	Swirler hub diameter	m
d_{ia}	Inner diameter of inner annulus	m
d_p	Particle diameter	m

E_a	Activation energy	$J.mol^{-1}$
E_{ij}	Curvature term in the RSM	$m^2.s^{-3}$
F_i	Particle body force in the i direction	$m.s^{-2}$
Fr	Froude number $\left(\dfrac{U_o}{(gd_b)^{1/2}} \left(\dfrac{1}{(S_{Fr}+1)^{3/2}} \right) \right)$	-
f	Solids feed-rate	$kg.s^{-1}$
f_{cu}	Weight fraction copper in feed	-
f_{fe}	Weight fraction iron in feed	-
fg	Feed grade	wt% Cu
f_h	Fraction of the heat of reaction returned to particle	-
f_{max}	Maximum solids feed-rate	$kg.s^{-1}$
f_s	Weight fraction sulfur in feed	-
f_v	Volume Fraction of the Particles	-
G	Group combustion number	-
G_b	Turbulent kinetic energy production by bouyancy	$kg.(m.s^3)^{-1}$
G_k	Turbulent kinetic energy production rate	$kg.(m.s^3)^{-1}$
G_x	Axial flux of linear momentum	$kg.m.s^{-2}$
G_ϕ	Axial flux of angular momentum	$kg.m^2.s^{-2}$
g	Gravitational acceleration	$m.s^{-2}$
H_{loss}	Furnace heat losses	W
h	Specific enthalpy	$J.kg^{-1}$
h_i	Specific enthalpy of component i	$J.kg^{-1}$
h_{N2}	Nitrogen specific enthalpy	$J.kg^{-1}$
h'	Fluctuating fluid enthalpy	$J.kg^{-1}$
I	Radiation intensity	$W.m^{-2}$
I_t	Inlet flow turbulence intensity	-
I_1	Bessel function	-
I_2	Bessel function	-
K_c	PI controller proportional constant	$(V.s).kg^{-1}$
K_j	Jet centerline velocity fitting parameter	m
K_m	Stokes-Cunningham correction factor	-
K_p	Equilibrium constant	-
k	Turbulent kinetic energy	$m^2.s^2$
k_a	Absorption coefficient	
k_c	Intrinsic reaction rate constant	$m.s^{-1}$
k_e	Effective thermal conductivity	$W.(m.K)^{-1}$
k_h	Particle heat transfer coefficient	$W.(m^2.K)^{-1}$
$k_{h,c}$	Cloud heat transfer coefficient	$W.(m^2.K)^{-1}$
k_m	Mass transfer coefficient	$m.s^{-1}$
k_{ov}	Overall reaction rate coefficient	$m.s^{-1}$
k_s	Scattering coefficient	m^{-1}
k_{SO2}	Reaction rate constant	$kmol_{SO_2}.\left(m^3_{cat}.s\right)^{-1}$
k'_c	Intrinsic reaction rate based on particle mass	$m^3.(kg.s)^{-1}$
L	Shaft length	m

Symbol	Description	Units
L_w	Wake length	m
L_{Ra}	Characteristic length for the Rayleigh number (shaft length)	m
L_x	Distance from furnace entrance	m
L_w'	Dimensionless wake length	-
MW_{O2}	Molecular weight of oxygen	$kg_{O_2}.kmol_{O_2}^{-1}$
m	Swirl burner design equation parameter	-
m_{ave}	Average particle mass	kg
m_{CuFeS2}	Particle mass	kg
m_i	Particle mass in the ith stream	kg
m_p	Particle mass	kg
$m_{p,o}$	Initial particle mass	kg
$\dot{m}$	Burning rate of a single particle	$kg.s^{-1}$
$\dot{m}_{cloud}$	Burning rate of a single particle within the cloud	$kg.s^{-1}$
$\dot{m}_{Cu_2S}$	Mass flow rate of Cu_2S	$tonnes.hr^{-1}$
$\dot{m}_{feed}$	Feed mass flow rate	$tonnes.hr^{-1}$
$\dot{m}_{FeO}$	Mass flow rate of FeO	$tonnes.hr^{-1}$
$\dot{m}_{FeS}$	Mass flow rate of FeS	$tonnes.hr^{-1}$
$\dot{m}_i$	Mass flow rate of component i	$tonnes.hr^{-1}$
$\dot{m}_{matte}$	Matte mass flow rate	$tonnes.hr^{-1}$
$\dot{m}_o$	Fresh mixture mass flow rate	$kg.s^{-1}$
$\dot{m}_{N_2}$	Mass flow rate of nitrogen	$tonnes.hr^{-1}$
$\dot{m}_{O_2}$	Mass flow rate of oxygen	$tonnes.hr^{-1}$
$\dot{m}_r$	Recirculating mass flow rate	$kg.s^{-1}$
$\dot{m}_{SO_2}$	Mass flow rate of sulfur dioxide	$tonnes.hr^{-1}$
$\dot{m}'_{O_2}$	Oxygen consumption rate	$kg.s^{-1}$
$\dot{m}''$	Mass burning rate of a single particle per unit surface area	$kg.(m^2.s)^{-1}$
$\dot{m}'''$	Volumetric mass source	$kg.(m^3.s)^{-1}$
$\dot{m}_k'''$	Volumetric mass source of component k	$kg.(m^3.s)^{-1}$
$\dot{m}_{O_2}'''$	Volumetric oxygen mass consumption rate	$kg.(m^3.s)^{-1}$
N	Number of particles represented by particle track	-
N_{si}	Particle separation number $\left(\dfrac{K_m \rho_p d_p^2 U}{18 \mu D_s} \right)$	-

Nu	Nusselt number	-
Nu_{cl}	Cloud Nusselt number $\left(\dfrac{k_{h,c}d_b}{\lambda}\right)$	-
Nu_{coop}	Co-operative Nusselt number	-
Nu_{iso}	Isolated particle Nusselt number $\left(\dfrac{k_h d_p}{\lambda}\right)$	-
n	Particle number density	m^{-3}
n_r	Reaction order	m
P	Gas pressure	Pa
$P_{dynamic}$	Dynamic pressure	Pa
P_{ij}	Production term in the RSM	$m^2.s^{-3}$
Pe_t	Turbulent Peclet number $\left(\dfrac{\mu_t}{\mu}Pr\right)$	-
P_{O2}	Oxygen partial pressure	Pa
Pr	Prandtl number $\left(\dfrac{C_p\mu}{\lambda}\right)$	-
Pr_ε	Turbulent Prandtl number for the diffusion of the dissipation rate of turbulent kinetic energy	-
Pr_k	Turbulent Prandtl number for diffusion of turbulent kinetic energy	-
Pr_t	Turbulent Prandtl number $\left(\dfrac{C_p\mu_e}{\lambda_e}\right)$	-
P_S	Scattering phase function	-
P_{SO2}	Sulfur dioxide partial pressure	Pa
P_{SO3}	Sulfur trioxide partial pressure	Pa
P_{static}	Static pressure	Pa
p'	Fluctating pressure	Pa
q	Heat flux	$W.m^{-3}$
$\dot{q}'''$	Volumetric heat source	$W.m^{-3}$
R	Universal gas constant	$J.(mol.K)^{-1}$
Ra	Jet Rayleigh number $\left(\dfrac{gL_{Ra}\rho\Delta\rho C_p}{\mu\lambda}\right)$	-
R_c	Chemical resistance	$(m^2.s).kg^{-1}$
Re_{cl}	Cloud (or jet) Reynolds number $\left(\dfrac{\rho U_o d_b}{\mu}\right)$	-
Re_p	Particle Reynolds number $\left(\dfrac{\rho|u-u_p|d_p}{\mu}\right)$	
R_{ij}	Rotation term in the RSM	$m^2.s^{-3}$
R_m	Mass transfer resistance	$(m^2.s).kg^{-1}$

r	Radial co-ordinate direction	m
r_m	Ratio of the recirculating mass flow rate to the inlet flow rate	-
r_{SO2}	Reaction rate	$kmol_{SO_2} \cdot \left(m^3_{cat} \cdot s\right)^{-1}$
S	Swirl number	-
Sc_t	Turbulent Schmidt number $\left(\dfrac{\mu_e}{\rho D_e}\right)$	-
S_e	Energy source term to gas phase equation	$W.m^{-3}$
S_{Fr}	Stoichiometric term in the modified Froude number	-
Sh	Sherwood number	-
S_{ij}	Curvature source term in RSM	$m^2.s^{-3}$
S_m	Mass source term to gas phase continuity equation	$kg.(m^3.s)^{-1}$
S_{O2}	Oxygen mass source	$m.s^{-1}$
$S_{p,r}$	Momentum source term to the radial gas phase momentum equation	$kg.(m.s)^{-2}$
$S_{p,z}$	Momentum source term to the axial gas phase momentum equation	$kg.(m.s)^{-2}$
$S_{p,\theta}$	Momentum source term to the swirl gas phase momentum equation	$kg.(m.s)^{-2}$
$S_{s,k}$	Species source term to gas phase equation	$kg.(m^3.s)^{-1}$
S_{SO2}	Sulfur dioxide mass source	$m.s^{-1}$
St	Stokes Number $\left(\dfrac{\rho_p d_p^2 \varepsilon u'}{5.4\mu k^{3/2}}\right)$	-
S_V	Particle surface area pre unit cloud volume	m^{-1}
s	Radiation intensity direction	m
T	Temperature	K
T_e	Characteristic eddy lifetime	s
T_L	Gas phase Lagrangian time scale	s
$T_{L,p}$	Particle Lagrangian time scale	s
T_p	Particle temperature	K
$T_{p,i}$	Particle ignition temperature	K
T_∞	Far field gas phase temperature	K
t	Time	s
U	Gas velocity	$m.s^{-1}$
U_t	Particle terminal velocity	$m.s^{-1}$
U_o	Initial jet velocity or burner exit velocity	$m.s^{-1}$
u	Gas phase axial velocity	$m.s^{-1}$
u_p	Particle velocity	$m.s^{-1}$
$u_{p,i}$	Particle velocity in i co-ordinate direction	$m.s^{-1}$
u'_i	Fluctating gas phase velocity in the i component direction	$m.s^{-1}$
u'_p	Fluctating particle velocity	$m.s^{-1}$
$u'_{p,i}$	Fluctating particle velocity in i co-ordinate direciton	$m.s^{-1}$
V_{cell}	Cell volume	m^3
Vm	Volume of well mixed region	m^3

Symbol	Description	Units
V_p	Volume of plug flow region	m^3
v	Radial velocity	$m.s^{-1}$
$\dot{v}$	Inlet volumetric flow rate	$m^3.s^{-1}$
w	Tangential velocity	$m.s^{-1}$
w_g	Guassian distributed random number	$s^{1/2}$
w_p	Particle reaction rate	$kmol.s^{-1}$
w_s	Particle reaction rate based on surface conditions	$kmol.s^{-1}$
X	Particle conversion	-
X_{ra}	Jet wall attachment length	m
X'	Modified particle conversion	-
x	Axial position	m
x_i	Co-ordinate direction	m
x_p	Particle relaxation distance	m
x'_p	Dimensionless particle relaxation distance	-
Y_c	Controller output	V
Y_{CO2}	Carbon dioxide mass fraction	$kg_{CO_2}.kg_{gas}^{-1}$
Y_k	Mass fraction of component k	$kg_k.kg_{gas}^{-1}$
Y_{O2}	Oxygen mass fraction	$kg_{O_2}.kg_{gas}^{-1}$
Y'_k	Fluctuating mass fraction of component k	$kg_k.kg_{gas}^{-1}$
z	Axial co-ordinate direction	m
α	Particle momentum equation constant	$m.s^{-1}$
α_p	Particle energy equation constant	K
α'	Swirl vane angle	rad
β_b	Coefficient of Thermal Expansion	K^{-1}
β_p	Particle energy equation constant	s^{-1}
ΔH	Heat of reaction	$J.kg^{-1}$
Δt	Time step	s
ε	Dissipation rate of turbulent kinetic energy	$m^2.s^{-3}$
ε_c	Error in controller input	$kg.s^{-1}$
$\varepsilon_{c,n}$	Error in controller input at nth time step	$kg.s^{-1}$
$\varepsilon_{c,n-1}$	Error in controller input at (nth-1) time step	$kg.s^{-1}$
ε_{ij}	Dissipation term in RSM	$m^2.s^{-3}$
ε_p	Particle porosity	-
ε_r	Particle emmissivity	-
ϕ	Transportable quantity	-
ϕ_t	Thiele modulus	-
ϕ_{ij}	Pressure strain term in RSM	$m^2.s^{-3}$
γ	Heat transfer correlation constant	-
η	Oxygen-to-concentrate ratio	-
η_c	Combustion effectiveness factor	-
η_h	Heat transfer effectiveness factor	-
η_p	Particle reaction effectiveness factor	-

φ	Heat transfer correlation constant	-
κ	Heat transfer correlation constant	-
λ	Gas phase thermal conductivity	$W.(m.K)^{-1}$
μ	Viscosity	$Pa.s$
μ_e	Fluid effective viscosity	$kg.(m.s)^{-1}$
μ_t	Turbulent viscosity	$kg.(m.s)^{-1}$
ν	Kinematic viscosity	$m^2.s^{-1}$
ν_{CO2}	Stoichiometric coefficient for carbon dioxide	$kg_{CO_2}.kg_{char}^{-1}$
ν_i	Stoichiometric coefficient of component i	$kg_i.kg_{feed}^{-1}$
ν_{O2}	Stoichiometric coefficient for oxygen	$kg_{O_2}.kg_{char}^{-1}$
θ	Thring-Newby parameter	-
θ_R	Radiation intensity equivalent temperature	K
ρ	Density	$kg.m^{-3}$
ρ_a	Ambient gas density	$kg.m^{-3}$
ρ_o	Fresh mixture gas density	$kg.m^{-3}$
ρ_p	Particle density	$kg.m^{-3}$
σ	Oxygen enrichment of feed gas (volume fraction of oxygen in the feed gas)	-
σ_{sb}	Stefan-Boltzman constant	$W.(m^2.K^4)^{-1}$
Ω	Out-scattering direction of radiation in the Radiative Transfer Equation	steradians
Ω_k	Angular velocity	$rad.s^{-1}$
Ω'	In-scattering direction of radiation in the Radiative Transfer Equation	steradians
τ	Shear stress	Pa
τ_c	Cloud combustion time	s
τ_{col}	Time between interparticle collisions	s
τ_h	Cloud heat-up time	s
$\tau_{I,c}$	PI controller Integral time constant	s
τ_{iso}	Isolated particle combustion time	s
τ_p	Pore tortuosity	-
τ_{res}	Cloud residence time	s
$\tau_{r,p}$	Particle relaxtion time	s
τ_{rr}	Viscous flux of r-momentum in r-direction	Pa
τ_{rz}	Viscous flux of z-momentum in r-direction	Pa
τ_{zz}	Viscous flux of z-momentum in z-direction	Pa
$\tau_{\theta r}$	Viscous flux of r-momentum in θ-direction	Pa
$\tau_{\theta z}$	Viscous flux of z-momentum in θ-direction	Pa
ω_j	Quadrature summation term	-
ξ_i	Directional cosines	-
ψ	Convective heat transfer constant	-

Acknowledgements

1 Introduction

1.1 Flash Smelting

Outokumpu and Inco developed the flash smelting process co-currently in the 1930's to 1940's. Since then, the Outokumpu process has become the most popular method to pyrometallurgically treat copper sulfide minerals. A diagram of an Outokumpu flash furnace is shown below in Fig. 1-1.
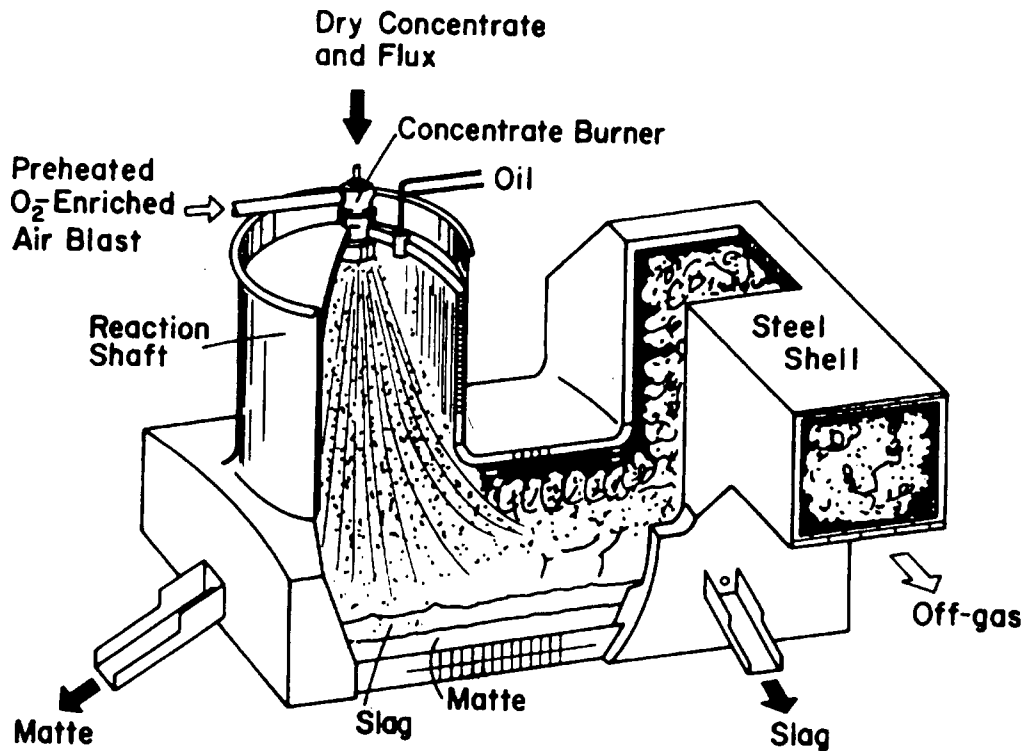
Figure 1-1: Outokumpu Flash Smelting Furnace[1]

1

Concentrate, flux and oxygen-enriched air are injected from the top of the reaction shaft and are heated to ignition by convection from the surrounding gases and radiation from the furnace walls. Once ignited, the sulfide particles react with the available oxygen and fall through the reaction shaft before being collected in the settler where a molten bath is formed. Within the bath, iron oxide and silica flux react to form a liquid fayalite slag while the remaining copper, iron and sulfur species form a more dense matte phase. The slag and matte are tapped from the furnace at regular intervals.

Chalcopyrite-based concentrates, which consist of a mixture of chalcopyrite and pyrite and have a grade of between 25 and 30 weight percent copper, have been the most common feed material for copper flash smelters. As a result, the design and operation of copper flash furnaces has developed around the use of chalcopyrite concentrates. However recently, so-called high-grade concentrates have become important to the flash smelting process as they are being used to supplement chalcopyrite concentrates. These high-grade concentrates are based on secondary copper sulfide minerals such as bornite or chalcocite. One of the most important of these is Escondida concentrate.

High-grade concentrates influence the flash smelting behaviour of the blend through their intrinsic kinetics and their influence on the furnace heat and mass balance. Most modern flash smelters are operated autogeneously, with all of the heat required to maintain the furnace at temperature being supplied from the exothermic combustion reactions. The oxygen concentration in the feed-gas (termed "enrichment") is controlled to maintain the furnace temperature. Performing a heat and mass balance over BHP's San Manuel furnace indicates that in order to smelt chalcopyrite to an aim matte grade of

63 wt% (defined as the weight percent copper in the matte), the oxygen enrichment is approximately 50 vol%. As the quantity of fuel in the blend is depleted by adding high-grade concentrates, the amount of dilution nitrogen must be reduced. At an Escondida loading of approximately 45 wt%, representing the maximum possible loading of the Escondida in the blend, the required oxygen enrichment is 100 vol%. The influence of high-grade concentrate on the heat and mass balance of the furnace is discussed in more detail in Section 1.3.

While an Escondida loading of 45-wt% represents the theoretical upper limit, BHP's San Manuel flash smelter cannot attain this loading. At oxygen enrichments greater than approximately 80-vol %, unsmelted concentrate begins to form at the bottom of the reaction shaft causing the furnace to fail.[2] As a result, to ensure stable operation, the BHP San Manuel furnace is restricted to operate at oxygen enrichments less than 80-vol%. This phenomenon has been observed in other flash smelters using Escondida concentrate and also in the BHP San Manuel furnace when other high-grade concentrates have been used. Some flash smelters have been able to increase the Escondida loading of the blend by adding pyrite to the blend.[3]

1.2 Escondida Concentrate

Escondida, which is located in northern Chile, is the world's largest copper mine[4] producing 800,000 tonnes per year of copper as cathode and concentrate. As of May, 1996, Escondida's proven and probable reserves were estimated to be 2.1 billion tonnes, with an average grade of 1.28% copper and an economic cut-off of 0.7% copper, giving the mine a productive life in excess of 40 years. At a copper price of $US0.80 per

pound these reserves are equivalent to $US47 billion dollars, making the mine important to all project partners, especially BHP, which owns 57.5% of the project and operates the mine on behalf of the other project partners.

The chemical analysis of Escondida concentrate is shown in Table 1-1 in comparison with San Manuel Concentrate, which is a typical chalcopyrite based concentrate. Also shown in Table 1-1 is a typical aim mate grade for the flash smelting process. It shows that Escondida has a high copper, and correspondingly low iron, content. Note that this grade is changing with time. However, the chalcocite content will remain high throughout the life of the mine.

Table 1-1: Escondida Concentrate Composition (Percent by Mass)

Element	Escondida Concentrate	San Manual Concentrate	Aim Matte Grade
Cu	49.0	29.4	63
Fe	11.9	31.6	13.4
S	26.7	29.9	23.6
Gangue	12.4	9.1	-

A mineralogical study of the concentrate has shown that Escondida consists of approximately 64.1 wt% chalcocite, 26.2 wt% pyrite and 12.4% gangue. SEM analysis showed that single particles can range in composition from pure mineral phases to mixtures of mineral phases in any combination, with chalcocite tending to concentrate in the smaller size, as shown in Fig. 1-2.
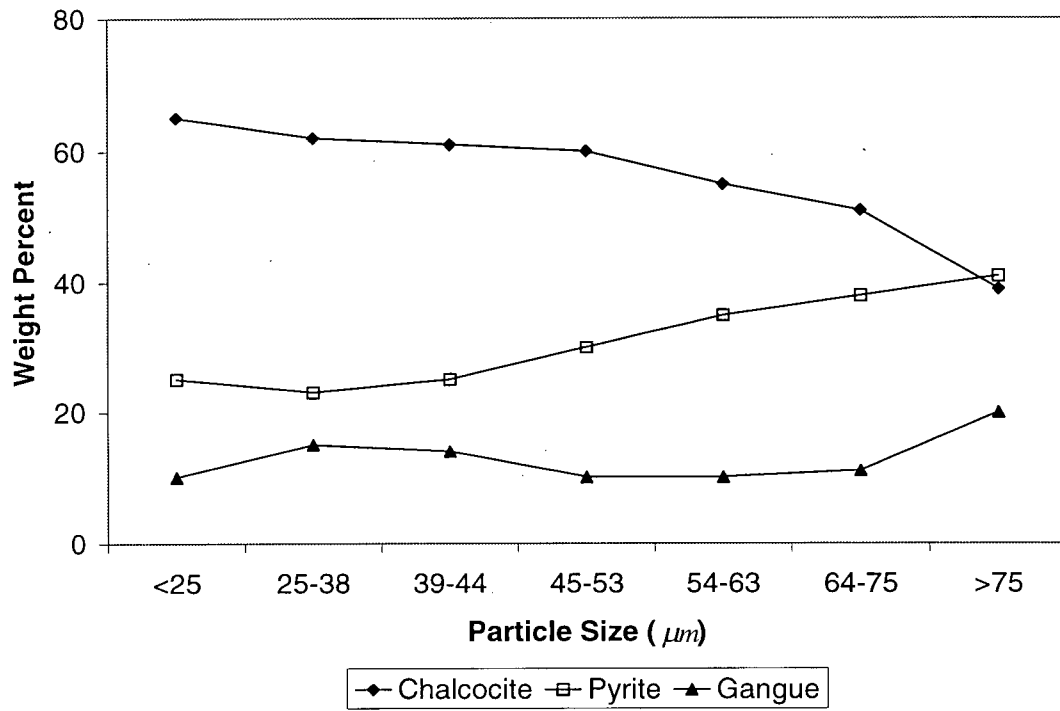
Figure 1-2: Escondida Concentrate Mineralogical Composition as a Function of Particle Size

Figure 1-3 shows the weight percent of the different particle types as a function of
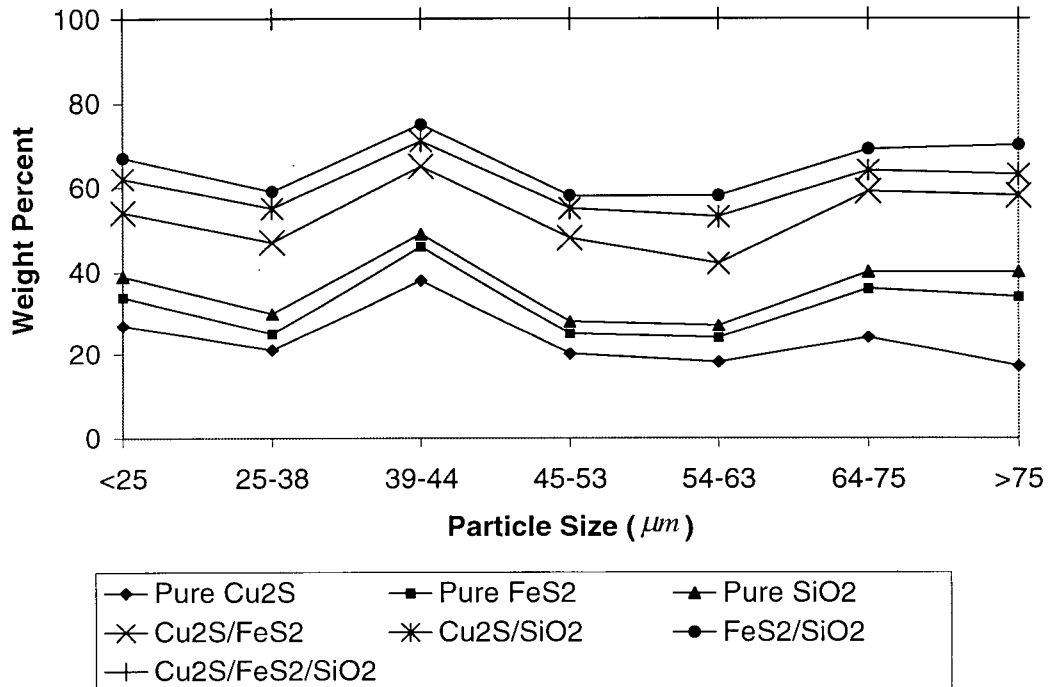
particle size.

Figure 1-3: Escondida Concentrate Particle Types as a Function of Particle Size

Escondida concentrate is toll smelted; this means that the Escondida mine pays treatment and refining charges for smelters to process the concentrate, with the mine taking delivery of the refined copper. By understanding the problems associated with the smelting of Escondida concentrate the mine can facilitate the smelting of Escondida concentrate which will result in a direct economic benefit to the Escondida mine.

Therefore it is the aim of this study to determine the effects of adding Escondida concentrate to the blend with the hope of increasing the Escondida loading that can be treated by a flash smelting furnace. Because similar problems have been observed for other high-grade concentrates, results obtained from this study can also be applied to other high-grade concentrates.

6

1.3 Influence of High-Grade Concentrate on Furnace Operation

As high-grade concentrate is added to the blend, two important constraints influence the flash smelting characteristics of the blend. Firstly, the aim matte grade and production rate are constrained to optimise the operational performance of the entire production train. Secondly, most modern Outokumpu furnaces are operated autogeneously, with all of the heat required to maintain the furnace temperature being supplied from the exothermic combustion reactions. These two constraints place restrictions on two key operating parameters, the oxygen-to-concentrate ratio, which is governed by the extent of reaction required to achieve the aim matte grade, and the level of oxygen enrichment, which is controlled in order to maintain the furnace heat balance. The oxygen-to-concentrate ratio is defined as the kilograms of oxygen charged to the furnace per kilogram of concentrate, while the oxygen enrichment is defined as the volume percent oxygen in the feed gas. The definition for the oxygen enrichment and oxygen-to-concentrate ratio are discussed in more detail by Biswas and Davenport[5].

Here we provide an analysis of the influence of high-grade concentrate on the heat and mass balance of a flash furnace, with particular reference to its effect on the oxygen-to-concentrate ratio and the level of oxygen enrichment. The analysis is based on the theory of flash smelting described by Davenport and Partelpoeg[1]. In this analysis, chalcopyrite is used to represent a typical grade concentrate, while Escondida represents a high-grade concentrate.

1.3.1 Furnace Mass Balance

The furnace mass balance is primarily concerned with achieving the aim matte grade and production rate. This is achieved by controlling the concentrate feed-rate and oxygen-to-concentrate ratio.

1.3.1.1   Concentrate Feed Rate

High-grade concentrate contains more copper per unit mass than a typical chalcopyrite-based concentrate. Therefore, as it is added to the blend, in order to achieve the same matte grade and production rate, the concentrate feed rate must decrease. This can be shown by conducting a copper balance over the furnace assuming that all of the copper reports to the matte phase. The concentrate feed rate is related to the concentrate and aim matte grades and the aim matte production rate by:

$$\dot{m}_{feed} = \frac{amg}{fg}\dot{m}_{matte} \qquad\qquad (1\text{-}1)$$

1.3.1.2   Oxygen-to-Concentrate Ratio

If concentrate particles are exposed to a hot environment with sufficient oxygen to achieve complete reaction, the particles react to form a Fe_3O_4/CuO mixture. In a flash smelter, in order to achieve the aim matte grade, the oxygen-to-concentrate ratio is controlled to stop the reaction at an intermediate stage.

8

Figure 1-4 describes the overall process in the flash smelter reaction shaft and

bath and shows that a concentrate can be represented as a mixture of Cu_2S, FeS and

volatile sulfur, while the matte can be represented as a mixture of Cu_2S and FeS.
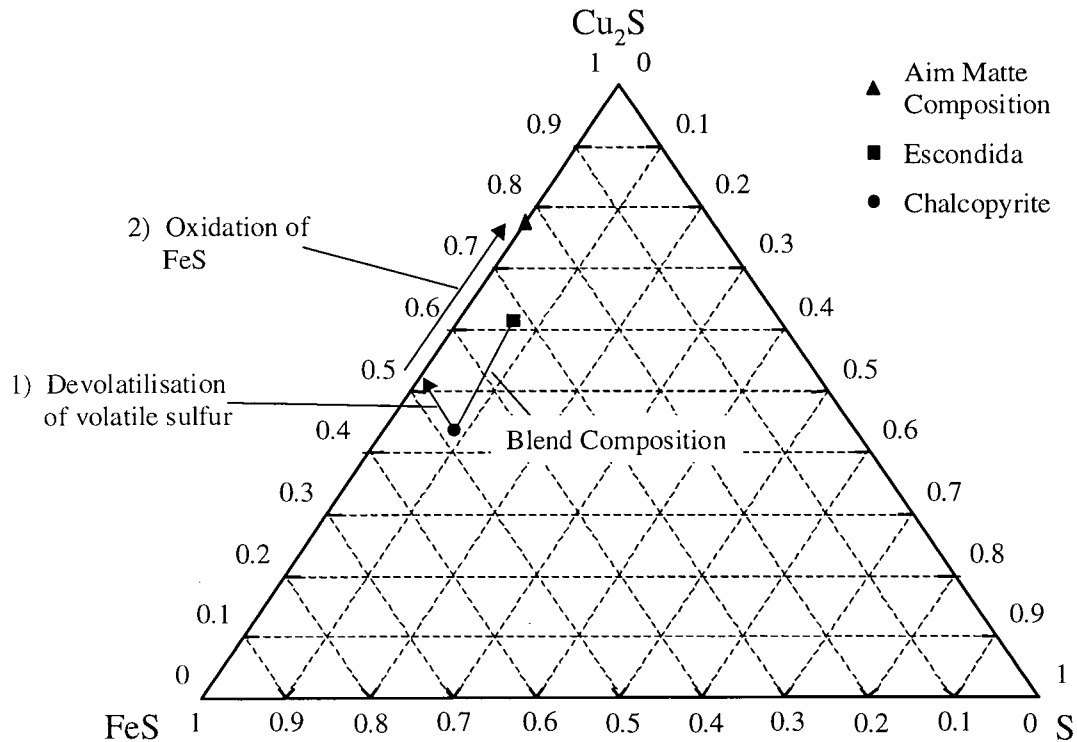
Figure 1-4 : Flash Smelting Ternary Diagram

Figure 1-4 shows that the overall smelting process can be described in two steps.

Firstly the volatile sulfur is released and reacts with oxygen to form sulfur dioxide

leaving a Cu_2S/FeS mixture. Once the volatile sulfur is removed the FeS reacts with the

remaining oxygen to produce FeO and sulfur dioxide leaving a matte phase of the desired

grade.

This two-step description is an overall representation of the smelting process.

However, because individual particles follow unique trajectories through the shaft,

particles undergo different extents of reaction. Particles which experience a relatively hot, oxygen rich environment are over-oxidised while other particles encountering a cooler or lower oxygen environment are under-oxidised. Once the particles fall into the bath, they react with the slag and matte, with the bath composition approaching thermodynamic equilibrium. As a result, the global mass balance for the flash smelting process can be described by the following set of reactions, assuming that chalcopyrite is the main constituent of the concentrate:

$$CuFeS_2 \rightarrow FeS + \frac{1}{2} Cu_2S + \frac{1}{4} S_2 \qquad (1\text{-}2)$$

$$\frac{1}{2} S_2 + O_2 \rightarrow SO_2 \qquad (1\text{-}3)$$

$$FeS + \frac{3}{2} O_2 \rightarrow FeO + SO_2 \qquad (1\text{-}4)$$

$$2FeO + SiO_2 \rightarrow Fe_2SiO_4 \qquad (1\text{-}5)$$
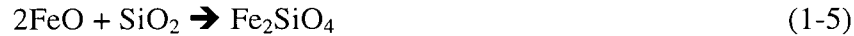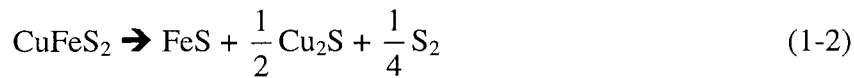
Reaction (1-2) goes to completion since the loss of volatile sulfur is a function of temperature alone. Reaction (1-3) also goes to completion because the gas phase oxidation of sulfur is much faster than the heterogeneous oxidation of FeS. The extent of conversion for Reaction (1-4) is limited by the amount of oxygen added to the concentrate so as to only oxidise sufficient FeS to produce the aim matte grade. The oxygen-to-concentrate ratio is clearly important as it limits how much FeS reacts and therefore determines the matte grade. These reactions represent the global mass balance, however, because individual particle experience unique conditions within the furnace some particles will be over-oxidised with some of the chalcocite reacting according to:

$$Cu_2S + 2O_2 \rightarrow 2CuO + SO_2 \qquad (1\text{-}6)$$

Upon entering the hearth the CuO reverts back to Cu_2S through reaction with FeS.

A mass balance over the furnace allows determination of the oxygen-to-concentrate ratio required to achieve the matte grade. If silica and nitrogen are ignored, then the concentrate and oxygen streams are the only furnace inputs, while the output streams are FeO, FeS, Cu_2S and SO_2. An elemental balance together with a constraint equation to ensure that the aim matte grade is achieved can be used to determine the flow rates of each stream. Table 1-2 shows the five equations that define the furnace mass balance. In these equations the coefficients arise from the mass fraction of the given constituent in the material. These equations are derived by Davenport and Partelpoeg[1] and assume that all of the copper reports to the matte phase and that no Fe_3O_4 is present in the slag phase.

Table 1-2: Flash Furnace Mass Balance Equations

Element	Balance
Copper	$0.7988\,\dot{m}_{Cu_2S} = f_{cu}\,\dot{m}_{feed}$
Iron	$0.635\,\dot{m}_{FeS} + 0.777\,\dot{m}_{FeO} = f_{fe}\,\dot{m}_{feed}$
Sulfur	$0.201\,\dot{m}_{Cu_2S} + 0.365\,\dot{m}_{FeS} + 0.5\,\dot{m}_{SO_2} = f_s\,\dot{m}_{feed}$
Oxygen	$\dot{m}_{O_2} - 0.223\,\dot{m}_{FeO} - 0.5\,\dot{m}_{SO_2} = 0$
Overall	$(0.799 - amg)\dot{m}_{Cu_2S} - (amg)\dot{m}_{FeS} = 0$

This set of linear equations can be represented in matrix form as follows:

$$
\begin{bmatrix}
0.798 & 0 & 0 & 0 & 0 \\
0 & 0.635 & 0.777 & 0 & 0 \\
0.202 & 0.365 & 0 & 0.5 & 0 \\
0 & 0 & 0.223 & 0.5 & -1 \\
(0.798 - amg) & -amg & 0 & 0 & 0
\end{bmatrix}
\begin{bmatrix}
\dot{m}_{Cu_2S} \\
\dot{m}_{FeS} \\
\dot{m}_{FeO} \\
\dot{m}_{SO_2} \\
\dot{m}_{O_2}
\end{bmatrix}
=
\begin{bmatrix}
f_{cu}\,\dot{m}_{feed} \\
f_{fe}\,\dot{m}_{feed} \\
f_{s}\,\dot{m}_{feed} \\
0 \\
0
\end{bmatrix}
\qquad (1\text{-}7)
$$

This matrix equation can be inverted, and the five unknown flow rates can be determined by solving the equation:

$$
\begin{bmatrix}
\dot{m}_{Cu_2S} \\
\dot{m}_{FeS} \\
\dot{m}_{FeO} \\
\dot{m}_{SO_2} \\
\dot{m}_{O_2}
\end{bmatrix}
=
\begin{bmatrix}
0.798 & 0 & 0 & 0 & 0 \\
0 & 0.635 & 0.777 & 0 & 0 \\
0.202 & 0.365 & 0 & 0.5 & 0 \\
0 & 0 & 0.223 & 0.5 & -1 \\
(0.798 - amg) & -amg & 0 & 0 & 0
\end{bmatrix}^{-1}
\bullet
\begin{bmatrix}
f_{cu}\,\dot{m}_{feed} \\
f_{fe}\,\dot{m}_{feed} \\
f_{s}\,\dot{m}_{feed} \\
0 \\
0
\end{bmatrix}
\qquad (1\text{-}8)
$$

If the concentrate composition is known together with the aim matte grade and production rate, then Equation (1-1) can be used to determine the concentrate feed rate and Equation (1-8) can be solved to give the oxygen feed rate and the oxygen to concentrate ratio.

Using the above technique to close the furnace mass balance, assuming an aim matte grade and production rate of 63 wt% and 110 tph respectively, the oxygen-to-concentrate ratio can be determined as a function of Escondida loading. Table 1-3 shows the total concentrate feed rate and composition, oxygen flow rate and oxygen-to-concentrate ratio as a function of Escondida loading.

Table 1-3: Mass Balance Calculations

Escondida Loading Wt%	Concentrate Feed rate (tph)	Concentrate Grade Wt%	Oxygen Flow rate (tph)	Oxygen to Concentrate Ratio
0	200	34.7	57.0	0.285
5	195	35.6	53.9	0.275
10	192	36.5	51.0	0.265
15	188	37.5	48.1	0.255
20	184	38.5	45.4	0.245
25	181	39.5	42.7	0.236
30	177	40.5	40.2	0.226
35	174	41.5	37.7	0.216
40	171	42.5	35.4	0.206

As the Escondida loading increases from 0 to 40 wt%, the concentrate grade increases from 35 to 42 wt% Copper and, as a direct result of Equation (1-1), the required concentrate feed rate decreases from 200 to 171 tph. Also, as Escondida is added to the blend, less iron and sulfur are required to be oxidised to achieve the aim matte grade. As a result, the oxygen-to-concentrate ratio decreases from 0.285 to 0.206, increasing the particle number density of the cloud. As shown in Chapter 3, the particle number density of the cloud is important in determining the interactive effects within the cloud during cloud combustion and is therefore expected to influence the burning rate of the cloud.

1.3.2 Heat Balance

While the mass balance is concerned with maintaining the matte grade and production rate, the heat balance is aimed at maintaining the desired matte, slag and off-gas temperature, while ensuring that the furnace operates autogeneously. This is achieved by controlling nitrogen feed to the furnace.

The oxidation reactions for sulfur and FeS are exothermic, liberating heat, which, for a chalcopyrite-based concentrate burning in pure oxygen, is in excess of that required to maintain the flash smelter at its operating temperature. As a result, dilution nitrogen is added to the reaction gas to carry excess heat away in the furnace off-gases. For an industrial furnace, the process parameter used to control the flow of dilution nitrogen is the level of oxygen enrichment. The oxygen enrichment required to close the heat balance can be determined from a steady state heat balance over the furnace. Figure 1-5 shows the heat inputs and outputs for a flash furnace.
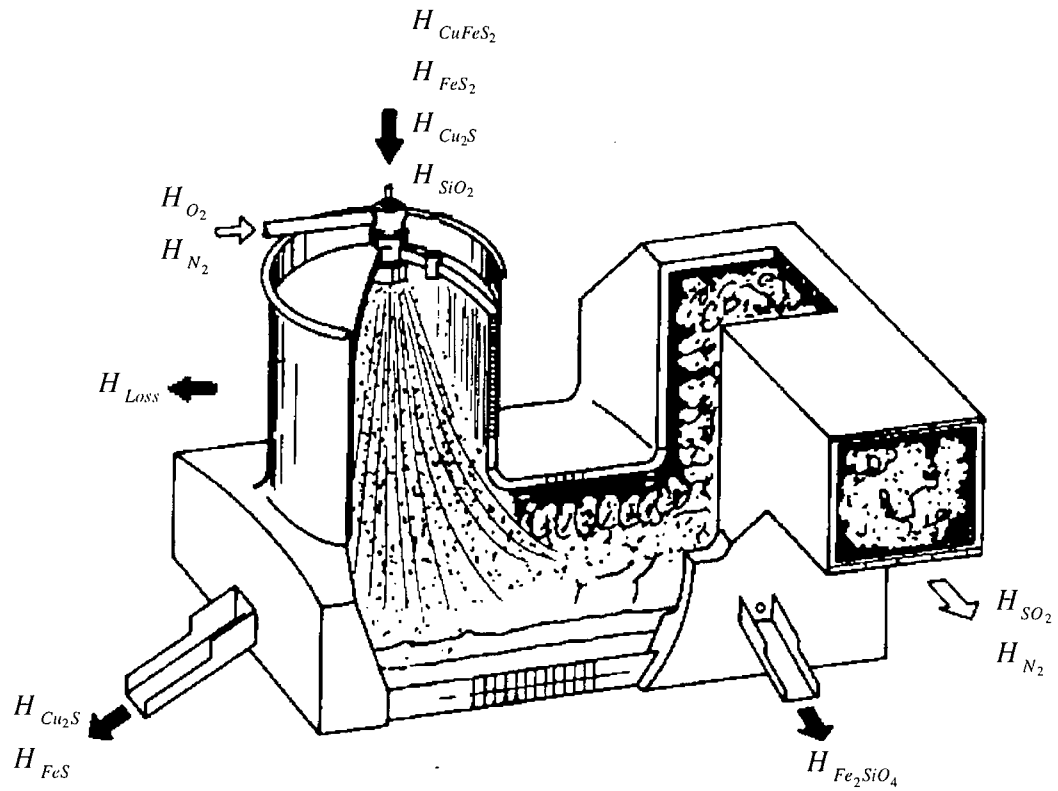
Figure 1-5: Heat Inputs and Outputs of the Furnace

The enthalpies of the input streams are balanced by the enthalpies of the output streams and the heat losses from the furnace i.e.:

$$\dot{m}_{N_2} h_{N_2,in} + \sum \dot{m}_{i,in} h_{i,in} = \sum \dot{m}_{i,out} h_{i,out} + \dot{m}_{N_2} h_{N_2,out} + H_{loss} \qquad (1\text{-}9)$$

Here h_i is the specific enthalpy of species i at the stream temperature and $\dot{m}_i$ is the corresponding mass flow rate. If the aim matte slag and off-gas temperatures are known and the mass balance, (Equation (1-8)), is solved, then the only unknown in Equation (1-9) is the nitrogen mass flow rate. Hence the required nitrogen flow rate and the level of oxygen enrichment can be determined by rearranging Equation (1-9) to give:

$$\dot{m}_{N_2} = \frac{\sum \dot{m}_{i,in} h_{i,in} - \sum \dot{m}_{i,out} h_{i,out} - H_{loss}}{h_{N_2,out} - h_{N_2,in}} \qquad (1\text{-}10)$$

For high-grade concentrates, less iron and sulfur are required to be oxidised. As a result, less heat is liberated in achieving the aim matte grade and production rate. However, the heat load on the furnace remains relatively constant as both the matte production rate and furnace heat losses remain unchanged. Therefore, less dilution nitrogen is required to close the heat balance and the oxygen enrichment of the reaction gas increases. At some concentrate grade, the required oxygen enrichment is 100%, representing the upper limit on the concentrate grade that can be smelted autogeneously.

The oxygen enrichment for a typical furnace can be determined as a function of the Escondida loading using Equation (1-10). The mass flow rate of each stream can be obtained from the mass balance calculations and the specific enthalpies of the species can

15

be calculated from values listed by Davenport[1] assuming matte, slag and off-gas temperatures of 1220, 1260 and 1400 °C, respectively. The only difficult term to determine in Equation (1-10) is the furnace heat loss term. In this study this value was assumed to be 22MW[3], a typical value for an industrial furnace. Table 1-4 shows the concentrate feed rate, oxygen and nitrogen feed rates, oxygen partial pressure and gas to concentrate ratio as functions of Escondida loading.

Table 1-4: Heat Balance Calculations

Escondida Loading (wt%)	Concentrate Feed rate (tph)	Oxygen Flow rate (tph)	Nitrogen Flow rate (tph)	Oxygen Enrichment (vol %)	Gas-to-Concentrate ratio
0	200	57.0	54.5	47	0.558
5	195	53.9	46.7	50	0.514
10	192	51.0	39.3	53	0.470
15	188	48.1	32.2	56	0.426
20	184	45.4	25.3	61	0.383
25	181	42.7	18.7	66	0.339
30	177	40.2	12.4	73	0.295
35	174	37.7	6.2	84	0.252
40	171	35.4	0.3	98	0.208

As Escondida is added to the blend, the amount of dilution nitrogen required falls considerably until, at an Escondida loading of approximately 40 wt%, pure oxygen is required to maintain the heat balance. This increase in the oxygen enrichment, coupled with the decrease in the oxygen-to-concentrate ratio, lowers the gas velocity at the burner exit and increases the particle number density of the cloud. At an Escondida loading of 40 wt%, the burner exit velocity is 3.33 times lower and the particle number density 2.85 time higher than the respective values for a chalcopyrite-based concentrate. These two factors are expected to affect the flash smelting process adversely.

1.4 Chapter Summary

Escondida is an important high-grade concentrate which is toll smelted. Addition of excessive quantities of Escondida concentrate to the blend of the flash smelter may cause operational difficulties. In particular, at Escondida loadings lower than the theoretical limit, unsmelted concentrate is observed to form at the bottom of the reaction shaft. It is the aim of this project to understand and suggest solutions to the problems associated with the flash smelting of Escondida and other high-grade concentrates.

2 Literature Review

As will be seen in the following literature review, many studies have been conducted on the intrinsic reaction rate, the single particle combustion mechanisms, and the modelling of a flash smelting flame for different copper sulfide minerals. However, there have been few studies reported on the flash smelting behaviour of a concentrate blend. Results from the heat and mass balance analysis of Chapter 1 shows that to fully understand the effect of high-grade concentrates on the flash smelting process requires knowledge not only of their intrinsic reaction rates, but also of their effect on the smelting characteristics of the blend. Section 2.2 briefly describes work conducted by workers in the coal combustion field who developed the concept of group combustion theory which can be applied to this problem. Because these theories are new to copper concentrate flash smelting, they are discussed in more detail in Chapter 3.

2.1 Sulfide Flash Smelting

2.1.1 Single Particle Kinetics

2.1.1.1 Reaction Mechanisms and Kinetics

2.1.1.1.1 Chalcopyrite

Chaubal and Sohn[6] determined the pre-exponential factor and activation energy for chalcopyrite oxidation in the absence of mass transfer limitations using a thermogravimetric technique and X-ray diffraction to determine the reaction pathway. At

temperatures below 600°C the reaction proceeded by surface oxidation of the chalcopyrite to copper sulfate and hematite, while at temperatures above 600°C the mechanism was assumed to be decomposition of chalcopyrite to chalcocite and phyrotite followed by oxidation of these sulfides.

Munroe et al[7] used an electrically heated laboratory scale flash smelting reactor to investigate the reactions of chalcopyrite and pyrite during the flash smelting process. Samples of partially reacted concentrate were collected from the reactor and studied via an optical microscope and electron microprobe analysis. Results showed that for oxygen-to-concentrate ratios lower than that required for complete reaction, most particles consisted of intermediate solid solution intergrown with bornite, magnetite, copper, silica and copper iron spinel. From these results, Munroe developed a complex mechanism for the oxidation of chalcopyrite which is described in [7].

2.1.1.1.2 Chalcocite

A thermogravimetric technique was used by several authors[8-11] to study the oxidation kinetics of chalcocite. In all these studies, investigation of the partially reacted pellets revealed a chalcocite core surrounded by a layer of Cu_2O which in turn was surrounded by a layer of CuO. Kim and Themelis[9] determined the activation energy for the oxidation of Cu_2S to CuO in the absence of mass transfer limitation to be $E_a = 520 \frac{kJ}{mol}$, showing that the oxidation reaction is sensitive to the pellet temperature.

Henderson[12] investigated the roasting characteristics of pyrite, chalcopyrite, bornite and chalcocite and found that minerals which contain high levels of iron reacted faster than those with lower iron levels. Asaki et al.[13-17] studied the oxidation of mixed copper iron sulfide pellets using a thermogravimetric technique and found that the reaction proceeded via a two-stage mechanism. Iron was initially oxidised at the pellet surface with no sulfur dioxide being produced. Once the sulfide had become sufficiently depleted in iron, the sulfur began to react in parallel with the iron.

2.1.2 Laminar Flow Furnace

With the exception of Munroe[7], all studies cited above used thermogravimetric techniques to observe the oxidation reactions. In these studies, the heat and mass transfer conditions experienced by the pellets did not reflect those experienced by the particles in a flash smelting furnace. Therefore, other studies have been conducted using a laminar flow furnace which more accurately approximates the conditions experienced by particles in the flash smelting furnace.

Jorgensen and Segnitt[18] used a laminar flow furnace to study the oxidation of chalcopyrite as a function of furnace temperature, oxygen partial pressure and particle size. The reaction rate was monitored by determining the change in the particle's sulfur content as a function of the furnace residence time. Studying the reaction in this manner allowed the reaction rate to be observed and showed that the reaction pathway could be broken into three different regimes. Upon entering the furnace the particles underwent a

preheat stage where they were heated to their ignition temperature; in this stage essentially no reaction occurred. After ignition, the particle entered the combustion stage where the reaction proceeded at an almost constant rate, indicating that the combustion process was controlled by oxygen mass transfer to the particle surface. Towards the end of the reaction, the rate decreased, and this stage was termed particle burnout.

Jorgensen[19] conducted further experiments using a two-colour pyrometer to measure particle temperatures and developed a mathematical model to compute the temperature and composition histories of the particle. Accurately predicting the measured temperatures required the model to assume a copper vaporisation rate much higher than would be expected from the measured temperatures. This anomaly can be explained by the low sampling frequency of the two-colour pyrometer which was insufficient to resolve the maximum temperature reached by the particle during combustion. Later work by Tuffrey[20-22] used an improved data acquisition system to measure the particle temperature and therefore allowed the temperature history of the combusting particle to be resolved in finer detail.

Hahn and Sohn[23] investigated the ignition and combustion characteristics of a chalcopyrite concentrate using a laminar flow furnace with the aim of validating a single particle combustion model which was used to describe particle combustion in a CFD model of a flash furnace shaft. Results from the laminar flow furnace study showed that the reaction time decreased with decreasing particle diameter, increasing wall temperature and increasing oxygen partial pressure. CFD model results showed that the overall reaction time of the particles in the flash furnace is more sensitive to particle size

21

than in the laminar flow furnace because of the continually decreasing oxygen concentration experienced in the flash furnace.

Since these pioneering studies, other authors have used laminar flow reactors to study the single particle combustion kinetics of a range of copper and nickel sulfide minerals. Some of these studies can be found in [24-27].

2.1.3 Single Particle Combustion Models

Shook et al.[28] developed a model for single particle combustion of chalcocite and used it to investigate the dusting phenomena of Inco's MK concentrate. Incorporated into the model was the assumption proposed by Jorgensen[19] that the particle was limited to temperatures below copper's boiling point due to copper vaporisation. Results showed good agreement between the predicted and measured ignition temperatures; however, at temperatures close to copper's boiling point, the predicted particle mass loss rate and temperatures were lower then those observed in experiments. As a result, the authors concluded that copper vaporisation below the boiling point did not limit particle temperature and that particle fragmentation and dusting were caused by copper boiling within the particle. The authors were then able to determine the oxygen partial pressure, gas phase temperature and particle sizes that resulted in the particle temperature exceeding copper's boiling point and therefore gave rise to particle fragmentation and dusting.

2.1.4 Sulfide Flame Studies

Shook[29] studied the flash converting flame produced from Inco's MK concentrate in a pilot scale flash smelter with the aim of reducing dust formation within the flame. A CFD model was developed to describe the process and, among other things, predicted the temperature and oxygen concentration fields within the flame that were coupled with results from the single particle combustion model to determine regions in the flame where dusting was expected to occur. Further analysis of the CFD results showed that large variations in the degree of particle reaction were predicted because of the temperature and concentration gradients within the flame. Particles at the outer edge of the jet were heated rapidly, experienced a high oxygen concentration and therefore reacted to copper oxide, while particles close to the jet centre were heated less rapidly and experienced a lower oxygen concentration and therefore remained under-reacted.

Munroe[30] simulated the flash smelting of copper concentrates in a 0.13 m diameter by 2 m long flash reactor. The degree of particle oxidation and stream temperature were studied as functions of oxygen enrichment, concentrate feed rate and oxygen loading. He defined the oxygen loading as the mass of oxygen to mass of concentrate ratio.

The effect of increasing oxygen enrichment was to increase the stream temperature, moving the flame front closer to the burner tip. Increasing the concentrate feed rate delayed the onset of the flame due to increased heat load. As the oxygen loading was increased, the peak temperature increased until a maximum was reached at an oxygen loading of 0.45. Further increases in oxygen loading caused a reduction in the

peak stream temperature and a delay in flame formation. This was attributed to the increased heat load that results from the greater gas mass flowrate at the higher oxygen loadings.

Both these studies show that heat and mass transfer within the concentrate cloud are important in determining the time to reach ignition and the variation in the degree of oxidation of individual particles. Therefore any study that attempts to describe the effect of Escondida on the flash smelting process must consider the effect of Escondida loading on the heat and mass transfer within the particle cloud.

Many other authors have conducted CFD studies simulating combustion reactions within a flash smelting shaft with the aim of gaining insight into the phenomena occurring within the flame. Some of these are given in references [23,31-37]

2.2 Ignition and Combustion Theory

Studies on flash smelting have focused on reaction-pathway, single particle combustion models and CFD models to predict the reaction rate of the particles within the flash furnace. In these studies, the effect of individual variables on the reaction rate were investigated and, while this is useful, it does not help gain an in-depth understanding of the important physical phenomena occurring within the flame of a flash smelter. Conversely a large amount of work has been conducted on pulverised coal combustion, and various studies have found that the particle number density of the cloud is important in determining the heat and mass transfer conditions experienced within the cloud. Results from these studies can be used to help understand phenomena occurring in

24

flash smelting. Following is a brief discussion of these studies. Because of their importance to the flash smelting of high-grade concentrate, they are discussed in more detail in Chapter 3.

2.2.1 Interactive Effects[38]

When a particle reacts within a cloud, interactive effects, such as competition for available oxygen and the insulating effect of surrounding particles, alter the Sherwood and Nusselt numbers experienced by the particles within the cloud. As a result, the ignition and combustion characteristics of the particles within the cloud differ from those of an isolated particle. Gieras et al[39] were among the first authors to realise that interparticle spacing was important in influencing the total reaction time of the particles within the cloud. Ryan and Annamalai[40] showed that the group combustion number, which incorporates the effect of interparticle spacing through the particle number density, can be used to describe the interactive effects occurring in group combustion. In Equation (2-1), G is the group combustion number, n is the particle number density, d_p is the particle diameter and d_b is the burner diameter.

$$G = \frac{\pi}{2} n d_p d_b^2 \qquad (2\text{-}1)$$

They showed that the ignition time of a cloud of coal particles is made up of four different time scales and used the group combustion number to describe the influence of interparticle space on these time scales. The first time scale is the thermal wave penetration time, which can be thought of as the time required to heat the cloud to the ignition temperature. The second time scale is the particle heat-up time, i.e. the time

25

required to heat individual particles. Within the cloud a mass transfer time scale is also important in determining the time required to achieve a flammable mixture in the gas phase due to pyrolysis and diffusion of chemical species within the cloud. The final time scale is the induction time for chemical reactions.

Their results indicated that, for small group combustion numbers, increasing the group combustion number causes an increase in ignition time due to the higher thermal load which increased the thermal wave penetration time. As the group combustion number was further increased, a flammable gas mixture could form, allowing homogenous ignition to occur outside the cloud. During this stage, an increase in the group combustion number causes two competing effects: the increase in the particle number density provides additional volatiles which reduce the flammable mixture formation time but increases the thermal load and therefore the thermal wave penetration time. For intermediate group combustion numbers the decrease in the flammable mixture formation time is greater than the increase in the thermal wave penetration time, causing a decrease in the ignition time. As the group combustion number increases further, the thermal wave penetration time begins to dominate causing an increase in the ignition time. Figure 2-1 shows the change in combustion behavior as the particle number density and thus the group combustion number is increased.

Single Particle	Intermediate	Group
Heterogeneous	Homogeneous	Combustion
Combustion	Combustion	

Increasing Group Combustion Number
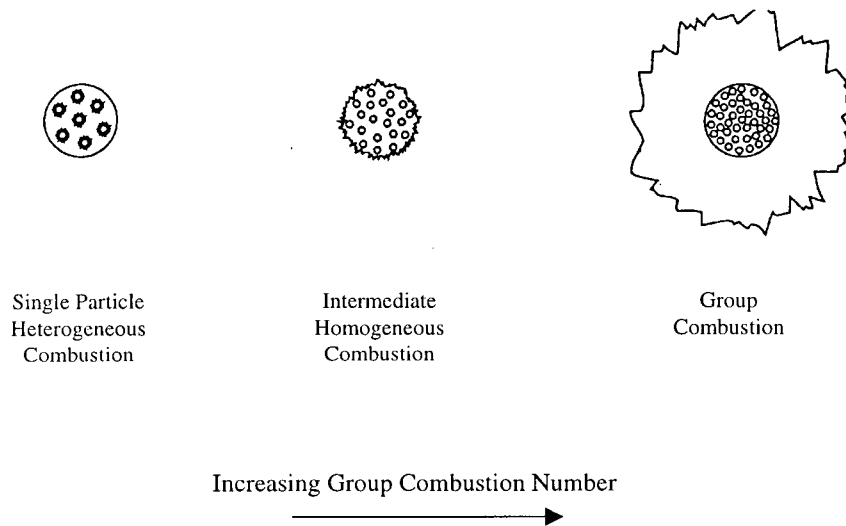
Figure 2-1: Cloud combustion behavior as a function of Group Combustion

2.2.1.1 Cloud Reaction Time

As shown by Jorgensen[19], the reaction time for a sulfide particle can be broken into the time required to reach ignition and the combustion time of the particle and hence both of these must be known to determine the total reaction time. While predicting the ignition and combustion times for a single particle is relatively straightforward, interactive effects within the cloud make prediction of the ignition and combustion times of the cloud more difficult.

2.2.1.2 Cloud Ignition Time

Many studies have been conducted to determine the ignition temperature and the ignition time of a particle using the Frank-Kamenetsky method. Essenhigh[42] offers a review of the current knowledge on ignition theory for particles. Ryan and Annamalai[40] and Krishna and Berlad[42] have extended this theory to include the ignition of a cloud and have shown that the heat transfer within the cloud can be described using a heat

27

transfer effectiveness factor. The heat transfer effectiveness factor relates the heat transfer coefficient experienced by a particle within the cloud to the heat transfer coefficient of an isolated particle. By defining a heat transfer effectiveness factor in this manner allows the ignition temperature and time of the cloud to be calculated using the single particle model with the heat transfer coefficient for an isolated particle modified by the heat transfer effectiveness factor.

2.2.1.3 Cloud Combustion Time

Annamalai and Ramalingam[43] developed the conservation equations for mass, species and heat in order to describe the combustion rate of a coal particle cloud. Under the simplifying assumptions of an isothermal cloud with no Stefan flow, these equations reduced to those which describe the combustion of a porous coal particle which has been discussed in detail elsewhere.[44-48] In their study, Annamalai and Ramalingam[43] defined a combustion effectiveness factor which is analogous to the pellet, or particle, effectiveness factor for porous char combustion. In the equation describing combustion effectiveness factor, the square root of the group combustion number is identical to the Thiele modulus for porous char combustion. Hence the combustion rate of the cloud is expected to decrease as the group combustion number of the cloud increases.

2.2.1.4 Summary of Interactive Effects

Results from the studies conducted on the interactive effects that occur during group combustion show that the ignition and combustion times of the cloud can be predicted using a single particle model by adequately defining heat transfer and combustion effectiveness factors. Using these effectiveness factors allows the reaction

time of the flash smelting cloud to be determined and the important physical phenomena within the cloud to be understood.

2.3 Chapter Summary

Thermogravimetric techniques have been used to determine the intrinsic kinetics of sulfide mineral oxidation; however, the heat and mass transfer conditions for these experiments do not reflect those experienced in a flash furnace. As a result, laminar flow furnaces have been used to study oxidation kinetics in an environment that more closely reflects those experienced in the flash furnace. From these studies, important phenomena such as particle fragmentation and copper vaporisation have been observed and models have been developed to describe the single particle combustion of sulfide minerals. CFD models have also been developed to account for heat and mass transfer in a flash smelting flame with the aim of predicting the reaction rate of the particles in the flash furnace.

While these studies allowed considerable advancement of the flash smelting process, they do not provide the insight required to understand the effect of adding high-grade concentrate to the blend. Group combustion theory provides the tools required to analyse the influence of high-grade concentrate on the flash smelting characteristics of the blend. Studies on interactive effects during coal ignition and combustion have used the group combustion number together with heat transfer and combustion effectiveness factors to account for the interactive effects during pulverised coal combustion. These studies have shown that as the group combustion number of the cloud increases, both the heat transfer and combustion effectiveness factors decrease, increasing the total reaction time of the cloud.

3 Group Combustion Theory

3.1 Group Ignition and Combustion

When two isolated particles, burning in air, are brought into close proximity, interactive effects between particles tend to reduce the burning rate of the individual particles. As most practical applications involve the combustion of a cloud of particles, interactions are expected to have a significant effect on the ignition and combustion characteristics of the particles within the cloud.

Group combustion studies have focused on developing techniques to predict the interactive effects within the cloud and have, in general, used correction factors to modify isolated particle combustion models to account for these effects. These studies show that interactions between particles are significant when the inter-particle spacing is sufficiently small that the heat and mass transfer boundary layers of neighbouring particles overlap, resulting in a decrease in the Nusselt and Sherwood numbers of individual particles.

Ryan and Annamalai[40] developed a model to study heat and mass transfer within a cloud of coal particles. Using dimensional analysis, the conservation equations defined a Group Combustion Number:

$$G = \frac{\pi}{2} n d_p d_c^2 \qquad (3\text{-}1)$$

It was found that this number was important in describing diffusion controlled combustion of a char particle cloud.

The two diffusional processes important to cloud combustion are heat transfer prior to ignition and heat and mass transfer during the combustion reaction. The first process influences both the ignition temperature of the cloud and the time required to reach ignition, while the second determines the combustion time of the cloud.

3.1.1 Ignition

3.1.1.1 Single Particle Ignition

To understand the ignition of a particle cloud one must first understand the ignition of an isolated particle. The ignition of isolated coal particles has been thoroughly studied for both homogeneous and heterogeneous ignition. Ignition is said to be homogeneous when the devolatilising species ignite in the gas phase, while heterogeneous ignition occurs when oxygen reacts directly with the particle surface. Heterogeneous ignition has been studied in detail because an analytical approach is possible, with many of the results transferable to homogeneous ignition.

Essenhigh et al.[41] reviewed the current theories on ignition and developed the critical conditions required for heterogeneous ignition. They showed that the ignition temperature of a particle could be determined as a function of the furnace atmosphere and the heat transfer experienced by the particle. Their results showed that conditions that reduce the particle heat transfer coefficient lowered the particle ignition temperature.

31

3.1.1.2 Group Ignition

In group ignition, interactive effects tend to lower the particle Nusselt number and therefore the particle ignition temperature. Annamalia et al[38] extended the Frank-Kamenetsky technique[49] for determining the ignition point of a single particle to account for interactive effects within the cloud. They found that a critical heat transfer Damkohler number exists above which ignition occurs. For a spherical cloud this Damkohler number is 3.32. The critical heat transfer Damkohler number is given by:

$$Da_{crit} = \frac{\left(Gd_p AY_{O_2}\rho\Delta H\right)}{2\lambda MW_{O_2}}\left(\frac{E_a}{RT_{p,i}^2}\right)\exp\left(\frac{-E_a}{RT_{p,i}}\right) \qquad (3\text{-}2)$$

Solution of Equation (3-2) shows, that for the same ambient conditions, as the group combustion number of the cloud increases the ignition temperature of the cloud decreases.

3.1.1.2.1 Heat transfer effectiveness factor

The cooperative heat transfer effects associated with cloud ignition are advantageous in reducing the ignition temperature of the particles. However they also reduce the rate of heat transfer to the particles prior to ignition, which may result in an increase in the time required to reach ignition.

By treating a particle cloud as a large single particle, Krishna and Berlad[42] determined the influence of interactive effects on the rate of heat transfer within the cloud. They conducted a heat balance to determine the steady state temperature of the

cloud assuming the gas temperature and oxygen mass fraction were uniform throughout the cloud. Their heat balance not only accounts for the heat loss and generation for a single particle, but also for the heat loss and generation for the entire cloud. Results showed that the influence of interactive effects on the heat transfer within the cloud could be accounted for by suitably modifying the Nusselt number of the individual particles within the cloud. This modified Nusselt number was termed the cooperative Nusselt number and can be used to define a heat transfer effectiveness factor, i.e. the ratio of the cooperative to the isolated particle Nusselt number, given by:

$$\eta_h = \frac{Nu_{coop}}{Nu_{iso}} = \frac{3}{\dfrac{Nu_{iso}}{Nu_{cl}}G + 3} \qquad (3\text{-}3)$$

Note that in Equation (3-3) Nu_{cl} refers to the Nusselt number of the cloud and describes the rate of heat transfer through the boundary layer between the cloud and its surroundings. As a result it is defined as follows:

$$Nu_{cl} = \frac{k_{h,c} d_c}{\lambda} \qquad (3\text{-}4)$$

In Equation (3-4) $k_{h,c}$ is the heat transfer coefficient describing the rate of heat transfer through the boundary layer between the cloud and the surroundings, d_c is the cloud diameter and λ is the gas phase thermal conductivity within the cloud. When considering the cloud issuing from a burner the cloud diameter at the burner exit can be considered equal to the burner diameter. While the cloud spreads after exiting the burner, there is no clear estimate of the cloud diameter as a function of downstream distance from the burner

tip. Hence for the remainder of this work the cloud diameter is assumed to be equal to the burner exit diameter.

Equation (3-3) shows that the heat transfer effectiveness factor has an upper bound of one and is closest to unity at low group combustion numbers and high cloud Nusselt numbers. Accounting for the interactive effects in this manner allows the ignition properties of the cloud to be determined using an isolated particle model with the isolated particle Nusselt number replaced by the cooperative Nusselt number.

3.1.1.2.2 Cloud Nusselt Number

For flash smelting, the particle cloud leaves the burner and forms a jet[23] i.e. a fully separated flow. In jet flows, the boundary layer is not attached to a wall but rather extends into the reaction shaft. The boundary layer between the jet and the surrounding recirculation zone controls the rate of heat transfer to the jet[50]. Several studies have been conducted to investigate heat transfer within the boundary layer of separated flows[51-56]. In these studies the Nusselt number has been related to the Reynolds number of the flow by a relationship of the form:

$$Nu = \gamma \, \mathrm{Re}^{\kappa} \tag{3-5}$$

In Equation (3-5) the characteristic length for both the Nusselt and Reynolds number is the length that describes the boundary layer of the separated flow. For this problem the separated boundary layer results from the jet issuing from the burner tip. Hence the characteristic length is burner (or cloud) diameter. The cloud Nusselt number has already been defined (Equation (3-4)), while the cloud Reynolds number is defined by:

$$Re_{cl} = \frac{\rho U_o d_b}{\mu} \qquad (3\text{-}6)$$

Table 3-1 shows the values of γ and κ determined in different studies, together with the flow geometry investigated in each case.

Table 3-1: Experimental Coefficients for Equation (3-5)

Study	γ	κ	Flow Geometry
Dirix and Van der Wiele[51]	3.1e-4	2	Plunging liquid jet
Vaitiekunas etal[52]	0.109	0.701	Separated flow over a flat plate
Avramenk[53]	0.0535	0.733	-
Scherer and Wittig[54]	0.108	0.701	Backward facing step
Shuja and Habib[55]	0.627	0.632	Annular diffuser
Kang etal[56]	52.02	1	Confined jet

These studies show a large variation in both coefficients. In particular, the exponent, κ, varies from 0.63 to 2. For combustion processes, the heat transfer to the jet is governed, to a large extent, by the burner design. Because there is a wide variation in the observed Nusselt number correlations for relatively simple flow geometries, it is expected that the burner design is important in determining the rate of heat transfer and therefore the Nusselt number between the cloud and the surroundings. Therefore burner stability analysis is discussed in Chapter 4.

3.1.1.2.3 Cloud Ignition Time

Equation (3-2) allows the ignition temperature of the particles within the cloud to be determined, while Equation (3-3) estimates the particle Nusselt number. Therefore, by conducting a heat balance over the particles within the cloud, the time required for the

cloud to reach ignition can be determined. If chemical heating is assumed negligible before ignition, then Equation (3-7) can be used to describe the particle heat balance prior to ignition.

$$m_p C_p \frac{dT_p}{dt} = \frac{\lambda Nu_{coop}}{d_p} A_p \left(T_\infty - T_p\right) + \varepsilon_r \sigma_{sb} A_p \left(T_\infty^4 - T_p^4\right)$$ (3-7)

In Equation (3-7) λ is the gas phase thermal conductivity and ε_r is the particle emmissivity. Implicit in this equation is the assumption that no temperature gradients exist within the particle. The Biot number for a sulfide particle is of the order of 0.01 to 0.02 and hence the assumption of an isothermal particle is valid.

Figure 3-1 shows how the time required to reach ignition varies with the group combustion number. In this analysis, the group combustion number was varied by changing the particle number density of the cloud while maintaining the particle diameter and cloud radius constant. The particle heat transfer effectiveness factor was calculated assuming that both the isolated particle and cloud Nusselt numbers were 2. A Nusselt number of 2 is for the conditions of pure conduction to a sphere. Hence these conditions assume that both the particles and the cloud are spherical and that the slip velocity between the particles and the gas and between the cloud and surroundings is negligible. This assumption is valid for the particles, as they are sufficiently small that the particle Reynolds number is close to zero. It is less valid for the cloud as a whole because the cloud Reynolds number is significant. However, because the purpose on this analysis was to investigate the effect of the group combustion number of the time required to reach ignition, these assumptions should not dramatically affect the shape of the curve.
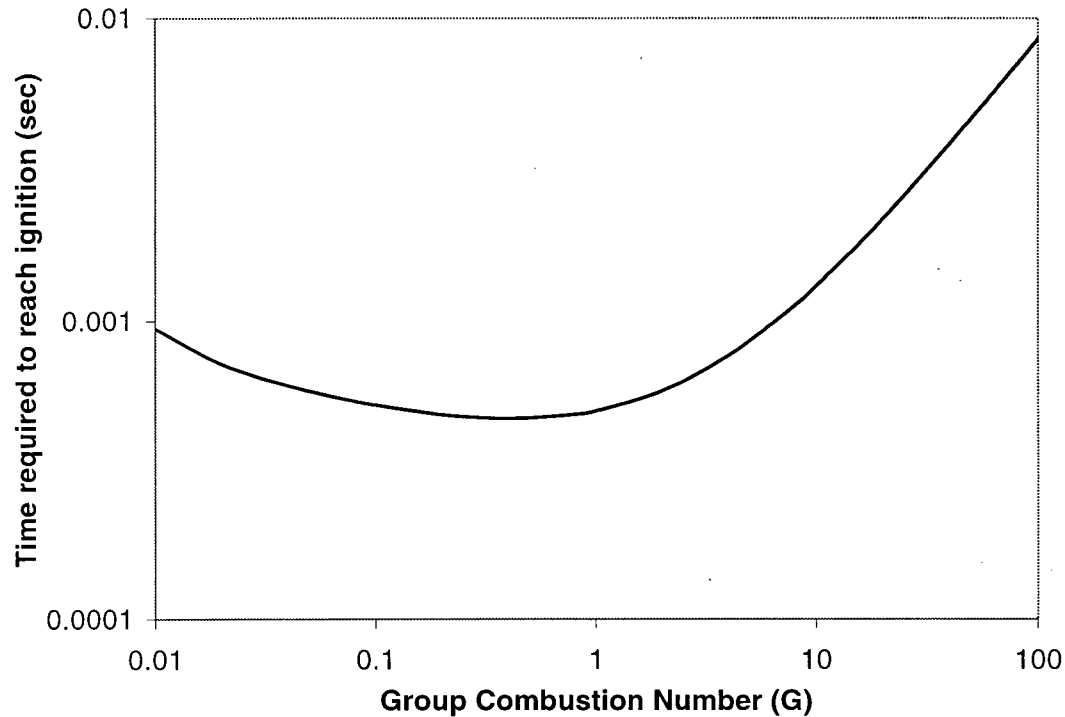
Figure 3-1: Ignition Time of a Sulfide Cloud as a Function of the Group Combustion Number ($dp = 20\mu m$, $d_c = 25.4mm$, $T_\infty = 1123K$, $E_a = 240$ kJ/mol, $A = 3.7 \times 10^{12}$ m/s, $P_{O2} = 0.4atm$)

Figure 3-1 shows that initially, as particles are added to a particle cloud, the time required to reach ignition decreases due to the reduction in the cloud ignition temperature. However, as the group combustion number of the cloud is further increased the time required to reach ignition begins to increase. This is caused by the reduced Nusselt number of the individual particles resulting in a reduction in the rate of heat transfer to the particles within the cloud.

This shows that while interactive effects are important in reducing the ignition temperature of the particles within a cloud, these same interactions are responsible for increasing the time required for the cloud to reach ignition.

3.1.2 Combustion

Particles within a particle cloud can be considered to burn according to the single particle model. However, because the gas phase properties vary throughout the cloud, the burning rate of the particles also varies. Therefore, to understand how particles burn in a cloud requires knowledge of both single particle combustion kinetics and the rates of heat and mass transfer within the cloud. The combustion of a single particle is considered next, followed by a discussion on combustion of a particle cloud.

3.1.2.1   Single Particle Heterogeneous Combustion

3.1.2.1.1   Char reaction pathway

Char combustion is, in general, assumed to proceed by char gasification followed by homogeneous combustion of carbon monoxide to carbon dioxide, with the reaction pathway described by:

$$2C + O_2 \rightarrow 2CO \qquad\qquad\qquad (3\text{-}8)$$

$$C + CO_2 \rightarrow 2CO; \qquad\qquad\qquad (3\text{-}9)$$

$$2CO + O_2 \rightarrow 2CO_2 \qquad\qquad\qquad (3\text{-}10)$$
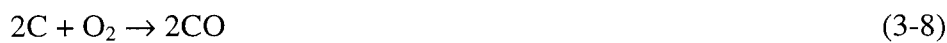
For sulfide particles, the particles are liquid during the combustion process, hence the reaction pathway is assumed to be the direct oxidation of sulfur to sulfur dioxide at the particle surface with negligible "ash layer" resistance[28]. Therefore, in the following

analysis of both single particle and cloud combustion, char is assumed to react solely via Equation (3-8).

3.1.2.1.2   Char Reaction Rate

Once a particle has ignited, two phenomena occur that influence the combustion rate of a char particle. Firstly, at the particle surface, oxygen is consumed and carbon dioxide is produced, causing concentration gradients to be set up around the particle. The oxygen concentration gradient limits the rate of oxygen mass transfer to the particle surface and results in a resistance to the combustion process. Secondly there is a net mass addition to the gas phase, requiring a net mass flux away from the particle. This phenomenon is known as Stefan flow; because the net mass flux is away from the particle, the rate of oxygen transfer is reduced, therefore reducing the combustion rate. Libby and Blake[57] developed a quasi-steady approximate expression for the combustion rate of a small char particle. From their analysis it can be shown that the burning rate of a single spherical particle is given by:

$$\dot{m} = Sh\pi\rho D d_p \ln\left(\frac{1+B_\infty}{1+B_w}\right) \tag{3-11}$$

where $B_i = \dfrac{Y_{O_2,i}}{v_{O_2}} + \dfrac{Y_{CO_2,i}}{v_{CO_2}}$

If it is assumed that the effect of Stefan flow is negligible, that the rate of combustion is controlled by diffusion of oxygen to the particle surface and that the ambience contains no carbon dioxide, Equation (3-11) can be simplified to:

$$\overset{\bullet}{m} = Sh\pi\rho D d_p \frac{Y_{O_2,\infty}}{v_{O_2}} \tag{3-12}$$

This equation is identical to that derived considering the general resistance model which assumes that the rate is controlled by a series of resistances. The two resistances that control the combustion of a solid char particle are due to oxygen mass transfer to the particle surface and due to the intrinsic reaction rate. Using the general resistance model, assuming no resistance to oxygen mass transfer through an ash layer, the burning rate of the particle can then be calculated from:

$$\overset{\bullet}{m}'' = \frac{Y_{O_2\infty}}{v_{O_2}\left(R_m + R_c\right)} \tag{3-13}$$

where $R_m = \dfrac{1}{\rho k_m}$ and $R_c = \dfrac{1}{\rho k_c}$

3.1.2.1.2.1   Porous Char Combustion

The above analysis assumes that the char particles are solid spheres and that oxygen reacts at the external surface. However, char particles are porous and therefore oxygen permeates through the particle and reacts with its internal surface area. As a result the measured combustion rate of a porous char particle does not in general agree with that predicted from either Equations (3-11) or (3-13).

The reaction rate of porous particles has been studied in detail with particular reference to catalysis. Because oxygen reacts as it diffuses into the particle, an oxygen concentration gradient exists within the particle and the overall reaction rate is lower than

40

that based on external surface conditions. A particle effectiveness factor has been defined to account for the reduced rate.[44-48] This factor is defined as the ratio of the actual reaction rate to the rate that would be observed if the oxygen concentration throughout the particle equaled the concentration at the particle surface. The effectiveness factor is defined by:

$$w_p = \eta_p k_c A_p C_A \mid_s \tag{3-14}$$

$$\eta_p = \frac{w_p}{w_s} \tag{3-15}$$

This definition reduces the problem to one of determining the particle effectiveness factor. Two methods can be used to determine the reaction rate of the porous particles. If the local oxygen concentration is known throughout the particle, then the local reaction rate can be determined and integrated over the particle to give the overall reaction rate. A simpler method, however, is to calculate the rate of oxygen diffusion into the particle. Both of these methods require the oxygen concentration to be known as a function of particle radius.[58] This can be determined by solving the oxygen conservation equation over the particle. If the combustion process is assumed to be quasi-steady with Stefan flow negligible, the oxygen conservation equation simplifies to a mole balance described by:

$$\frac{d^2C}{dr^2} + \frac{2}{r}\frac{dC}{dr} - \frac{k'_c \rho_p C}{D_{eff}} = 0 \tag{3-16}$$

with boundary conditions

$$\frac{dC}{dr} = 0 \text{ at } r = 0 \text{ and } C = C_s \text{ at } r = \frac{d_p}{2}$$

This equation can be integrated to give an equation that describes the oxygen concentration profile within the particle:

$$\frac{C}{C_s} = \frac{d_p}{2r} \frac{\sinh\left(6\phi_t \frac{r}{d_p}\right)}{\sinh(3\phi_t)} \tag{3-17}$$

ϕ_t is termed the Thiele modulus, defined by:

$$\phi_t = \frac{d_p}{6} \sqrt{\frac{k'_c \rho_p}{D_{eff}}} \tag{3-18}$$

Differentiating Equation (3-17) at the particle surface allows the rate of oxygen diffusion into the particle and therefore the reaction rate to be determined. Then by substituting the expression for the rate of oxygen diffusion at the particle surface into Equation 3-14, the effectiveness factor can be calculated, yielding:

$$\eta_p = \frac{1}{\phi_t}\left(\frac{1}{\tanh 3\phi_t} - \frac{1}{3\phi_t}\right) \tag{3-19}$$

Small values of ϕ_t imply that the diffusivity is much greater than the reaction rate and the oxygen concentration is uniform throughout the particle. The effectiveness factor is then close to unity. At high values of ϕ_t the diffusivity is low compared to the reaction rate and therefore the reaction is limited to a small zone close to the external surface of the particles. This results in a small value of the effectiveness factor.

It is important to note that in the definition of the Thiele modulus, the diffusivity is not the continuum diffusivity, but rather an effective diffusivity which accounts also for the added resistance caused by Knudsen diffusion within the pore and the effect of pore structure. For a single pore the diffusivity is given by:

$$D_{pore} = \frac{1}{\frac{1}{D_{AB}} + \frac{1}{D_k}} \qquad (3\text{-}20)$$

Wheeler[59] developed a model to predict the effective diffusivity within the pellet. It is given by:

$$D_{eff} = \frac{\varepsilon_p D_{pore}}{\tau_p} \qquad (3\text{-}21)$$

Using the effectiveness factor defined in Equation (3-14) allows the general resistance model for isolated particle combustion to be modified to account for the combustion of a porous char particle. In the general resistance model when considering a porous char particle the chemical resistance term is then modified by writing:

$$R_c = \frac{1}{\eta_p \rho k_c} \qquad (3\text{-}22)$$

3.1.2.2   Group Combustion

Particles within the cloud do not burn at the rate predicted from the isolated particle model using the ambient conditions at the cloud surface, but rather they burn at a

43

rate governed by the local gas phase conditions within the cloud. The challenge of group combustion studies has been to predict how the local gas phase conditions vary throughout the cloud so as to allow the burning rate of the individual particles, and therefore of the entire cloud, to be predicted.

One way to analyse cloud combustion[40] is to develop conservation equations for the gas phase assuming that the particles act as sources of mass, species and enthalpy and that these source terms are distributed uniformly throughout the cloud. The conservation equations for a spherical cloud, assuming that ρD is constant, are:

Mass

$$\frac{\partial \rho}{\partial t} + \frac{1}{r^2}\frac{\partial \rho v r^2}{\partial r} = \dot{m}'''$$

(3-23)

Species

$$\frac{\partial \rho Y_k}{\partial t} + \frac{1}{r^2}\frac{\partial \rho v r^2 Y_k}{\partial r} - \frac{1}{r^2}\frac{\partial}{\partial r}\left(\rho D r^2 \frac{\partial Y_k}{\partial r}\right) = \dot{m}_k'''$$

(3-24)

Energy

$$\frac{\partial \rho h}{\partial t} + \frac{1}{r^2}\frac{\partial \rho v r^2 h}{\partial r} - \frac{1}{r^2}\frac{\partial}{\partial r}\left(\rho D r^2 \frac{\partial h}{\partial r}\right) = \dot{q}'''$$

(3-25)

In these equations $\dot{m}'''$, $\dot{m}_k'''$ and $\dot{q}$ are the mass, species and enthalpy source terms due to particle and gas phase reactions.

These equations are the general conservation equations describing the group combustion of a spherical cloud. Under certain conditions these equation can be simplified. For the experimental set-up used in this study, several assumptions can be made. Firstly, the burning rate is sufficiently low that quasi-steady conditions can be assumed and Stefan flow can be neglected. Secondly, because of the small cloud radius and small particle diameter, the cloud can be assumed to be isothermal. Finally the particles are assumed to be monosized spheres. Using these assumptions, the burning rate can be determined by calculating the rate of oxygen diffusion within the cloud, and Equation (3-24) can be simplified to give:

$$\frac{d^2 Y_{O_2}}{dr^2} + \frac{2}{r}\frac{dY_{O_2}}{dr} = \frac{\dot{m}_{O_2}'''}{\rho D} \qquad (3\text{-}26)$$

The oxygen mass source in Equation (3-26) is simply the burning rate for an isolated particle model multiplied by the particle number density of the cloud, and is given by:

$$\dot{m}_{O_2}''' = S_V v_{O_2} \, \dot{m}'' = S_V \frac{Y_{O_2}}{R_m + R_c} \qquad (3\text{-}27)$$

where $S_V = \pi n d_p^2$, $R_m = \dfrac{1}{\rho k_m}$ and $R_c = \dfrac{1}{\eta_p \rho k_c}$.

Substituting Equation (3-27) for the mass source into Equation (3-26) gives:

$$\frac{d^2 Y_{O_2}}{dr^2} + \frac{2}{r}\frac{dY_{O_2}}{dr} - \frac{S_V}{\rho D(R_m + R_c)} Y_{O_2} = 0 \qquad (3\text{-}28)$$

45

If the burning rate of the individual particles within the cloud is governed by external diffusion, then the group combustion number can be defined as:

$$G = \frac{S_v d_c^2 Sh}{4 d_p}$$

(3-29)

In this equation if the Sherwood number is taken as 2, which implies there is no relative motion between the gas and particles within the cloud, then the group combustion number defined here becomes that defined in Equation (3-1).

Equation (3-24) then becomes:

$$\frac{d^2 Y_{O_2}}{dr^2} + \frac{2}{r} \frac{dY_{O_2}}{dr} - \frac{4}{d_c^2} G Y_{O_2} = 0$$

(3-30)

This is similar to Equation (3-19) with the Thiele modulus for the particle replaced by $G^{1/2}$. Therefore the oxygen mass fraction within the cloud can be calculated from:

$$\frac{Y_{O_2}}{Y_{O_2,c}} = \frac{d_c}{2r} \frac{\sinh\left(G^{1/2} \frac{2r}{d_c}\right)}{\sinh\left(G^{1/2}\right)}$$

(3-31)

This suggests that an effectiveness factor can be defined analogous to that defined in porous char combustion. The effectiveness factor is the ratio of the burning rate of an individual particle within the cloud to the burning rate of an isolated particle experiencing the same conditions as those at the cloud surface. This is defined as:

$$\eta_c = \frac{\overset{\bullet}{m}_{cloud}}{\overset{\bullet}{m}_{iso}}$$

(3-32)

Table 3-2 lists the effectiveness factors for three different cloud geometries.

Table 3-2: Cloud Combustion Effectiveness Factors for Different Cloud Geometries

Cloud Geometry	Effectiveness Factor (η_{com})	Approximate Effectiveness Factor for G>100
Sphere	$\dfrac{3}{G^{1/2}}\left[\dfrac{1}{\tanh\left(G^{1/2}\right)}-\dfrac{1}{G^{1/2}}\right]$	$\dfrac{3}{G^{1/2}}$
Cylinder	$\dfrac{2}{G^{1/2}}\dfrac{I_1\left(G^{1/2}\right)}{I_0\left(G^{1/2}\right)}$	$\dfrac{2}{G^{1/2}}$
Slab	$\dfrac{1}{G^{1/2}}\tanh\left(G^{1/2}\right)$	$\dfrac{1}{G^{1/2}}$

This shows that a small isothermal cloud can be treated in a similar manner to a large porous char particle. It also shows that due to competition for available oxygen within the cloud the burning rate of a single particle within the cloud is lower than for an isolated particle. The decrease can be determined using the effectiveness factors defined in Table 3-2.

3.2 Implications for Flash Smelting

Adding high-grade concentrate to the blend affects both the group combustion number and the Nusselt number of the cloud, therefore influencing the heat-up and combustion times of the cloud and hence the stability of the furnace operations.

The group combustion number defined in Equation (3-1) has been redefined in terms of parameters that are commonly used in flash smelting[60] with:

47

$$G = 3.93 \left(\frac{\sigma}{\eta \rho_p} \right) \left(\frac{d_b}{d_p} \right)^2 \qquad\qquad (3\text{-}33)$$

Equation (3-33) shows that the group combustion number is proportional to the oxygen enrichment (σ) and inversely proportional to the oxygen-to-concentrate ratio (η).

As shown by the heat and mass balance calculations in Chapter 1, addition of high-grade concentrate to the blend increases the oxygen enrichment and lowers the oxygen-to-concentrate ratio. Both of these increase the group combustion number of the cloud. Table 3-3 shows the oxygen enrichment, the oxygen-to-concentrate ratio and the group combustion number of the cloud entering the flash furnace as a function of the Escondida loading of the blend. The group combustion number is seen to increase by a factor of nearly 3 as the Escondida loading increases from 0 to 40 wt%.

Table 3-3: Flash Smelting Cloud Properties as a Function of Escondida Loading

Escondida Loading	Oxygen to Concentrate ratio	Oxygen Enrichment (vol %)	Group Combustion Number ($\times 10^{-6}$)	Gas Velocity (m/s)	Total Mass Flow-rate (tph)	Solids Mass Flow-rate (tph)
0	0.285	47	2.3	80	311	200
5	0.275	50	2.5	71.9	296	195
10	0.265	53	2.7	64.3	282	192
15	0.255	56	3.0	56.9	268	188
20	0.245	61	3.4	49.8	255	184
25	0.236	66	3.9	42.9	242	181
30	0.226	73	4.5	36.5	230	177
35	0.216	84	5.4	30	218	174
40	0.206	98	6.6	23.9	207	171

Also listed in Table 3-3 is the burner exit velocity which decreases by a factor of 3.3 as the Escondida loading increases from 0 to 40 wt%. This implies that the cloud

Nusselt number decreases by a factor between 1.8 and 11, depending on the relationship between the jet Reynolds and Nusselt numbers.

Knowing how the group combustion and cloud Nusselt numbers vary with the addition of Escondida to the blend allows the heat transfer and combustion effectiveness factors to be estimated. The heat transfer effectiveness factor is inversely proportional to the group combustion number and directly proportional to the cloud Nusselt number and therefore decreases by a factor of between 5.3 and 32 as the Escondida loading increases from 0 to 40 wt%. The combustion effectiveness factor is inversely proportional to the square root of the group combustion number and hence is expected to decrease by a factor of 1.7 as the Escondida loading increases from 0 to 40 wt%.

This shows that as high grade concentrate is added to the blend, it has the largest effect on the heat transfer effectiveness factor and is therefore expected to have the greatest influence on the heat-up time of the cloud. Any adverse effect on furnace stability caused by adding high-grade concentrate to the blend is expected to be caused by the increase in the heat up time of the cloud.

3.3 Chapter Summary

Studies on coal combustion have shown that interactive effects reduce the Nusselt and Sherwood numbers of individual particles within the cloud, thereby reducing the combustion rate of the cloud. These studies use effectiveness factors to describe the influence of the cloud properties, defined by the group combustion number, on the rates of heat and mass transfer to individual particles within the cloud. These effectiveness factors are defined as the ratio of the rate of heat transfer or combustion of an individual

particle within the cloud to the rate of heat transfer or combustion of an isolated particle exposed to the same ambient conditions as the cloud. Defining the effectiveness factors in this way allows the cloud combustion rate to be determined based on the single particle combustion model, with suitable modification of the rate of heat and mass transfer to account for particle interactive effects. Studies have shown that the heat transfer effectiveness factor is inversely proportional to the group combustion number and proportional to the cloud Nusselt number, while the combustion effectiveness factor is inversely proportional to the square root of the group combustion number. If it is assumed that these effectiveness factors can be applied to sulfide flash smelting, then the combustion rate of the sulfide cloud can be estimated once the effectiveness factors are determined.

Based on heat and mass balances as high-grade concentrate is added to the blend, the group combustion number increases along with the oxygen enrichment, while the oxygen-to-concentrate ratio and burner exit velocity decrease. The increase in the group combustion number and the decrease in the burner exit velocity cause the heat transfer effectiveness factor to decrease, increasing the heat-up time of the cloud. On the other hand, the increase in oxygen partial pressure and reduction in the oxygen-to-concentrate ratio cause the combustion time of the cloud to decrease. This suggests that the major influence of high-grade concentrate is to increase the heat-up time of the cloud, which adversely affects the stability of the furnace.

4 Burner Design Theory

In the previous chapter the heat transfer effectiveness factor was shown to be related to the cloud Nusselt number which in turn was related to the burner design. Hence, although flash smelting is a metallurgical process aimed at producing a liquid matte phase, it is in essence a combustion process, limited by the same phenomena governing burner stability as other combustion processes. This chapter discusses the combustion phenomena important to burner design and then relates these to flash smelting.

4.1 Flame Stabilisation

As discussed by Beer and Chigier[50] and Glassman,[61] two phenomena define the stability limits for a premixed fuel burner: flash-back and blow-off. Flash-back occurs when the gas velocity is lower than the mixture burning velocity and causes the flame to propagate against the gas flow, back up the burner. Blow-off occurs when the gas velocity everywhere exceeds the burning velocity of the mixture and, as a result, the flame propagates downstream and extinguishes. By considering these two situations the stable operating regime of a burner can be defined:[50]

"A stable flame will occur when at some point in the flow field the gas velocity is equal to and opposite the flame burning velocity and everywhere else the gas velocity exceeds the burning velocity of the mixture."

The first condition ensures the flame is anchored at some point in the flow field, while the second ensures that flash-back cannot occur. Intrinsic to this definition is the concept of a flame burning velocity, defined as the velocity at which unburned gases move through the combustion wave in the direction normal to the wave surface. As the flow can be either laminar or turbulent, there is a laminar[62] and turbulent[63-65] burning velocity. The laminar burning velocity is a function of the gas mixture alone, whereas the turbulent burning velocity is a function of the laminar burning velocity and the turbulence of the flow.

4.1.1 Laminar Pre-Mixed Flame Stabilisation

Lewis and Von Elbe[66] found that a premixed laminar flame is stabilised in the low flow region of the jet boundary layer that forms between the core of the jet and the surrounding atmosphere. In this region the local mixture burning velocity is lower than that of the bulk mixture due to the heat and species sink effect caused by the close proximity of the burner wall. The combination of these two phenomena then determines the stability limits of a laminar premixed flame.

4.1.2 Flame Stabilisation in High Velocity Flows

For high-speed flows the jet boundary layer formed at the burner exit is too thin to allow flame stabilisation.[61] Therefore an improved stabilisation technique is required for these flows. This is accomplished by creating a recirculation zone where hot combustion products are used to continuously prepare the fresh mixture for ignition[61,67].

Re-circulation zones can be produced by several means. Those important to flash smelting are the use of a confined jet, a bluff body and swirl.

4.1.2.1 Confined Jet Flows

For an enclosed jet such as that issuing into a combustion chamber, the entrainment of the jet is inhibited and an external re-circulation zone establishes itself in order to compensate for the lack of gas available for entrainment. The details of this re-circulating flow are important, as its size and strength influences both the stability and combustion length of turbulent flames.

Thring and Newby[68] proposed a simple theoretical treatment to determine the re-circulating mass flow rate of a confined jet by assuming that the entrainment rate of the jet was unaffected by the enclosure. They showed that the recirculating mass flow rate could be calculated:

$$\frac{\dot{m}_r}{\dot{m}_o} = \frac{0.47}{\theta} - 0.5 \quad \text{where} \quad \theta = \frac{d_b}{D_c}\left(\frac{\rho_o}{\rho_a}\right)^{1/2} \tag{4-1}$$

This shows that the recirculating mass flow-rate increases with increasing mainstream flow rate, furnace chamber diameter and ambient gas density, while decreasing with increasing burner diameter and fresh mixture density.

While the recirculation zone formed by a confined jet provides heat to the fresh mixture, thus enhancing burner stability, it is an external recirculation zone, and some heat is lost to the furnace walls, reducing burner stability. Both bluff body and swirl

stabilisation produce internal recirculation zones that maximise the heat transferred from the recirculation zone to the fresh mixture, enhancing burner stability above that of a confined jet.

4.1.2.2　Bluff Body Stabilisation

At sufficiently high flow rates, when a bluff body is placed in a flow, a re-circulation zone (or wake) forms behind the body. The rate of heat and mass transfer between the wake and the mainstream flow is high, and if combustion occurs, hot products are carried upstream by the recirculation zone where they can prepare the fresh mixture for ignition. The stability limits of a bluff body stabilised burner require an understanding of this recirculation zone and a knowledge of flame propagation in regions of high velocity gradients.[50,61]

4.1.2.2.1　Wake Flows

The proportion of the mainstream flow contained within the re-circulation zone determines the strength of the vortex and is important when considering flame stability. Two geometric factors, namely the blockage ratio and the forebody angle of the bluff body, influence the size and shape of the wake. For isothermal flows, Davis and Beer[69] measured the effect of both of these factors on the recirculation zone at high approach flow Reynolds numbers (Re>10^4), while Besalpov[70] extended this to include the effect of combustion.

54

4.1.2.2.1.1 Blockage Ratio

The blockage ratio of a bluff body is defined as the ratio of the projected area of the body to the flow area of the tube i.e. $B_R = \left(\dfrac{d_{bb}}{d_b} \right)^2$. Davies and Beer[69] showed, for a disc, that as the blockage ratio increased from 0.11 to 0.54 the non-dimensional length of the vortex (defined as $L_w' = L_w/d_{bb}$) decreased from 2.6 to 1.2. This implies that an increase in the blockage ratio caused a decrease in the size of the recirculation zone. However by redefining the non-dimensional length in terms of the burner diameter, the blockage ratio can be shown to have a negligible effect on the vortex length. More important to burner stability is the effect of blockage ratio on the recirculating mass flow-rate. Davies and Beer[69] showed that as the blockage ratio increased from 0.11 to 0.54, the recirculating mass flow-rate increased from 5 to 25 % of the fresh mixture mass flow rate, suggesting that the stability of a bluff body stabilised burner improves with increasing blockage ratio.

4.1.2.2.1.2 Forebody Angle

The forebody angle influences the flow around the bluff body and in particular the maximum radius of, and the mass flow rate in, the recirculation zone. Figure 4-1 shows the definition of the forebody angle.
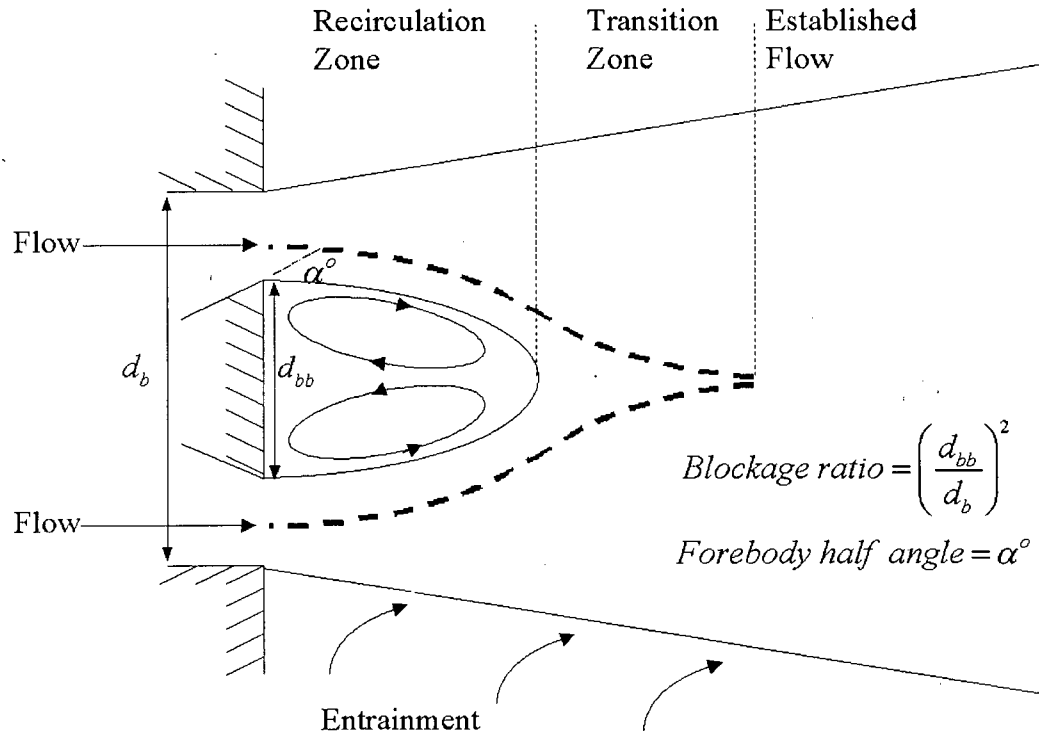
Figure 4-1: The Flow in the Wake of a Bluff-Body[50]

Davies and Beer[69] studied three different geometries: a disc, a 45° cone and a cylinder. The disc produced the recirculation zone with the largest radius while the cylinder produced the recirculation zone with the smallest radius. The recirculating mass flow-rate in the vortex showed the same trend, with a disc giving a mass recirculating flow-rate of 15% and a cylinder producing a mass flow-rate of 4% of the fresh mixture flow rate, indicating that a disc would give better stability.

4.1.2.2.1.3   Effect of Combustion on the Wake

Bespalov[70] studied the effect of combustion on the size and strength of the re-circulation zone. He used a 60° V-shaped cone and showed that the non-dimensional length of the wake increased from 1.6 without combustion to 6 with combustion. The

56

volumetric flow-rate of the wake increased by a factor of six due to the increased temperature. However, the maximum velocity in the vortex remained unchanged.

4.1.2.2.2 Combustion in High Velocity Gradient Flows

Realising that the size and strength of the recirculation zone is important in bluff body stabilisation, Beer and Chigier[50] calculated the blow-off limits of a burner from a heat balance over the wake, assuming it to be a well-mixed region. By equating the heat generated in the wake to that removed by transfer to the cold mixture, a maximum gas velocity was calculated for given dimensions of the bluff body. Above the maximum velocity, the heat required to prepare the fresh mixture for ignition exceeded that which could be supplied by the recirculation zone, resulting in blow-off. They showed that the blow-off condition of a bluff body burner is given by:

$$\frac{U}{P^{n_r-1}d_{bb}} = \text{constant} \tag{4-2}$$

This shows that the blow-off limit increases with increasing size of the bluff body.

4.1.2.3 Swirl Stabilisation

When rotating motion is imparted to a gas mixture upstream from a burner exit, the jet exiting the burner has a tangential velocity component in addition to axial and radial velocity components. This tangential component increases the divergence of the jet. Because the flow is restrained by viscous forces and is subject to radial pressure forces, a recirculation zone can form close to the burner exit as shown in Figure 4-2.
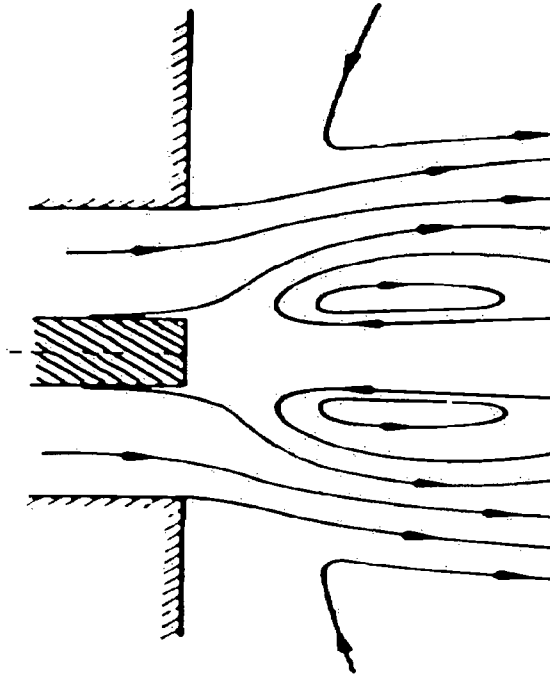
Figure 4-2: Streamlines for a Swirling Flow[50]

A non-dimensional parameter, termed the swirl number, can be used to characterise the swirl intensity of the flow. It is defined as the ratio of the flow's tangential and axial momentum components and is given by[50]:

$$S = \frac{2G_\phi}{d_b G_x}$$

(4-3)

where

$$G_\phi = \int_0^{d_b/2} 2\pi r w r \rho u \, dr = const \quad \text{and} \quad G_x = \int_0^{d_b/2} 2\pi r u \rho u \, dr + \int_0^{d_b/2} 2\pi r P \, dr = const$$

(4-4)

58

In flows where the swirl number is less than 0.6, no internal recirculation zone forms. The major effect of the swirling motion is then to increase the entrainment rate of the jet. Such jets are in general not widely used for combustion. However, for flows with swirl numbers greater than 0.6 an internal re-circulation zone forms and acts as a storage zone for heat and chemically active species, enhancing flame stability.[50]

4.1.2.3.2 Swirl Generation

Several methods can be used to induce swirl into a pipe flow as discussed by Beer and Chigier[50]. In the current study and in most industrial situations, guide vanes are used to generate swirling motion. When using guide vanes, the swirl number can be calculated from:

$$S = \frac{2}{3} \left(\frac{1 - \left(\frac{d_h}{d_b} \right)^3}{1 - \left(\frac{d_h}{d_b} \right)^2} \right) \tan \alpha' \tag{4-5}$$

Hence the swirl number of the flow increases as the angle of the guide vanes increases, and as the ratio of the hub radius to the burner radius decreases.

4.1.2.3.3 Operating strategy

Many different swirl burner variations are used for pulverised coal combustion to improve combustion efficiency and pollution control. One of the simplest designs uses a central tube to inject the solids and a primary gas stream into the combustion chamber. Secondary air is then injected in an annulus surrounding the central tube, with swirl

imparted to this secondary gas stream[50]. For this burner design, the solids are injected directly into the internal recirculation zone, allowing rapid heating of the particles in an oxygen-depleted environment. Upon exiting the recirculation zone, the particles react with the oxygen in the secondary gas stream. Because the particles are injected directly into the hot recirculation zone, the stability limits of the burner increase compared to a confined jet flame.

For this burner design, Beer and Lee[71] showed that the combustor volume could be represented as a well-mixed region and a plug flow region in series. They showed that the burner performance could be optimised by varying the proportion of the mean particle residence time spent in the two regions and that the particle residence time distribution could be controlled by varying the swirl number. Using a water model, they showed that the proportion of particle residence time in the well mixed region passed through a minimum as the swirl intensity increased and that the combustor performance was optimised at the swirl number that gave the minimum particle residence time in the well mixed region.

4.2 Flash Smelting Burner Design

The burner design used in the San Manuel furnace is shown in Figure 4-3.
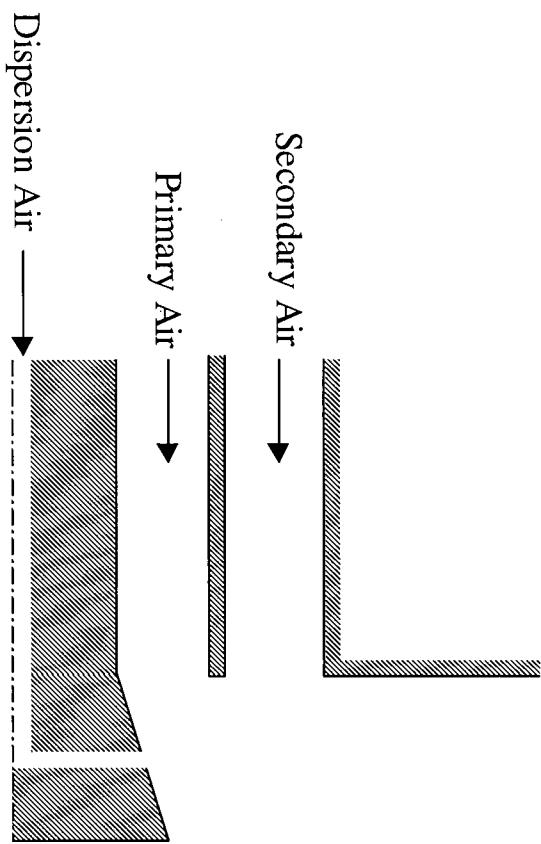
Figure 4-3: San Manuel Dispersion Burner

This is commonly termed a dispersion burner within the flash smelting community. However, it is essentially a bluff-body burner. Concentrate is carried via a primary gas stream in an inner annulus, with a secondary gas stream carrying the remaining oxygen required for reaction in an outer annulus. A dispersion cone is located at the burner exit with its purpose being to enhance particle dispersion and promote mixing of the primary and secondary air streams. This is achieved through direct impingement of the primary stream onto the cone and by the use of a high pressure dispersion air stream which issues radially outward from the cone.

4.2.1 San Manuel Burner Performance

Many studies have been conducted to improve burner performance.[23,29,31-37,72-74] However, few of these appear to have used the knowledge available on flame stabilisation. One study of interest here is that conducted by Adams et al[36] on the reaction shaft of the San Manuel furnace. While results of the study are proprietary and cannot be discussed in detail, Figures 4-4 and 4-5 show some qualitative results which can be used to infer burner performance.

Figure 4-4 shows the velocity field directly below the burner exit. A recirculation zone of approximately 1.1 times the burner diameter (approximately 0.7 m) is formed below the dispersion cone. This length is typical of that found by Davies and Beer[69] for the recirculation zone produced by a bluff body burner without combustion. Note that the exact dimensions of the burner are not given as these are proprietary.
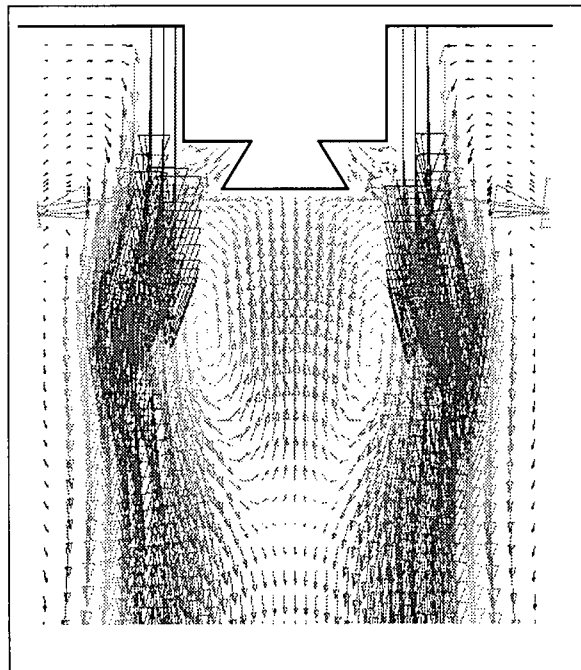
Figure 4-4: San Manuel Burner Velocity Field

Figure 4-5 shows the gas phase temperature field within the reaction shaft. It shows the gas temperature remains low directly below the burner until ignition occurs resulting in a sharp temperature rise approximately 1.3 m below the burner tip.
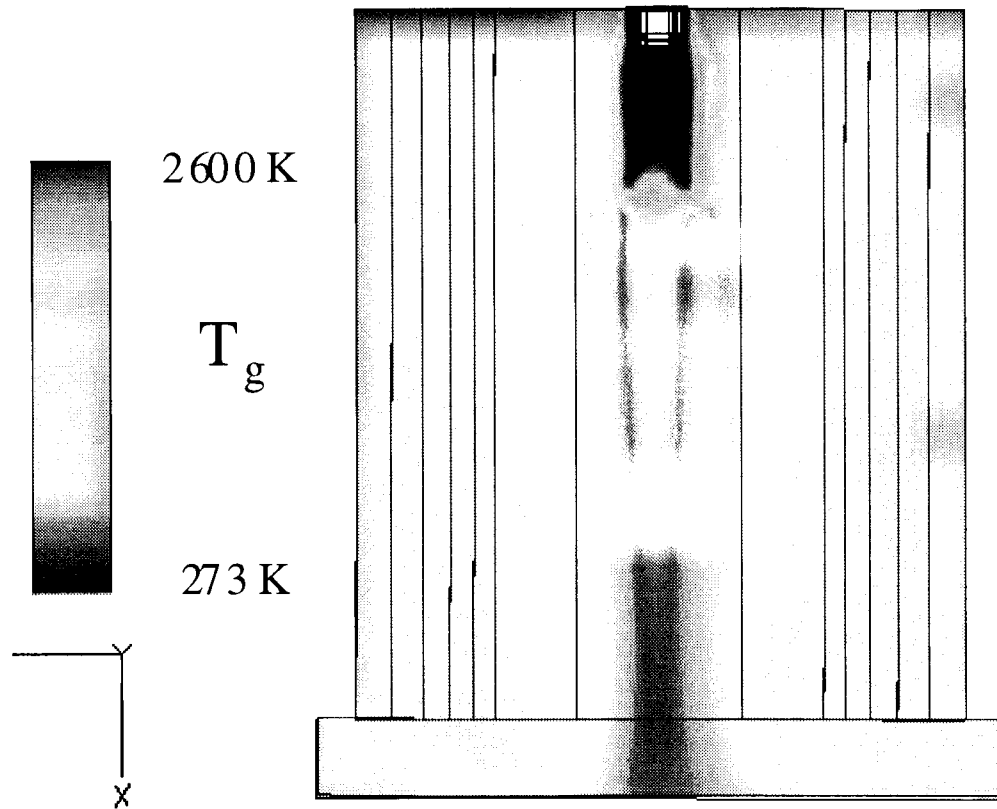
Figure 4-5: San Manuel Shaft Temperature Field

Considering these two figures together, it can be concluded that ignition occurs past the recirculation zone eliminating the stabilising effect of the bluff body burner. Figure 4-4 also shows that the dispersion cone has a minimal effect on particle dispersion due to the large momentum ratio between the secondary and primary air streams.

These results imply that the San Manuel burner behaves essentially as a straight tube burner with the flame being stabilised by the external recirculation zone. Using the flame stabilisation techniques discussed above, the performance of the San Manuel burner could be improved by:

1) Eliminating the dispersion air as its influence is negligible;

2) Reducing the momentum ratio between the secondary and primary air streams; and

3) Reducing the secondary air stream velocity to ensure that ignition occurs before reaching the end of the recirculation zone.

4.2.2 Swirl Burner Design

The above improvements should enhance stability of the current burner, thereby allowing greater flexibility in furnace operation. However, swirl burners can be used to achieve even greater operating flexibility through the use of moveable swirl vanes which allow the swirl intensity of the flow to be varied as the fuel and load demands change. This is important when considering the flash smelting of high-grade concentrate because, as shown in Table 3-3, the burner exit velocity decreases considerably as high-grade concentrate is added to the blend.

Many different configurations are possible when designing a swirl burner. One such design discussed earlier in this chapter used the secondary air to produce the swirling motion with the primary air stream being injected directly into the recirculation zone as shown in Figure 4-6.
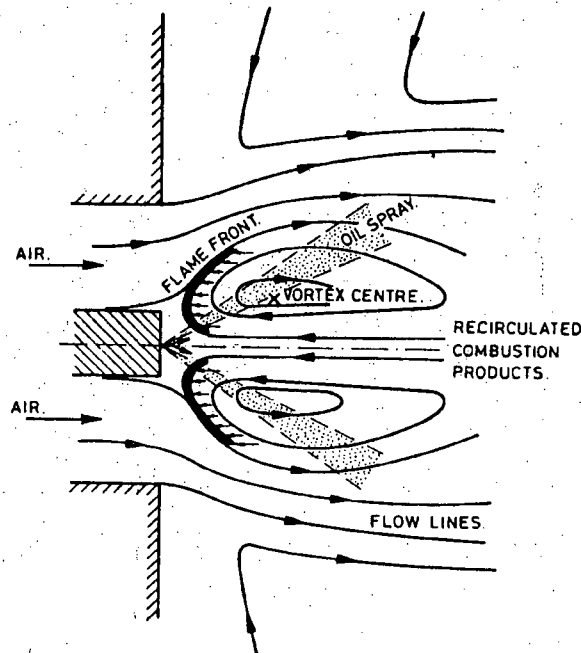
Figure 4-6: Swirl Burner Design[50]

This design results in rapid heating of the particles, enhancing burner stability. However, it cannot be used for sulfide flash smelting because of the large momentum associated with the particles.

Consider char combustion which proceeds according to Equation (4-6).

$$C + O_2 => CO_2 \qquad\qquad (4\text{-}6)$$

If air is used as the reaction gas then the gas-to-solids mass ratio is 12.6 (assuming 10% excess air) whereas for sulfide flash smelting this ratio varies from 0.6 to 0.2. This large difference in the gas-to-solids mass ratio changes the relative importance of the gas and solids momentum flow rate to the furnace. If the solid and gas phases are assumed to

have the same velocity then, for char combustion the solids momentum represents approximately 8% of the total momentum flow whereas for sulfide flash smelting the solids momentum represents approximately 70% of the total momentum flow. This high relative solids momentum flow rate associated with sulfide flash smelting would result in the collapse of the recirculation zone shown in Figure 4-6, eliminating the stabilising effect of the burner.

This suggests that for sulfide flash smelting producing the desired recirculation zone requires swirl to be imparted to both the primary and secondary air streams. Basu et al[75] discuss this burner type and offer a design procedure to calculate the critical burner parameters, these being:

1) the primary and secondary air velocities;

2) the ratio of the primary and secondary air stream momentum flow rates;

3) the inner diameter of the inner annulus;

4) the exit nozzle geometry; and

5) the swirl intensity of the primary and secondary air streams.

Using this procedure it is possible to suggest a swirl burner design capable of smelting concentrate blends with high Escondida loadings.

The first three parameters that must be set are the velocities and the mass flow rate ratio of the primary and secondary air streams. Basu et al[75] list the values of these parameters for different coal types. If lignite is used as the design basis, then Table 4-1 lists the velocities and mass flow rate ratio of the primary and secondary air streams.

Table 4-1: Swirl Burner Design Velocities and Mass Flow Ratio

Primary air velocity	20 m/s
Secondary air velocity	25 m/s
Primary to Secondary air mass flow ratio	0.2

Using these gas velocities, if the total required gas flow rate is known then the primary (A_1) and secondary (A_2) air streams flow areas can be determined. The aim of this design is to develop a burner capable of smelting concentrate blends over the entire span of Escondida loadings at a capacity of 69.3 tph of copper production. Therefore the primary and secondary air stream flow areas were calculated using the velocities listed in Table 4-1 and data from Table 3-3 for an Escondida loading of 20 wt-%, which represents the mid range value.

Once the primary and secondary air stream flow areas have been determined, the inner diameter of the inner annulus can be calculated from:

$$d_{ia} = m\sqrt{\frac{1}{1-m^2}\frac{4}{\pi}(A_1 + A_2)} \qquad (4\text{-}7)$$

In Equation (4-7) m is usually between 0.3 and 0.5 and was set to 0.4 for this case.

With respect to the exit nozzle geometry, Basu et al[75] suggest a nozzle length of between 0.15 and 0.3 m with a half angle of 5 to 15°. For this design a length of 0.3 m and a half angle of 10° were chosen.

Figure 4-7 is a schematic of the burner design determined from this procedure.
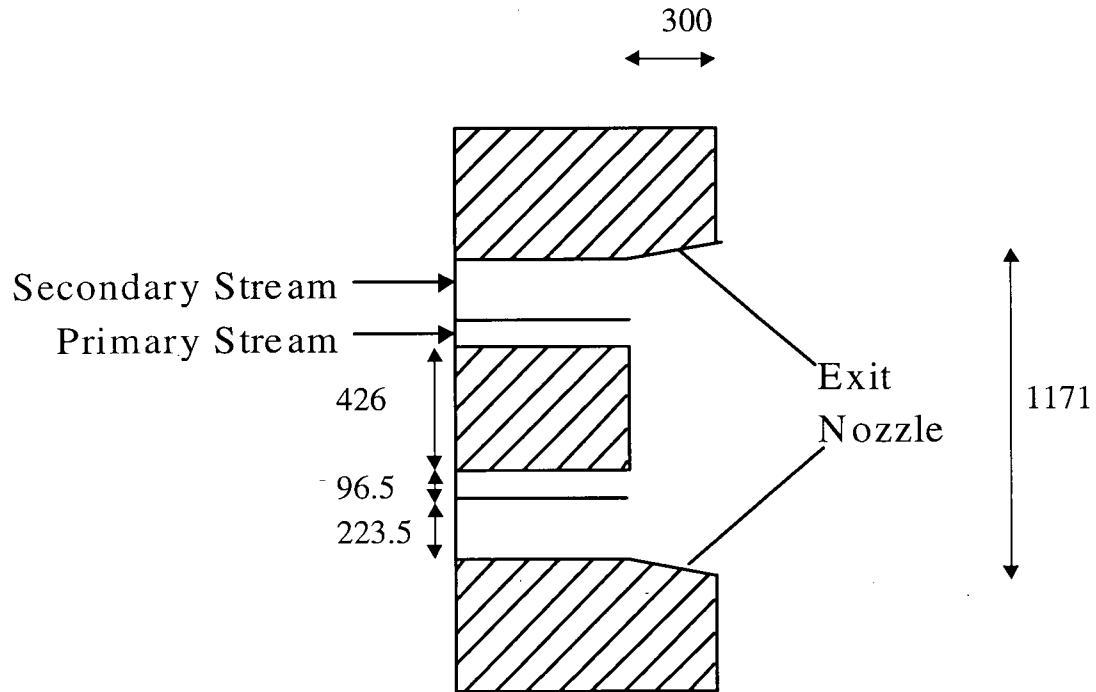
Figure 4-7: Flash Smelting Swirl Burner Design (All dimensions in mm)

4.3 Chapter Summary

This chapter has shown that stable burner operation for high-speed flows is achieved through the formation of a recirculation zone which carries heat from the combustion zone back to the fresh mixture, preparing it for ignition. Results from a study conducted by Adams et al[36] on the San Manuel burner indicate that the burner exit velocity is too high resulting in ignition downstream from the internal recirculation zone formed below the dispersion cone. Hence the burner behaves similar to a straight-tube burner with the external recirculation zone stabilising burner operation. This form of stabilisation in general results in lower stability then an internal recirculation zone.

Therefore the current burner design could be improved by reducing the burner exit velocity to promote ignition before the end of the internal recirculation zone.

Swirl burners can give better stability then bluff-body burners because the swirl intensity of the flow can be varied as the burner load changes. Based on the design for coal burners given by Basu et al,[75] a swirl burner design is suggested for testing in the flash smelting of high-grade concentrates.

5   Scope and Objectives

5.1   Overall Project Objectives

The literature concerning flash smelting shows that considerable experimental work has been conducted on the combustion characteristics of chalcopyrite and chalcocite. Mathematical models have also been developed to predict the flash smelting behaviour of these minerals. Both the experimental studies and mathematical models provide predictions for the extent of reaction of the particles as a function of key operating parameters. However, no attempt has been made to determine the key phenomena that limit the flash smelting process when different minerals are combined to form a concentrate blend.

When Escondida concentrate is added to the concentrate blend, industrial flash smelters observe smelting failure at Escondida loadings lower then the theoretical upper limit. Because no studies have been published concerning the influence of blending concentrates on flash smelting characteristics of the blend, the cause of the failure at high Escondida loadings has remained unexplained.

Based on results from a furnace heat and mass balance, as high-grade concentrate is added to the blend:

1)   the oxygen-to-concentrate ratio decreases;

2)   the level of oxygen enrichment increases; and

3)   The total solids feed-rate to the furnace decreases.

70

All three of these cause the burner exit velocity to decrease while the first two increase the particle number density of the concentrate cloud emerging from the burner. Group combustion theory predicts that the particle number density of the concentrate cloud is important in determining the specific combustion rate of the particles within the cloud. Expressions have been developed to determine the combustion rate of a particle within a cloud as a function of the particle number density. These expressions show that as the particle number density increases, the specific combustion rate of the particles within the cloud decreases as compared to an isolated particle. Burner stability analysis shows that a burner flame is stabilised by the recirculation of hot combustion products, which heats the fresh mixture and prepares it for ignition. The strength of the recirculation zone determines the stability limits of the flame and is itself a function of the burner design and the momentum of the fresh mixture exiting the burner. The furnace heat and mass balance analysis together with group combustion theory and burner stability analysis indicate that adding high-grade concentrate to the blend may adversely affect the stability of the flash smelting process.

To understand why a flash smelting furnace fails as Escondida concentrate is added to the blend requires a fundamental understanding of the key phenomena occurring in a flash smelting furnace. This fundamental understanding is not currently available. Therefore the primary objectives of this project were as follows:

1) To determine the critical phenomena affecting the flash smelting process as high-grade concentrate is added to the blend;

2) To utilise this information to recommend improvements to the flash smelting furnace and burner with the aim of increasing the Escondida loading of the blend that can be treated.

To accomplish these two objectives, an experimental investigation has been performed using the UBC flash reactor. This study has been designed to determine if group combustion theory applies to sulfide flash smelting, and then to investigate alternative burner designs. The experimental study also provides information to develop a mathematical model of the flash smelting flame. The mathematical model has been used to gain insight into the important phenomena occurring in the flame and to predict the manner in which an industrial flash furnace behaves as high-grade concentrate is added to the blend.

5.2 Experimental Objectives

The objectives for the experimental study are as follows:

1) To investigate the effect of the group combustion number on the heat-up and combustion characteristics of a concentrate cloud. The group combustion number was varied by changing the particle size, oxygen-to-concentrate ratio, oxygen enrichment and the Escondida loading of this cloud;

2) To apply group combustion theory in order to define key phenomena that limit the flash smelting process as high-grade concentrate is added to the blend;

3) To investigate the effect of different burner designs on the flash smelting characteristics of the blend; and

4) To apply these results by suggesting improved operating strategies and burner designs, which allow blends with higher Escondida loadings to be treated.

5.3 Mathematical Modeling Objectives

The objectives of the mathematical model are as follows:

1) To predict the experimental data generated by the UBC flash reactor in order to provide insight into the important phenomena occurring in the UBC flash reactor; and

2) To provide a tool that predicts the performance of an industrial furnace as high-grade concentrate is added to the blend.

6 Experimental Design

6.1 Introduction

The experimental study had two aims, firstly to investigate the applicability of group combustion theory to the combustion of sulfide particle clouds and secondly to investigate the performance of different burner designs. Several techniques have been developed to investigate interactive effects during combustion processes and include laminar flow reactors[76-79], shock tubes[80], thermogravimetric techniques[81-85] and stirred reactors[86-87]. Because the project had the two aims of investigating interactive effects and the performance of different burner designs, it was decided to construct a cylindrical shaft reactor similar to a laminar flow reactor. This reactor design has several advantages over other possible designs. Firstly, the geometry and flow properties (i.e. a jet flow issuing into a cylindrical shaft) are similar to those of an industrial flash smelter, and secondly, both interactive effects and different burner designs can be studied using the same reactor.

It is worth noting at this point that the aim of the project was not to investigate the performance of an industrial or pilot scale flash smelting furnace. Therefore, no attempt was made to ensure strict similitude between the flash reactor and an industrial flash furnace.

6.2 Equipment Design

In the flash reactor, a pre-mixed concentrate and gas stream is injected via a burner into the hot reaction shaft. The burner produces a cylindrical cloud which moves down through the furnace where it is heated and reacts with the available oxygen producing a matte phase. By collecting solid and gas samples at different distances from the burner tip, the extent of reaction can be followed allowing, the influence of interactive effects to be determined.

To investigate interactive effects requires that the furnace temperature and group combustion number be controlled throughout each run. To achieve this required several ancillary systems to be used. Figure 6-1 shows the flash reactor and associated ancillary equipment that was used to control the experiment at the desired level. Table 6-1 lists the important equipment.
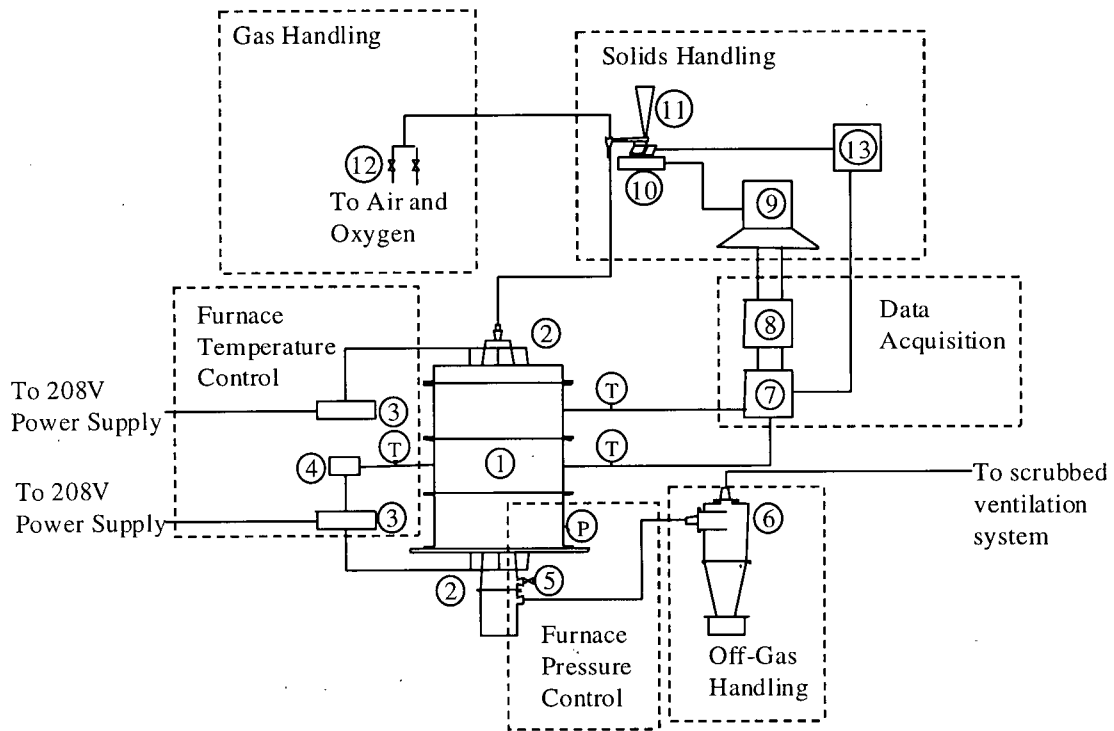
Figure 6-1: Flash Reactor with Associated Ancillary Equipment

Table 6-1: Equipment List

Equipment Number	Item	Quantity
1	Furnace	1
2	3.3kW Silicon carbide heating elements	6
3	SCR controller	2
4	Omega CN9000A temperature controller	1
5	51mm Gate valve	1
6	Cyclone	1
7	Data collection board	1
8	Signal conditioning card (SC-2040)	1
9	Data acquisition computer with a PCI-MIO-16E-4 data acquisition board	1
10	PE-11 Mettler balance	1
11	FT-01 Vibratory feeder	1
12	Rotameter	2
13	0-10V to 0-110V Converter	1

6.2.1 Flash Reactor Design

The Flash reactor was constructed from three 460 mm high by 1067 mm diameter steel sections, each lined with 178 mm thick Claycast 60 refractory and backed by 50 mm of highly insulating PK19, giving a working diameter of 611 mm. The working volume was divided into an inner reaction shaft having a diameter of 195 mm and an outer annulus of 208 mm. Four 313 mm long bottomless mullite crucibles were stacked one on top of the other to form the reaction shaft, giving a total length of 1252 mm. Six 3.3 kW silicon carbide heating elements, used to maintain the furnace temperature, were placed in the annulus of the furnace. Five view-ports were placed at 150 mm intervals in the bottom two furnace sections allowing the reactions to be observed, and gas and solid samples to be collected. A stainless steel hearth section was located at the exit of the refractory-lined furnace to collect the reacted solids and quench the furnace off-gases. Figure 6-2 shows the Flash Reactor with its critcal dimensions.

Claycast 60 refractory
178mm on side walls
95mm on furnace top
75mm on furnace bottom

50mm of PK19 Insulating
board

50mm diameter view-ports equally
spaced at 150mm along shaft
length

Outer annulus

Reaction shaft

Outer annulus

1530

208 | 195 | 208

1057
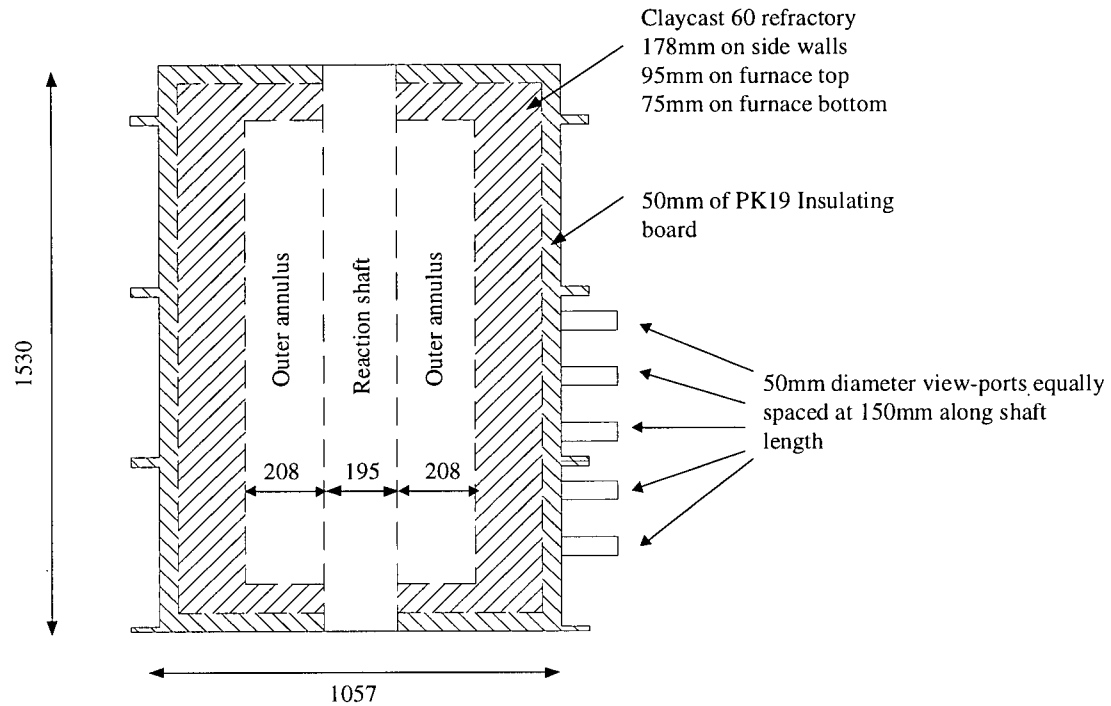
Figure 6-2: Flash Smelting Reactor (All dimensions in mm)

6.2.2 Ancillary Systems

Six ancillary systems serviced the furnace and controlled the operating conditions.

These were:

1) Gas delivery;

2) Solids delivery;

3) Off-gas handling;

4) Furnace pressure control;

5) Furnace temperature control; and

6) Data acquisition.

Each of these systems is described below.

78

6.2.2.1 Gas Delivery

Two Matheson 605 rotameters controlled the total flow-rate and oxygen concentration of the gas entering the furnace. The oxygen concentration was controlled by mixing medical grade oxygen, from a 67.7 Nm^3 capacity cylinder, with compressed air supplied from the building compressed air line. To obtain the required flow-rates the rotameters were operated at 103 kPa gauge pressure with each rotameter calibrated for the gas that it delivered. Appendix A1 shows the calibration curves for each rotameter. After the gases were mixed they were injected at the end of the solids vibratory feeder where the solids were entrained. The solids and gas then entered the furnace as a pre-mixed stream.

6.2.2.2 Solids Delivery

A FT0 Syntron vibratory feeder with a 3 kilogram capacity hopper was used to convey the solids along a 25.4 mm diameter tube. At the end of the tube, they were entrained into the furnace gas stream. In order to maintain the desired oxygen-to-concentrate ratio, the solids feed-rate was controlled using a loss-in-weight feedback control loop. The vibratory feeder was placed on a PE-11 Mettler balance equipped with a RS-232 output. This output was sent to a data acquisition computer and the feed-rate was determined by tracking the loss in weight. The feed-rate was determined by taking the slope of the balance reading versus time over a five second interval.

The feedback control-loop controlled the voltage to the vibratory feeder in order to maintain the solids feed-rate at the desired level. A standard digital PI control

79

algorithm was used to control the feeder. The output from the PI algorithm was a 0-10 V signal which controlled the voltage to the vibratory feeder from 0-110 V using a crydom 10PCV2415 analog input power controller. The block diagram for the control loop is shown in Fig. 6-3.
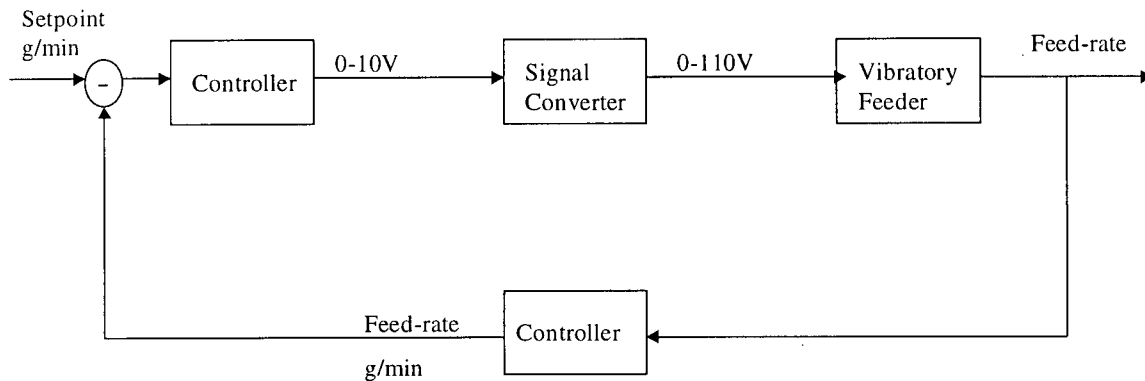
Figure 6-3: Solids Feed-rate Feedback Control Loop Block Diagram

Labview, a commercially available data acquisition and control software package, was used to write the digital PI algorithm.

The standard PI control equation is:

$$Y_c = K_c \left(\varepsilon_c(t) + \frac{1}{\tau_{I,c}} \int \varepsilon_c(t) dt \right)$$

(6-1)

which can be discretised to give:

$$\Delta Y_c = K_c \left(\varepsilon_{c,n} \left(1 + \frac{\Delta t}{\tau_{I,c}} \right) - \varepsilon_{c,n-1} \right)$$

(6-2)

The PI control parameters K_c and τ_I are used to tune the controller for a specific process. The parameters of the feeder control loop are listed in Table 6-2.

Table 6-2: Solids Feed-rate PI Controller Parameters

Parameter	Value
K_c (-)	0.001
$\tau_{I,c}$ (s)	2

6.2.2.3   Furnace Pressure Control

A scrubbed ventilation system was connected to the exit of the furnace, allowing the furnace to be operated at a vacuum, minimising dusting and sulfur dioxide escape. Throughout each run the furnace pressure was manually controlled in order to minimise air infiltration into the furnace. The pressure was controlled by monitoring the furnace pressure 150 mm above the furnace exit using a 0-60 Pa Magnihelic pressure gauge, and then adjusting a 50 mm gate valve located 100 mm above the hearth exit allowing infiltration air to enter the hearth. Adjusting the air infiltration rate into the hearth controlled the furnace pressure, but also quenched the furnace gases and increased the total gas flow-rate, allowing the off-gas cyclone to operate more efficiently.

6.2.2.3.1   Air Infiltration Rate

Air infiltration into the furnace affects the final matte grade due to the increased amount of oxygen available for reaction. Hence the furnace air infiltration rate was determined as a function of furnace vacuum and taken into account when the required gas flow-rates were calculated.

81

To determine the air infiltration rate, the flow to the furnace was measured and maintained using calibrated 605 rotameters, while the flow exiting the furnace was measured by an orifice plate. The difference between the gas flow to the furnace and the gas flow leaving the furnace was then taken as the air infiltration rate. Appendix A1 shows the calibration curve for the orifice plate. Figure 6-4 shows the effect of furnace vacuum on the air infiltration rate and indicates that:

1) the air infiltration rate is not a function of the gas flow entering the furnace; and

2) the air infiltration rate decreases as the furnace vacuum is reduced.
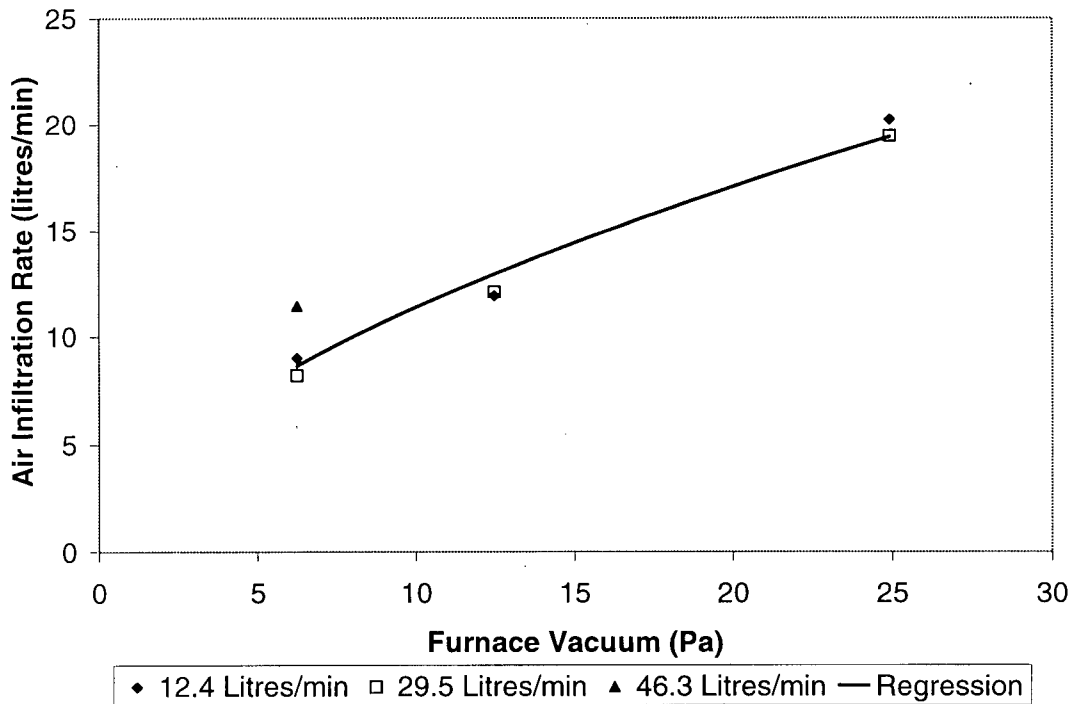
Figure 6-4 : Furnace Air Infltration Rate v's Furnace Vacuum for Different Gas Feedrates.

For all runs the furnace was operated at a vacuum of 5 Pa, giving an air infiltration rate of 8.1 litres/min which equates to an oxygen infiltration rate of 1.7 litres/min. The required oxygen flow rate for the experimental runs varied from

7.5litres/min to 10.2 litres/min. Therefore the oxygen infiltration rate accounts for between 16 to 22% of the total oxygen requirements. While this is a significant portion of the total oxygen requirements, it was necessary to run the furnace at a vacuum of 5 Pa as lower furnace vacuums could not be accurately maintained.

6.2.2.4 Furnace Temperature Control

Six silicon carbide heating elements were used to heat the furnace. Three elements hung from the top of the furnace and three extended up from the bottom of the furnace, providing a large isothermal zone. The two sets of three elements were connected via a three-phase delta arrangement.

The power supplied to each set of elements was controlled using a Model 664K Research Inc. three-phase, phase angle power controller connected to a 208 V three phase power supply. The top set of elements was controlled manually, while a CN9000A Omega feedback temperature controller with a 4-20 mA output controlled the bottom set of elements using a platinum/platinum-10 %Rhodium (type S) control thermocouple located at the furnace centre. The furnace temperature was controlled by selecting an adequate power setting for the top set of elements and allowing the temperature controller to adjust the power setting to the bottom elements. Five type S thermocouples were positioned at 150 mm intervals along the reaction shaft length and their outputs were sent to the data acquisition and control computer where they were displayed. This allowed the power to the top set of elements to be adjusted iteratively until the furnace axial temperature gradient was minimised. The axial temperature range within the furnace was typically within $\pm 5^{\circ}C$ of the furnace setpoint.

6.2.2.5   Off-Gas Handling

Upon entry to the hearth, the furnace gases were mixed with dilution air, which quenched the furnace gas and increased the total flow. This mixed gas stream was then sent to a cyclone where carry-over-solids were separated from the gas stream. The off-gases were then passed through the ventilation scrubbers where the sulfur dioxide and sulfur trioxide were removed. The solids were collected from the cyclone and were then used to close the mass balance.

6.2.2.6   Sampling

Both gas and solids were sampled at different furnace levels to gain an insight into the reaction rate within the cloud. The oxygen, nitrogen and sulfur dioxide concentrations were determined, and the particle reaction rate was monitored by examining the desulfurisation of the particles.

6.2.2.6.1   Gas Analysis

Gas samples were analysed using:

1) a Varian 3400 Gas Chromatagraph (GC) to determine the oxygen and nitrogen concentration; and

2) a Model PIR-2000 Horiba general purpose Infra-red gas analyser to determine the SO_2 concentration.

A gas sample was taken from each sample-port, at the furnace centre-line, using a water-cooled probe shown in Figure 6-5. Gas was withdrawn from the furnace at a rate

of 0.5 l/min using a Gast diaphragm positive displacement pump. This flow represents approximately 1.5% to 5% of the total gas flow entering the furnace. So while the sampler was not iso-kinetic the small sample flow rate relative to the input furnace flow rate ensured minimal disturbance of the combustion process due to the presence of the sampler.

Once filtered to remove any dust particles, the sample passed through the infrared SO_2 analyser. When a steady state sulfur dioxide concentration was reached, the sulfur dioxide concentration was recorded and a gas sample was injected into the GC to determine the oxygen and nitrogen concentrations.
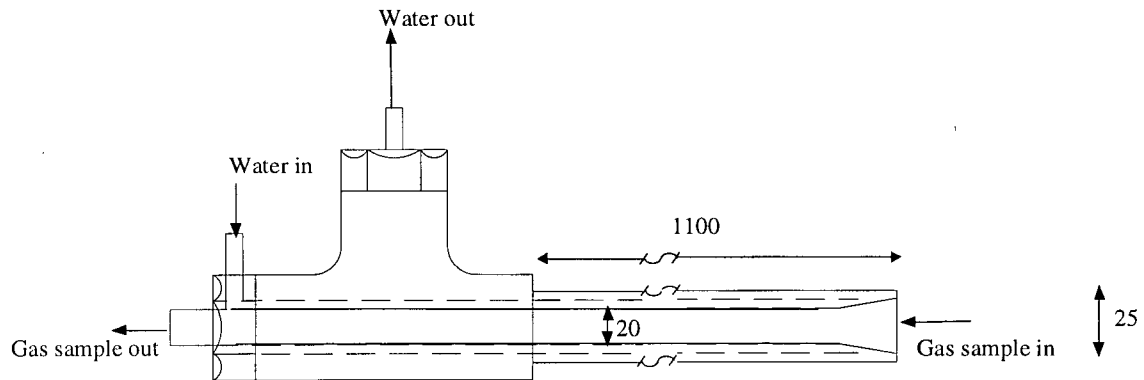
Figure 6-5: Water-Cooled Gas Sampler

6.2.2.6.1.1   Sulfur Trioxide Concentration

To close the mass balance over the furnace requires the gas composition to be known. The above gas analysis allows the oxygen, nitrogen and sulfur dioxide concentrations to be determined. However, sulfur dioxide and oxygen are capable of reacting further to produce sulfur trioxide.

$$SO_{2(g)} + \frac{1}{2} O_{2\ (g)} \rightarrow SO_{3(g)} \qquad\qquad\qquad (6\text{-}3)$$

The sulfur trioxide concentration within the furnace depends upon the equilibrium relationship between sulfur dioxide, oxygen and sulfur trioxide and the reaction kinetics.

6.2.2.6.1.1.1 Thermodynamic Equilibrium

The equilibrium composition of the gas can be determined from the equilibrium constant which is defined as:

$$K_P = \frac{P_{SO_3}}{P_{SO_2} P_{O_2}^{1/2}} \qquad\qquad\qquad (6\text{-}4)$$

Using data obtained from HSC[88] the equilibrium constant for the reaction at the three furnace temperatures used for the experiments are:

Table 6-3: Oxygen/Sulfur Dioxide/Sulfur Trioxide Equilibrium Constant

Furnace temperature ($^{\circ}$C)	Equilibrium Constant K_P
850	0.2432
950	0.0444
1000	0.0211

The low values for the equilibrium constant indicates that the left hand side of Reaction (6-3) is favoured at high temperatures and that for the conditions experienced in the flash reactor the equilibrium sulfur trioxide composition is of the order of 0 to 5 vol-%.

The reaction kinetics determine the rate at which Reaction (6-3) reaches equilibrium and therefore the sulfur trixoide concentration within the furnace. Ladner and Pankhurst[89] showed that the kinetics of the uncatalised reaction are slow with no appreciable reaction occurs during their experiments. However it is known that many metal oxides catalyse the reaction[90]. This is important because metal oxides are present within the furnace and include the reaction products such as copper and iron oxides and the metal oxides present in the ceramic crucibles which forms the reaction shaft wall.

Because there is a large number of metal oxides present within the furnace it is impossible to accurately predict the kinetics of the reaction. However it is possible to estimate the order of magnitude of the reaction rate using data for a commercial catalyst. Doering et al[91] modelled the oxidation of sulfur dioxide over a vanadium oxide catalyst and showed that the reaction could be described by:

$$r_{SO_2} = k_{SO_2} \frac{P_{O_2}^{1/2} P_{SO_2}}{P_{SO_3}} \left(1 - \frac{B_{SO_2}}{K_p} \right) \tag{6-5}$$

where

$$k_{SO_2} = 333 \exp\left(\frac{-92050}{RT} \right), B_{SO_2} = \frac{P_{SO_3}}{P_{O_2}^{1/2} P_{SO_2}} \text{ and } \log(K_p) = \frac{4921}{T} - 4.6658$$

If the above equation is assumed true for the conditions within the flash reactor then the reaction rate can be estimated. Implicit to this assumption is that the reaction rate constant, k_{SO2}, describes the condition of the metal oxides within the furnace. This

assumption is invalid because the reaction rate constant depends on the structure of the catalyst. However, Equation (6-5) should provide an order of magnitude estimate of the reaction rate.

For a typical experimental run the gas flow rate to the furnace is 20 l/min and the solids feedrate is 60 g/min. Assuming all of the solids catalyse the reaction and that the initial oxygen and sulfur dioxide partial pressure are 0.2atm and the initial sulfur trioxide partial pressure is 0 atm, Figure 6-6 show the species composition as a function of time for a furnace temperature of 850°C.
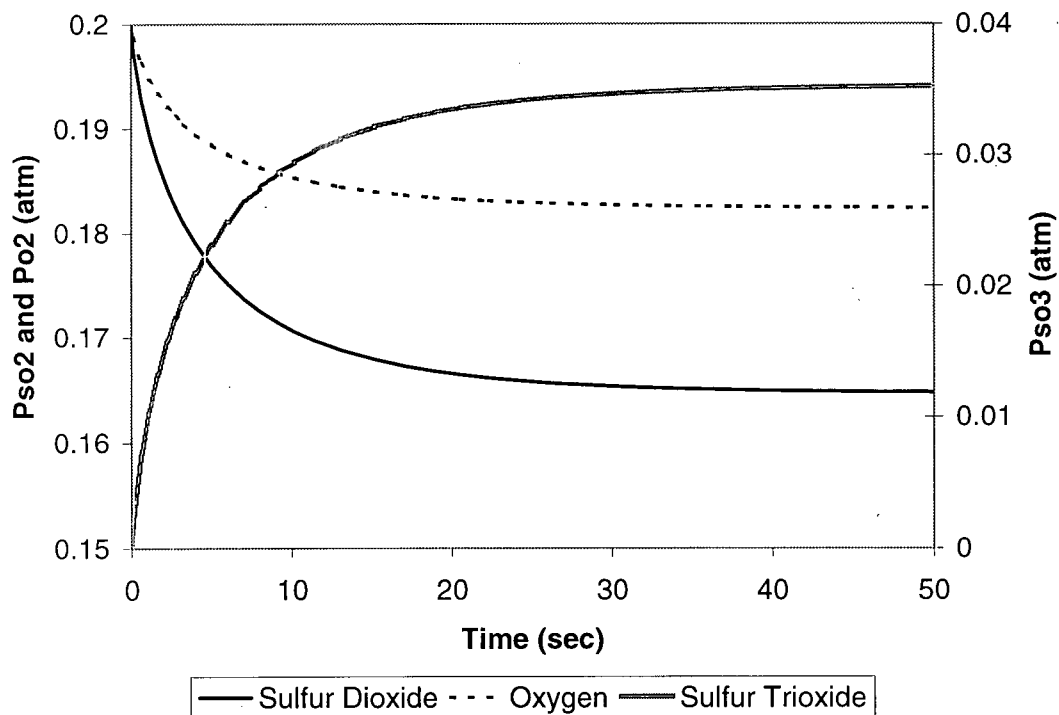
Figure 6-6: O₂, SO₂ and SO₃ Partial Pressures vs Time

This analysis indicates that the reaction takes between 10 and 30 seconds to reach equilibrium, while the residence time of the gas within the reactor is between 1 to 10

seconds. Therefore, although the reaction does not reach equilibrium, there does exist a measurable quantity of sulfur trioxide present within the reactor, with the equilibrium concentration representing the maximum possible sulfur trioxide concentration within the reactor.

6.2.2.6.2 Solids Analysis

Solids were collected from the furnace using a water-cooled impingement style sampler. The impingement surface was a flat plate. Because the sampler was water-cooled, the particle reaction was quenched upon contact. In some cases a thick layer of particles collected on the sampler, insulating the upper layer of the particles from the water-cooling. As a result, upon withdrawal from the furnace the sample was still glowing indicating the reaction had not been adequately quenched. In such cases the sample was discarded and a new sample collected. When collecting the new sample the sampler residence time within the shaft was reduced so as to minimise the sample buildup on the probe.

Metal dividers were welded to the sampler to divide the collection surface into five sections. Sections one and five were at the same radial position within the cloud as were sections two and four. Hence samples from sections one and five and samples from section two and four were combined. This gave three radial samples for each furnace level, allowing the radial variation in the particle desulfurisation to be determined. Figure 6-7 shows the water-cooled sampler with some critical dimensions.

While no analysis has been conducted it is believed that the sampler retained the majority of the particles that hit its surface. This is because the sampler was water-cooled, allowing a thin condensed film of water to form on the impingement surface, generating a "sticky" surface for the particles that hit surface.
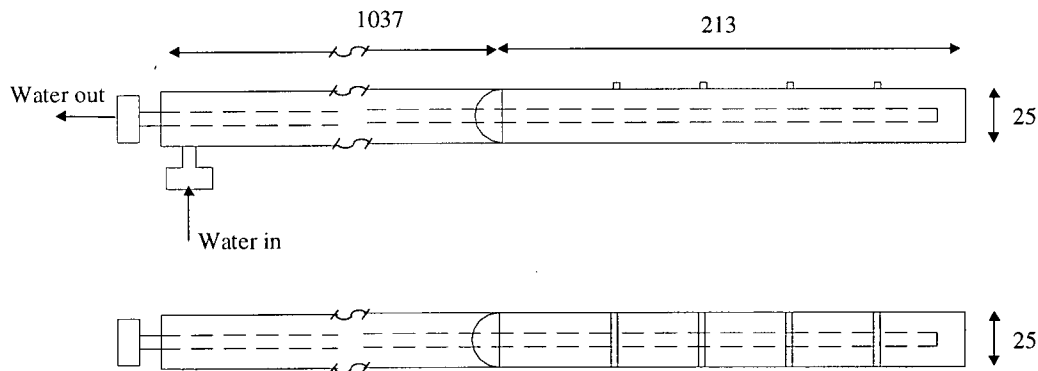
Figure 6-7: Water-Cooled Solids Sampler

6.2.2.6.2.1   Sampler Collection Efficiency

The sampler was not iso-kinetic, but rather relied on the particles impinging on, and being retained by, the flat sampler surface. The efficiency of the sampler can be estimated as a function of gas velocity, particle size and furnace temperature using a correlation described by Perry[92]. Figure 6-8 shows the collection efficiency of an impingement separator.
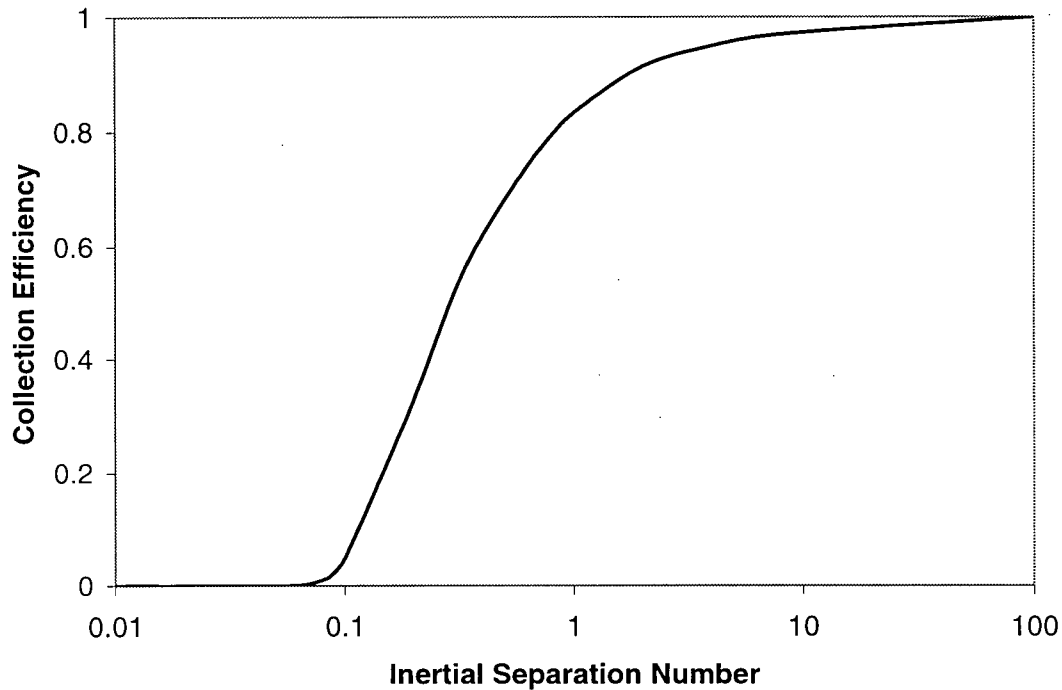
Figure 6-8: Impingement Separator Collection Efficiency

This figure shows the collection efficiency is a function of the inertial separation number which is given by Equation (6-6).

$$N_{S,i} = \frac{K_m \rho_p d_p^2 U}{18 \mu D_s} \tag{6-6}$$

Equation (6-6) together with Figure (6-8) shows that low collection efficiencies occur for small particle sizes, low gas velocities, low particle densities and high gas viscosities. Because all four of these parameters vary either within or between experimental runs, the collection efficiency of the sampler will also vary.

91

1) Small particle sizes and low gas velocities occur for runs with high group combustion numbers and therefore the collection efficiency for these runs is expected to be poor.

2) Sulfide minerals are generally more dense than oxides and because oxides are produced during the reaction it is expected that the sampler will preferentially collect sulfide minerals.

3) The gas viscosity increases with furnace temperature and therefore the collection efficiency is expected to decrease with increasing gas viscosity.

Figures 6-9 and 6-10 show the predicted sampler collection efficiency as a function of particle size and gas velocity for the typical conditions at the burner exit for a sulfide and oxide respectively. For these plots the furnace temperature was assumed to be 1000°C giving a gas viscosity of 3.8×10^{-5}Pa.s. The densities of the minerals were taken as 4500 and 2000[92] for the sulfide and oxide respectively.
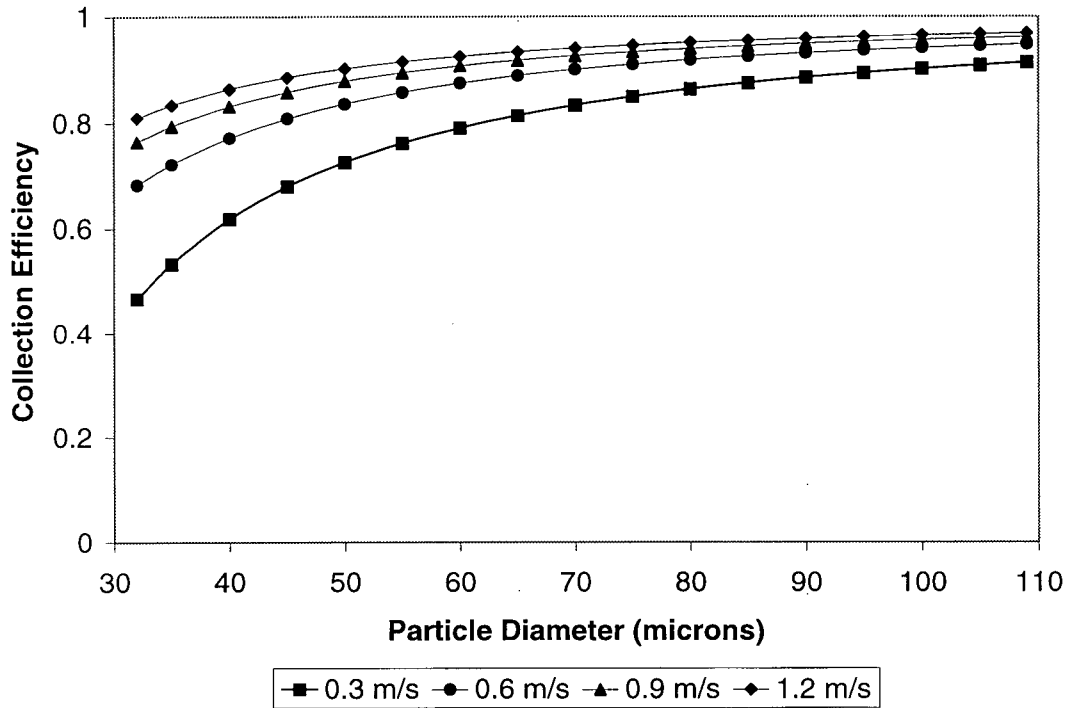
Figure 6-9: Solid Sampler Sulfide-Collection Efficiency
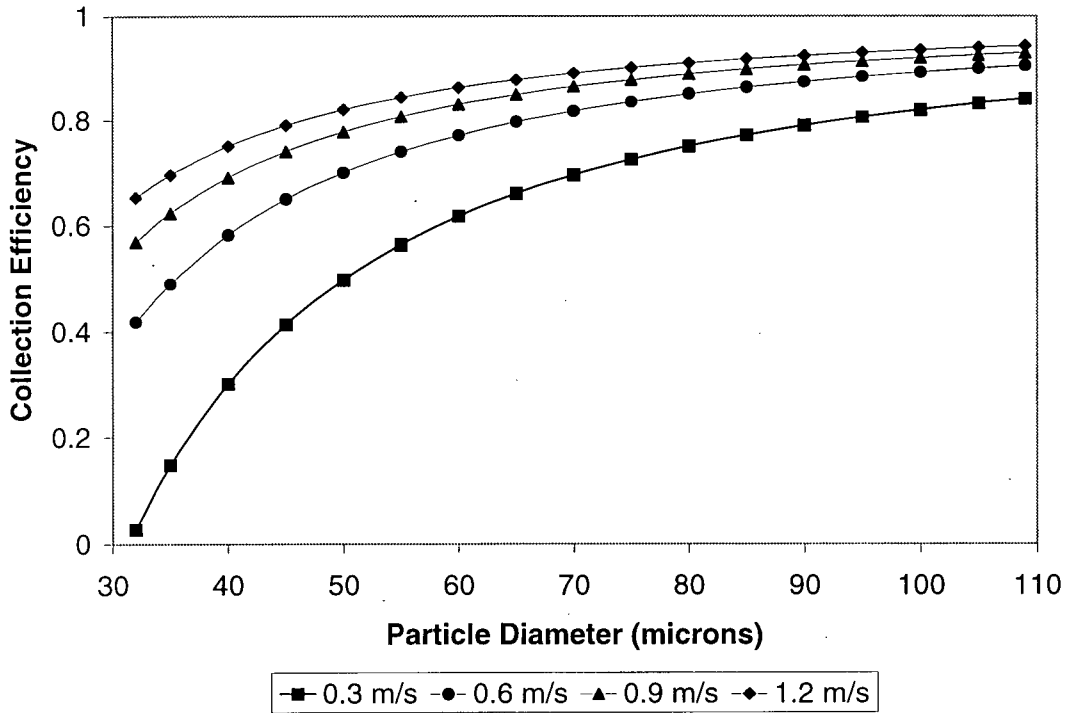
Figure 6-10: Solid Sampler Oxide-Collection Efficiency

Inspection of Figures 6-9 and 6-10 shows that the collection efficiency of the sampler is poorest for low gas velocities and small particle sizes. However, the collection efficiency converges towards 100% for large particle sizes. These figures also show that the collection efficiency of the sampler is higher for sulfides compared to oxides, with the largest discrepancies occurring for small particle sizes and low gas velocities. Typically the oxide-collection efficiency of the sampler is between 60% to 95% of the sulfide-collection efficiency of the sampler. However for a particle size of 32 μm and a gas velocity of 0.3 m/s, the oxide-collection efficiency is only 5% of the sulfide-collection efficiency.

Because the sampler preferentially collects sulfide particles, the extent of reaction calculated from the samples will be lower than the actual extent of reaction, implying that the reaction rate determined from experiments is lower than the actual reaction rate. This discrepancy will be small for most experimental conditions. However, for experiments with small particles sizes and low gas velocities (i.e. runs with large group combustion numbers) this discrepancy is expected to be significant and to result in a reported reaction rate that is significantly lower than the actual reaction rate.

6.2.2.7   Data Acquisition

Figure 6-1 shows the data acquisition system used to control the solids feed-rate and to monitor the temperature profile of the furnace. A PCI-MIO-16E-4 board with a SC2040 signal conditioning card was used to interface a 166 MHz Pentium computer to the thermocouple signals and feeder control signal. The output from the ME-11 balance was sent directly to the computer via the RS-232 input.

94

6.3 Experimental Runs

Two sets of experiments were conducted to investigate:

1) Group combustion of a sulfide cloud;

2) The effect of burner design on the combustion of sulfide clouds.

6.3.1 Group Combustion Theory

The first set of experiments were designed to investigate how the group combustion number of a sulfide cloud influences the heat-up and combustion time of the cloud. Three different furnace temperatures were used; 850, 950 and 1000°C. The group combustion number of the cloud was varied by adjusting the particle size, aim matte grade, Escondida concentrate loading and oxygen pressure. A straight tube burner was used for these runs as it provided a well-defined cloud radius, and therefore a well defined group combustion number at the burner exit.

For all of these runs the total mass flowrate to the furnace was maintained at 75 g/min. As a result the solids feedrate to the furnace varied from between 15 to 60 g/min, depending in the oxygen-to-concentrate ratio and the oxygen enrichment.

The group combustion number is proportional to the oxygen partial pressure and inversely proportional to the oxygen-to-concentrate ratio and the square of the particle diameter. This equation allowed the limits of the experimental parameters to be set. Figure 6-11 shows the range of oxygen intensities, defined as oxygen enrichment of the reaction gas divided by the oxygen-to-concentrate mass flowrate ratio, and group combustion numbers studied in the experiments, while Table 6-4 lists the run parameters.

95
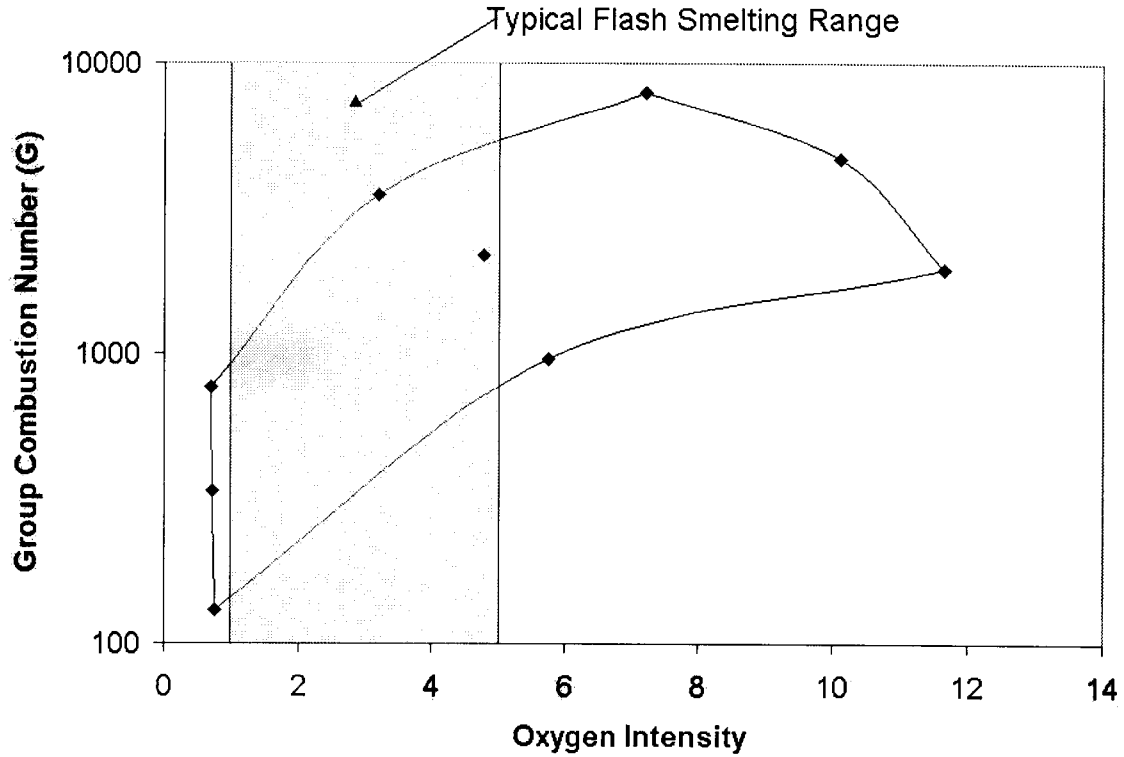
Figure 6-11: Range of Conditions Covered in Experimental Runs

Table 6-4: Experimental Run Parameters

Run	Escondida Loading (wt%)	Particle Diameter Range (μm)	Matte Grade (wt%)	Oxygen Enrichment (vol %) (σ)	Group Combustion Number	Reynolds Number	Oxygen to Concentrate Mass Flow Ratio (η)	$\dfrac{\sigma}{\eta}$
1	0	26-38	100	21	767	2061	0.301	0.70
2	0	46-53	100	21	334	2023	0.289	0.73
3	0	76-88	100	21	130	1966	0.271	0.77
4	50	26-38	80	60	3512	795	0.188	3.19
5	80	46-53	70	75	2190	575	0.157	4.77
6	80	76-88	70	75	962	491	0.131	5.74
7	100	26-38	60	100	7935	401	0.139	7.22
8	100	46-53	55	100	4656	296	0.099	10.13
9	100	76-88	60	100	1950	260	0.086	11.65

The size fractions shown in Table 6-4 were obtained by screening the as received

concentrate using a series of Tyler screens. The characteristic lengths used to determine

96

the group combustion number were: the burner diameter to characterise the cloud diameter; and the arithmetic mean of the particle size fraction to characterise the particle diameter. The Reynolds number of the flow was calculated using the burner diameter as the characteristic length and the burner exit diameter as the characteristic velocity.

The two vertical lines in Figure 6-11 show the range of oxygen intensities for a typical industrial flash smelter. In Chapter 1 a heat and mass balance over a typical industrial flash smelter shows that a value of 1 to 2 for the oxygen intensity is typical for a furnace smelting a chalcopyrite concentrate, while a value of 4 to 5 is typical for a furnace smelting a high-grade concentrate with pure oxygen. Small values of oxygen intensity are seen to occur at:

1) low oxygen enrichment;

2) low Escondida loading; or

3) high matte grade.

Also, for a given oxygen intensity, the group combustion number increases with decreasing particle size.

6.3.2 Burner Design

A straight tube burner provides a well-defined group combustion number at the burner exit and lends itself to studies of heat and mass transfer in a particle cloud. However, its stability limits make it unacceptable for use on an industrial scale. Based on the burner stability analysis discussed in Chapter 4, the re-circulation zone produced by a burner is important in stabilising the flame, as it recycles heat from the combustion zone

back to the cold gas and solids. For a straight tube burner an external re-circulation pattern is produced. However, most industrial burners use either bluff body or swirl stabilisation to produce an internal re-circulation zone, with the aim of improving burner stability. As a result, the combustion characteristics of both a bluff body and a swirl burner were investigated. In both cases the existing straight tube burner was modified to give the desired burner design. Two runs were conducted for each burner configuration with a high group combustion number and one at a low group combustion number corresponding to runs 2 and 8 in Table 6-4.
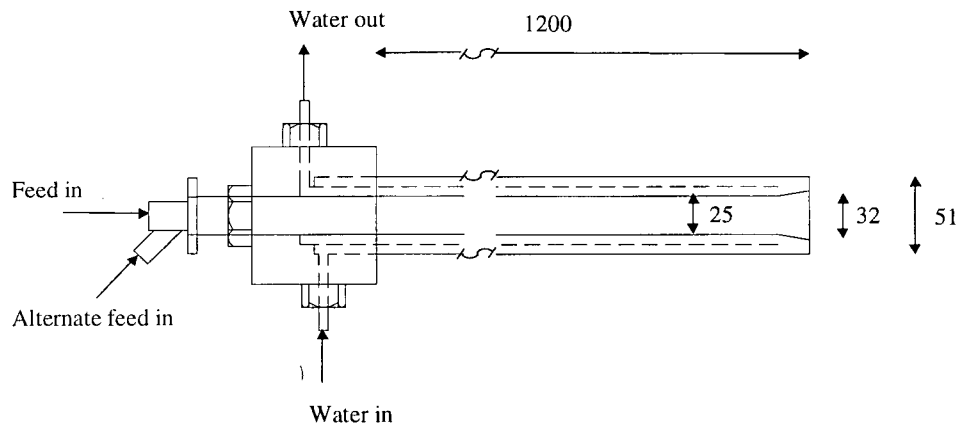
Figure 6-12: Straight-tube Burner (All dimensions in mm)

6.3.2.1   Bluff Body Burner

A water-cooled bluff body was placed at the exit of the straight tube. Water-cooling was supplied by a 6 mm pipe which doubled as the support for the bluff body. The gas and solids were injected into the annulus as a pre-mixed stream. Figure 6-13 shows the dimensions of the bluff body.

98
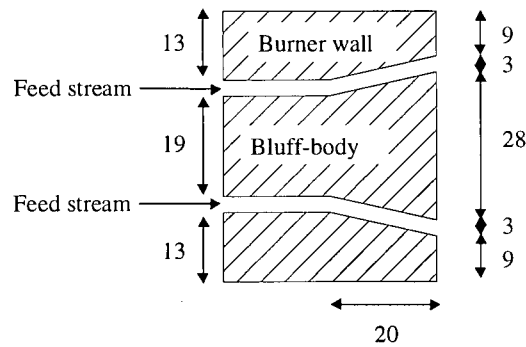
Figure 6-13: Bluff Body Tip Dimensions (All Dimensions in mm)

This shows that the fore-body angle of the bluff body is 24° and the annulus at the burner exit is 3mm wide giving a blockage ratio of 0.76.

6.3.2.2 Swirl Burner

Once again the feed entered as a premixed stream for the swirl burner. In order to create the swirling motion of the gas stream a 45° helical gear was placed in the annulus of the burner. Figure 6-14 shows the helical gear used to create the swirl. The dimensions of the gear are shown in Table 6-4.
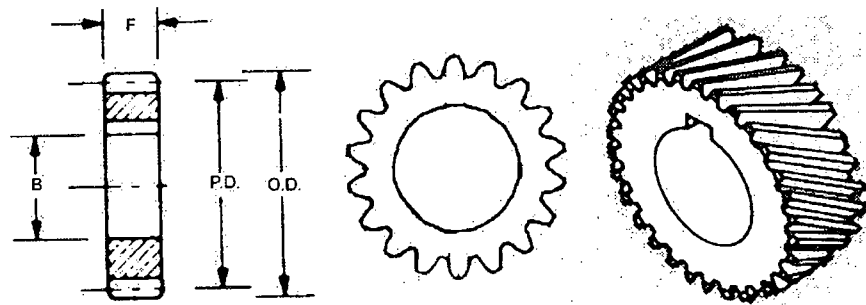
Figure 6-14: 45° Helical Gear used as Swirl Generator

Table 6-5: Helical Gear Dimensions

P.D (mm).	O.D.(mm)	F(mm)	B(mm)
20.32	21.844	22.225	12.7

The swirl number of the gas was calculated from:

$$S = \frac{2}{3}\left(\frac{1-\left(\frac{d_h}{d_b}\right)^3}{1-\left(\frac{d_h}{d_b}\right)^2}\right)\tan\alpha' \qquad\qquad (6\text{-}7)$$

Here α' is 45° (i.e. angle of the helical gear), d_h=18.80mm and d_b = 21.84 giving a swirl number of 0.93. At S>0.6 a re-circulation zone forms at the burner exit. The internal re-circulation zone can be considered as a well-stirred region having a temperature equal to that of the flame and a gas composition equal to the combustion products.

It is worth noting that because the cloud radius is poorly defined for the swirl and bluff-body burners the cloud radius was assumed to be equal to the straight-tube burner diameter, when determining the group combustion number.

6.4 *Experimental Procedure*

Before each run the furnace temperature was established and the ventilation system turned on to maintain the furnace vacuum at 5 Pa. The flow-rate, oxygen concentration and solids feed-rate were then set using the 605 rotameters and the solids feedback control loop, respectively. Once the feed had been started, no samples were collected for the first five minutes allowing the furnace to reach steady state. Solids were

then collected from each sample level (5 levels in all) across the diameter of the shaft and divided into three separate radial samples as described above. After all of the solid samples were collected, gas samples were withdrawn from the furnace centre-line through each sample-port. Once the gas samples had been collected, the run was completed and the feed to the furnace turned off. The furnace temperature fell, and the ventilation system was turned off once the temperature reached 600°C. At the completion of the run, solids were collected from the hearth walls and cyclone allowing a mass balance to be completed. Table 6-6 shows an Experimental Checklist for each experiment.

Table 6-6: Experimental Run Checklist

Action	Check
Set Furnace Temperature	
Turn on ventilation system	
Turn burner water cooling on	
Insert burner	
Set gas flow-rate	
Set solids feed-rate and start feeder (record initial mass)	
Wait 5 minutes to allow flow to reach steady state	
Turn solids sampler water cooling on	
Collect Solids samples from each view-port	
Turn-off water	
Turn on water	
Collect Gas analysis from each view-port	
Turn off water	
Shut off solids	
Shut off gas	
Turn furnace temperature down	
Record mass delivered	
Remove burner	
Collect solids from cyclone, hearth and walls and record weight	

7 Group Combustion Model for Sulfide Flash Smelting

Group combustion theory relates the burning rate of a particle within a cloud to the burning rate of an isolated particle. Therefore analysis of the experimental results in terms of group combustion theory requires a single particle model to be developed and extended to account for group combustion. Following is a description of the model and the technique used to determine the heat transfer and combustion effectiveness factors for each experimental run.

7.1 Model Development

This model uses the equations developed by other authors to describe the combustion of single sulfide particles[19,23,28] as a function of oxygen concentration, furnace temperature and particle size. However, the heat transfer and combustion rates used by these other authors were modified through the use of the heat transfer and combustion effectiveness factors to account for interactive effects. Matlab was used to develop the model. The code is given in Appendix A2.

7.1.1 Particle Conversion

The oxidation of chalcopyrite can be assumed to proceed via:

$$6CuFeS_2 + 19O_2 => 6CuO + 2Fe_3O_4 + 12SO_2 \qquad (7\text{-}1)$$
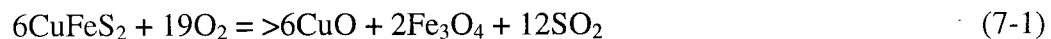
For this reaction the particle conversion can be defined as the mass of chalcopyrite reacted divided by the initial mass of chalcopyrite present in the particle i.e.:

$$X = \frac{m_{CuFeS_{2\,initial}} - m_{CuFeS_{2\,remain}}}{m_{CuFeS_{2\,initial}}} \tag{7-2}$$

This definition of the particle conversion assumes the reaction eventually goes to completion. However, in flash smelting the reaction is stopped at an intermediate stage by supplying insufficient oxygen to achieve complete reaction. Hence a better definition of the particle conversion is: mass of chalcopyrite reacted divided by the aim amount of chalcopyrite which has to be reacted in order to achieve the desired matte grade. Therefore the particle conversion is redefined as:

$$X' = \frac{m_{CuFeS_{2\,initial}} - m_{CuFeS_{2\,remain}}}{m_{CuFeS_{2\,initial}} - m_{CuFeS_{2\,aim}}} \tag{7-3}$$

Because the mass of unreacted chalcopyrite varies linearly with the particle mass, the conversion can be redefined as:

$$X' = \frac{m_{p,0} - m_p}{m_{p,0} - m_{p,aim}} \tag{7-4}$$

In this equation the aim particle mass is given from an equation which relates the final particle mass to the initial particle mass and the oxygen to concentrate ratio:

$$m_{p,aim} = m_{p,o}(1 - 0.263\eta) \tag{7-5}$$

This equation can be derived based on the fact that the final particle mass various linearly from $m_{p,o}$ to $0.855 m_{p,o}$ as the oxygen to concentrate ratio increases from 0 to 0.553.

Using Equation (7-5) in conjunction with Equation (7-4) allows the extent of reaction to be monitored throughout the combustion process. If the reaction is assumed to follow Equation (7-1), then the particle conversion, X', can be redefined in terms of the deviation from aim sulfur, where:

$$X' = \frac{f_{s,0} - f_{s,p}}{f_{s,0} - f_{s,p,aim}}$$

(7-6)

Here f_s is the mass fraction of sulfur in the sample.

7.1.2 Combustion Kinetics

If the reaction is assumed to be first order and to follow the general resistance model, then the instantaneous reaction rate can be defined as the rate of oxygen consumption:

$$\dot{m}'_{O_2} = \eta_c k_{ov} A_p C_{O_2} MW_{O_2}$$

(7-7)

with $k_{ov} = \dfrac{k_m k_c}{k_m + k_c}$ where $k_m = \dfrac{D Sh}{d_p}$, $k_c = A \exp\left(\dfrac{-E_a}{RT}\right)$ and $D = D_o \left(\dfrac{T}{T_0}\right)^{1.75}$

In Equation (7-7) η_c has been included to account for the interactive effects during combustion. A Sherwood number of 2 was used in this model as it is shown in Chapter 8 that the particles accelerate quickly to the gas velocity. This implies that there is no slip velocity between the particles and the gas.

7.1.3 Particle Mass

Once the instantaneous reaction rate is known the instantaneous particle mass loss rate can be determined from:

$$\frac{dm_p}{dt} = -0.263\,\dot{m}'_{O_2} \tag{7-8}$$

In Equation (7-8) the constant is derived from the stoichiometry of Reaction (7-1) assuming the Fe_3O_4 and CuO remain within the particle. Equation (7-8) can be integrated to give the particle mass as a function of time.

7.1.4 Oxygen Concentration

If it is assumed that the gas phase volume remains constant throughout the combustion process then the change in oxygen concentration as the reaction proceeds is given by:

$$\frac{dC_{O_2}}{dt} = -\dot{m}'_{O_2}\,\frac{P}{\eta m_{p,o} R T_\infty} \tag{7-9}$$

This equation can be integrated to give the oxygen concentration as a function of time.

As shown in Chapter 6 the leakage rate of air into the furnace is significant at approximately 10 to 20% of the total oxygen requirement. The leakage was accounted for modifying the initial oxygen concentration and oxygen-to-concentrate ratio, which assumes that all leaks mix instantaneously with the inlet mixture. A better way to account for the leaks may be to assume they are introduced linearly along the furnace shaft length. However because the variation of the lengths along the shaft length is

unknown, it was decided to assume the leaks were introduced instantaneously with the fresh mixture.

7.1.5 Particle Temperature

The particle temperature varies throughout the combustion process due to heating by convection, radiation and chemical reaction. If heating by radiation is neglected and the particle Biot number is small such that the particle temperature is uniform, then the particle temperature is given by Equation (7-10).

$$m_p C_p \frac{dT_p}{dt} = \frac{\lambda \eta_h Nu_{iso}}{d_p} A_p \left(T_\infty - T_p\right) + \dot{m}'_{O_2} \Delta H \qquad (7\text{-}10)$$

In this equation η_h has been used to account for the interactive effects. As with Equation (7-7) the isolated particle Nusselt number was assumed to be 2 because the slip velocity between the particles and the gas is negligible.

As shown in Section 9.3.4 on the CFD model development radiation can be safely neglected for conditions within the UBC flash reactor as its influence on the predicted cloud combustion rate is negligible.

This model assumes a closed system and therefore the gas temperature should rise along with the solids temperature. However the model assumes that the gas temperature T_∞ remained constant throughout the calculation. This assumption is not expected to introduce large errors because as shown in the results for the CFD study (discussed in

106

Chapter 10), for most of the conditions studied here, the strong recirculation present minimises the gas phase temperature gradients within the furnace.

7.1.6 Solution Procedure

Equations (7-8), (7-9) and (7-10) can be solved simultaneously to give the particle mass as a function of time, which can then be used to compute the particle conversion X'. Figure (7-1) shows the solution procedure used to solve Equations (7-8), (7-9) and (7-10).
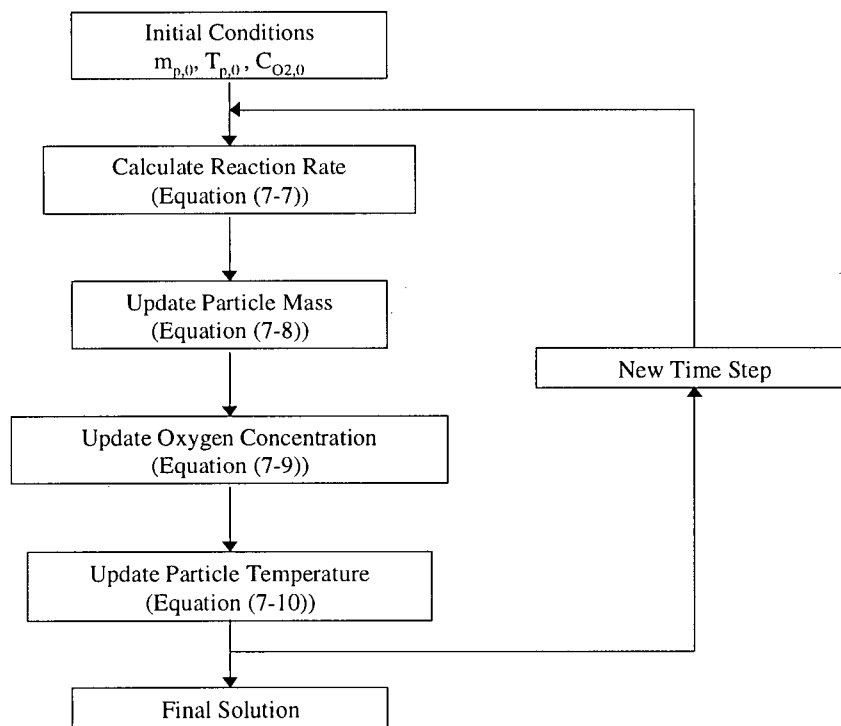
Figure 7-1: Solution Procedure for the Group Combustion Model

Equations (7-8) and (7-9) can be solved using Euler's method, assuming that the gas phase oxygen concentration, particle mass and temperature remain unchanged over each small time step while Equation (7-10) is solved using the following equation:

$$T_p(t + \Delta t) = \alpha_p + (T_p(t) - \alpha_p) e^{-\beta_p \Delta t}$$ (7-11)

where $\alpha_p = T_\infty + \dfrac{\dot{m}'_{O_2} \Delta H}{m_p C_p}$ and $\beta_p = \dfrac{\lambda \eta_h Nu_{iso} A_p}{d_p m_p C_p}$

7.1.7 Example Solution

Solving Equations (7-8), (7-9) and (7-10) allows the gas phase oxygen concentration, particle mass and temperature to be determined. Figures 7-1 and 7-2 show the particle temperature and conversion respectively calculated by the model for the conditions listed in Table 7-1.

Table 7-1: Cloud Combustion Model Parameters.

Parameter	Value
Particle diameter (μm)	45
Initial oxygen partial pressure (atm)	0.47
Initial oxygen-to-concentrate ratio (-)	0.285
Activation energy (kJ/mol)	250
Pre-exponential factor (m/s)	5×10^{12}
Heat transfer effectiveness factor (-)	0.1
Combustion effectiveness factor (-)	0.05
Initial cloud temperature ($^\circ$C)	25
Furnace temperature ($^\circ$C)	850

Before discussing the results from the model it is worth noting the following assumptions:

1) The particles are assumed to be spherical;

2) The slip velocity between the particles and the gas is assumed to be negligible;

3) The leaks were assumed to mix instantaneously with the fresh mixture;

108

4) Radiation was ignored; and

5) The gas phase temperature was assumed constant throughout the calculation.
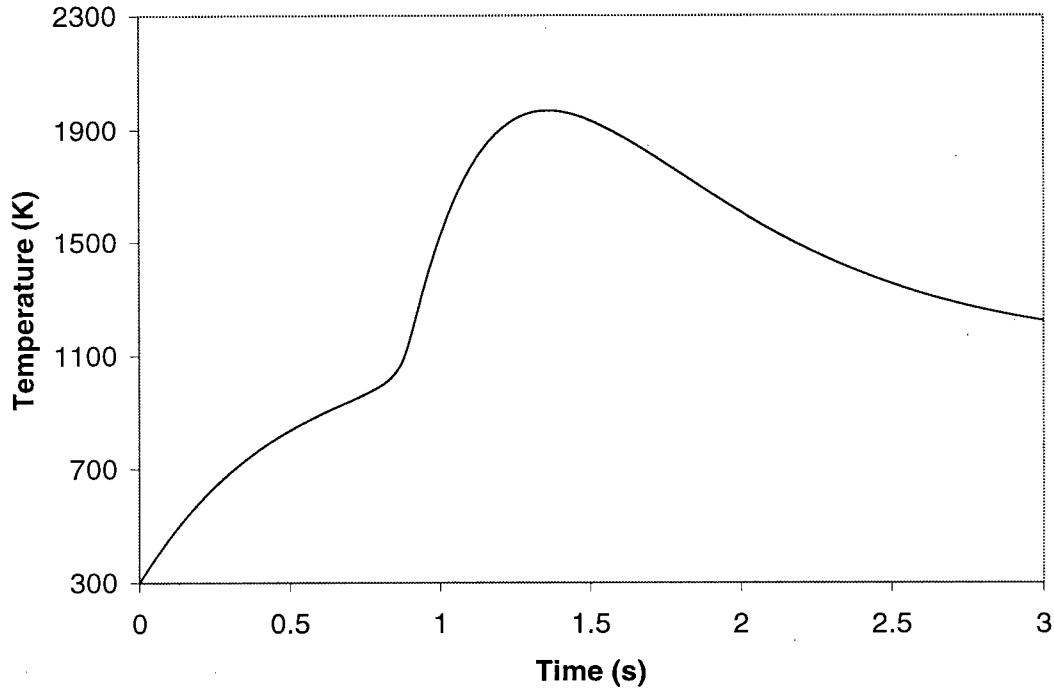
Figure 7-2: Predicted Particle Temperature vs Time for a Cloud with Initial Conditions Listed in Table 7-1

Figure 7-2 shows the predicted particle temperature as a function of time. For the first approximately 0.83s heating is by convection alone as the particle reaction rate is too low to aid in particle heating. However, once the particle reaches ignition its temperature rises rapidly due to the increase in particle heating caused by the exothermic chemical reaction. At approximately 1.4 s the particle temperature begins to decrease and to approach the furnace temperature of 1123 K due to the slower combustion rate caused by the reduced gas phase oxygen concentration.
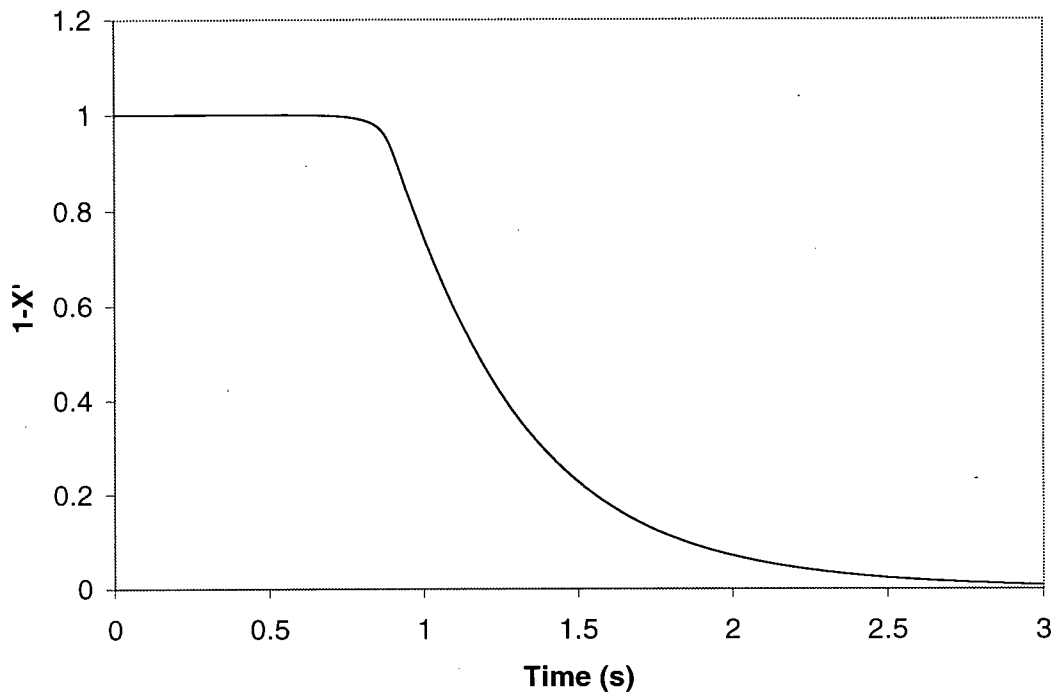
Figure 7-3: Predicted Unconverted Fraction vs Time for a Cloud with Initial Conditions Listed in Table 7-1

Figure 7-3 plots the particle conversion as a function of time and shows the same trend in Figure 7-2. Initially no reaction occurs until ignition and then the combustion proceeds at an initially fast but continually decreasing rate. The decline in combustion rate is caused by the depletion of oxygen in the gas phase.

7.2   Model Fitting Algorithm

As will be seen in Chapter 8, the goal of the group combustion study was to determine the influence of the furnace operating conditions on the heat transfer and combustion effectiveness factors. The raw data from the experimental runs were used to determine the cloud conversion as a function of furnace residence time and the heat

transfer and combustion effectiveness factors were calculated by minimising the error between the group combustion model and experimental results. Figure 7-4 shows the minimisation algorithm.
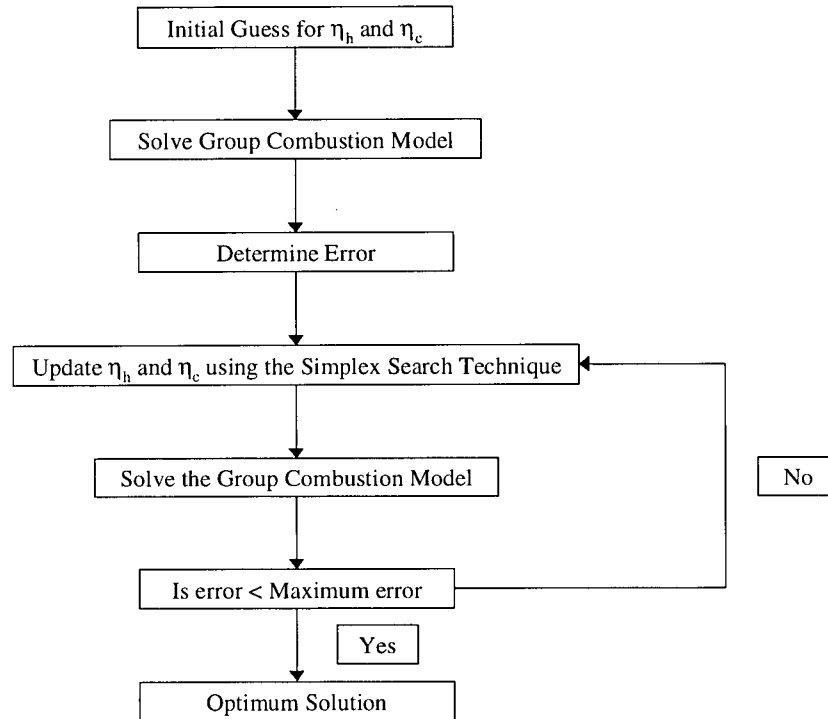
Figure 7-4: Minimisation Algorithm

The optimisation technique used fmins, a standard Matlab function to determine the heat transfer and combustion effectiveness factors. This function uses the Nelder-Mead simplex search, which is a direct search method that does not require gradients or other derivative information. Further information on the Nelder-Mead simplex search technique can be found in [93] and [94]. Appendix A2 shows the Matlab code used to implement the optimisation technique.

7.3 Chapter Summary

Using the definitions for the heat transfer and combustion effectiveness factors from Chapter 3 allowed a single particle combustion model to be modified to account for interactive effects. However, because of the complex nature of the process several simplifying assumptions were required in order to develop this model. In later chapters these assumptions are shown to be reasonable for the conditions present in the UBC flash reactor. However the applicability of the model for other conditions is less certain.

The two assumptions of most concern when attempting to apply the model to other conditions are a negligible slip velocity between the particles and the gas and secondly that radiation can be ignored. A negligible slip velocity essentially assumes that the particles can be represented in an Eulerian frame, which ignores unique trajectories of individual particles. Under certain circumstances (i.e. when turbulent dispersion of the particles is large) this assumption dramatically influence the cloud combustion characteristics and the model cannot be used to predicted the cloud combustion rate. Secondly in situations were radiation is important this model cannot be used to accurately predict the heat transfer rate to the particles rendering the model useless.

While these two assumptions limit the model applicability, it is still useful in highlighting the influence of interactive effects during sulfide flash smelting and its results can be used to infer the important mechanisms during sulfide flash smelting.

8 Results and Discussion

The experimental section of this study consisted of two complimentary investigations: the first was aimed at determining if group combustion theory could be applied to flash smelting, while the second studied the effect of burner design on the combustion characteristics of sulfide particle clouds. In both studies, the influence of different parameters on the cloud reaction rate was investigated by observing the cloud conversion as a function of time.

To ensure that the furnace was operating according to design, a global mass balance was conducted for the first four experimental runs. Closure of the mass balance ensured that no significant losses were unaccounted for and allowed the important output streams of the furnace to be determined.

8.1 Furnace Mass Balance

The furnace mass balance was conducted by comparing the mass of each element charged to the furnace, to the mass of each element collected from the furnace, once steady state conditions had been achieved. Figure 8-1 lists the furnace inputs and outputs and shows that there are three input and four output streams. To close the mass balance required the total mass and composition of each of these streams to be known.

Off Gas

N_2
O_2
SO_2
SO_3

Feed Gas

N_2
O_2

Cyclone

Cu
Fe
S
O
Gangue

Air Leaks

N_2
O_2

Feed Solids

Cu
Fe
S
Gangue

Hearth

Cu
Fe
S
O
Gangue

Furnace Walls

Cu
Fe
S
O
Gangue
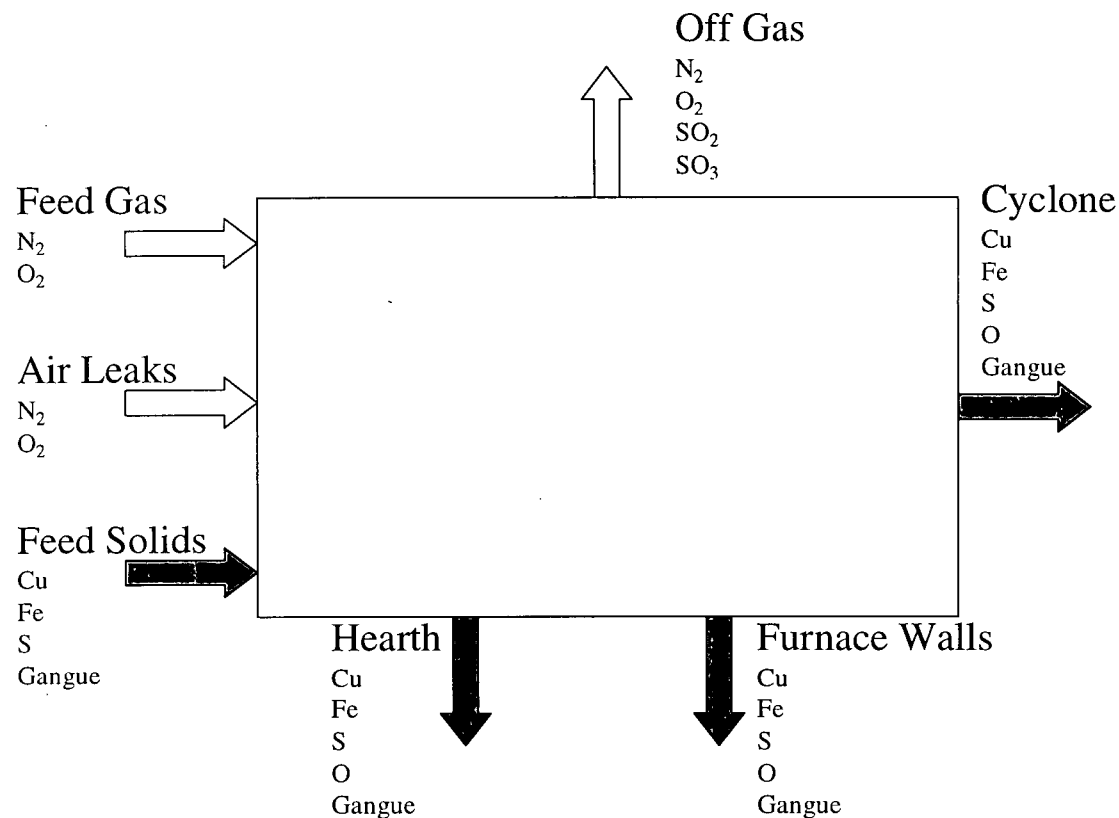
Figure 8-1: Furnace Mass Balance Streams

8.1.1 Input Streams

The three furnace input streams were the feed gas, feed solids and air infiltration streams. The feed gas stream was maintained at a constant flow rate and oxygen partial pressure throughout the run, while the solids feed-rate was controlled at a constant value. A sample of the solids feed stream was analysed to determine its copper, iron, sulfur and gangue content. Analysis of the gangue material showed that it consisted primarily of silica and alumina. Therefore the oxygen present was assumed to be inert, allowing the gangue to be treated as a pseudo-element with respect to the mass balance. For all runs the furnace vacuum was manually controlled at 5 Pa which, as explained in Section 6.2.2,

114

resulted in an air infiltration rate of 8.1 litres/min which represents approximately 16 to 22% of the available oxygen. As the composition and flow-rate of each input stream was known and the duration of each experimental run was recorded, the total mass of each element charged to the furnace could be calculated.

8.1.2 Furnace Output Streams

The four output streams were the furnace off-gas and the solids collected from the furnace hearth, furnace walls and cyclone. An off-gas sample was collected from the furnace exit and analysed for nitrogen, oxygen and sulfur dioxide while a sulfur trioxide concentration was estimated assuming that $O_2/SO_2/SO_3$ were in equilibrium. Section 6.2.2.6 shows there is insufficient furnace residence time to ensure the $O_2/SO_2/SO_3$ system reaches equilibrium. However, equilibrium value provides an upper bound on the oxygen and sulfur mass balances.

The off-gas flow-rate was calculated from the total gas flow rate entering the furnace using nitrogen as a tie element. The solids from the furnace hearth, furnace walls and cyclone were collected and weighed, with a sample from each being analysed for copper, iron, sulfur and gangue.

8.1.3 Furnace Balance

Table 8-1 shows the mass of each element charged to the furnace and the mass of each element collected from the furnace together with the error between the mass charged and the mass collected. Table 8-2 shows the experimental conditions for each of the four runs. It is worth noting that a mass balance was only conducted for the first four

115

experimental runs as analysing hearth, wall and cyclone samples for all runs was too expensive.

Table 8-1: Furnace Mass Balance (grams)

Run	Component	Input	Hearth	Walls	Cyclone	Off-Gas	Total Out	% Error
1	Copper	582	371	100	86	0	558	-4.24
	Iron	568	405	108	80	0	594	4.54
	Sulfur	628	98	7	18	477	599	-4.55
	Oxygen	802	164	81	44	477	764	-4.70
	Gangue	141	65	25	14	0	104	-26.28
2	Copper	1229	756	167	159	0	1082	-12.02
	Iron	523	428	94	35	0	526	6.74
	Sulfur	920	198	44	17	529	773	-14.41
	Oxygen	894	149	33	29	529	714	-17.26
	Gangue	187	63	14	11	0	78	-53.03
3	Copper	718	487	99	119	0	705	-1.81
	Iron	647	471	96	67	0	634	-1.98
	Sulfur	792	246	50	25	377	698	-11.87
	Oxygen	848	140	28	39	666	872	2.87
	Gangue	347	177	36	14	0	226	-34.80
4	Copper	1461	1099	98	126	0	1323	-9.46
	Iron	537	448	47	54	0	549	2.31
	Sulfur	944	302	10	40	191	543	-42.49
	Oxygen	413	166	54	31	214	465	+12.60
	Gangue	392	173	17	22	0	212	-45.86

Table 8-2: Experimental Conditions Relating to Table 8-1

Run	Escondida loading (wt%)	Oxygen enrichment (vol%)	Oxygen-to-concentrate ratio	Particle diameter (µm)	Furnace temperature (°C)
1	0	40	0.288	49.5	850
2	100	40	0.199	49.5	850
3	0	21	0.271	82	850
4	100	100	0.086	82	850

Four comments can be made concerning these results.

1) The mass of each element collected from the furnace agreed well with the mass charged to the furnace with a typical error of less then 15%. Agreement for the gangue is poor however. The only explanation that can be offered for the poor agreement is that particles containing considerable amounts of gangue will have a lower density than those consisting predominantly of sulfides. Because the collection efficiency of the cyclone increases with increasing particle density, (and because the cyclone efficiency is low as discussed below), it is expected that a larger proportion of particles containing gangue will escape capture and stay in the gas stream. This probably gave rise to the poor mass balance closure for the gangue.

2) In run 4 the sulfur balance was low while the oxygen balance was high. This suggests that the gas line used to collect the off-gas sample was not purged sufficiently to ensure that all of the air within the line was replaced by furnace gas. As a result the gas sample showed an artificially low sulfur dioxide content and high oxygen content.

3) For most elements the mass collected from the furnace was less than the mass charged to the furnace. This is to be expected as some of the solids were either retained within the annulus of the furnace or carried away in the off-gas stream.

4) For all runs the fractional split of the mass flows between the output streams is relatively constant. The material collected in the hearth for approximately 50% of the total exit mass flowrate. The off gas flow rate represents

approximately 30% while the mass collected from the walls and cyclone each represent approximately 10% for the total exit mass from the furnace.

8.1.3.1 Cyclone Efficiency

Figure 8-2 shows the cyclone collection efficiency for sulfides and oxides. This was calculated using the procedure given by Perry[92]. It indicates that for the particle sizes used in these experiments, the collection efficiency is less than 80%, explaining the discrepancies in the furnace mass balance. In these calculations the cyclone inlet velocity was taken as 2.35 m/s which is equivalent to a volumetric flow rate of 60 l/min. This volumetric flow rate was determined (from the air infiltration study discussed in Section 7.2.2) to be the total furnace exit flow rate.
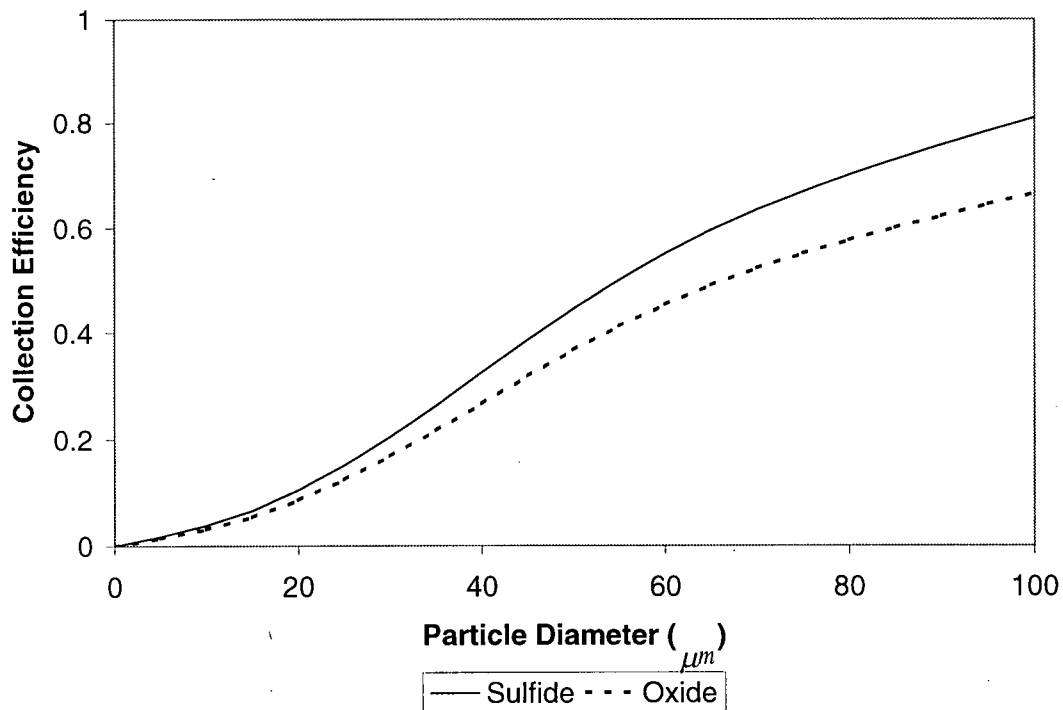
Figure 8-2: Cyclone Collection Efficiency

The poor collection efficiency is due to the fact that the cyclone was originally designed for use in another process that used much higher gas flow rates, producing inlet velocity of approximately 18m/s. As most cyclones are designed to operating with gas velocities in the order of 15 to 20 m/s it is clear that gas velocities used in these experiments were too low to ensure optimum performance of the cyclone.

8.2 Group Combustion Study

The aims of the group combustion study were to:

1) determine if sulfide cloud combustion could be described using the group combustion model developed in Chapter 7;

2) determine if the functional dependencies of the heat transfer and combustion effectiveness factors on the group combustion number follow that predicted by Equation (3-3) and the expressions listed in Table 3-2, respectively;

3) use the derived relationships for the heat transfer and combustion effectiveness factors to determine the operating diagram of the UBC flash reactor; and

4) extend this knowledge to the operation of an industrial flash smelter.

These aims were achieved by studying the influence of the group combustion number on the cloud reaction rate. The group combustion number was varied by changing the oxygen partial pressure, oxygen-to-concentrate ratio, mean particle diameter and Escondida loading of the cloud with the operating conditions of each run given in Table 6-4.

8.2.1 Group Combustion Model

To determine if the group combustion model can be used to describe the experimental data, the cloud conversion predicted by the model was compared to experimental values. In this study the cloud conversion is defined (see Equation (7-6)) as the ratio of the mass of sulfur removed from the particle (or cloud) to the mass of sulfur required to be removed in order to achieve the desired matte grade. As seen from Equation (7-1) the iron content of the sample can be ignored as the reaction of iron and sulfur are assumed to proceed in parallel with the reaction rate of each species being related to the overall rate of oxygen consumption.

The model calculated the burning rate of the cloud for different particle sizes, oxygen partial pressures and furnace temperatures and predicted the cloud conversion as a function of time. Experimental values of the cloud conversion were calculated from the solid samples collected at different axial locations within the furnace. By assuming that the gas velocity decayed according to:[92,50]

$$U = U_o \qquad\qquad x \le \left[\left(\frac{\rho_o}{\rho_a} \right)^{1/2} K_j - a_j \right] \qquad\qquad (8\text{-}1a)$$

$$U = \frac{K_j U_o}{x + a_j} \left(\frac{\rho_o}{\rho_a} \right)^{1/2} \qquad x > \left[\left(\frac{\rho_o}{\rho_a} \right)^{1/2} K_j - a_j \right] \qquad\qquad (8\text{-}1b)$$

The residence time of the particle at the different axial locations could be estimated from:

$$\tau_{res} = \int_0^{L_x} \frac{dx}{U} \qquad (8\text{-}2)$$

where the slip velocity between the particles and gas is assumed to be 0. This is a reasonably assumption as shown below. Equation (8-2) then permits the cloud conversion to be determined as a function of time.

8.2.1.1   Particle Velocity

Equation (8-2) can only be used if the slip velocity between the gas and the particles is low and the particles accelerate rapidly to the gas velocity.

The magnitude of the slip velocity can be estimated from the particles terminal velocity, which for the Stokes law region (Re$_p$< 0.1) is given by:

$$U_t = \frac{g d_p^2 (\rho_p - \rho)}{18\mu} \qquad (8\text{-}3)$$

For conditions in the UBC flash reactor Equation (8-3) gives a terminal velocity of 0.016 to 0.26 m/s as the particle size increases from 20 to 80μm, which represents approximately 1 to 25% of the flow velocity.

Clift et al[95] describe an analysis which allows the time and distance required for a particle to be accelerated from rest to various fractions of its terminal velocity. Their analysis shows that, for the conditions present within the UBC flash reactor, a dimensionless distance of approximately 5000 is required for the particle to achieve 99%

of its terminal velocity, assuming creeping flow conditions. The dimensionless displacement is given by:

$$x'_p = \frac{36\mu^2}{d_p^4 g\rho(\rho_p - \rho)} x_p \qquad (8-4)$$

This gives a required distance of 8×10^{-5} and 0.02 m to achieve 99% of the particle terminal velocity, which is approximately 2% of the shaft length.

This analysis shows that the slip velocity and distance required for the particle to reach its terminal velocity is negligible for small particles, allowing Equation (8-2) to be used to estimate the particle residence time. However the assumption is less valid for the larger particle sizes, in particular the slip velocity becomes considerable for particle greater than approximately 50 µm. Because a large portion of the experimental runs were conducted with particle diameters less than 50µm this technique can still be used.

8.2.1.2 Fitting Algorithm

The group combustion model contains four fitting parameters, namely the activation energy and pre-exponential factor for the combustion reaction and the heat transfer and combustion effectiveness factors. The values of these four parameters had to be estimated for the model to accurately predict the burning rate of the cloud. Hence a parameter estimation algorithm was used to determine these parameters, optimising the fit between the group combustion model and experimental data.

Initially the activation energy and pre-exponential factors were fitted for each run. However these parameters were found not to differ significantly on a statistical basis between runs. Therefore the activation energy and pre-exponential factor were estimated using data from all experimental runs, while the heat transfer and combustion effectiveness factors were estimated for each individual run. Figure 8-3 shows the optimisation algorithm used to determine the four parameters.
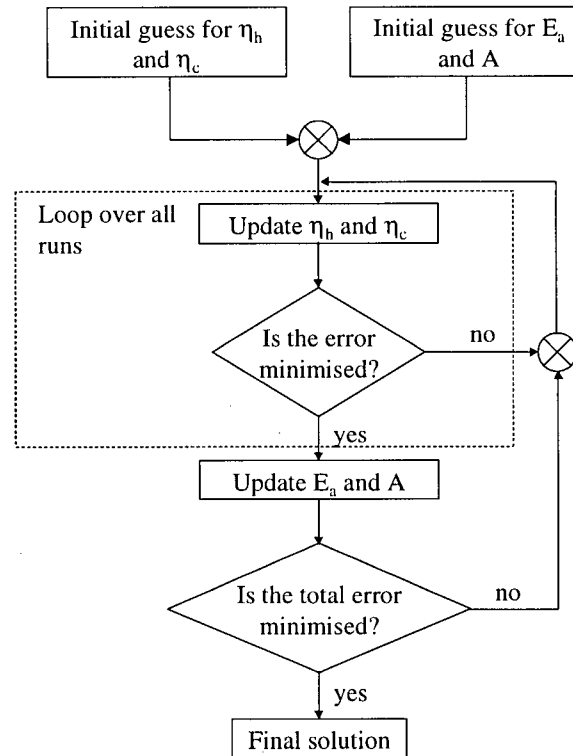
Figure 8-3: Parameter Estimation Algorthim

Because four fitting parameters were used to fit the data caution should be used when attempting to infer furnace performance from these parameter. In particular the activation energy, pre-exponential factor and the heat transfer effectiveness factor are significantly influenced by the ignition point of the cloud. Hence some of the variation in

these three parameters is due to the fact that are defined by the ignition point of the cloud. However, these interactions are minimised by having the activation energy and pre-exponential factor being fit over all runs.

8.2.1.3 Kinetic Parameters

Table 8-3 lists the activation energy and pre-exponential factor together with their 95% confidence intervals, for the combustion reaction determined from this study. The value of 240 ± 41 kJ/mol for the activation energy compares favourably with the value of 215 kJ/mol determined by Chaubal and Sohn[6] who used a thermogravimetric technique to study the oxidation of chalcopyrite.

Table 8-3: Cloud Activation Energy and Pre-Exponential Factor

Activation Energy $\left(\dfrac{kJ}{mol}\right)$	Pre-Exponential Factor $\left(\dfrac{m}{s}\right) \times 10^{12}$
240 ± 41	3.7 ± 1.6

The error associated with activation energy is approximately 16%, which is acceptable. However the error associated with the pre-exponential factor is larger at approximately 40%. This large error results because the ignition temperature (represented by point I in Figure 8-5) influences both the pre-exponential and heat transfer effectiveness factor and is determined from the Damkohler Number (See Section 3.1.1) which contains the ratio of the heat transfer effectiveness factor to the pre-exponential factor. Taking these two points together implies that some of the scatter present in the pre-exponential factor results from the fact that both parameters were used to fit the experimental data. By allowing the pre-exponential factor to be fitted using the

data for all runs reduced the uncertainty in both the pre-exponential and heat transfer effectiveness factor.

8.2.1.3.1 Cloud Activation Energy

For these runs the composition of the cloud varied from between 100 wt% San Manuel concentrate to 100 wt% Escondida concentrate. San Manuel concentrate is approximately 80 to 90 wt% chalcopyrite and 10 to 20 wt% pyrite, while Escondida concentrate is approximately 65 wt% chalcocite and 25 wt% pyrite. The activation energies of chalcopyrite, pyrite and chalcocite are 215[6], 150[96] and 520[9] kJ/mol respectively. Therefore if the activation energy of the cloud was a linear function of its composition, then the activation energy would be expected to range from approximately 209 kJ/mol to 376 kJ/mol. This was not observed, with the cloud activation energy remaining constant over all Escondida loadings, suggesting that the cloud's activation energy is a non-linear function of its composition. A possible explanation for this is as follows.

The activation energy of the cloud will remain at or close to that of the low activation energy material providing there is enough low activation energy material present so that upon ignition, sufficient heat is released thereby promote ignition of the high activation energy material. Only when there is insufficient low activation material present to promote ignition of the high activation energy material will the clouds activation energy begin to increase. If this theory is true, then the cloud activation energy as a function of its composition may be as indicated in Figure 8-4.
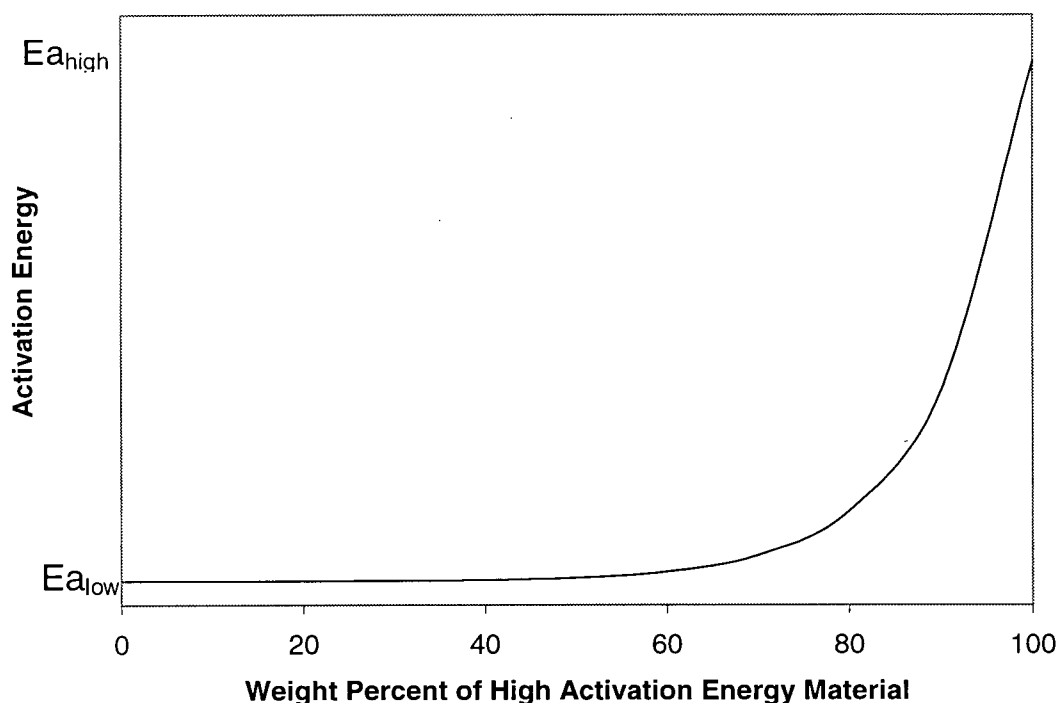
Figure 8-4: Possible Variation of Cloud Activation Energy with Composition

These results suggest that, because the activation energy and pre-exponential factor do not depend appreciably on the Escondida loading of the cloud, the problems observed by industrial smelters are not caused by the intrinsic reaction kinetics of Escondida concentrate. Before this can be confirmed, further work is essential to fully understand the influence of different minerals on the effective activation energy and pre-exponential factor of a particle cloud.

8.2.1.4   Model Fit

Figure 8-5 is a plot of the experimental and predicted deviation from aim sulfur (See Equation (7-6) for a definition of the deviation from aim sulfur) for a typical run.

126

The R-squared value of the fit is, R^2=0.99, indicating that a satisfactory fit can be obtained between experimental data and the group combustion model.
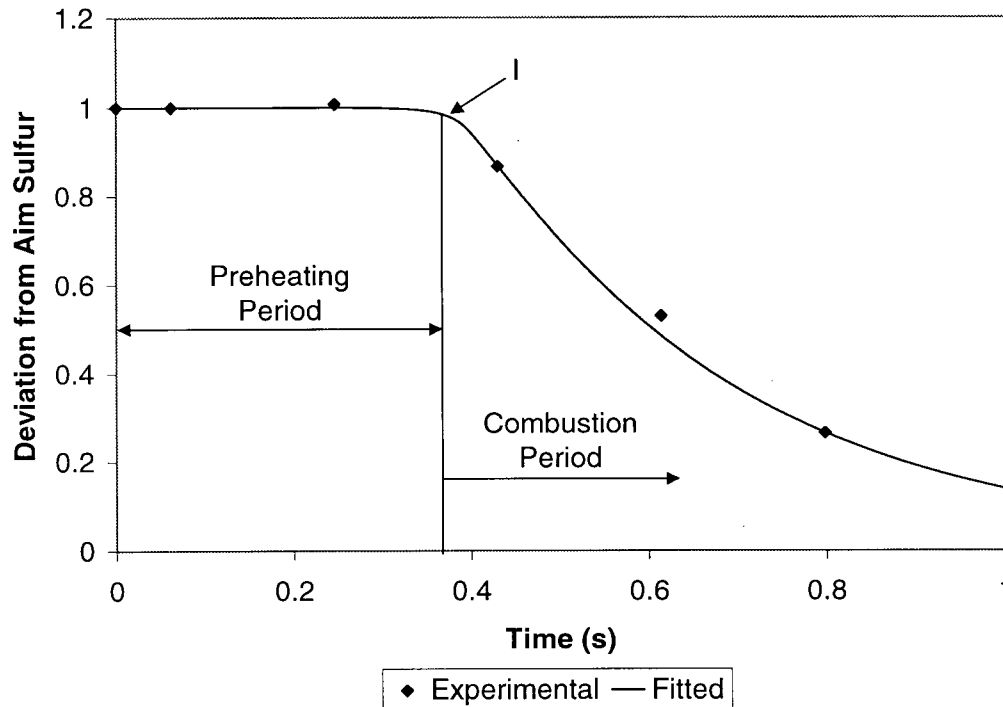
Figure 8-5: Comparison of the Group Combustion Model Predictions and Experimental Data: d_p=42μm, P_{o2} = 0.4atm, η = 0.288, T = 850°C, η_c = 0.055, η_h = 0.088

Figure 8-5 shows that the total reaction time can be broken into two regions. The first region is the pre-heat zone and represents the time required to preheat the cloud to the ignition temperature. In this region negligible reaction occurs and heating is via convection and radiation. After ignition the cloud enters the combustion zone that provides the time to carry out the combustion reaction. In the combustion zone, the reaction proceeds at an initially fast rate. However, oxygen is continually depleted throughout the reaction, causing the observed reduction in the reaction rate.

8.2.2 Particle heat transfer effectiveness factor

If heat transfer within the cloud obeys group combustion theory the heat transfer effectiveness factor should follow the relationship given by Equation 3-3. For each run, the group combustion number was known, the isolated particle Nusselt number was assumed to be 2, and the heat transfer effectiveness factor was calculated using the above fitting algorithm. Therefore the cloud Nusselt number could be calculated and should obey the general correlation for convective heat transfer derived from dimensional analysis[97-98].

$$Nu = f\left(\text{Re}, \text{Ra}, \text{Pr}\right) \tag{8-5}$$

8.2.2.1 Furnace Flow Regime

Equation (8-5) can be simplified depending on the flow regime present within the furnace. For flows governed by forced convection, the Reynolds number is important while the Rayleigh number is important for natural convection dominated flows, with both the Rayleigh and Reynolds numbers being important for transitional flows.

Delichatsios[99] developed a diagram to determine the transition from momentum to buoyancy controlled jet diffusion flames. This diagram is shown in Figure 8-6.
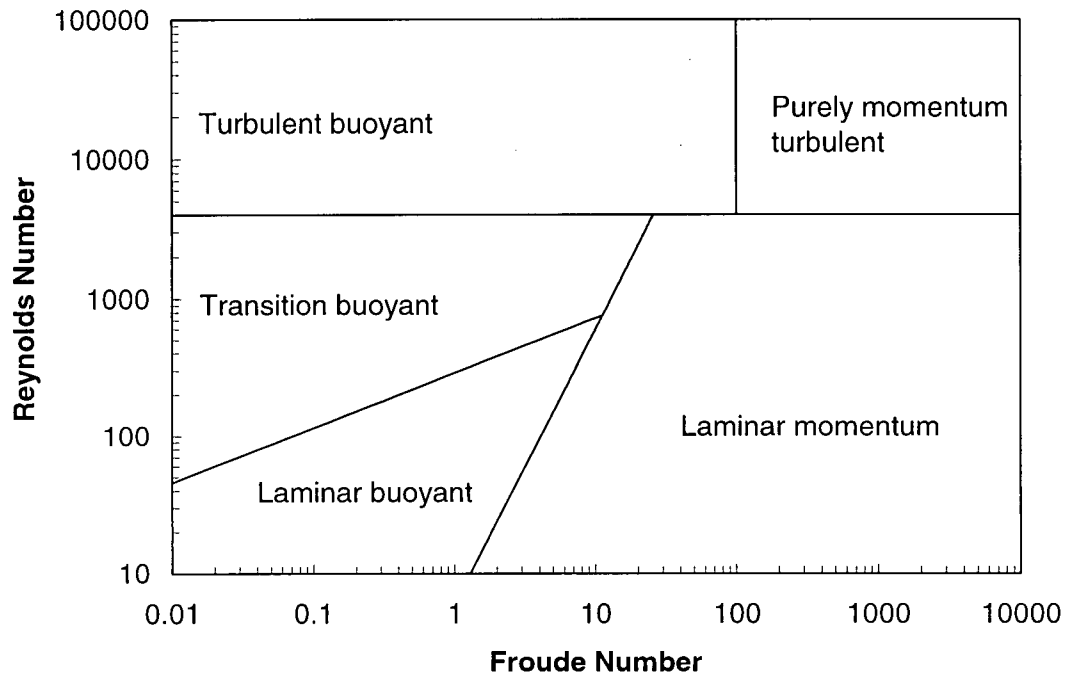
Figure 8-6: Flow Regimes for Jet Diffusion Flames

The Froude number in Figure 8-6 is given by:

$$Fr = \frac{U_0}{\left(gd_b\right)^{1/2}} \frac{1}{\left(S_{Fr}+1\right)^{3/2}}$$

(8-6)

where S_{Fr} is the air-to-fuel mass stoichiometric ratio, related to the oxygen-to-concentrate ratio and oxygen enrichment according to:

$$S_{Fr} = \left(1+\frac{7}{8}\left(\frac{1-\sigma}{\sigma}\right)\right)\eta$$

(8-7)

129

For conditions within the UBC flash reactor the jet Reynolds number varies from 3000 to 7000, while the Froude number varies from 0.3 to 2. Therefore the flame is expected to be buoyant, indicating that the cloud Nusselt number should be correlated against the Rayleigh Number.

$$Nu_{cl} = \gamma Ra^{\psi} \tag{8-8a}$$

where

$$Ra = \frac{gL_{Ra}^3 \rho \Delta \rho C_p}{\mu \lambda} \tag{8-8b}$$

In Equation (8-8a) the Prandtl number is assumed to remain constant with its influence being accounted for through the proportionality constant. The characteristic length used to determine the Rayleigh number was taken to be the furnace length which was 1.2 m. Recall from Chapter 3 that the cloud Nusselt number describes the heat transfer through the separated boundary layer between the jet issuing from the burner and the surrounding atmosphere. Hence the characteristic length used for the cloud Nusselt number is the burner diameter.

8.2.2.2 Cloud Nusselt Number

The density difference in the Rayleigh number is usually caused by temperature variations. However, for a particle-laden jet, the presence of the particles increases the effective density of the mixture and this must be accounted for when determining the jet

Rayleigh number. Relationships for the effective mixture density and the density of the furnace atmosphere are:

$$\rho_o \approx \frac{P}{RT_o}\left(32\frac{\sigma}{\eta} + 4\sigma + 28\right) \qquad\qquad (8\text{-}9a)$$

$$\rho_a \approx \frac{P}{RT_\infty}(36\sigma + 28) \qquad\qquad (8\text{-}9b)$$

These equations are derived in Appendix A3. Equation (8-9b) assumes that no particles are present within the furnace ambience and that all the oxygen that enters the furnace is converted to sulfur dioxide. Using the above equations the cloud Nusselt number can be plotted against the jet Rayleigh number as shown in Figure 8-7.
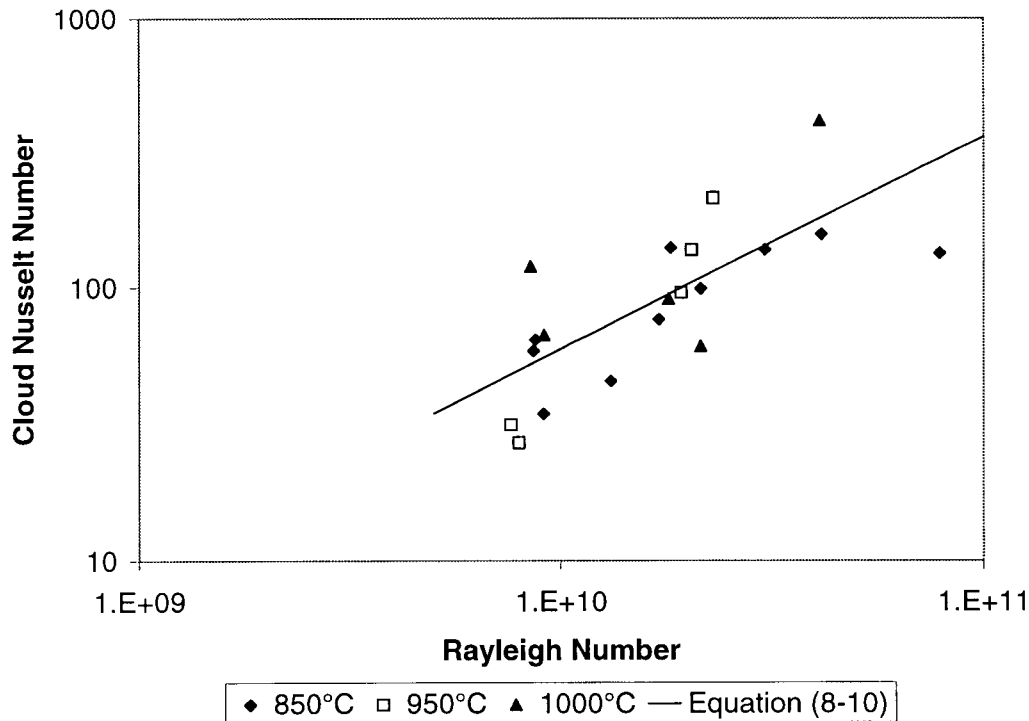
Figure 8-7: Cloud Nusselt Number vs. Cloud Rayleigh Number

131

Equation (8-10) shows the least squares regression fit to the data together with the 90% confidence interval for the parameter estimates.

$$Nu_{cl} = \exp\left(-13.4 \pm 3.5\right) Ra^{\left(0.76 \pm 0.15\right)} \qquad (8\text{-}10)$$

The fit for the exponent is reasonable with a confidence interval of $\pm$ 20%. However the confidence interval for the proportionality constant is extremely large extending over several orders of magnitude. This large confidence interval results because the jet Rayleigh number is large, and therefore a small variation in the exponent, ψ, results in a large change in the value for Ra^{ψ}, which is reflected in the confidence interval for the proportionality constant. By setting the exponent of the Rayleigh number to 0.76 the confidence interval for the proportionality constant can be reduced. Equation (8-11) shows the least squares regression fit for the data assuming the exponent on the Rayleigh number is 0.76.

$$Nu_{cl} = \left(1.54 \pm 0.22\right) \times 10^{-6} Ra^{0.76} \qquad (8\text{-}11)$$

In Equation (8-11) the confidence interval associated with proportionality constant has been reduced to approximately $\pm$ 15%. This indicates that the large error associated with the proportionality constant in Equation (8-10) results from the large value of the Rayleigh number and the variation in its exponent.

It can be concluded that the relationship for the heat transfer between a sulfide particle cloud and its surroundings can be fitted reasonably well by group combustion theory, with natural convection dominating the flow pattern within the furnace.

8.2.3 Combustion effectiveness factor

If the combustion of a sulfide cloud obeys group combustion theory, then the combustion effectiveness factor should follow the expressions listed in Table 3-2. Figure 8-8 plots the experimentally determined combustion effectiveness factor against the group combustion number.
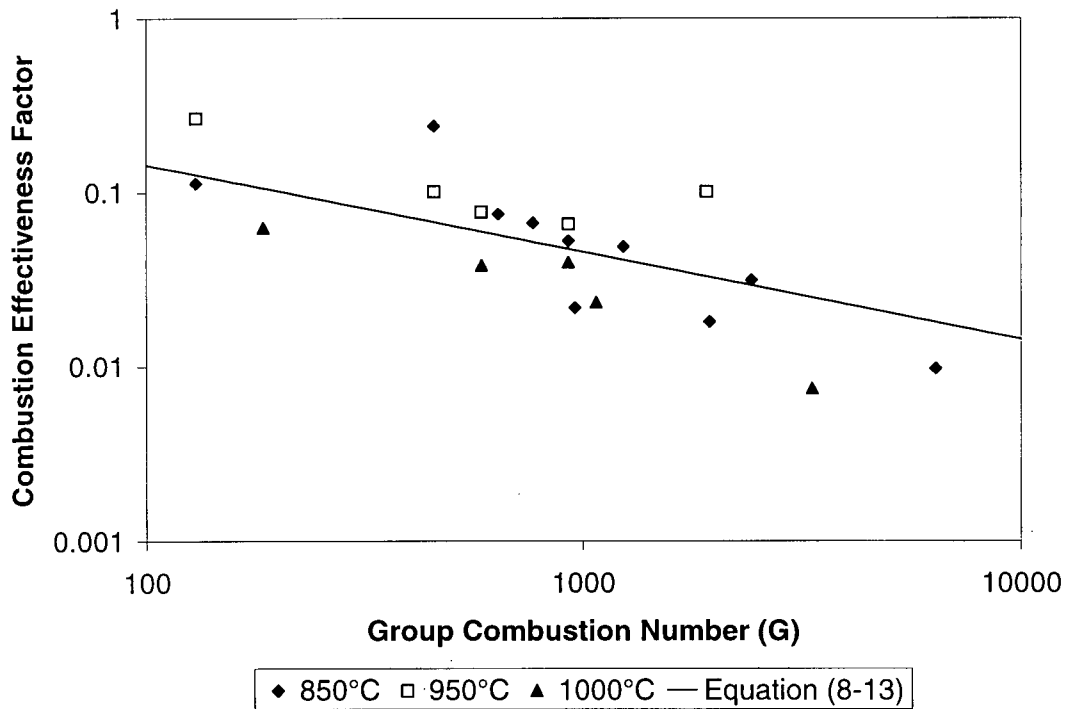
Figure 8-8: Combustion Effectiveness Factor vs Group Combustion Number

The least squares fit of the data, together with the 90% confidence interval for the parameter estimates is given by Equation (8-12). Because the combustion effectiveness factor varies over 1.5 orders of magnitude, the parameters in Equation (8-12) were

133

estimated using the sum of the square of the relative errors bewteen the experimental and predicted values.

$$\eta_c = \frac{(1.75 \pm 1.51)}{G^{(0.57 \pm 0.13)}} \tag{8-12}$$

As with the cloud Nusselt number, the confidence interval for the exponent of the group combustion number is acceptable. However there is again a large error in the proportionality constant which results from the large group combustion numbers.

8.2.3.1 Solid Sampler Bias

As discussed in Section 6.2.2.6 the solid sampler preferentially collects sulfides over oxides, with this discrepancy being largest at low gas velocities and small particle sizes. This bias results in a calculated reaction rate that is lower than the true rate causing a lower-than-expected combustion effectiveness factor to be predicted.

For the experiments conducted in this study, low gas velocities result from high oxygen enrichment and low oxygen-to-concentrate ratios. Therefore according to Equation 3-30, the sampler bias will be largest at high group combustion numbers. Also, as shown by Shook et al[28], high oxygen enrichment and small particle sizes increase the propensity for dust formation (generation of micron sized particles through particle explosions), further accentuating the sampler bias at high group combustion numbers. This is expected to result in over-estimation of the dependence of the combustion

134

effectiveness factor on the group combustion number, resulting in an exponent which has an absolute value which is apparently larger than the true value.

8.2.3.2   Improved Estimate

Because the theoretical value of the exponent in Equation (8-12) is within the confidence interval for the experimentally determined value, the exponent for the group combustion number was held constant at –0.5 and the regression was recalculated to give the following fit.

$$\eta_c = \frac{(1.44 \pm 0.21)}{G^{1/2}} \qquad (8\text{-}13)$$

Equation (8-13) can only be used providing that the minimisation function used to determine the coefficients has a "shallow" minimum and the value of the objective function for Equation (8-13) is close to that for Equation (8-12). The sum of the squares of the relative error was used as the objective function and had a value of 10.83 and 11.33 for Equations (8-12) and (8-13), respectively. This shows that the change in the objective function is approximately 5%, indicating the Equation (8-13) closely approximates Equation (8-12) and can be used to adequately describe the experimental data.

Equiation (8-13) shows that a resonable fit exists between group combustion theory and the experimental results, suggesting that the combustion of a sulfide cloud does obey group combustion theory.

135

8.2.4 Influence of Group Combustion on the Burning Rate

Equations (3-3) and (8-13) show that as the group combustion number increases, the heat transfer and combustion effectiveness factors decrease. This does not imply that clouds with large group combustion numbers burn more slowly than clouds with small group combustion numbers. Rather it implies that clouds with large group combustion numbers burn relatively slower for clouds with small group combusiton numbers when compared to a single particle experiencing the same ambient conditions. Conditions that give rise to slow burning rates for single particles also produce slow burning rates for a cloud of particles. This can be shown by considering the relationship between the cloud burning time and particle diameter, assuming that the oxygen enrichment, oxygen-to-concentrate ratio and furnace temperature all remain unchanged.

As shown by the analysis developed in Appendix A4, the combustion time of an isolated particle burning under diffusional control is proportional to the square of the particle diameter.

$$\tau_{iso} \propto d_p^2 \tag{8-14}$$

On the other hand, for a particle within a cloud the burning time is proportional to the burning time of the isolated particle and inversely proportional to the combustion effectiveness factor. Equation 8-12 shows that the combustion effectiveness factor is inversely proportional to the square root of the group combustion number, while Equation 3-30 shows that the group combustion number is inversely proportional to the

square of the particle diameter. Hence the combustion effectiveness factor is proportional to the particle diameter, i.e.

$$\tau_c \propto \frac{\tau_{iso}}{\eta_c} \propto d_p^2 G^{1/2} \propto d_p \qquad (8\text{-}15)$$

Therefore as the particle diameter decreases, the group combustion number of the cloud increases. The burning time of the cloud continues to decrease, but it does not decrease as quickly as the burning time of an isolated particle.

8.2.5 Furnace Operating Diagram

The above results show that group combustion theory can be used to predict the heat-up and combustion time of the cloud as a function of particle size, oxygen partial pressure, oxygen-to-concentrate ratio and furnace temperature. With respect to flash smelting, the sum of the heat-up and combustion times of the cloud represents the minimum shaft residence time required to complete the reaction. If the particles are assumed to accelerate rapidly to the gas velocity (See Equation(8-3)), then the particle residence time within the furnace is inversely proportional to the gas feedrate. Also for flash smelting the solids and gas feedrates are related through the oxygen-to-concentrate ratio and the oxygen enrichment. Therefore by equating the shaft residence time to the sum of the cloud heat-up and combustion times, the maximum solids feedate that can be smelted by the furnace can be calculated as a function of the furnace operating parameters. Attempting to treat feedrates in excess of this maximum limit would result in

shaft failure which can result in insufficient particle residence time within the shaft to allow complete reaction, thereby causing under-reacted material to enter the hearth.

8.2.5.1 Heat Transfer Analysis

Assuming radiative heat transfer is negligible (See Secition 9.3.4) and that the isolated particle Nusselt number is 2, the energy balance over the particle is given by:

$$m_p C_p \frac{dT_p}{dt} = \eta_h \frac{2\lambda}{d_p} A_p \left(T_\infty - T_p \right)$$
(8-16)

This equation assumes that there are no temperature gradients within the cloud or particles. The implications of this assumption are discussed in Section 8.2.5.1.2.

8.2.5.1.1 Cloud Heat-up Time

Equation (8-16) can be rewritten as:

$$\frac{dT_p}{dt} = \frac{12\lambda\eta_h}{\rho_p C_p d_p^2} \left(T_\infty - T_p \right)$$
(8-17)

This can be integrated between the clouds initial and ignition temperatures to give the heat-up time of the cloud.

138

$$\tau_h = \frac{\rho_p C_p d_p^2}{12\lambda\eta_h} \ln\left(\frac{T_\infty - T_{p,o}}{T_\infty - T_{p,i}}\right) \qquad (8\text{-}18)$$

If the ignition temperature of the cloud is assumed constant, then Equation (8-18) shows that the cloud heat-up time is proportional to the square of the particle diameter and inversely proportional to the heat transfer effectiveness factor.

$$\tau_h \propto \frac{d_p^2}{\eta_h} \qquad (8\text{-}19)$$

For large group combustion numbers, the heat transfer effectiveness factor is proportional to the cloud Nusselt number and inversely proportional to the group combustion number. Furthermore, Equation (3-31) shows that the group combustion number is proportional to the oxygen enrichment and inversely proportional to the oxygen-to-concentrate ratio and the square of the particle diameter. Equation (8-10) shows that the cloud Nusselt number is proportional to the Rayleigh number, which in turn is approximately proportional to the square of the mixture density. For typical values of the oxygen enrichment and oxygen-to-concentrate ratios experienced in flash smelting, the mixture density given by Equation (8-9a) is approximately proportional to the oxygen enrichment and inversely proportional to the oxygen-to-concentrate ratio. Hence the particle heat-up time is proportional to:

$$\tau_h \propto \frac{G d_p^2}{Nu_{cl}} \propto \frac{\sigma}{\eta d_p^2} d_p^2 \left(\frac{\eta}{\sigma}\right)^{2\psi} \propto \left(\frac{\eta}{\sigma}\right)^{2\psi-1} \qquad (8\text{-}20)$$

Here ψ is the exponent on the Rayleigh number in the heat transfer correlation given by Equation (8-10).

8.2.5.1.2 Particle and Cloud Biot Numbers

As shown in Section 3.1.1 the Biot number of a sulfide particle is typically 0.01 to 0.02 implying that the assumption of an isothermal particle is valid. However, the cloud Biot number is more difficult to determine as the cloud consists of a gas undergoing turbulent motion. Hence the thermal conductivity used to calculate the Biot number should be the turbulent thermal conductivity. Results from the CFD study, which is discussed in Chapters 9 and 10, show that the clouds turbulent thermal conductivity varies from 0.5 to 10 $\frac{W}{mK}$, depending on the turbulence properties of the cloud. If the cloud Nusselt number is taken as 100 (from Figure 8-7) then the cloud Biot number varies between 0.2 and 4, indicating that significant thermal gradients exist within the cloud and suggesting that Equation (8-16) cannot be used to predict the particle heat-up time.

Using analysis developed in Appendix A5, Figure 8-9 shows the ratio of the average particle heat-up time when thermal gradients within the cloud are accounted for to the particle heat-up time predicted by Equation (8-18). Two cases are considered one for a cloud Biot number of 0.2 and the other for a cloud Biot number of 4.
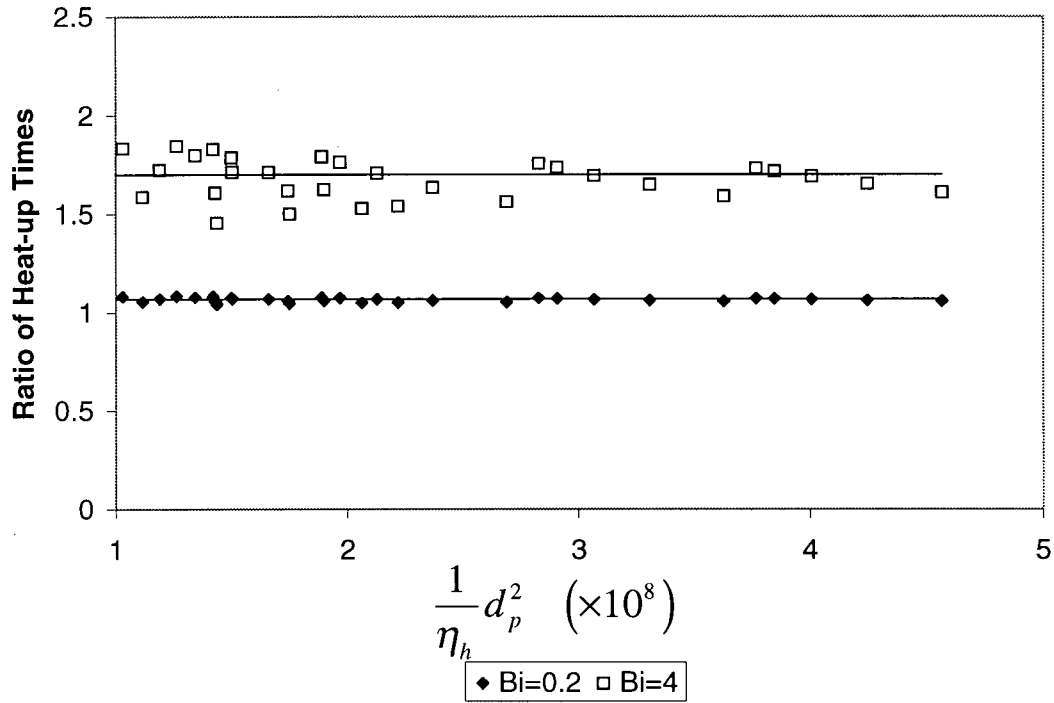
Figure 8-9: Ratio of the Predicted Particle Heat-up Time when Thermal Gradients within the Cloud are Accounted for to the Particle Heat-up Time Predicted from Equation (8-9)

Figure 8-9 shows that the presence of the thermal gradients within the cloud introduces a lag, causing the particle heat-up time to increase above that predicted from Equation (8-18). However, Figure 8-9 also shows that the ratio of the particle heat-up time, as a function of $\dfrac{d_p^2}{\eta_h}$, remains relatively constant, for constant cloud Biot numbers.

This implies that while Equation (8-18) cannot be used to predict the particle heat-up time, Equations (8-19) and (8-20) are valid (as a first approximation) and can be used in the following analysis.

8.2.5.2 Cloud Combustion Time

A similar analysis to that described above (See Appendix A4) can be used to show that the cloud combustion time is proportional to the oxygen-to-concentrate ratio and the square of the particle diameter, and inversely proportional to the oxygen enrichment and combustion effectiveness factor, ie.

$$\tau_c \propto \frac{d_p^2 \, \eta}{\eta_c \, \sigma} \tag{8-21}$$

The combustion effectiveness factor is inversely proportional to the square root of the group combustion number. Hence the combustion time can be written as:

$$\tau_c \propto \frac{d_p^2 \, \eta}{\eta_c \, \sigma} \propto G^{1/2} d_p^2 \frac{\eta}{\sigma} \propto \left(\frac{\sigma}{\eta}\right)^{1/2} \frac{d_p^2 \, \eta}{d_p \, \sigma} \propto \left(\frac{\eta}{\sigma}\right)^{1/2} d_p \tag{8-22}$$

8.2.5.3 Shaft Residence Time

Since the particle accelerate quickly, the particle residence time within the shaft is approximately proportional to the shaft length and inversely proportional to the burner exit velocity (U_o), with the burner exit velocity being proportional to the oxygen-to-concentrate ratio and solids feed rate, and inversely proportional to the oxygen enrichment. Therefore the residence time is:

$$\tau_{res} \propto \frac{L}{U_o} \propto \frac{L\sigma}{\eta f} \tag{8-23}$$

8.2.5.4 Maximum Solids Feed Rate

The maximum solids feed rate, f_{max}, that can be smelted within the furnace occurs when the sum of the heat-up and combustion time of the cloud equals the shaft residence time, ie:

$$\frac{\sigma L}{\eta f_{max}} = A_f \left(\frac{\eta}{\sigma} \right)^{2\psi - 1} + B_f d_p \left(\frac{\eta}{\sigma} \right)^{1/2} \tag{8-24}$$

In Equation (8-24) A_f and B_f are proportionality constants which depend on, among other things, the shaft diameter, burner diameter, furnace temperature, particle density and particle specific heat. This equation can be rearranged to give:

$$f_{max} = \left(\frac{A_f}{L} \left(\frac{\eta}{\sigma} \right)^{2\psi} + B_f \left(\frac{d_p}{L} \right) \left(\frac{\eta}{\sigma} \right)^{3/2} \right)^{-1} \tag{8-25}$$

8.2.5.4.1 Relative Importance of the Heat-up and Combustion Times

Equation (8-25) may be simplified if the heat-up and combustion times differ greatly in magintude. In the case where the heat-up time of the cloud is dominant the maximum solids feedrate can be given by:

$$f_{\max} = \left(\frac{A_f}{L} \left(\frac{\eta}{\sigma} \right)^{2\psi} \right)^{-1} \tag{8-26}$$

whereas when the combustion time is dominant:

$$f_{\max} = \left(B_f \frac{d_p}{L} \left(\frac{\eta}{\sigma} \right)^{3/2} \right)^{-1} \tag{8-27}$$

By considering Equations (8-18) and (A5-11) the heat-up and combustion times for the cloud can be estimated. For the range of Group Combustion numbers studied in these experiments, the heat-up time of the cloud represents between 5 and 10% of the total reaction time, suggesting that the total reaction can be described adequately by the cloud combustion time. This was confirmed by plotting the maximum solids feedrate, determined from the group combustion model, against those predicted by Equations (8-26) and (8-27). These plots are shown in Figure 8-10.

The maximum solids feedrate calculated by the group combustion model was determined by solving the model (discussed in Chapter 7), using the experimentally determined heat transfer and combustion effectiveness factors. This allowed the reaction time of the cloud to be determined. The solids feedrate that produced the shaft residence time equal to the predicted reaction time was then calculated from (8-23) and (8-2). The resulting solids feedrate represents the maximum solids feedrate that can be treated by the furnace.

The maximum solids feedrates determined from Equation (8-26) were calculated

using values of $\psi = 0.76$ and $A_f = 0.024$ (m.s).kg^{-1} while for Equation (8-27) $B_f = 744.5$

s.kg^{-1} was used. These values of A_f and B_f were determined by conducting a least

squares regression fit for Equation (8-25) using the maximum solids feedrate preidcted

from the group combustion model. A value of $\psi = 0.76$ was used as this is the value that

gives the best fit to the experimental data.
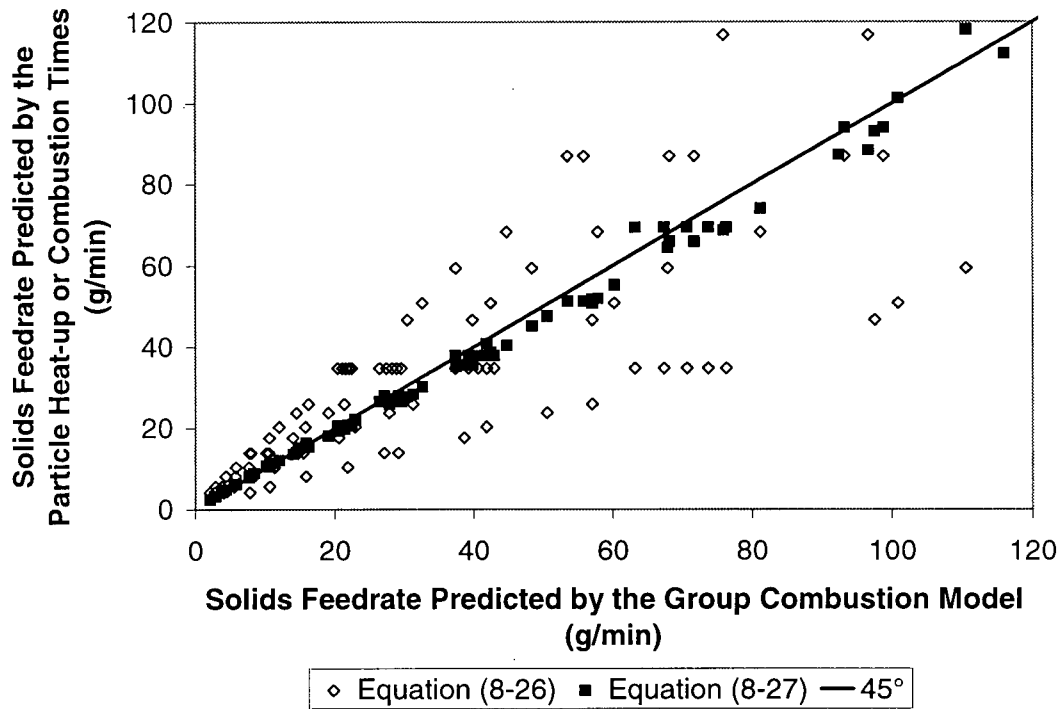
**Figure 8-10: Maximum Solids Feed-rate as a Function of the Cloud Heat-up
(Equation (8-26)) and Combustion (Equation (8-27)) Times**

In Figure 8-10 the abscissa is the maximum solids feedrate predicted by the group

combustion model while the ordinate axis represents the maximum solids feedrate

predicted from Equations (8-26) and (8-27). A perfect fit between the group combustion

145

model and Equations (8-26) or (8-27) is represented by the 45° line. As seen in the figure the solids feedrate predicted from Equation (8-27) (i.e. when the particle combustion time dominates the reaction time) closely follows the 45° line. On the other hand, there is significant scatter for the solids feedrate predicted from Equation (8-26) (i.e. when the particle heat-up time dominates the reaction time). Hence it can be concluded that the combustion time dominates the overall reaction time within the UBC flash reactor and that Equation (8-27) can be used to describe furnace operation.

As will be seen throughout the remainder of this Chapter (and in Chapter 10), the dimensionless group $\left(\dfrac{d_p}{L}\right)\left(\dfrac{\eta}{\sigma}\right)^{3/2}$ is proposed as an important parameter which describes the operation of a shaft for a given set of operating parameters. This quantity is referred to below as the "shaft smelting index".

8.2.5.5   UBC Flash Reactor Operating Diagram

Figure 8-11 shows the stable operating region for the furnace at each of the three temperatures used in this study. This diagram was developed by solving the group combustion model using the experimentally determined values for the heat transfer and combustion effectiveness factors (Equations (8-10) and (8-13)). The solids feedrate that produced a furnace residence time equal to the cloud reaction time was then taken as maximum solids feedrate. It is this value that is represented below.

146

$$t_{reaction} > t_{residence}$$

$$t_{reaction} < t_{residence}$$

Solids Feed-rate (g/min)

Smelting Index $(\times 10^5)$

—— 850°C —— ·950°C ==△== 1000°C
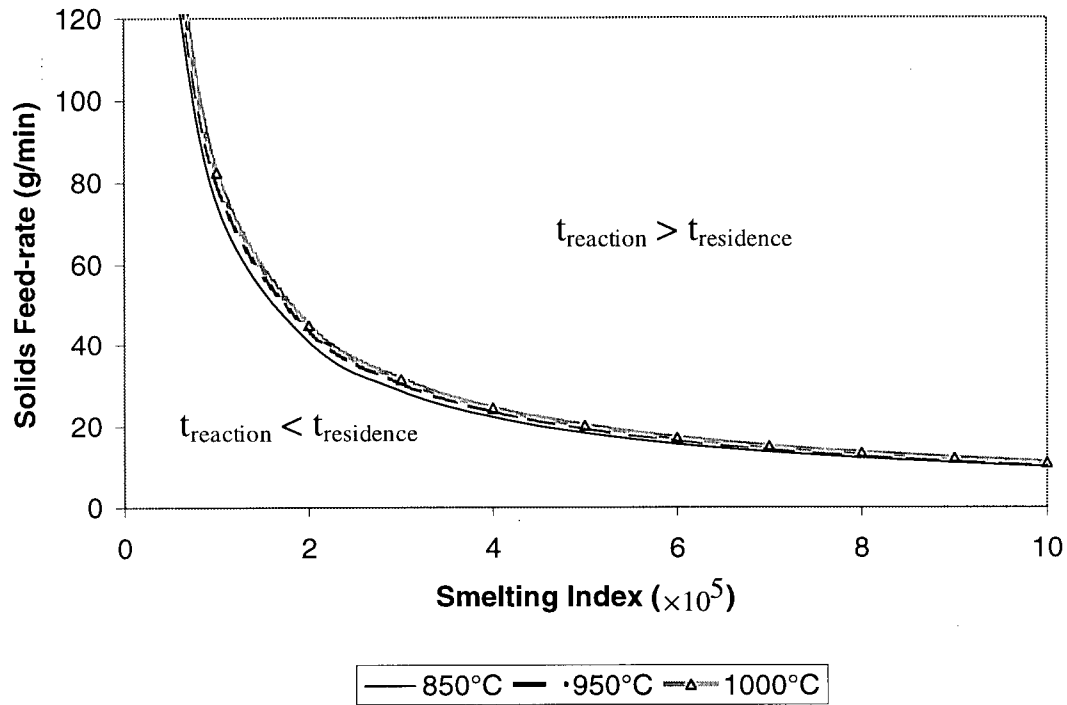
Figure 8-11: UBC Flash Reactor Operating Diagram

Figure 8-11 shows that high solids feed rates are possible at small values of the shaft smelting index. This corresponds to small particle diameters, low oxygen-to-concentrate ratios, high oxygen enrichment or a long shaft length. Small particle diameters, low oxygen-to-concentrate ratios and high oxygen enrichments tend to decrease the combustion time of the cloud, while low oxygen-to-concentrate ratios, high oxygen enrichment and a long shaft length increase the residence time of the particles within the shaft. Both the reduction in the reaction time and the longer shaft residence times increase the maximum solids feedrate that can be treated by the furnace, explaining the trend observed above.

147

8.2.6 Flash Furnace Operating Diagram

A similar analysis can be conducted to determine the operating limits for an industrial flash furnace. However, not only is the ratio of the reaction to the shaft residence times important for this case, but also the furnace heat and mass balances place restrictions on the allowable feed rates.

8.2.6.1 Influence of Group Combustion on the Furnace Operating Limits

For an industrial flash furnace, the expressions for the combustion and shaft residence times are identical to those for the UBC flash reactor. However, the burner exit velocities are approximately two orders of magnitude greater in an industrial flash smelter than in the UBC flash reactor. This implies that forced convection dominates the flow within the furnace. Recall from Chapter 3 that the cloud Nusselt number describes the heat transfer through the separated boundary layer between the jet issuing from the burner and the surrounding atmosphere. Hence according to studies conducted on heat transfer to separated flows[51-56] the cloud Nusselt number is of the form:

$$Nu_{cl} = \gamma \, \mathrm{Re}_{cl}^{\kappa} \, \mathrm{Pr}^{\varphi} \tag{8-28}$$

In Equation (8-28) the Reynolds number Re_{cl} is the reynolds number of the cloud and is given by:

$$\mathrm{Re}_{cl} = \frac{\rho_o U_o d_b}{\mu} \tag{8-29}$$

In Equation (8-29) the density of the cloud is given by Equation (8-9a). This assumes that the gas/solids mixture is treated as a single phase with the presence of the particles increasing the "fluid" density. The characterisitic velocity is taken to be the burner exit velocity and the characteristic length is the burner diameter.

8.2.6.2 Cloud heat-up time

The Reynolds number of the cloud is proportional to its density and velocity. Equation (8-9a) shows that the cloud density is proportional to the oxygen enrichment and inversely proportional to the the oxygen-to-concentrate ratio, while the cloud velocity is proportional to the oxygen-to-concentrate ratio and solids feedrate and inversely proportional to the oxygen enrichment. Hence the cloud Nusselt number is given by:

$$Nu_{cl} \propto f^{\kappa} \tag{8-30}$$

Therefore the cloud heat-up time can be written:

$$\tau_h \propto \frac{Gd_p^2}{Nu_{cl}} \propto \frac{\sigma}{\eta d_p^2} d_p^2 \left(\frac{1}{f}\right)^{\kappa} \propto \frac{\sigma}{f^{\kappa}\eta} \tag{8-31}$$

8.2.6.3 Maximum solids feed rate

The maximum solids feed rate that can be smelted is then be given by:

$$\frac{\sigma L}{f_{\max}\eta} = A_f \frac{\sigma}{f_{\max}^{\kappa}\eta} + B_f d_p \left(\frac{\eta}{\sigma}\right)^{1/2} \qquad (8\text{-}32)$$

which can be rearranged to give:

$$\frac{A_f}{L} f_{\max}^{1-\kappa} + B_f \left(\frac{d_p}{L}\right)\left(\frac{\eta}{\sigma}\right)^{3/2} f_{\max} - 1 = 0 \qquad (8\text{-}33)$$

In this equation A_f and B_f are proportionality constants which are unique for each flash furnace and depend on such factors as the shaft diameter, burner diameter and furnace temperature. For a given furnace this equation can be solved to give the maximum solids feedrate as a function of the shaft smelting index.

8.2.6.4 Influence of the Furnace heat and mass balance on the Furnace Operating Limits

In order to satisfy the furnace heat and mass balance, a minimum feedrate exists which is required to maintain the products at temperature and supply sufficient heat to provide the furnace heat losses. This can be represented as:

$$\eta f \Delta H - H_{loss} = f\left(\left(\sum_i v_i h_i\right)_{out} - \left(\sum_i v_i h_i\right)_{in}\right) \qquad (8\text{-}34)$$

This can be rearranged to give:

$$f_{min} = \cfrac{\cfrac{H_{loss}}{\Delta H}}{\eta - \cfrac{\left(\left(\sum_i v_i h_i\right)_{out} - \left(\sum_i v_i h_i\right)_{in}\right)}{\Delta H}} \qquad (8\text{-}35)$$

8.2.6.5 Furnace Operating Region

Figure 8-12 plots the maximum and minimum solids feed rate that can be smelted within the furnace residence time, together with the minimum feed rate required to maintain the furnace heat balance. The intersection of these three curves represents the allowable furnace operating window. These curves have been generated for an arbitrary furnace with arbitary values of A_f = 1015 (m.hr).tonnes^{-1}, B_f = 1000 hr.tonnes^{-1} and κ = 1.5. Hence the numerical values shown in Figure 8-12 are for illustrative purposes only. They cannot be used to infer the quantitative performance of any particular furnace or burner design.
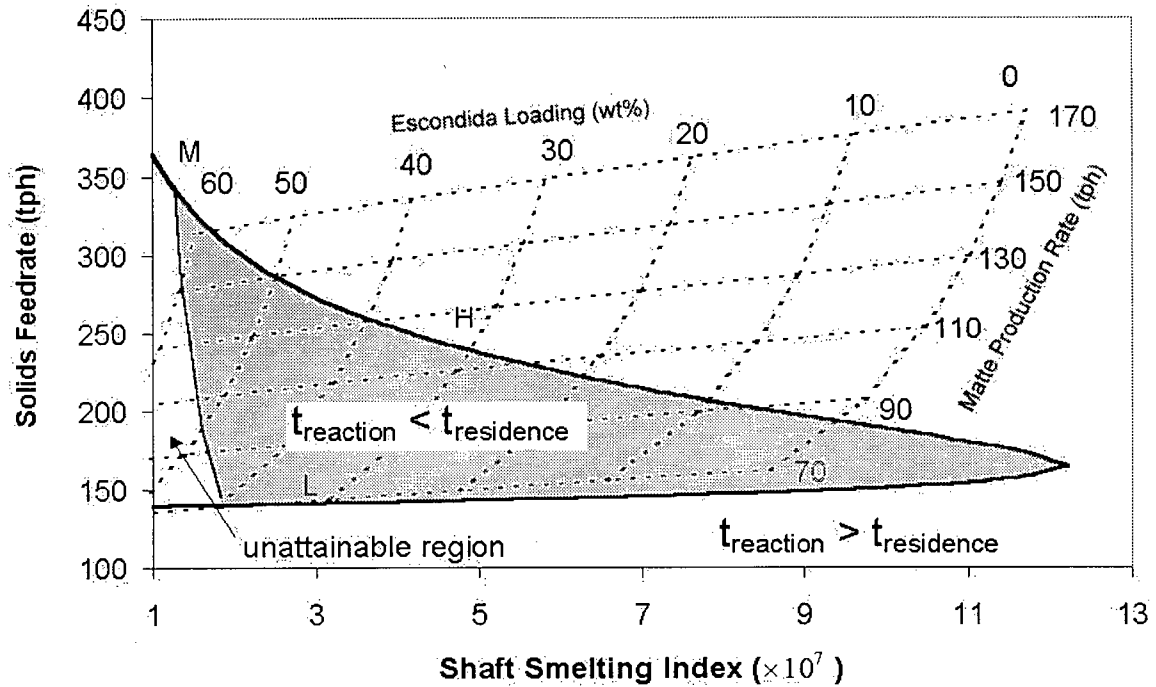
Figure 8-12: Industrial Flash Smelter Operating Diagram

The most important feature of Fig. 8-12 is the existence of a maximum and minimum feed rate which can be smelted in the given shaft residence time. The minimum feedrate represents a lower intensity mode of operation. In this mode the burner exit velocity is low, producing a low cloud Nusselt number and therefore a low heat transfer effectiveness factor. Hence the heat-up time dominates the overall reaction time of the cloud. The maximum feed rate represents a high intensity mode of operation. In this mode the burner exit velocity and therefore the cloud Nusselt number and heat transfer effectiveness factor are high, with the overall reaction time governed by the combustion time of the cloud. At some value of the shaft smelting index, the minimum

152

and maximum feedrate lines converge, and at values greater than this no feedrate exists at which the concentrate can be smelted by the furnace.

The minimum feed rate defined by the furnace heat and mass balance is also important in determining the furnace operating limits. At high oxygen-to-concentrate ratios, the minimum feed rate is lower than the furnace operating window and does not affect furnace operation. However, at low oxygen-to-concentrate ratios, the minimum feedrate increases sharply until, at some Escondida loading, it exceeds the maximum feedrate that can be smelted within the shaft residence time. This is indicated by point M in Fig. 8-12.

8.2.6.6   Influence of High-Grade Concentrate on Furnace Operation

Figure 8-12 shows that the smelting index describes the operation of the furnace. The influence on high-grade concentrate on furnace operation is a result of the influence of the oxygen-to-concentrate ratio and oxygen enrichment. Overlayed on Figure 8-12 is a skewed checkerboard pattern representing the required solid feed rates for a series of aim matte production rates and Escondida loadings. For these calculations the aim matte grade was held constant at a value of 63 wt%. The "near-horizontal" lines represent constant matte production rates, whereas the "near-vertical" lines represent constant Escondida loadings. These lines were produced by calculating the oxygen-to-concentrate ratio and oxygen enrichment from the heat and mass balances in Chapter 1.

153

As the Escondida loading of the blend increases, the shaft operation moves towards the low intensity limit until, at an Escondida loading corresponding to point L in Fig 8-12, the low intensity limit of the furnace is reached. Any further increase in the Escondida loading would cause the shaft to fail. In this mode of operation, the shaft fails because of the low burner exit velocity. Therefore, to smelt concentrate blends containing higher Escondida loadings requires the burner exit velocity to increase. This can be achieved by increasing the matte production rate. As the matte production rate increases the shaft moves away from its low intensity limit until at some feed rate the high intensity limit is reached, corresponding to point H on Fig. 8-12. Any further increase in the production rate results in failure. In this mode of operation failure is due to the high burner exit velocity.

8.2.6.7 Implications to Flash Smelting Operating Strategy

This analysis shows that furnace failure results from either a too high or a too low burner exit velocity and that addition of high-grade concentrate lowers the burner exit velocity. Therefore if it is desired to increase the throughput of a high-grade concentrate, several options are available to achieve this goal. Which option is chosen depends on the operating level of the furnace and other operational constraints.

If the furnace is operating at its high intensity limit, addition of high-grade concentrate offers a natural way of decreasing the burner exit velocity and increasing the matte production rate. However, if the furnace were to operate at its low intensity limit, then addition of high-grade concentrate would cause failure. For this case, an increase in

the throughput of high-grade concentrate would require an increased heat transfer rate between the cloud and the surroundings. This could be achieved in several ways. Firstly, the matte production rate could be increased, thereby increasing the burner exit velocity and cloud Nusselt number. This method is suitable if the flash furnace is the bottleneck of the plant and an increase in the matte production rate is desired. Secondly, a supplementary fuel (such as coal, natural gas or pyrite) could be added to the blend. Addition of a supplementary fuel increases the total oxygen requirements of the furnace and decreases the required oxygen enrichment, consequently increasing the burner exit velocity and the cloud Nusselt number. This method increases the amount of high-grade concentrate that can be smelted while maintaining a constant aim matte production rate. Finally an improved burner with better heat transfer charactersitics may be installed. This improves furnace flexibility by allowing a greater turndown in the burner exit velocity and is the focus of the second part of this study.

Before the operating diagram developed here can be used, plant trials must be conducted to determine its validity. The plant trials should be similar to those conducted in this study where the effect of the cloud's oxygen-to-concentrate ratio and oxygen enrichment on the reaction rate is determined by collecting samples of the reaction products at different furnace heights. The deviation from aim sulfur can then be determined allowing the heat transfer and combustion effectiveness factors to be determined.

8.2.7 Future Work

Several factors which have not been included in the current investigation may cause the operating diagram for an industrial flash smelter to differ from that derived above:

1) Influence of particle size distribution; and

2) The large group combustion numbers of a flash furnace flame.

8.2.7.1 Particle Size Distribution

For the experiments conducted in the UBC flash reactor, the particle size distribution was tightly controlled such that it could be assumed that the particles were monosized in any individual experiment. However, for an industrial flash smelter, a size distribution exists within the furnace which will influence the interactive effects within the cloud and may change the heat transfer and combustion effectiveness factors. Therefore studies should be conducted to determine the effect of particle size distribution on the burning characteristics of the cloud.

8.2.7.2 Large Group Combustion Numbers

The maximum group combustion number which could be acheived in this study was approximately 6000. However, for an industrial flash smelter, the group combustion number is approximately 100,000. Because the combustion effectiveness factor is analogous to the effectiveness factor for a porous char particle, low combustion effectiveness factors are similar to low effectiveness factors for char particles. For char

156

particles, low effectiveness factors imply that the combustion reaction is restricted to a region close to the particles surface. If this is true for high group combustion numbers then, as high-grade concentrate is added to the blend, burning is confined to a region close to the outer edge of the cloud. This results in particles close to the outer edge of the cloud being over-oxidised while particles in the interoir of cloud remain under-oxidised. Therefore studies should be conducted to determine the effect of group combustion number on the radial variation of the reaction rate within the cloud.

8.3 Burner Design

The aim of the burner design study was to provide insight into the best burner type for use in a sulfide flash smelter. Three different designs were studied, namely a straight-tube, a bluff body and a swirl burner, with the three designs discussed in detail in Section 6.3.2. As with the group combustion study, the performance of the burners was monitored by calculating the deviation from aim sulfur at different levels within the furnace. Because the goal of the flash smelting process is to treat as much concentrate as possible, a "good" burner design is one which promotes rapid desulfurisation, whereas a "bad" burner design results in slow desulfurisation.

Table 8-4 shows the process parameters used to compare the performance of the different burner designs. An experimental run was conducted with all three burners for each set of conditions, allowing the performance of the different burner types to be compared over a wide range of conditions. For all runs the oxygen enrichment was set at 21-vol% in order to provide a high burner exit velocity, thereby ensuring formation of a recirculation zone at the exit of the swirl and bluff-body burners.

157

Table 8-4: Experimental Conditions for Each of the Three Burner Designs

Run No.	Oxygen-to-concentrate ratio	Oxygen enrichment (vol %)	Particle diameter(μm)	Escondida loading (wt%)
1	0.295	21	42	0
2	0.253	21	82	0
3	0.0963	21	42	100
4	0.121	21	69.5	100

Figures 8-13 to 8-16 show the deviations from aim sulfur for each burner for the above experimental conditions.
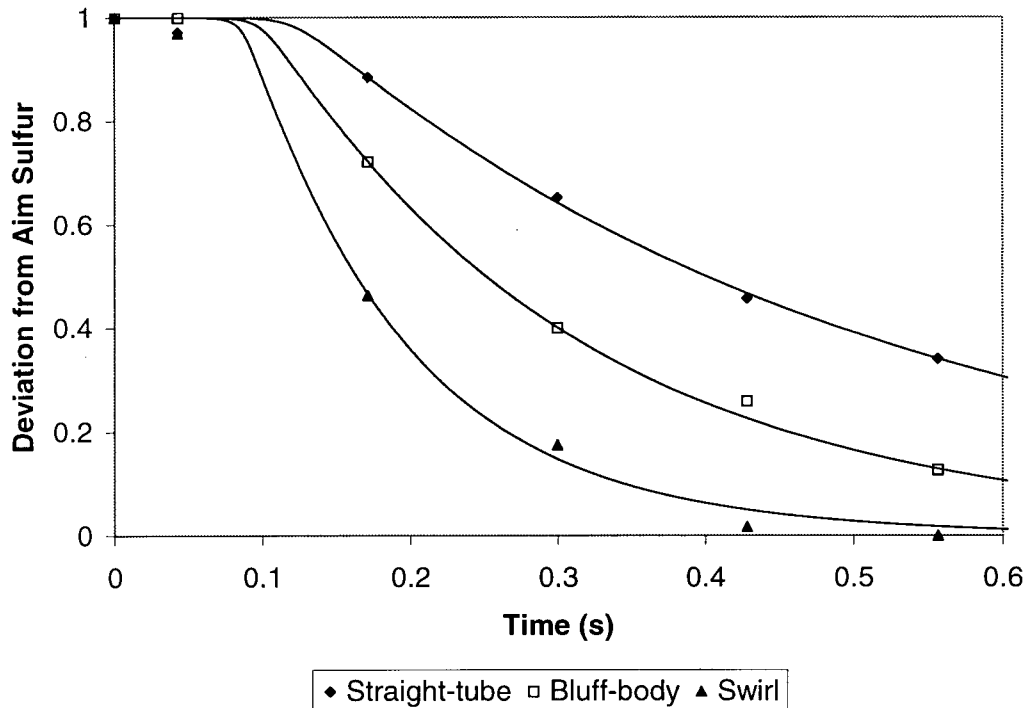
Figure 8-13: Comparison of the Different Burner Designs for Run 1 (See Table 8-4)

158
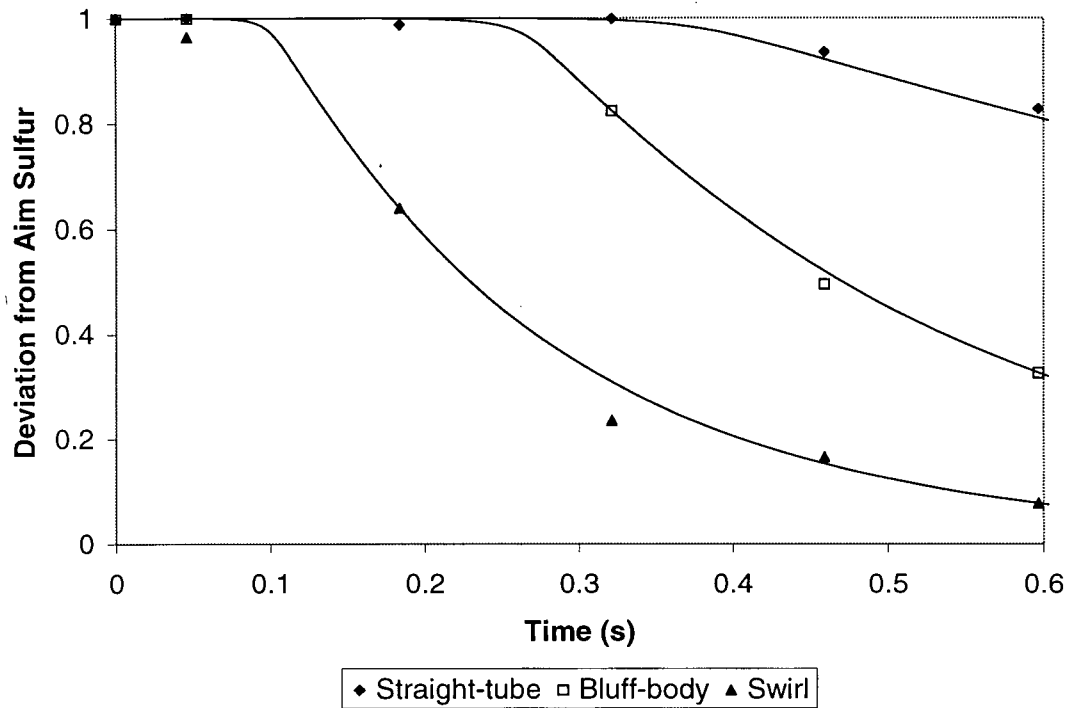
Figure 8-14: Comparison of the Different Burner Designs for Run 2 (See Table 8-4)
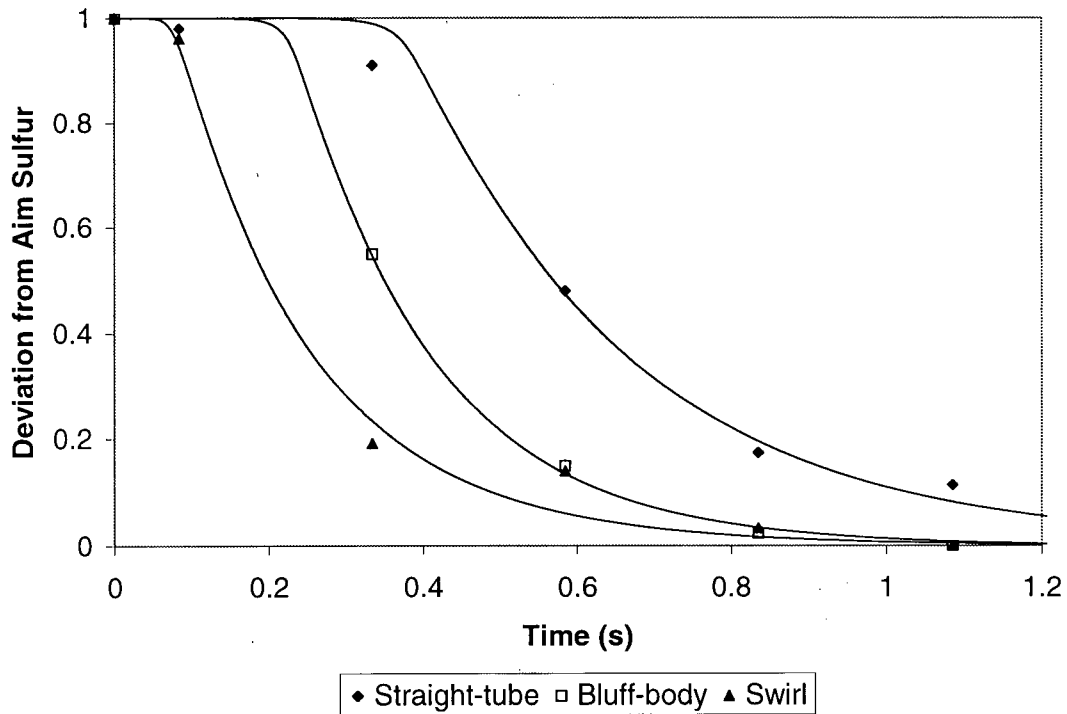
Figure 8-15: Comparison of the Different Burner Designs for Run 3 (See Table 8-4)
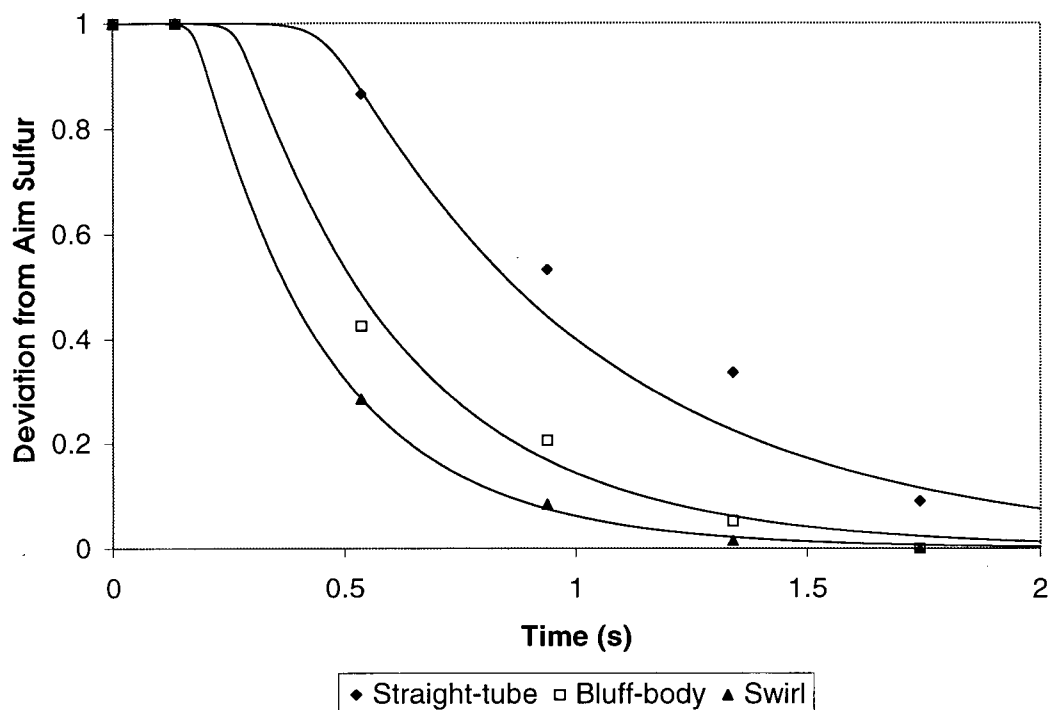
Figure 8-16: Comparison of the Different Burner Designs for Run 4 (See Table 8-4)

8.3.1 Furnace Operating Diagram

Using the same technique as for the group combustion study, the heat transfer and combustion effectiveness factors were calculated. Table 8-5 lists the relationships for the cloud Nusselt number and combustion effectiveness factor for both the bluff-body and swirl burner, with the combustion effectiveness factor assumed to be proportional to $G^{-1/2}$ as discussed above. Because only four runs were conducted, the statistical significance of the parameters listed in Table 8-5 is low. Therefore any conclusions based on these equations should be treated with caution.

Table 8-5: Burner Heat Transfer and Combustion Characteristics

Burner Design	Cloud Nusselt Number	Combustion Effectiveness Factor
Bluff-body	$Nu_{cl} = \exp\left(-14.0 \pm 3.1\right) Ra^{(0.78 \pm 0.12)}$	$\eta_c = \dfrac{(2.59 \pm 1.09)}{G^{1/2}}$
Swirl	$Nu_{cl} = \exp(-4.3 \pm 3.5) Ra^{(0.39 \pm 0.14)}$	$\eta_c = \dfrac{(3.05 \pm 1.36)}{G^{1/2}}$

Using these relationships the furnace operating diagram for the different burner types can be calculated and is shown in Figure 8-17.
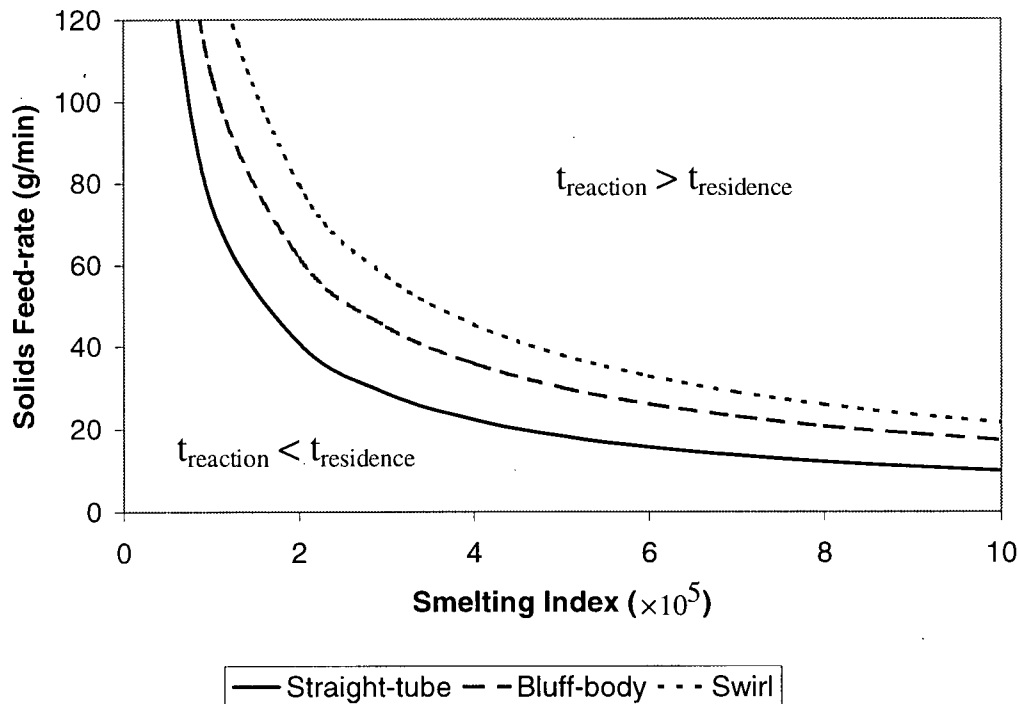
Figure 8-17: Furnace Operating Diagram for the Different Burner Designs

This Figure shows that, for the same conditions, the swirl burner is capable of processing approximately twice as much concentrate within the same shaft length as the straight-tube burner, while the bluff-body burner shows intermediate performance. If this improved

161

performance could be extended to an industrial flash smelter the benefits would be significant. To examine this possibility, a CFD study was conducted to examine the performance of the straight-tube and swirl burners, thereby providing the knowledge necessary to suggest an improved burner design for an industrial flash smelter. The CFD model is discussed in Chapter 9, while the results of the study are discussed in Chapter 10.

8.4 Findings and Recommendations

Results from this experimental study show that:

1) Sulfide particle clouds obey group combustion theory;

2) Group combustion theory can be used to predict the operating window of the UBC flash reactor and of industrial flash smelters. In both cases, the smelting index describes the furnace operation. For the UBC flash reactor, the maximum solids feed rate increases as the smelting index decreases, while for an industrial flash furnace, maximum and minimum solids feed rates exist which can be smelted within the furnace residence time. The upper limit represents the furnace operating in a high intensity mode in which the burner exit velocity is high and furnace residence time is low. Hence it is impossible to complete cloud heat-up and combustion within the furnace residence time. The lower limit represents the furnace operating in a low intensity manner in which the burner exit velocity is low and the overall reaction time is governed by the cloud heat-up time, leading to furnace failure.

3) As high-grade concentrate is added to the blend, the burner exit velocity decreases, pushing the furnace operation towards its low intensity limit. To increase the throughput of high-grade concentrate requires the burner exit velocity to increase. This can be achieved by:

    a) increasing the matte production rate;

    b) adding a supplementary fuel, such as coal, natural gas or pyrite; or

    c) improving the burner design to enhance heat transfer between the cloud and its surroundings.

4) Results from the burner design study show that the swirl burner gives superior results to both the bluff-body and straight-tube burner.

5) Further work is required to validate the findings of this study:

    a) to determine the influence of different cloud mineralogical compositions on the effective activation energy of the cloud;

    b) to determine the effect of particle size distribution on the cloud heat transfer and combustion effectiveness factors;

    c) to analyse the influence of high group combustion numbers on the burning charactersitics of the cloud;

    d) industrial trials to determine the validity of Figure 8-12; and

    e) industrial trials to determine the best burner design for flash smelting of high-grade concentrates.

9 CFD Model Development and Validation

A Computational Fluid Dynamics (CFD) model of the UBC flash reactor was developed to gain insight into the phenomena occurring during flash smelting. This model was tuned against experimental results and then extended to predict the operational performance of an industrial flash furnace.

9.1 Choice of Commercial Code

Many CFD models of the flash smelting process[23,29,30-37] have been developed in the past, with the majority of these assuming two-dimensional axi-symmetric steady state conditions. Due to the increase in computer power, three-dimensional steady state models have recently been developed.[36]

Some of these models[23,29,30,36] were developed using specifically written code, which resulted in long model development and validation stages. However, in the past decade commercial CFD packages have become available allowing the time required for model development to be dramatically reduced. As a result, it was decided to use a commercial package to develop the model used in this study.

The two most popular commercial packages available today are Fluent[100] and CFX[101]. Both of these were originally developed to study pulverised coal combustion and are capable of solving for turbulent, reacting flows in complex geometries with radiative heat transfer and combustion of a dispersed phase.

164

Eastwick et al.[102] compared the predictions of both packages to experimental data for the pulverised coal combustion in a 2.5 MW swirl burner. This coal burner has a solids feedrate in the order of 0.1 $\frac{kg}{s}$ Therefore the results of Eastwick et al[102] are in the same range as the current work. Their results show that close to the burner tip (i.e. within 1 to 2 burner diameters) the predictions by both packages are in good agreement with experimental data. However, further downstream from the burner tip the predictions by both packages become less accurate. In particular, CFX over-predicted the size of the internal recirculation zone, resulting in inaccurate predictions for the temperature, and species concentration fields. Eastwick et al. attributed the over-prediction of the internal recirculation zone to an incorrect devolatilisation model used by CFX to describe volatiles release. They concluded that both packages were capable of predicting global flow features, allowing trends to be investigated, but neither package was capable of determining exact flow details. It was decided to use Fluent[100] to develop the model.

It is worth noting at this point that as shown by Eastwick et al[102] model predictions should be treated cautiously when being used for detailed design purposes. Nevertheless, the results presented by Eastwick suggest that model prediction are sufficiently accurate to study the broad effects caused by general changes in the shaft and burner.

9.2 CFD Model Development

9.2.1 Problem Definition

A two-dimensional axi-symmetric model, incorporating a swirl momentum equation was used to describe the furnace/burner arrangement. Figure 9-1 shows the geometry and boundary conditions used by the model.
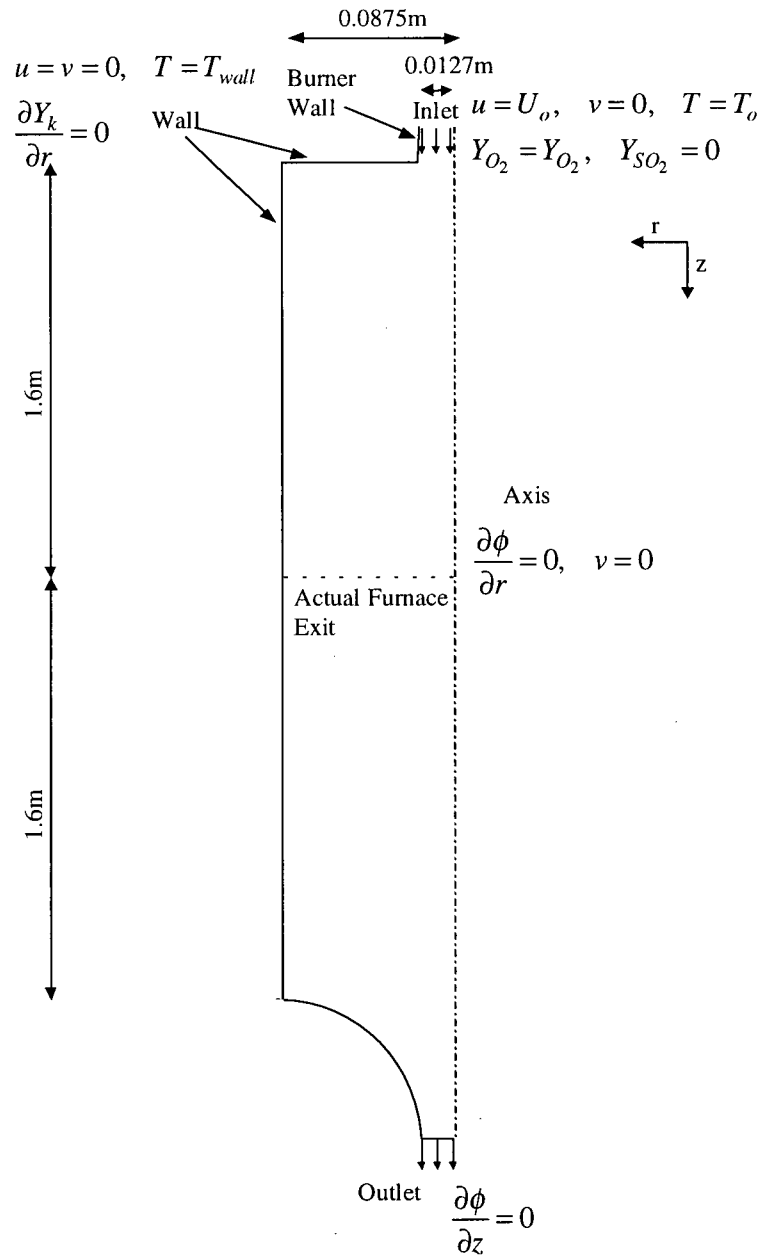
Figure 9-1: Model Geometry and Boundary Conditions

Figure 9-1 shows that the computational domain extends past the furnace exit. This was necessary because ending the computational domain at the furnace exit resulted in the model predicting an inflow at the furnace exit. This reverse flow at the exit arose from the strong recirculation present within the furnace, and because its properties (i.e. temperature and species concentrations) were unknown, the problem was ill-defined. Reducing the diameter of the exit and ending the domain downstream from the furnace exit eliminated the prediction of a reverse flow at the exit, producing a well-defined problem. This did not introduce significant errors into the model predictions because the outlet of the computational domain was located far downstream from the furnace exit. Hence any inaccuracies generated by the outlet were not propagated as far back in the computational domain so as to impact on the model predictions within the furnace.

As can be seen in Figure 9-1 solids and gas enter the furnace burner as a premixed stream. Upon entering the furnace the stream is heated by convection and radiation. The particles ignite and react with the available oxygen to form a matte phase before leaving through the furnace exit.

To predict the combustion process required the model to be capable of solving the flow, temperature and species concentration fields within the furnace. This was achieved by solving the governing conservation equations with suitable boundary conditions. However, other sub-models including turbulence, radiation and discrete phase models were required to fully describe the problem.

167

9.2.1.1 Simplifying Assumptions

Several assumptions were made to simplify the model.

1) The problem was considered to be axi-symmetric.

2) The furnace was assumed to be at steady state.

3) The concentrate particles were assumed to be mono-sized spheres.

4) Particle-particle collisions were ignored.

5) Viscous dissipation was assumed to be negligible.

6) Air infiltration into the reactor was ignored.

7) Sulfur dioxide was the only gas species assumed to participate in radiation exchange.

8) The particle and furnace wall emissivities were assumed to have a constant value of 1.

9) The presence of the particles was assumed to have no effect on the gas phase turbulence.

Note that a value of 1 was assumed for the particle and furnace wall emissivities. This value was chosen as their actual values are unknown and a value of 1 represents the maximum possible radiation exchange between the walls and the particles.

9.2.1.2 Model Boundary Conditions

9.2.1.2.1 Gas Phase Boundary Conditions

Four boundary conditions were required to fully describe the model. A velocity inlet was used to define the velocity and scalar properties of the gas flow at the furnace entrance.

An outlet boundary condition which assumes that the flow is fully developed was used to describe the furnace exit. This boundary condition sets the streamwise gradients for all flow variables, except pressure, to zero (i.e. $\frac{\partial \phi}{\partial z} = 0$).

The furnace centreline was modelled as an axis boundary condition, which assumes axial symmetry. Hence the radial velocity and the gradient of all variables were set to zero at the axis (i.e. $\frac{\partial \phi}{\partial r} = 0$, $v = 0$).

A wall boundary condition was used to describe the burner and furnace walls. This boundary condition ensures a no-slip condition for the velocity ($u = v = 0$). Wall shear stresses were then calculated from the local flow conditions using a near wall model approach. This is discussed below. A constant temperature boundary condition was used for the energy equation with the heat transfer being computed from the local flow field. The burner wall was set to a temperature of 300 K (as the burner was water-cooled), while the furnace wall was set to the furnace temperature ($T_{burner} = 300, T_{wall} = T_{furn}$). A constant wall boundary condition for the furnace wall can

be justified from the experimental data which showed that the furnace wall temperature varied by ±5°C along its length (representing a ± 1% change in temperature). A zero normal gradient was assumed for all chemical species at the furnace wall($\frac{\partial Y_k}{\partial r} = 0$).

The presence of a wall influences the mean and fluctuating properties of a flow, which must be accounted for to accurately predict the velocity, temperature and species distributions. The major effect of the wall is the formation of a viscous sublayer, which limits the transfer of momentum and scalar variables. Fluent can account for the influence of this viscous sublayer in one of two ways.

Firstly a wall function can be used. In this approach the viscous sublayer is not resolved. Instead semi-empirical formulas are used to predict the velocity and shear stresses in the viscous sublayer based on the flow properties in the fully developed core. Launder and Spalding[103] give further information on the wall function approach. A second approach uses a near wall model whereby the viscous sublayer is resolved and the turbulent viscosity within the sublayer is computed from a semi-empirical equation. Wolfstein[104] gives further details on this approach.

The near wall model approach gives better predictions because the viscous sublayer is resolved. However, a fine mesh close to the wall is required to resolve the viscous sublayer. For the conditions present in the UBC flash reactor the viscous sublayer extends approximately 5mm[104] from the furnace wall while the grid used to solve the model has a near wall mesh spacing of 1mm. Hence the mesh is capable of resolving the viscous sublayer and therefore the near wall model approach was used.

With respect to the particles, the domain inlet and outlet were both set to an escape boundary condition. This boundary condition assumes that the particle exits the furnace, therefore terminating the particle trajectory calculations.

The walls were set to a trap type boundary condition. This is treated identically to the escape type boundary condition whereby the particle trajectory calculations were terminated and the particle was assumed to no longer participate in the calculation process. This boundary condition was chosen instead of the reflective boundary condition (discussed below), because inspection of the furnace walls after an experimental run showed them to be coated with solid material, indicating that the particles are trapped by the walls.

Because the axis represents a line of symmetry it was set to a reflective boundary condition. For this boundary condition the particle was assumed to undergo a "elastic collision" where the particle speed was unchanged and its angle of reflection was set to its angle of incidence. This is shown below in Figure 9-2.
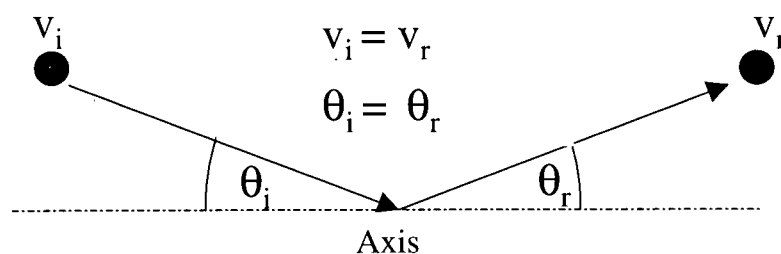
Figure 9-2: Particle Reflection Boundary Condition

9.2.1.3   Multi-Phase Flow Model

Because the flow consists of a gas-solids mixture a multi-phase flow model was required to account for the interactions between the individual phases. Fluent[100] has two sub-models available to predict multi-phase flows namely a Eulerian-Eulerian and a Eulerian-Lagrangian model. Both of these use interphase exchange terms to predict the influence of the different phases on each other. The differences between the models arise because of how these exchange terms are determined.

In the Eulerian-Eulerian model particle trajectories are not explicitly calculated. Instead a particle concentration field is calculated using a scalar conservation equation which requires the use of a particle dispersion tensor or particle diffusivity. Hence this model can only be used when the definition of a particle diffusivity is meaningful, such as in flows with high particle loadings. A major disadvantage of this model is that because particle trajectories are not explicitly calculated, the description of complex phenomena such as combustion is difficult to implement.

On the other hand, in the Eulerian-Lagrangian model, particle trajectories are explicitly calculated. Therefore, providing sufficient particle trajectories are calculated, this model can be used to predict a wide range of multiphase flows. The major disadvantage of this model is that the influence of particle-particle collisions on the particle trajectory is difficult to implement. As a result, the application of the model has been limited to dilute flows, where inter-particle collisions are negligible.

Crowe[105] has shown that a dilute flow can be defined as one where the time between inter-particle collisions is much greater than the particle relaxation time. Based on kinetic theory Crowe[105] has shown that the interparticle collision time can be estimated from:

$$\tau_{col} = \frac{\sqrt{\pi} d_p}{24 f_v u'_p} \qquad (9\text{-}1)$$

While the particle relaxation time is given by:

$$\tau_{r,p} = \frac{\rho_p d_p^2}{18\mu} \frac{24}{C_D \, Re_p} \qquad (9\text{-}2)$$

In Equation (9-1) f_v is the volume fraction of the solids. In Equation (9-2) Re_p is the particle Reynolds number with the characteristic length being the particle diameter and the characteristic velocity being the slip velocity between the particle and the gas.

For this problem the solids volume fraction ranges from 5×10^{-4} to 1.5×10^{-3} while the particle diameter and fluctuating velocity are in the order of 80 μm (worst case scenario for the ratio between the particle collision and particle relaxation time) and 0.01m/s respectively. Therefore the time between interparticle collisions varies from 0.4 to 1.2 seconds while the particle relaxation time is approximately 10 ms. Hence the particle collision time is between 40 to 120 times greater than the particle relaxation time suggesting that the suspension can be considered to be dilute. Therefore the Eulerian-Lagrangian model was used to formulate the particle phase equations. Gouesbet and

Berlemont[106] discuss the Eulerian-Eulerian and Eulerian-Lagrangian approaches in detail.

Because the particles were modeled in a Lagrangian frame, their equations could not be solved simultaneously with the gas phase equations. As a result, a partial two-way coupling technique, shown in Figure 9-3, was used to obtain a converged solution.

This technique employs an iterative approach whereby the influence of the particles on the gas phase is accounted for through the addition of source terms to the gas phase conservation equations. Initially a set number of iterations of the gas phase equations are performed before the particle phase equations are solved. The particle source terms in the gas phase equations are then updated and the gas phase equations resolved with the new source terms. This iterative process continues until a converged solution is obtained.

```
┌─────────────────────────────┐
│ Initial guess for gas and particle │
│       phase equations        │
└─────────────────────────────┘
              │
              ▼
┌─────────────────────────────┐
│   Perform a set number of gas   │◄──────────┐
│    phase equation iterations    │           │
└─────────────────────────────┘           │
              │                            │
              ▼                            │
┌─────────────────────────────┐           │
│  Solve particle phase equations  │           │
└─────────────────────────────┘           │
              │                            │
              ▼                            │
┌─────────────────────────────┐           │
│   Update particle source terms in   │           │
│      the gas phase equations     │           │
└─────────────────────────────┘           │
              │                            │
              ▼                            │
┌─────────────────────────────┐           │
│   Have the gas and particle phase  │───────────┘
│      equations converged       │      no
└─────────────────────────────┘
              │
             yes
              ▼
┌─────────────────────────────┐
│         Final Solution          │
└─────────────────────────────┘
```
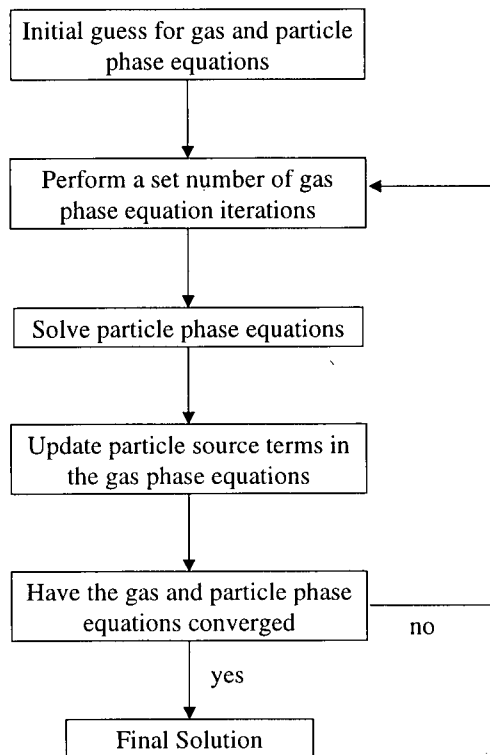
Figure 9-3: Gas and Particle Phase Equations Coupling Procedure

9.2.2 Gas Phase Equations

Given the boundary conditions and furnace geometry shown in Figure 9-1, the gas phase velocity, temperature and species concentrations within the furnace were computed using the gas phase mass, momentum, energy and species conservation equations.[107] Fluent formulates these in an Eulerian frame of reference and solves the Reynolds Averaged forms of these equations for a steady state, two dimensional, axi-symmetric model with swirl as follows:

Mass (Continuity)

$$\frac{\partial \rho u}{\partial z} + \frac{1}{r}\frac{\partial r \rho v}{\partial r} = S_m \qquad (9-3)$$

175

Axial Momentum

$$\rho v \frac{\partial u}{\partial r} + \rho u \frac{\partial u}{\partial z} = -\frac{\partial P}{\partial z} + \frac{1}{r}\frac{\partial r\tau_{rz}}{\partial r} + \frac{\partial \tau_{zz}}{\partial z} + S_{p,z} \tag{9-4}$$

Radial Momentum

$$\rho v \frac{\partial v}{\partial r} + \rho u \frac{\partial v}{\partial z} - \rho \frac{w^2}{r} = -\frac{\partial P}{\partial r} + \frac{1}{r}\frac{\partial r\tau_{rr}}{\partial r} + \frac{\partial \tau_{rz}}{\partial z} + S_{p,r} \tag{9-5}$$

Swirl momentum

$$\rho v \frac{\partial w}{\partial r} + \rho \frac{vw}{r} + \rho u \frac{\partial w}{\partial z} = \frac{1}{r^2}\frac{\partial r^2\tau_{\theta r}}{\partial r} + \frac{\partial \tau_{\theta z}}{\partial z} - S_{p\theta} \tag{9-6}$$

Energy

$$\rho u C_p \frac{\partial T}{\partial z} + \rho v C_p \frac{\partial T}{\partial r} = \frac{1}{r}\frac{\partial}{\partial r}\left(rk_e \frac{\partial T}{\partial r} \right) + \frac{\partial^2 k_e T}{\partial z^2} + S_e \tag{9-7}$$

Species

$$\rho u \frac{\partial Y_k}{\partial z} + \rho v \frac{\partial Y_k}{\partial r} = \rho \frac{1}{r}\frac{\partial}{\partial r}\left(rD_e \frac{\partial Y_k}{\partial r} \right) + \rho \frac{\partial^2 D_e Y_k}{\partial z^2} + S_{s,k} \tag{9-8}$$

These equations assume that heating by viscous dissipation is negligible.

The swirl momentum equation, which is a modified form of the angular momentum equation in the cylindrical co-ordinate system, was used to account for the swirling motion generated by the swirl burner. This equation was only solved for runs

176

where the swirl burner was used. It was assumed throughout that no gradients of any variable existed in the angular direction. For runs where the straight-tube burner was investigated the swirl momentum equation was ignored and w in Equation (9-5) was set to zero.

In these equations the transported quantities are the time-averaged values, and S_i are source terms used to account for the influence of the dispersed phase and radiative heat transfer on the transported quantities.

9.2.2.1 Turbulence Modelling

Because the velocity components in the above equations are time-averaged values, the shear stresses τ in Equations (9-4), (9-5) and (9-6) include both the viscous and Reynolds stresses. Reynolds stresses arise due to the fluctuating velocity components of the flow, and it is the role of the turbulence model to predict these Reynolds stresses.

9.2.2.1.1 Boussinesq's Eddy Viscosity

A large number of turbulence models use Boussinesq's eddy viscosity[108-110] to predict the Reynolds stresses. This approximation assumes the Reynolds stresses to be proportional to the time-averaged velocity gradient and allows the shear stresses to be expressed as the sum of the laminar and turbulent stresses. Therefore an effective fluid viscosity can be defined as:

$$\tau_{rz} = \mu \frac{\partial u}{\partial r} + \mu_t \frac{\partial u}{\partial r} = \mu_e \frac{\partial u}{\partial r} \tag{9-9}$$

9.2.2.1.2 The k-ε Model

The k-ε model is the standard turbulence model based on Boussinesq's eddy viscosity and is capable of predicting the turbulent properties of a wide range of flows. However, in flows with strong streamline curvature, rotation or buoyancy, the k-ε model tends to predict erroneous results. Qin[111] showed that for a sudden expansion, the k-ε model accurately predicted the length of the recirculation zone. However, it gave poor results for the turbulent properties of the flow in the region downstream of the recirculation zone.

9.2.2.1.3 Reynolds Stress Model

Amano and Goel[112] used the Reynolds Stress Model (RSM) to study the flow and heat transfer in a sudden expansion. They found that the RSM gave similar results to the k-ε model in the recirculation zone and superior results in the region downstream from the recirculation zone. As a result the RSM was used in this work to describe the turbulence within the flash reactor.

The Reynolds stress model solves transport equations for the individual Reynolds stresses and therefore accounts for the anisotropic nature of the eddy viscosity. The RSM used by Fluent for a two dimensional axi-symmetric model is given by:

$$u \frac{\partial \left(\overline{u'v'} \right)}{\partial z} + v \frac{\partial \left(\overline{u'v'} \right)}{\partial r} = D_{zr} + P_{zr} + \phi_{zr} + \varepsilon_{zr} + S_{zr} + E_{zr} \qquad (9\text{-}10a)$$

$$u\frac{\partial\left(\overline{u'u'}\right)}{\partial z}+v\frac{\partial\left(\overline{u'u'}\right)}{\partial r}=D_{zz}+P_{zz}+\phi_{zz}+\varepsilon_{zz}+S_{zz}+E_{zz} \tag{9-10b}$$

$$u\frac{\partial\left(\overline{v'v'}\right)}{\partial z}+v\frac{\partial\left(\overline{v'v'}\right)}{\partial r}=D_{rr}+P_{rr}+\phi_{rr}+\varepsilon_{rr}+S_{rr}+E_{rr} \tag{9-10c}$$

Here D_{ij} is a diffusive transport term, P_{ij} is a production term, ϕ_{ij} is a pressure-strain term, ε_{ij} is a dissipation term and S_{ij} and E_{ij} are curvature-related terms that arise when cylindrical co-ordinates are used. Because these terms are complex they are not described here but are listed in Appendix A6. The Reynolds Stress Model is discussed in more detail by Hanjalic[109] and Lakshminarayana[110].

9.2.2.1.4   Turbulent Transportation of Scalar Quantities

The Reynolds-averaged energy and species conservation equations contain similar terms to the Reynolds stresses, namely $\overline{u_i'h'}$ and $\overline{u_i'Y_k'}$, which are related to the Reynolds stresses through the turbulent Prandtl and Schmidt numbers:

$$\rho\overline{u_i'h'}=\frac{\mu_t}{\mathrm{Pr}_t}\frac{\partial h}{\partial x_i} \tag{9-11}$$

$$\rho\overline{u_i'Y_k'}=\frac{\mu_t}{Sc_t}\frac{\partial Y_k}{\partial x_i} \tag{9-12}$$

The turbulent Prandtl and Schmidt numbers relate the turbulent diffusion of momentum to the turbulent diffusion of energy and species respectively. Fluent assumes that the turbulent Prandtl and Schmidt numbers are constant throughout the domain,

179

implying the ratios of the turbulent diffusion of momentum to the turbulent diffusion of energy and species are constant throughout the computational domain.

To accurately predict the temperature and species concentration fields within the furnace requires the turbulent Prandtl and Schmidt numbers to be known. Schlichting[114] has shown that for jets, the turbulent Prandtl number is typically 0.5, while other authors[115-117] have shown that the turbulent Schmidt number of a jet varies between 0.62 to 0.81.

In this study the turbulent Prandtl number was used as a fitting parameter to match the predicted and experimentally determined temperature fields. This is discussed in Section 9.3.2. Because there was no simple way to determine the turbulent Schmidt number it was assumed to be equal to the turbulent Prandtl number.

9.2.2.1.4.1 Turbulent Viscosity

When using the Reynolds Stress model, the turbulent viscosity, in Equations (9-11) and (9-12) can be calculated from:

$$\mu_t = \rho C_\mu \frac{k^2}{\varepsilon}$$
(9-13)

Here k is the turbulent kinetic energy given by:

$$k = \frac{1}{2}\sum \overline{u_i'^2}$$
(9-14)

and ε is the dissipation rate of the turbulent kinetic energy given by:

$$\rho u \frac{\partial \varepsilon}{\partial z} + \rho v \frac{\partial \varepsilon}{\partial r} = \frac{1}{r} \frac{\partial}{\partial r} \left(r \frac{\mu_t}{\text{Pr}_\varepsilon} \frac{\partial \varepsilon}{\partial r} \right) + \frac{\partial^2 \left(\left(\frac{\mu_t}{\text{Pr}_\varepsilon} \right) T \right)}{\partial z^2} + C_{1\varepsilon} \frac{\varepsilon}{k} (G_k + (1 - C_{3\varepsilon} G_b) - C_{2\varepsilon} \rho \frac{\varepsilon^2}{k}$$

(9-15)

where

$$G_k = \mu_t \left(\left(\frac{\partial u}{\partial r} + \frac{\partial v}{\partial z} \right) \frac{\partial u}{\partial r} + \left(\frac{\partial u}{\partial r} + \frac{\partial v}{\partial z} \right) \frac{\partial v}{\partial z} \right), \quad G_b = -\frac{\mu_t}{\rho \text{Pr}_t} \left(g_r \frac{\partial \rho}{\partial r} + g_z \frac{\partial \rho}{\partial z} \right)$$ and $C_{1\varepsilon} = 1.44$

$C_{2\varepsilon} = 1.92$, $C_{3\varepsilon} = 0.09$, $\text{Pr}_k = 1$, $\text{Pr}_\varepsilon = 1.3$

In Equation (9-15) $C_{1\varepsilon}$, $C_{2\varepsilon}$, $C_{3\varepsilon}$, Pr_k, Pr_ε, are all empirical constants with the choice of their values being discussed in detail by Launder and Spalding.[103]

9.2.3 Discretisation and Grid Considerations

9.2.3.1 Discretisation

To obtain a solution to the governing differential equations requires the use of a computational grid, which allows the continuous nature of these equations to be represented in a discrete algebraic form. The discretisation process is described below.

Consider the steady state one-dimensional continuity and momentum equations.

$$\frac{\partial (\rho u)}{\partial x} = 0$$

(9-16)

$$\frac{\partial (\rho u u)}{\partial x} = -\frac{\partial P}{\partial x} + \frac{\partial}{\partial x} \left(\mu \frac{\partial u}{\partial x} \right) + S_{p,x}$$

(9-17)

181

These equations can be integrated over a Control Volume (V_c) using the Divergence Theorem. Applying the Divergence Theorem to the continuity equation gives:

$$\int_{V_c} \frac{\partial(\rho u)}{\partial x} dV = \int_{A_c} \rho u . dA \qquad (9\text{-}18)$$

In Equation (9-18) A_c is the surface area of the control volume. Therefore Equations (9-16) and (9-17) can be solved to give::

$$(\rho u A)_e - (\rho u A)_w = 0 \qquad (9\text{-}19)$$

$$(\rho u^2 A)_e - (\rho u^2 A)_w = -((PA)_e - (PA)_w) + \left(\mu \left(\frac{u_E - u_P}{\Delta x} \right) A \right)_e - \left(\mu \left(\frac{u_P - u_w}{\Delta x} \right) A \right)_w + V_C S_{p,x}$$
$$(9\text{-}20)$$

In these equations P, W and E are the nodal locations of three adjacent cells as shown in Figure 9-4 while w and e represent the "west" and "east" faces of centre control volume represented by nodal point P.
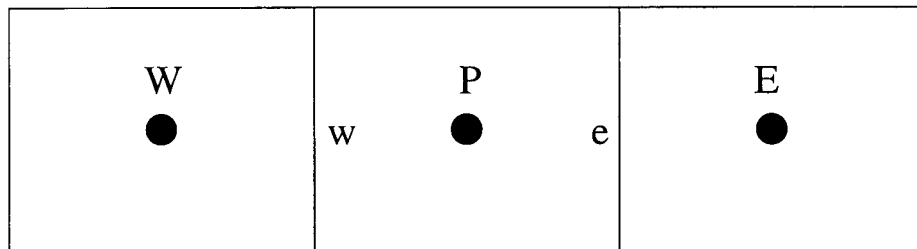
Figure 9-4: Computational Cell Definitions

When Equations (9-19) and (9-20) are written for each nodal point in the computational domain a solution can be obtained providing that the values for u and P at

182

the cell faces can be interpolated from the nodal values. Further details on the discretisation and interpolation schemes can be found in Fletcher[118-119] and Pantankar[120].

9.2.3.2 Sources of Error

Three broad errors are introduced during the discretisation process namely truncation errors, numerical diffusion and interpolation errors. These errors must be considered when attempting to obtain an accurate solution.

Truncation errors arise due to the finite differencing representation of the derivatives in the governing equations. Reducing the grid spacing in the computational domain reduces these errors.

Numerical diffusion arises due to one-dimensional interpolation schemes used to represent multi-dimensional flows. Errors associated with numerical diffusion are greatest when the flow is not aligned with the grid or when there are non-zero gradients of the dependant variable in the direction normal to the flow. Ensuring that grid lines are aligned with the flow can reduce this source of error. However, if this cannot be achieved, then its influence on the solution can be reduced by reducing the grid spacing of the computational domain.

Interpolation errors result because the function used in the interpolation scheme does not predict the true face value of the transportable quantity. These errors can be minimised by reducing the grid spacing and by selecting a physically meaningful interpolation scheme. Fluent has several interpolation schemes available. Two of the

more commonly used schemes are the Power Law[120] and Second Order Upwind Differencing schemes[121]. The Power Law Scheme is based on the exact solution of the one-dimensional convection-diffusion equation. This scheme is numerically stable and gives meaningful results. However, it is susceptible to numerical diffusion. On the other hand, the Second Order Upwind Differencing Scheme is less susceptible to numerical diffusion, but is also less stable than the Power-Law Scheme. Because the stability of the solution process was unaffected by the interpolation scheme, the second order upwind differencing scheme was used in the present case.

9.2.3.3   Grid Generation

As shown above, careful consideration must be given to grid spacing to ensure that that numerical errors are minimised. In addition to these considerations, the grid must be sufficiently fine to capture the important flow features such as wall and shear boundary layers, separated regions, and mixing zones. In particular, the grid spacing adjacent to the wall must be sufficiently fine to accurately predict the wall shear stress and heat transfer. Figure 9-5 shows the grid used in this study.
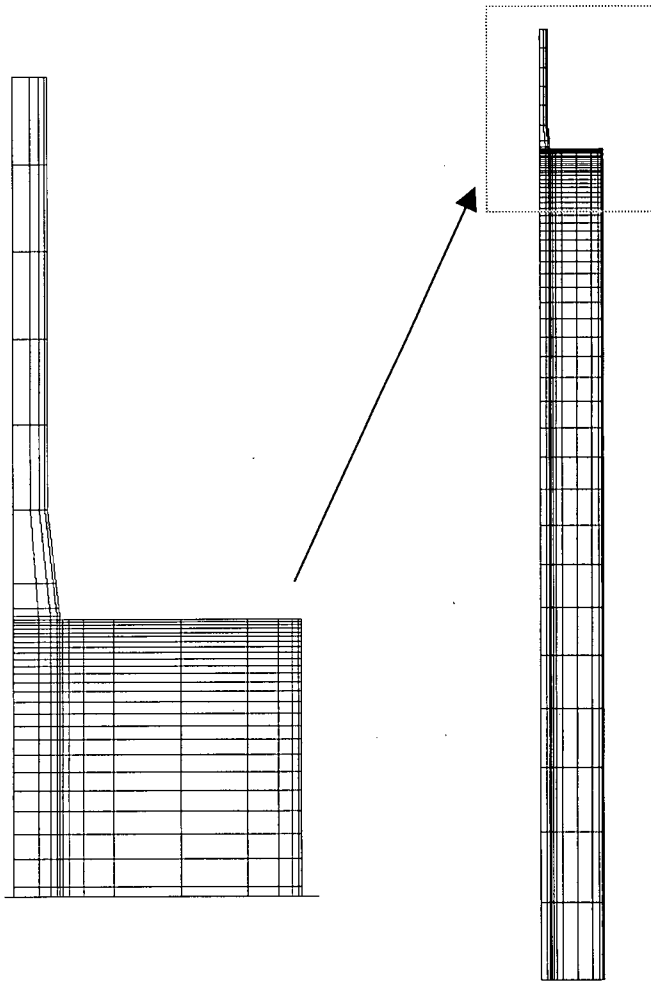
Figure 9-5: Computational Mesh Density Distribution

The grid depicted above has 800 nodal points which is insufficient to capture all of the important flow features and ensure that a grid-independent solution is obtained. However, it does show the grid density distribution used by the model. A fine mesh is employed close to the wall and burner tip so as to capture the wall and jet boundary layers.

A study was conducted to determine the mesh size required to obtain a grid-independent solution. This involved monitoring the change in the wall shear stress and heat flux predicted by the model as the grid size was increased. Five different mesh sizes were investigated with the coarsest (shown in Figure 9-5) consisting of 800 nodes. At each stage of mesh refinement the numbers of nodes in the radial and axial direction were doubled, increasing the total mesh size by a factor of four. Figure 9-6 shows the variation in the wall shear stress and heat flux as a function of mesh size.
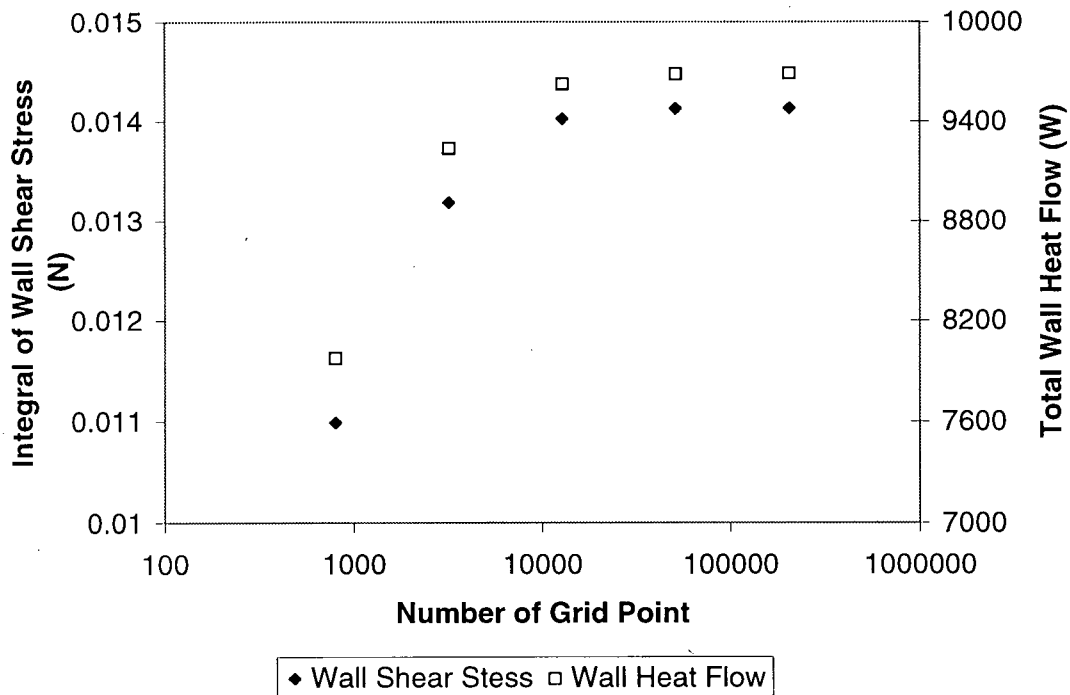
Figure 9-6: Grid Dependence Study Results

A grid independent solution was obtained for mesh sizes above approximately of 50,000 nodes. Any grid refinement above this adds to the computational expense without any improvement in the model predictions. Hence the model used a mesh of 51,200 nodes.

186

9.2.4 Radiation Modelling

The energy conservation equation describes the energy transfer within the reactor by convection and conduction. For high temperature combusting systems, radiation represents a significant mode of energy transfer which must be correctly described to predict the temperature field within the furnace with any accuracy. The radiative transfer equation (RTE) describing the energy transfer by radiation in an absorbing, emitting and scattering medium[122] is given by:

$$\frac{dI}{ds} = -(k_a + k_s)I + \frac{k_a \sigma_{sb} T^4}{\pi} + \frac{k_s}{4\pi} \int P_s(\Omega, \Omega')Id\Omega' \tag{9-21}$$

The RTE equates the change in radiation intensity, I, in the s direction to the attenuation caused by absorption and outward scattering and the addition caused by emission and inward scattering from other directions. Because of its complex nature, an exact solution to the RTE can only be obtained for simple one-dimensional cases. As a result, many methods have been developed to obtain approximate solutions based on simplifying assumptions. These different methods are discussed in references [123-130]. Fluent has two models available to describe the RTE in combusting systems, the P1 and the discrete ordinates method.

9.2.4.1 P1 Model

In the P1 model[123-124] the radiation intensity is expressed as a series of spherical harmonics, which allows the RTE to be simplified to:

$$\frac{1}{3}\nabla\frac{1}{k_a+k_s}\nabla\left(\theta_R^4\right)-k_a\left(\theta_R^4-T^4\right)=0 \qquad (9\text{-}22)$$

Here θ_R is the radiation temperature given by $\theta_R^4=\dfrac{I}{4\sigma_{sb}}$.

The accuracy of the P1 model under different conditions has been studied[121-122] and shown to give good results for optically thick media $((k_a+k_s)L>2)$ with its accuracy decreasing as the optical thickness falls below $(k_a+k_s)L=2$. These studies also showed that the accuracy of the model decreases when the radiation intensity is anisotropic, such as in situations where there are large temperature or particle concentration gradients.

9.2.4.2 Discrete Ordinates Method

The Discrete Ordinates method approximates the RTE by discretising the entire solid angle using a finite number of ordinate directions. The RTE is then re-written for each ordinate direction, with the integral term being replaced by a quadrature summation over all ordinate directions. Viskanta[123], Viskanta and Meguc[125] and Chandersekhar[127] discuss the discrete ordinates method in more detail. The discretised RTE used by Fluent is:

$$\sum_i \xi_i \frac{dI_{j'}}{dx_i} = -\left(k_a+k_s\right)I_{j'}+\frac{k_a\sigma_{sb}T^4}{\pi}+\frac{k_s}{4\pi}\sum_{j'}\omega_{j'}P_s\left(\Omega,\Omega'\right)I_{j'} \qquad (9\text{-}23)$$

As with the P1 model, studies have been conducted to determine the accuracy of the discrete ordinates method under different conditions[133-136]. These studies show that

the accuracy of the model decreases as the localised radiation sources and scattering become less important compared to absorption.

9.2.4.3　Choice of Radiation Model

Techniques discussed by Hottel and Sarofim[122] allow the absorption and scattering coefficients of the gas and particles within the UBC flash reactor to be estimated. Using these techniques, together with emissivity data for sulfur dioxide, it can be shown that the gas absorption coefficient is in the range 0 to 0.3 m^{-1}, while the particle absorption and scattering coefficients vary from 0.7 to 60 and 0.07 to 7 respectively. Therefore the localised radiation sources and scattering by the sulfide particles are more important than gas phase absorption. Hence the discrete ordinates method was chosen over the P1 method to model radiation in the flash reactor.

9.2.4.4　Coupling between the Energy Conservation Equation and the RTE

Once the radiation intensity has been determined from either the P1 or the discrete ordinates method, the heat flux arising from radiative transfer can be added to the energy equation using the source term:

$$-\nabla q = k_a I - 4 k_a \sigma_{sb} T^4 \tag{9-24}$$

9.2.5　Dispersed Phase Model

In Fluent, particles are modeled as a secondary dispersed phase with their mass, momentum and energy equations formulated in a Lagrangian frame of reference.

9.2.5.1 Trajectory Calculation

The particle trajectories are calculated by integrating:

$$\frac{dx_i}{dt} = u_{p,i} \tag{9-25}$$

In Equation (9-25) the particle velocity is calculated from a force balance where the particle inertia is equated to the forces acting on the particle.

$$\frac{du_{p,i}}{dt} = \frac{(u_i - u_{p,i})}{\tau_{r,p}} + g_i \frac{\rho_p - \rho}{\rho_p} + F_i \tag{9-26}$$

where $\tau_{r,p} = \frac{\rho_p d_p^2}{18\mu} \frac{24}{C_D \, Re_p}$ and $Re_p = \frac{\rho d_p |u - u_p|}{\mu}$

In Equation (9-26) $\tau_{r,p}$ can be considered as a particle relaxation time which is a measure of the time required for the particle to accelerate to the gas phase velocity.

If the body forces are assumed constant over a time step, then the particle force balance can be integrated to give:

$$u_{p,i}(t + \Delta t) = \left(u_{p,i}(t) - \alpha\right)\left(1 - e^{-\frac{\Delta t}{\tau_{r,p}}}\right) + \alpha \tag{9-27}$$

In Equation (9-20) α is given by:

$$\alpha = u + \tau_{r,p}\left(g_i\left(\frac{\rho_p - \rho}{\rho_p}\right) + F_i\right) \tag{9-28}$$

190

9.2.5.1.1 Turbulent Dispersion of Particles

In Equation (9-26), u_i is the instantaneous local gas velocity. However, only the time-averaged values are predicted from the Reynolds-averaged momentum equations. Therefore the influence of turbulent fluctuations on the gas phase velocity must be modelled in order to account for the turbulent dispersion of the particles. There are many ways of predicting the effect of turbulent fluctuations on particle dispersion, as discussed by Shirolkar et al[137].

In Fluent, the instantaneous gas velocity is obtained through the solution of the Langevin equation[138-139]:

$$du_i = \frac{1}{T_{L,p}} u_i dt + \left(\frac{2 u_i' u_i'}{T_{L,p}} \right)^{1/2} dw_g \qquad (9-29)$$

Here w_g is a Gaussian distributed random number and $T_{L,p}$ is the particle integral time scale which can be estimated from:

$$T_{L,p} = C_L \frac{k}{\varepsilon} \qquad (9-30)$$

In Equation (9-30) C_L is not well known and must be determined experimentally. However, it has been shown analytically[140] that C_L has a value of 0.3 for small particles that follow the gas stream. This analysis assumes that the particles have no inertia and respond instantaneously to the fluctuating gas phase velocity. But real particles do have inertia and do not respond instantaneously to the fluctuating gas phase velocity resulting in a value for C_L that is lower than 0.3. For this study C_L was used as a fitting parameter

191

to match the predicted and experimentally determined cloud burning rates. This is discussed in Section 9.3.3.

9.2.5.1.2 Energy Balance

Integrating the particle energy balance along its trajectory allows the particle temperature to be determined:

$$m_p C_p \frac{dT_p}{dt} = k_h A_p \left(T - T_p \right) + f_h \frac{dm_p}{dt} \Delta H + \varepsilon_r A_p \sigma_{sb} \left(\theta_R^4 - T_p^4 \right)$$

(9-31)

Equation (9-31) describes the energy balance and assumes that heating by convection, radiation and particle reaction causes the rise in particle temperature. For sufficiently small time steps Equation (9-31) can be linearised and integrated to yield:

$$T_p \left(t + \Delta t \right) = \alpha_p + \left(T_p(t) - \alpha_p \right) e^{-\beta_p \Delta t}$$

(9-32)

where

$$\alpha_p = \frac{k_h T + \varepsilon_r \sigma_{sb} \theta_R^4}{k_h + \varepsilon_r \sigma_{sb} T_p^3}, \quad \beta_p = \frac{A_p \left(k_h + \varepsilon_r \sigma_{sb} T_p^3 \right)}{m_p C_p}$$

In Equation (9-31), the heat transfer coefficient, k_h, is evaluated using the Ranz and Marshall correlation[141-142]:

$$Nu = 2 + 0.6 \, \mathrm{Re}_p^{1/2} \, \mathrm{Pr}^{1/3}$$

(9-33)

192

9.2.5.2 Particle Combustion Model

Results from Chapter 8 show that the group combustion model developed in Chapter 7 is capable of describing the combustion process, implying that the particle reaction can be described by:

$$6CuFeS_2 + 19O_2 => 6CuO + 2Fe_3O_4 + 12SO_2 \tag{9-34}$$
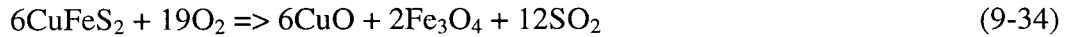
Fluent uses the general resistance model to predict the combustion rate of a particle, with the overall reaction rate constant given by the combined resistances of oxygen mass transfer to the particle surface and intrinsic reaction rate.

$$\dot{m}'_{O_2} = k_{ov} A_p MW_{O_2} C_{O_2} \tag{9-35}$$

$$k_{ov} = \frac{k_m k_c}{k_m + k_c} \tag{9-36}$$

The mass transfer coefficient is given by the Frossling equation (analogous to the Ranz and Marshall equation above):

$$Sh = \frac{k_m d_p}{D} = 2 + 0.6 Re^{\frac{1}{2}} Sc^{\frac{1}{3}} \tag{9-37}$$

while the intrinsic reaction rate constant is given by an Arrhenius type equation:

$$k_c = A \exp\left(\frac{-E_a}{RT_p}\right) \tag{9-38}$$

In Equation (9-38), results from Chapter 8 show that, the activation energy and pre-exponential factor are $240\frac{kJ}{mol}$ and $3.7 \times 10^{12}\frac{m}{s}$ respectively.

If the Fe_3O_4 and CuO remain in the particle after reaction, then Reaction (9-34) shows that the change in particle mass per kilogram of oxygen reacted is $-0.263\frac{kg}{kg_{O_2}}$ and therefore the particle mass can be calculated from:

$$\frac{dm_p}{dt} = -0.263\,\dot{m}'_{O_2} \qquad (9\text{-}39)$$

Once the reaction rate has been determined, the sources of mass, energy and species added to the individual control volume (or cells) of the gas phase equations can be calculated by determining the change in particle mass and temperature within the individual control volumes visited by a particle along its trajectory.

The mass added to the gas phase is equal to the mass lost from the particle and therefore:

$$S_m = -\frac{N\Delta m_p}{V_{cell}} \qquad (9\text{-}40)$$

The energy added to the gas phase equals the change in sensible enthalpy of the particle minus the heat gained by the particle due to reaction:

$$S_e = \frac{N\left(\overline{m_p}C_p\Delta T - \Delta m_p\Delta H\right)}{V_{cell}} \qquad (9\text{-}41)$$

194

Using Reaction (9-34) the mass of oxygen lost from the gas phase per change in particle

mass is $3.8 \frac{kg_{O_2}}{kg}$, while the addition of sulfur dioxide to the gas phase can be shown to be

$4.8 \frac{kg_{SO_2}}{kg}$ giving:

$$S_{O_2} = -3.8 \frac{N\Delta m_p}{V_{cell}} \quad (9\text{-}42)$$

and

$$S_{SO_2} = 4.8 \frac{N\Delta m_p}{V_{cell}} \quad (9\text{-}43)$$

It is worth noting that, based on thermodynamic and kinetic data, SO_3 is expected to be present at approximately 1 to 5 vol%. This is small enough that SO_3 was not considered by the model.

Because it is impossible to track all of the particles that enter the computational domain, each particle track represents a number of particles. Therefore in Equations (9-40) to (9-43) N is the number of particles represented by the particle track, while V_{cell} is the cell volume and Δm_p is the change in particle mass during its residence time within the cell.

9.3 Model Validation and Parameter Fitting

The CFD model used several fitting parameters to close the governing equations and allow a solution to be obtained; three of these were adjusted to tune the model output to experimental results, namely:

1) the turbulence intensity of the flow entering the furnace;

2) the turbulent Prandtl number; and

3) the integral time scale constant of the particles.

Model tuning was conducted at three stages of development. The turbulence model was tuned for an isothermal model, while the heat transfer was tuned for a non-isothermal non-reacting model. Finally particle dispersion was tuned using the complete model. In all cases the objective function used to fit the parameters to the experimental data was the sum of the squares of the relative errors, and a bisection technique was used to minimise the error.

9.3.1 Turbulence Intensity

To predict the Reynolds stresses and therefore the flow field within the furnace required an accurate estimate of the turbulence intensity of the inlet flow. This was achieved by treating the turbulence intensity of the inlet flow as a fitting parameter. The turbulence intensity of the flow was adjusted until the predicted furnace centerline velocity matched the experimentally determined centerline velocity profile within the UBC flash reactor. Because the model was used to predict the combustion process for

both the straight-tube and swirl burners, the turbulence intensity was tuned for both a non-swirling and a swirling flow.

A pitot tube,[92] which is based on the difference between the static and dynamic pressure of the flow, was used to determine the experimental centerline velocity profile, i.e.:

$$\Delta P = P_{static} - P_{dynamic} = \frac{1}{2}\rho U^2 \tag{9-44}$$

Figures 9-7 and 9-8 shows the experimental and predicted centerline velocity profiles for a non-swirling and swirling flow respectively. In these Figures the velocity profiles have been normalised with respect to the superficial inlet velocity. In both cases the superficial inlet velocity of the flow was 14.25 m/s, with a fitted turbulence intensity of 30% (using a sum of squares of the relative error). This inlet velocity is approximately 15 times greater than that used for the cloud combustion experiments (Section 6.3.1). This was necessary so that a measurable difference could be obtained between the static and dynamic pressures.
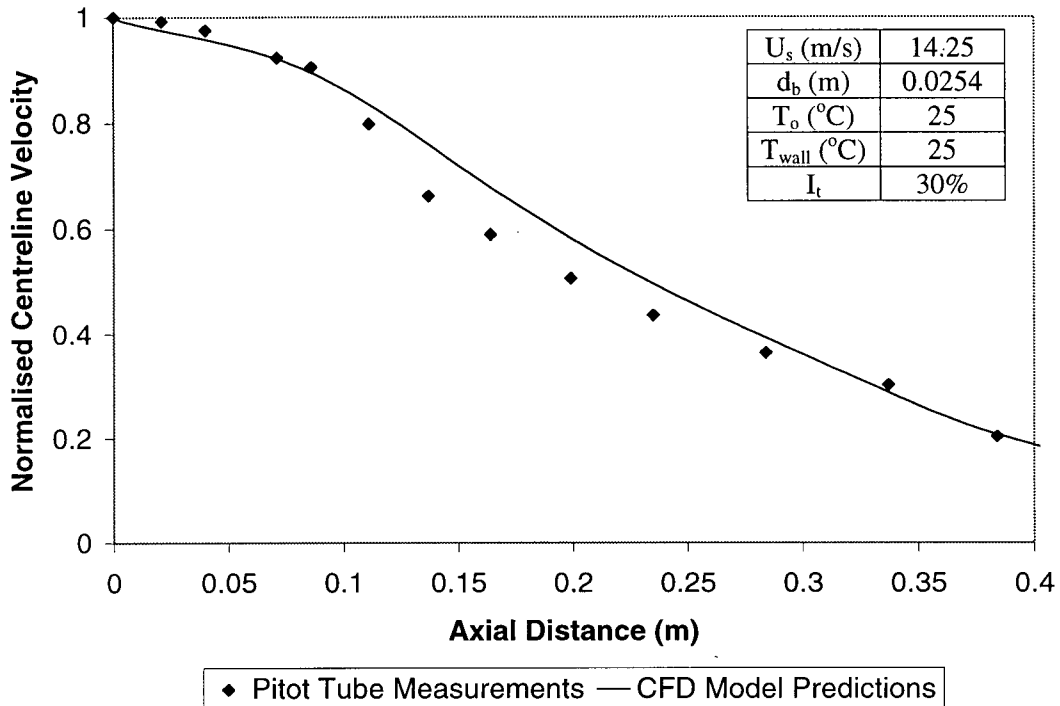
Figure 9-7: **Experimental and Predicted Centerline Gas Phase Axial Velocity Profiles for a Non-Swirling Flow.**
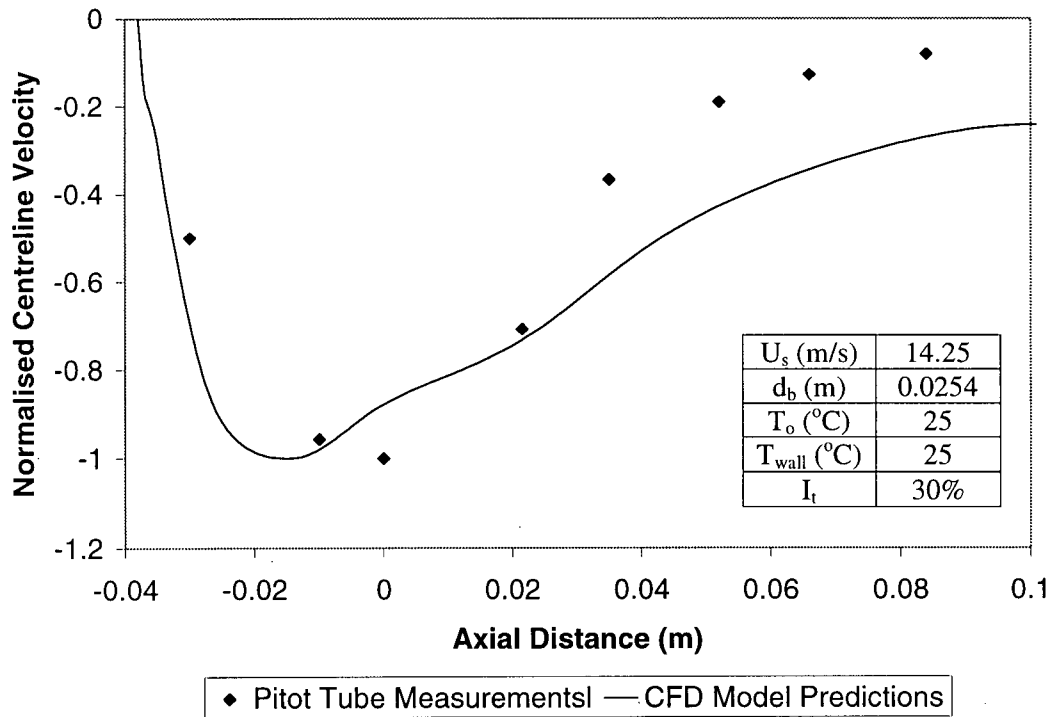
Figure 9-8: **Experimental and Predicted Centerline Gas Phase Axial Velocity Profiles for a Swirling Flow.**

For the swirl burner, because the swirl vanes were placed approximately 0.05m upstream from the burner exit the recirculation zone formed within the throat of the burner. Therefore to measure the size and strength of the recirculation zone required the flow inside the burner throat to be investigated, resulting in the negative values for the axial distance from the burner tip in Figure 9-8.

Figure 9-7 shows a good fit can be obtained between the experimental and predicted centreline axial velocity profile for a non-swirling flow, with an R-squared value of 0.957. However the fit for the swirl burner is less satisfactory with the model, over-predicting the size of the recirculation zone and resulting in an R-squared value of 0.749. The poor fit of the model likely results from the high degree of coupling between the momentum equations for swirling flow, large axial velocity gradients in the radial direction within the free vortex formed at the burner exit and the strong aniostropic nature of the eddy viscosity within the free vortex.

All of these factors tend to reduce the accuracy of the solution. Given the complex nature of the flow, the fit for the swirl burner was deemed to be satisfactory.

9.3.1.1   Influence of Flow Velocity and Swirl Vanes on the Inlet Turbulence Intensity

9.3.1.1.1   Inlet Velocity

Hinze[143] and Reynolds[144] have shown that pipe and jet flows exhibit Reynolds number similarity. This means that at sufficiently high Reynolds number the flow characteristics can be defined using one length and velocity scale. This suggests that for

this model, the turbulence intensity of the flow should not be a function of the inlet velocity.

While Reynolds number similarity can be assumed for a single phase flow, Kenning and Crowe[145] have shown that the presence of particles influences the turbulence of the gas phase. In particular small particles are expected to dampen turbulent fluctuations. Hence a sensitivity analysis was conducted to determine the influence of the inlet flows turbulence intensity on the predicted velocity field. In this study a superficial inlet velocity of 1.2m/s was used and the turbulence intensity was varied from 5 to 30%. Figure 9-9 shows the predicted furnace centerline velocity as a function for different assumed inlet turbulence intensities.

U_s (m/s)	1.2
d_b (m)	0.0254
T_o (°C)	25
T_{wall} (°C)	850
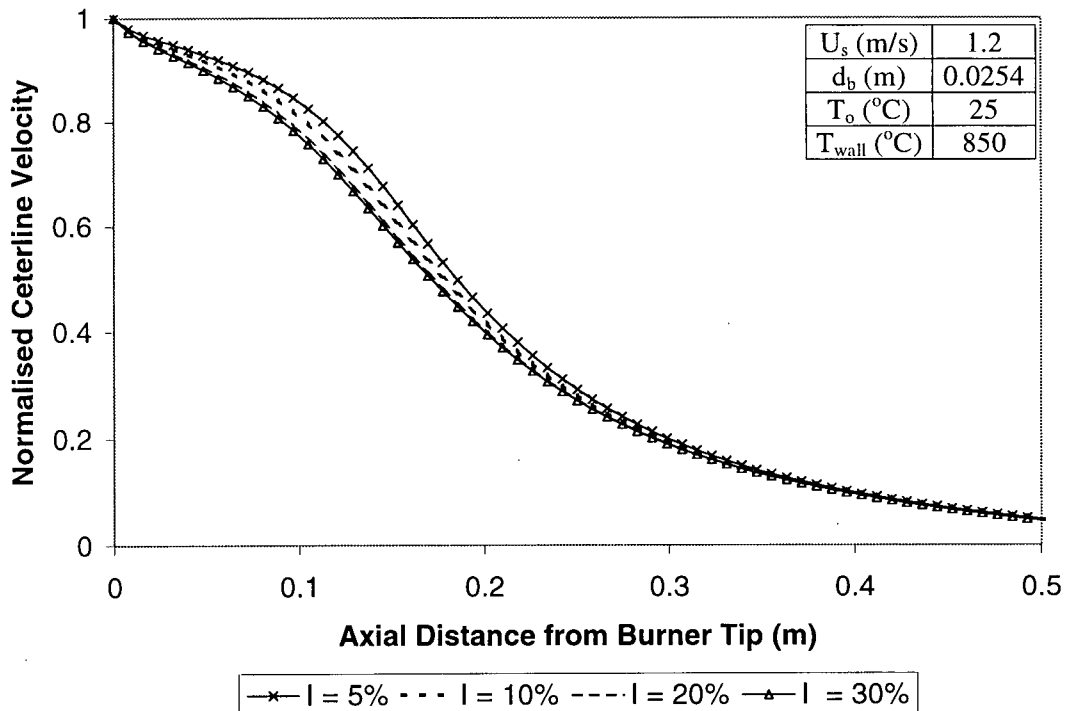
Figure 9-9: Predicted Furnace Centerline Velocity Profile for a Non-Swirling Flow for Different Assumed Inlet Turbulence Intensities.

This shows that for the straight-tube burner, the predicted centerline velocity of the flow is largely insensitive to the assumed value of the inlet turbulence intensity for inlet turbulence intensities greater than approximately 20%. However for turbulence intensities less than 20% the predicted velocity field close to the burner tip is influenced by the value assumed for the turbulence intensity. Hence for a particle-laden flow the presence of the particles may influence the predicted near-burner velocity profile. However, because the exact influence of the particles on the gas phase turbulence is not known, it was decided to use an inlet turbulence intensity of 30% for all subsequent runs where the straight-tube burner was investigated.

9.3.1.1.2   Swirl Vanes

Turbulence is generated when there are gradients in the mean velocity of the flow as shown by the turbulence production terms in the Reynolds Stress Model (Appendix A6). Swirl vanes create velocity gradients within the flow. Consequently, the presence of the swirl vane is expected to increase the turbulence intensity of the flow entering the furnace. Figure 9-10 shows the predicted furnace centerline velocity of the swirl burner for different assumed values for the turbulence intensity of the inlet flow.
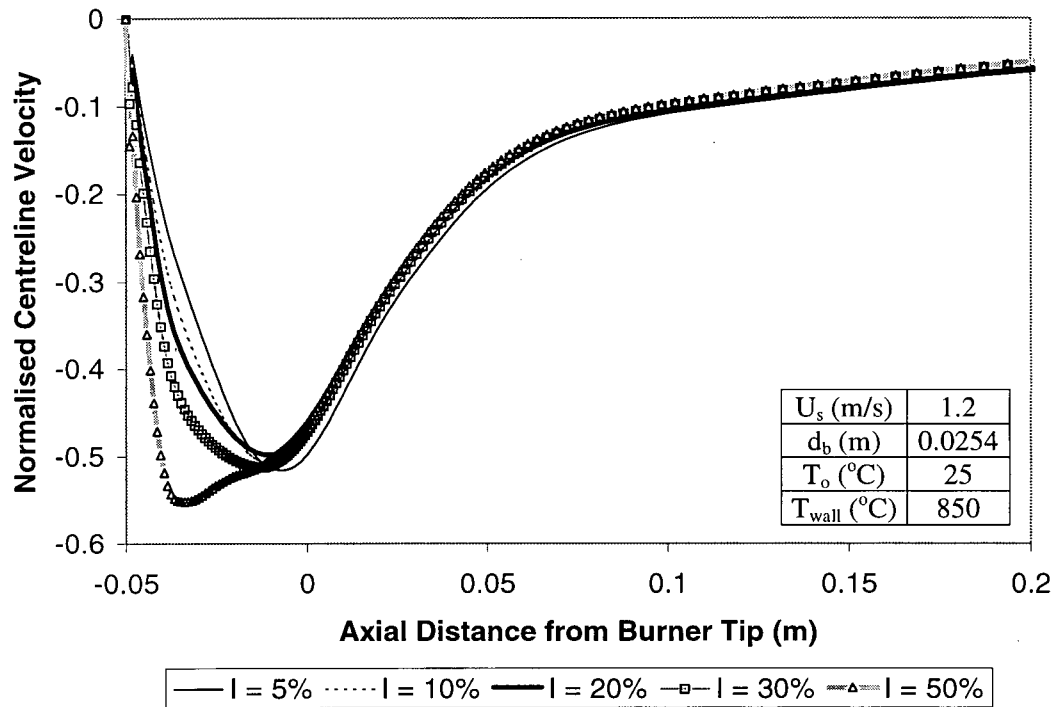
Figure 9-10: Predicted Furnace Centerline Velocity Profile for a Swirling Flow for Different Assumed Inlet Turbulence Intensities.

Figure 9-10 shows that within the throat of the burner (i.e. at axial distances less than 0) the predicted velocity profile is sensitive to the assumed value for the turbulence intensity. However, the velocity profile downstream from the burner exit (i.e. axial distances greater than 0) is insensitive to the assumed turbulence intensity. Hence, because the presence of the swirl vanes is expected to increase turbulence while the particles decrease turbulence, but both of these effects are ill-defined, the turbulence intensity was again set to 30% for all subsequent runs where the swirl burner was being investigated.

It is worth noting at this point that Kenning and Crowe[145] have shown that the particles reduce the gas phase turbulence. However it is difficult to quantify the amount

of extent of the damping. Therefore implementation of a "turbulence damping" model could not be justified.

9.3.2 Turbulent Prandtl Number

To predict the temperature field within the reactor required the turbulent Prandtl number of the flow to be estimated. Therefore the predicted furnace centreline temperature profile was tuned to an experimentally determined profile by fitting the turbulent Prandtl number of the flow. A suction thermocouple was used to obtain the experimental temperature profile. The theory of suction thermocouple measurements is discussed by Poirier and Geiger[146].

Figures 9-11 to 9-13 show experimentally determined and predicted centreline temperature profiles for an inlet flow of 53.7 litres/min and a fitted turbulent Prandtl number of 0.65 (using the sum of the square of the relative error) for a reactor wall temperatures of 750, 850 and 950°C, respectively. This flow is approximately two times greater than that used for the group combustion experiments in order to ensure that temperature gradient in the axial direction was sufficiently small to allow the temperature profile to be measured.
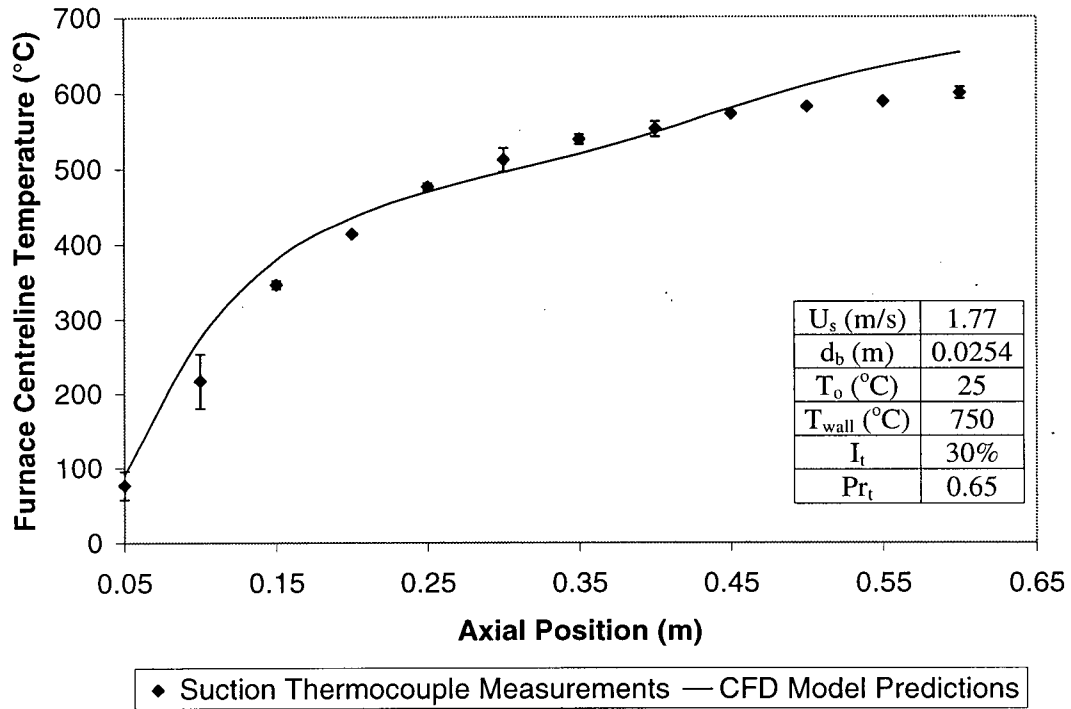
Figure 9-11: Experimental and Predicted Furnace Centreline Temperature for a Non-Swirling Flow and Furnace Wall Temperature of 750°C.
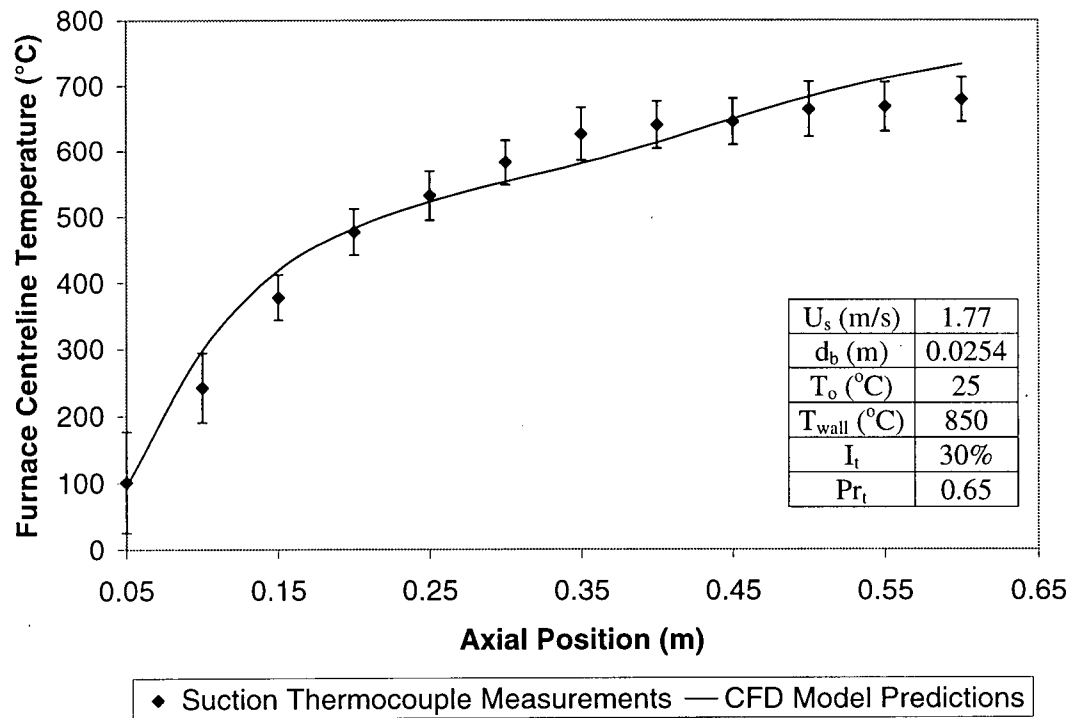
Figure 9-12: Experimental and Predicted Furnace Centreline Temperature for a Non-Swirling Flow and Furnace Wall Temperature of 850°C

204
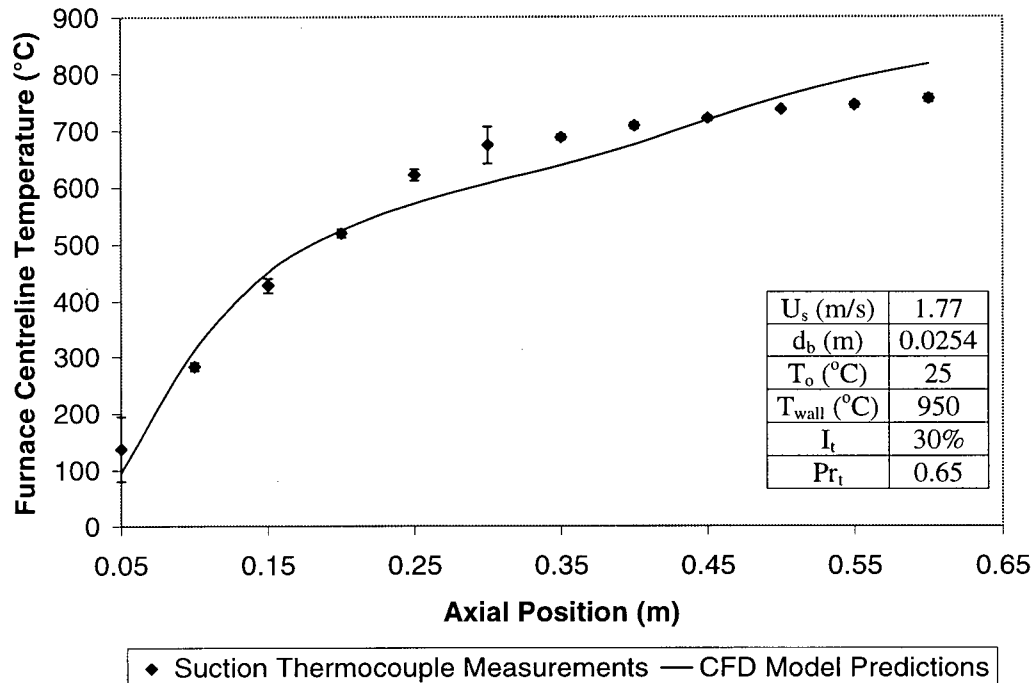
Figure 9-13: Experimental and Predicted Furnace Centreline Temperature for a Non-Swirling Flow and Furnace Wall Temperature of 950°C

These results show that a good fit can be obtained between the experimental and predicted furnace centreline temperatures for a non-swirling flow when a constant value of 0.65 is assumed for the turbulent Prandtl Number. This is within the range reported in literature.[114-15]

9.3.2.1 Influence of Flow Conditions on the Turbulent Prandtl Number

Many studies have been conducted to determine the turbulent Prandtl number of different flows.[114-117,147-149] These studies have shown that under certain conditions the turbulent Prandtl number is a function of the turbulence properties of the flow. Analysis reported by Kays[147] suggest that the turbulent Prandtl number is independent of the flow turbulence properties for turbulent Peclet Numbers in excess of 50. The turbulent Peclet number is defined as:

205

$$Pe_t = \frac{\mu_t}{\mu} \Pr \qquad\qquad (9\text{-}45)$$

Based on model predictions, the turbulent Peclet number of the flow used in this study varies from 20-200. Hence the turbulent Prandtl number is expected to be constant. This is reflected in the experimental results. Therefore a value of 0.65 was used for all subsequent runs.

9.3.3 Particle Integral Time Scale

The heat-up and combustion times of the particles within the cloud depend upon the intrinsic reaction rate and the heat and mass transfer conditions within the cloud. Group combustion theory shows that the rate of heat and mass tranfer within the cloud is a function of its particle number density. The local particle number density of the cloud depends upon the particle dispersion rate, which according to Equations (9-29) and (9-30) is related to the particle integral time scale constant. Therefore, to predict the cloud combustion rate requires the particle integral time scale constant to be determined. The particle integral time scale constant was used as a fitting parameter to match the predicted cloud combustion rate to the experimentally determined combustion rate, for both the straight-tube and swirl burners.

9.3.3.1 Straight Tube Burner

The integral time scale constant was determined by minimising the sum of the square of the relative error between the experimental and predicted desulfurisation rates for five straight-tube burner runs. Table 9-1 lists the parameters used in each of the five

runs. These runs were chosen as they represent the extremes of the conditions tested in the group combustion study (Section 6.3.1).

Table 9-1: Validation Runs for the Straight-Tube CFD Model

Run No.	Oxygen-to-concentrate ratio	Oxygen enrichment (vol %)	Particle diameter(μm)	Escondida loading (wt%)
1	0.301	21	32	0
2	0.271	21	82	0
3	0.139	100	32	100
4	0.089	100	82	100
5	0.188	60	49.5	80

Figures 9-14 to 9-18 show the predicted and experimental desulfurisation rates for the five experiments using a fitted integral time scale constant of 0.05.

U_s (m/s)	1.17
d_b (m)	0.0254
T_o ($^\circ$C)	25
T_{wall} ($^\circ$C)	850
I_t	30%
Pr_t	0.65
d_p (μm)	32
P_{O2} (atm)	0.21
η	0.301
C_L	0.05

♦ Experimental Samples —— CFD Model Predictions
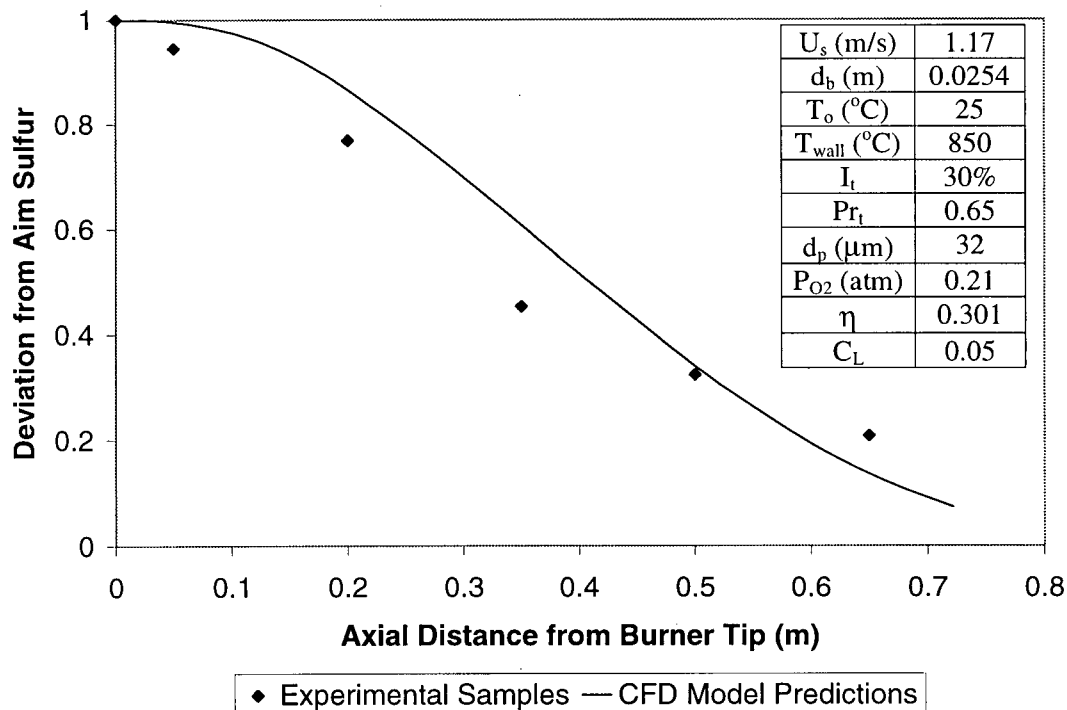
Figure 9-14: Comparison of the Predicted and Experimental Desulfurisation Rates For Run 1 in Table 9-1 (Non-Swirling Flow).

207

U_s (m/s)	1.12
d_b (m)	0.0254
T_o (^{o}C)	25
T_{wall} (^{o}C)	850
I_t	30%
Pr_t	0.65
d_p (μm)	82
P_{o2} (atm)	0.21
η	0.271
C_L	0.05

◆ Experimental Samples — CFD Model Predictions
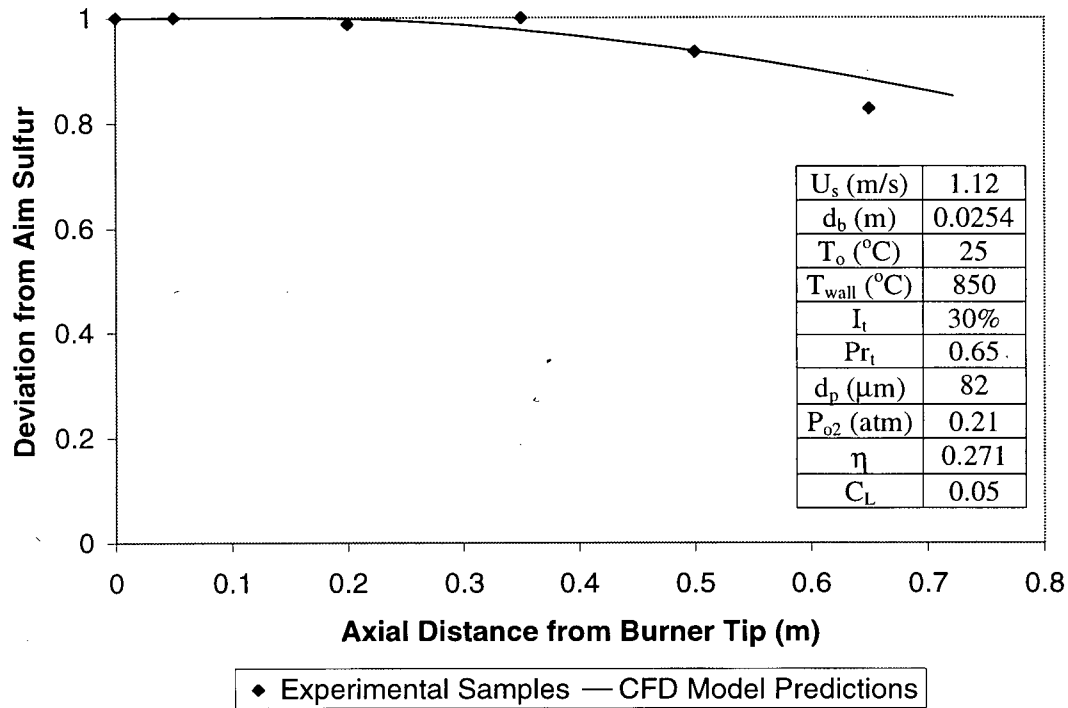
Figure 9-15: Comparison of the Predicted and Experimental Desulfurisation Rates For Run 2 in Table 9-1 (Non-Swirling Flow).

U_s (m/s)	0.27
d_b (m)	0.0254
T_o (^{o}C)	25
T_{wall} (^{o}C)	850
I_t	30%
Pr_t	0.65
d_p (μm)	32
P_{o2} (atm)	1
η	0.139
C_L	0.05

◆ Experimental Samples — CFD Model Predicted
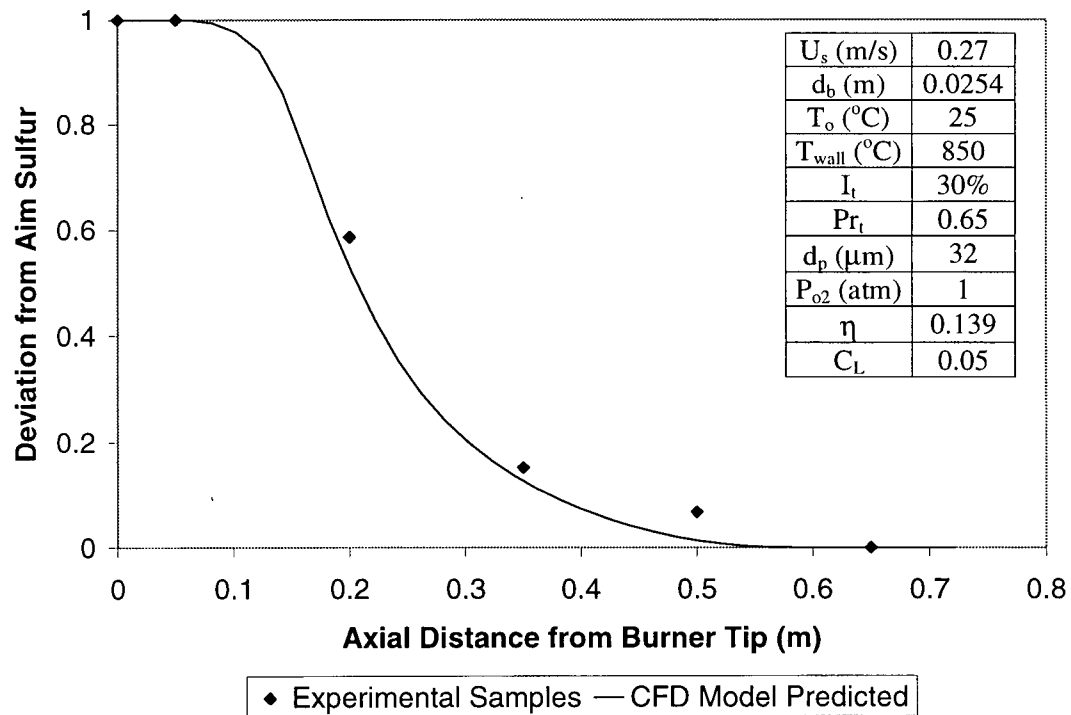
Figure 9-16: Comparison of the Predicted and Experimental Desulfurisation Rates For Run 3 in Table 9-1 (Non-Swirling Flow).
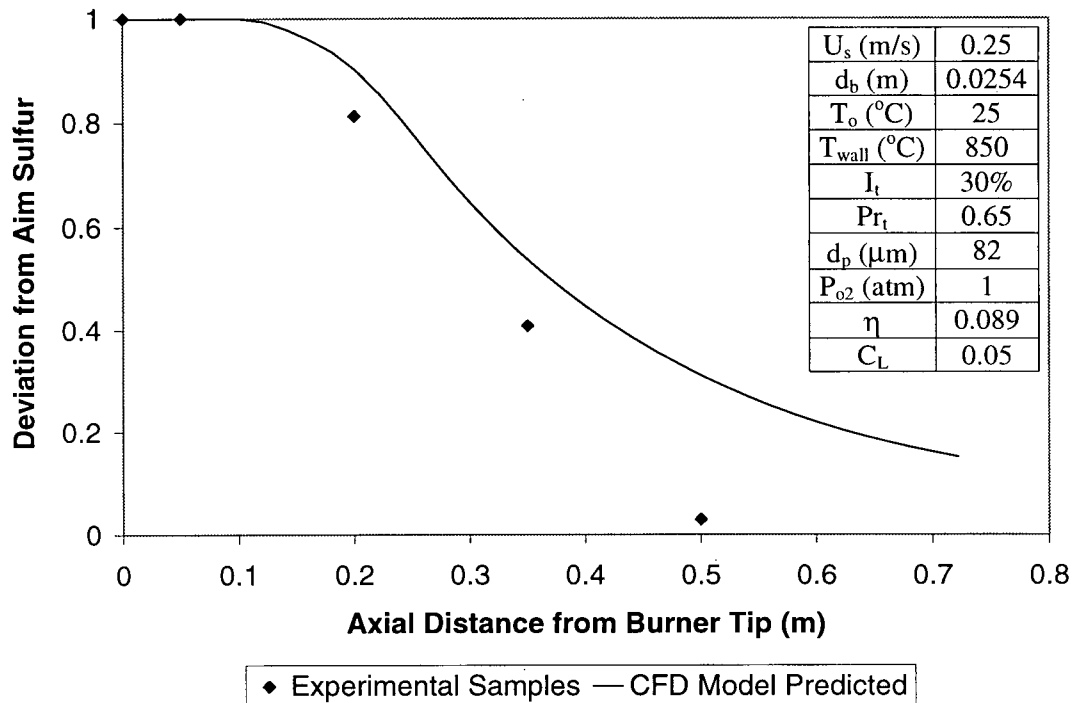
Figure 9-17: Comparison of the Predicted and Experimental Desulfurisation Rates For Run 4 in Table 9-1 (Non-Swirling Flow).
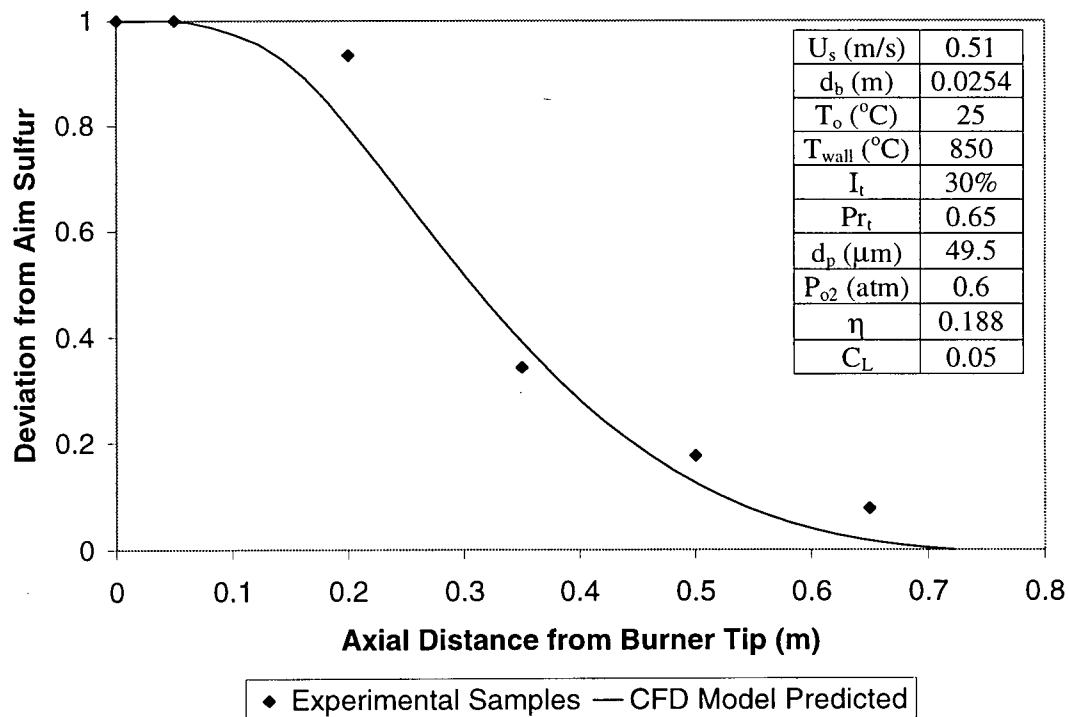
Figure 9-18: Comparison of the Predicted and Experimental Desulfurisation Rates For Run 5 in Table 9-1 (Non-Swirling Flow).

209

These results show that for the straight-tube burner the cloud combustion rate can be described using an integral time scale constant of 0.05 for all experimental conditions.

9.3.3.2 Swirl Burner

Using the particle integral time scale constant of 0.05 determined from the straight-tube burner runs the predicted desulfurisation rate of the cloud was compared to the experimentally determined desulfurisation rate for the four swirl burner runs. The experimental conditions are shown in Table 8-4. Figures 9-19 to 9-22 show the comparisons.

U_s (m/s)	1.17
d_b (m)	0.0254
T_o (°C)	25
T_{wall} (°C)	850
I_t	30%
Pr_t	0.65
d_p (µm)	42
P_{o2} (atm)	0.21
η	0.295
C_L	0.05

◆ Experimental Samples — CFD Model Predictions
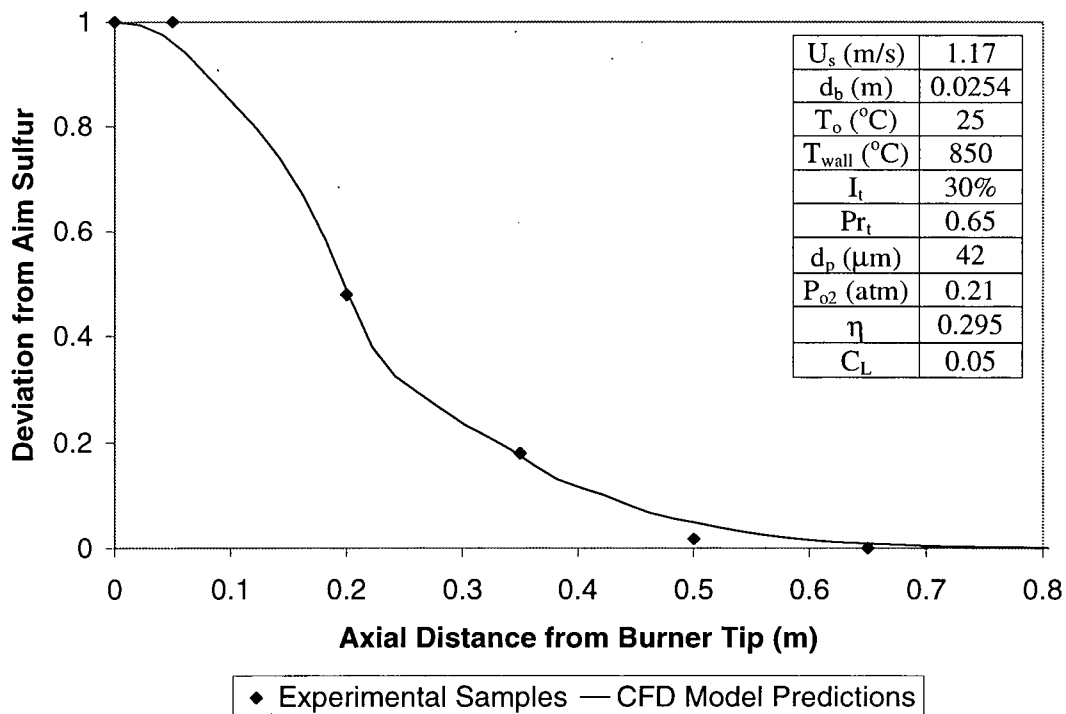
Figure 9-19: Comparison of the Predicted and Experimental Desulfurisation Rates For Run 1 in Table 8-4 (Swirling Flow).

U_s (m/s)	1.09
d_b (m)	0.0254
T_o (^{o}C)	25
T_{wall} (^{o}C)	850
I_t	30%
Pr_t	0.65
d_p (μm)	82
P_{o2} (atm)	0.21
η	0.253
C_L	0.05

◆ Experimental Samples — CFD Model Predictions
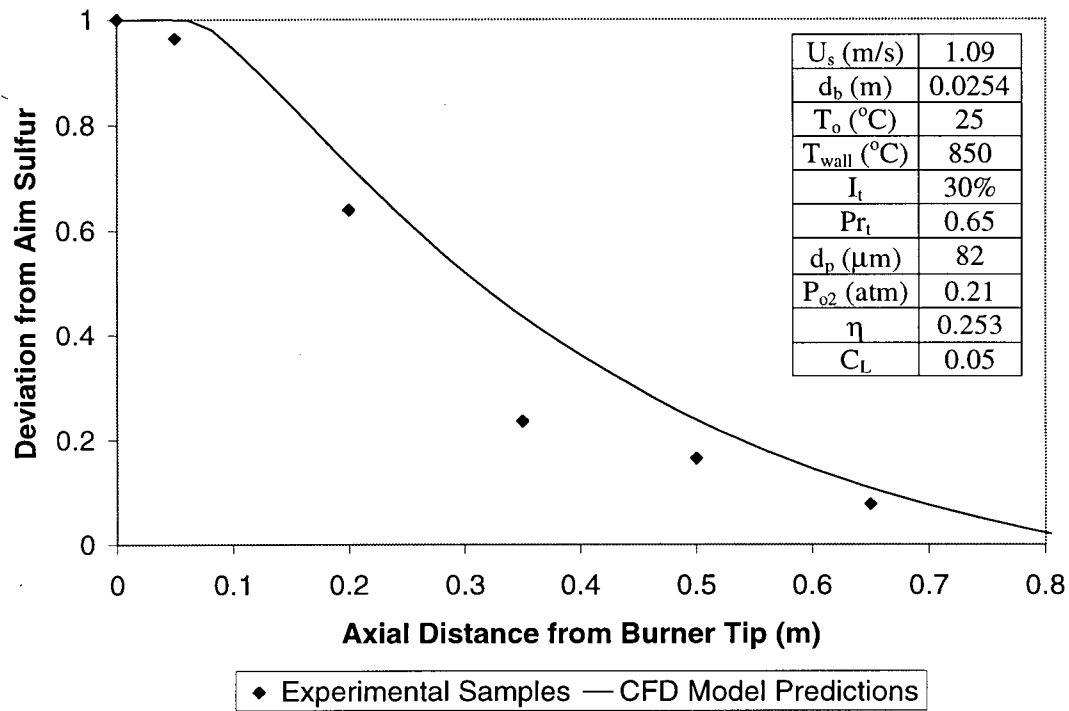
Figure 9-20: Comparison of the Predicted and Experimental Desulfurisation Rates For Run 2 in Table 8-4 (Swirling Flow).

U_s (m/s)	0.60
d_b (m)	0.0254
T_o (^{o}C)	25
T_{wall} (^{o}C)	850
I_t	30%
Pr_t	0.65
d_p (μm)	42
P_{o2} (atm)	0.21
η	0.096
C_L	0.05

◆ Experimental Samples — CFD Model Predictions
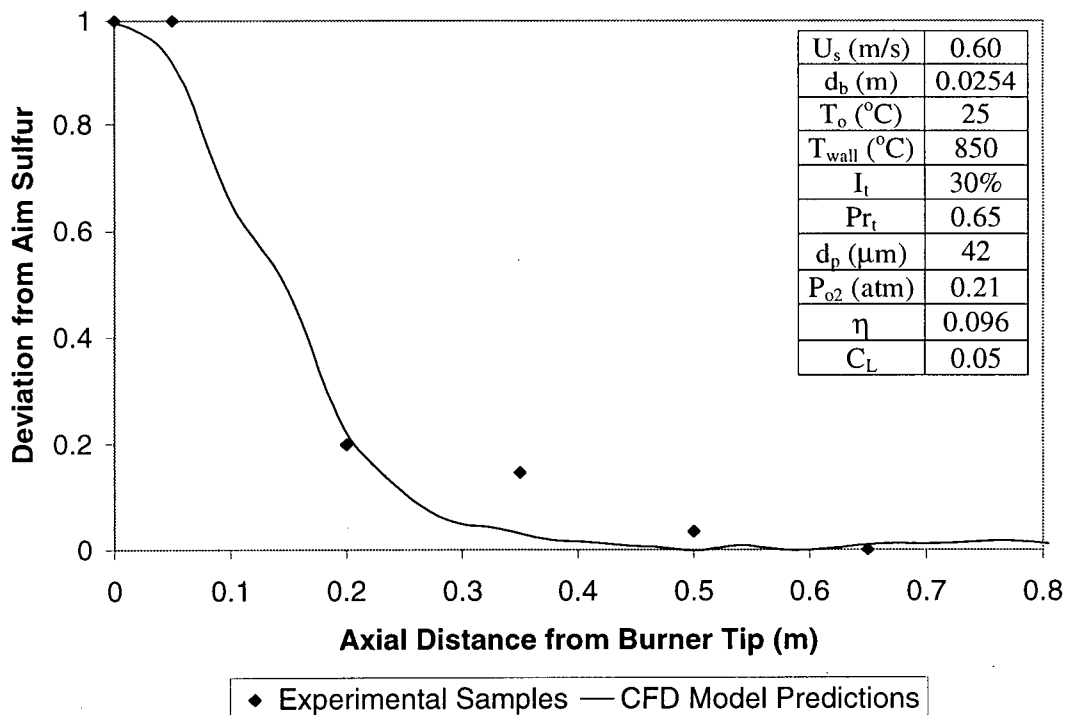
Figure 9-21: Comparison of the Predicted and Experimental Desulfurisation Rates For Run 3 in Table 8-4 (Swirling Flow).

211

U_s (m/s)	0.78
d_b (m)	0.0254
T_o (°C)	25
T_{wall} (°C)	850
I_t	30%
Pr_t	0.65
d_p (µm)	69.5
P_{o2} (atm)	0.21
η	0.121
C_L	0.05

♦ Experimental Samples — CFD Model Predictions
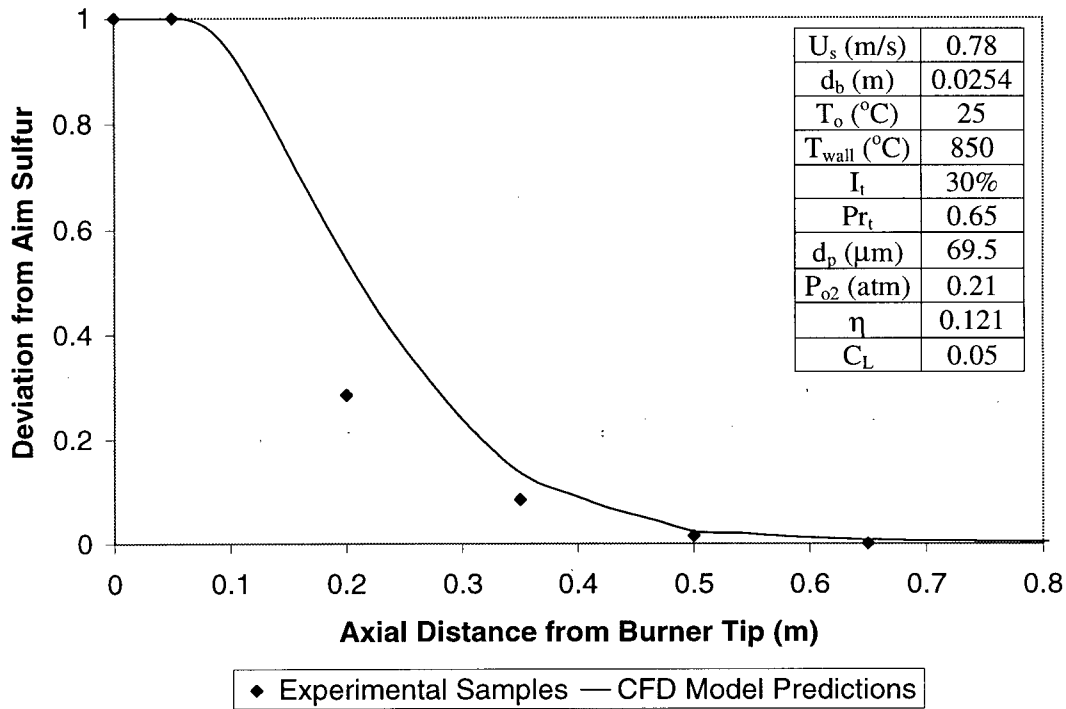
Figure 9-22: Comparison of the Predicted and Experimental Desulfurisation Rates For Run 4 in Table 8-4 (Swirling Flow).

As with the Straight-tube burner, these results show that the combustion rate of the cloud can be adaquately predicted using an integral time scale constant of 0.05. This is to be expected because the particle integral time scale constant describes the interaction between the particle and the turbulence field. As the particle and turbulence properties of the swirl burner are similar to those of the straight-tube burner, the particle integral time scale constant is also expected to be similar.

9.3.3.3   Influence of Particle Properties and Operating Condition on Integral Time Scale
              Constant

The results given above show that the particle integral time scale constant is independent of the particle and turbulence properties. This is confirmed by the work

212

conducted by Klose et al[150] who have shown that at high Stokes number (St>4) the particle integral time constant is low and essentially constant. The Stokes number relates the particle relaxation time (which is a measure of time required for the particle to reach its terminal velocity) to the characteristic eddy lifetime and is given by:

$$St = \frac{4}{3} \frac{\rho_p}{\rho} \frac{d_p^2}{C_D \, Re v T_e}$$

(9-46)

In Equation (9-46) T_e is the characteristic eddy lifetime which can be estimated from:

$$T_e = \frac{0.3k^{3/2}}{\varepsilon u'}$$

(9-47)

For the conditions investigated in this work the Stokes number varies from between 7 and 20, suggesting that the partice integral time scale constant should not be a function of the turbulence properties of the flow.

It is worth noting at this point that the particle integral time scale constant of 0.05 is low compared to typical experimental values, which vary from 0.1 to 0.6.[150] The explanation for this is that the influence of the particles on the gas phase turbulence is not accounted for. The presence of the particles is expected to dampen the turbulence. Hence the turbulence model over-estimates the turbulence field resulting in an over-estimation of the turbulent dispersion of the particles. Therefore to obtain the correct dispersion rate (which is inferred from the cloud combustion rate) requires a lower than expected value of the particle integral time scale constant.

A sensitivity analysis was conducted to determine the influence of the particle integral time scale constant on the predicted cloud burning rate. Figure 9-23 shows the predicted cloud desulfurisation rate for particle integral time scale constants of 0.025, 0.05 and 0.1.

U_s (m/s)	2
d_b (m)	0.0254
T_o (°C)	25
T_{wall} (°C)	850
I_t	30%
Pr_t	0.65
d_p (μm)	45
P_{O2} (atm)	0.21
η	0.3
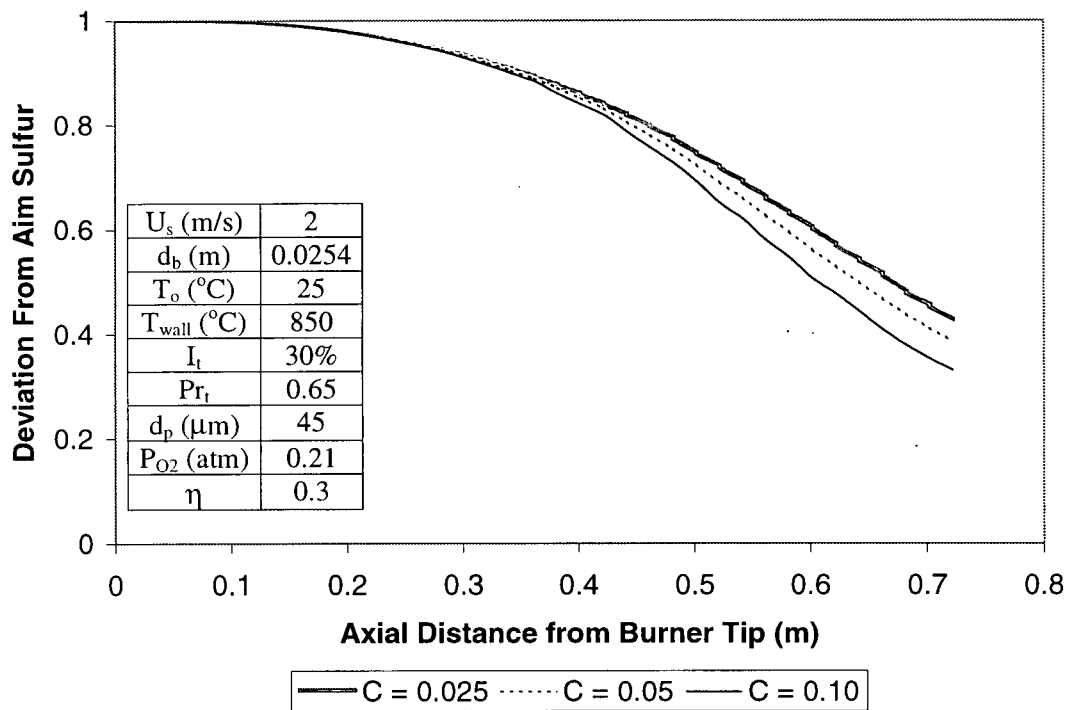
Figure 9-23: Sensitivity Analysis of the Predicted Cloud Burning Rate to the Particle Integral Time Scale Constant

The conditions used in the study are listed in the inset in the Figure. This shows that the desulfurisation rate is only slightly affected by halving and doubling the particle integral time scale constant. Hence a value of 0.05 for the particle integral time scale constant was used for all subsequent runs.

9.3.4 Sensitivity Analysis of the Radiation Model

The sub-model used to account for radiative heat transfer could not be easily validated. Therefore a sensitivity analysis was conducted to compare the predicted cloud burning rate for a typical run with and without radiation account for. Figure 9-24 shows the comparison. The conditions used to by the model are shown in the Figure inset. These conditions were used because the particle diameter is small the and the particle number density of the cloud is large. Hence radiation scattering by the cloud is expected to be maximised at these conditions.

U_s (m/s)	0.27
d_b (m)	0.0254
T_o (°C)	25
T_{wall} (°C)	850
I_t	30%
Pr_t	0.65
d_p (μm)	32
P_{o2} (atm)	1
η	0.139
C_L	0.05
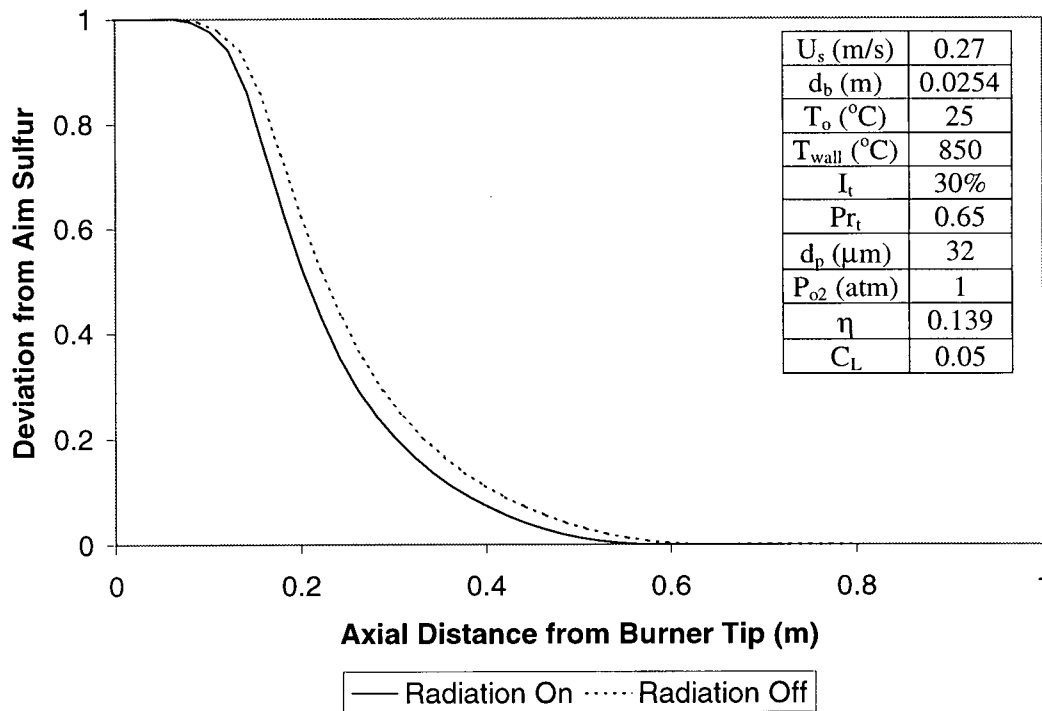
Figure 9-24: Predicted Cloud Burning Rate for a Typical Run (Conditions List in Inset) With and Without Radiation

Figure 9-24 shows that radiative transfer to the particles only slightly increases the burning rate of the cloud. Hence its influence can be safely neglected.

9.4 Summary

The CFD model results have been tuned against experimental results at three stages of model development. The model gives reasonable predictions of the combustion process occurring in the UBC flash reactor. Hence it can be used to investigate the important phenomena occurring within the reactor. If the values for the fitting parameters can be applies to the shaft of an industrial flash smelter, then the model can be extended to provide insights into the important phenomena occurring in the shaft of an industrial flash smelter.

The next chapter uses the CFD model to analyse phenomena within the UBC reactor, thereby explaining the superior performance of the swirl burner over the straight-tube burner. It also attempts to extend this knowledge to an industrial flash smelting furnace.

10 CFD Study Results

The CFD study was undertaken firstly to provide insight into the behaviour of the UBC flash reactor and to determine the reason for the superior performance of the swirl burner. Secondly, it allowed the performance of the swirl burner developed in Section 4.2.2 to be compared with the bluff body design used by most industrial flash smelters.

10.1 UBC Flash Reactor Study

For the UBC flash reactor study, nine runs were conducted using the validated CFD model outlined in Chapter 9. Table 10-1 lists the parameters for each run. The group combustion number in these runs varied from 219 to 12,520. For each run two cases were considered. One examined the straight-tube burner while the other investigated the swirl burner, resulting in a total of 18 runs overall.

Table 10-1: UBC Reactor Model Run Parameters

Run No.	Particle diameter (μm)	Oxygen Enrichment (vol %)	Oxygen-to-concentrate ratio	Group combustion number
1	60	21	0.3	219
2	60	21	0.2	328
3	60	50	0.3	521
4	45	21	0.2	584
5	45	100	0.3	1854
6	45	21	0.1	1168
7	30	21	0.1	2629
8	30	50	0.1	6260
9	30	100	0.1	12520

217

For each set of conditions a converged solution was obtained and the flow, temperature, discrete phase concentration and discrete phase burning fields were investigated. This information provided insight into the performance of the reactor and allowed the observed superior performance of the swirl burner to be explained. Once the reactor performance had been investigated, improved estimates of the cloud Nusselt number and combustion effectiveness factors were obtained.

2.1.1 Reactor Analysis

Figures 10-1 to 10-4 compares the flow, dispersed phase concentration, temperature and dispersed phase burning fields for runs 1 and 9 for both the straight tube and swirl burners. Table 10-2 shows the important conditions and model used to generate the predictions for Runs 1 and 9.

Table 10-2: Flow Conditions and Model Parameters Used to Generate Model Predictions for Runs 1 and 9 in Table 10-1

Parameter	Run 1	Run 9
Straight-tube burner superficial exit velocity (m/s)	2	2
Swirl burner superficial exit velocity (m/s)	2	2
Inlet temperature (^{o}C)	25	25
Furnace wall temperature (^{o}C)	850	850
Inlet flow turbulence intensity (-)	30	30
Turbulent Prandtl number (-)	0.65	0.65
Particle diameter (μm)	60	30
Inlet flow oxygen partial pressure (atm)	0.21	1
Inlet flow oxygen-to-concentrate ratio (-)	0.3	0.1
Particle integral time scale constant (-)	0.05	0.05

Studies have been conducted[68,151] on the recirculation zone of momentum-dominated enclosed jets (i.e. without a significant influence of natural convection) and have shown that the length of the recirculation zone can be estimated by:

$$X_{ra} = 2.925 D_c \tag{10-1}$$

For this reactor, the recirculation zone length as calculated by Equation 10-1 is approximately 0.56 m. In contrast to this, Figure 10-1 shows that the calculated external recirculation zone is predicted to extend the entire furnace length of 1.6m. This suggests that the flow within the furnace is not governed by forced convection but rather by natural convection type phenomenon.

5.2e-04	1.1e-03	8.2e-04	3.2e-04
4.5e-04	9.2e-04	7.1e-04	2.7e-04
3.7e-04	7.7e-04	5.9e-04	2.3e-04
3.0e-04	6.2e-04	4.7e-04	1.8e-04
2.2e-04	4.6e-04	3.5e-04	1.4e-04
1.5e-04	3.1e-04	2.4e-04	9.1e-05
7.5e-05	1.5e-04	1.2e-04	4.5e-05
0.0e+00	0.0e+00	0.0e+00	0.0e+00

a) Straight-tube burner Run 1   b) Straight-tube burner Run 9   c) Swirl burner Run 1   d) Swirl burner Run 9
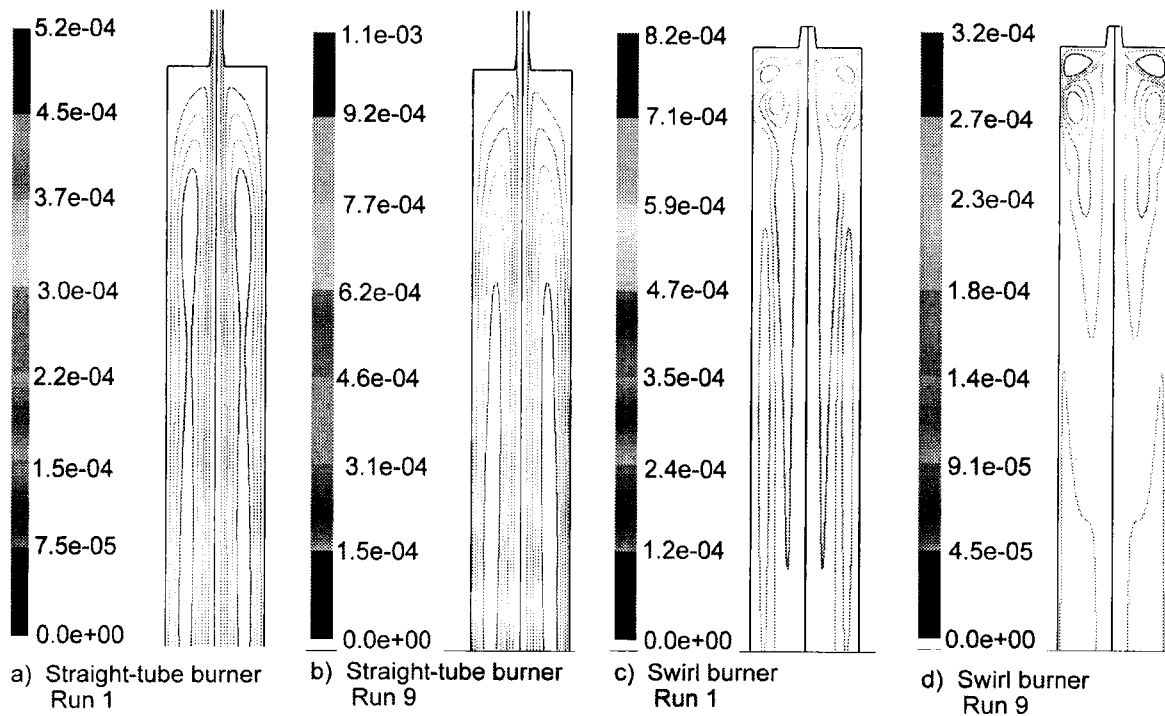
Figure 10-1: Furnace Stream Function (kg/s) for Run 1 and Run 9 Listed in Table 10-2.

Natural convection is generally driven by density differences caused by temperature gradients. One way to treat these flows is to use the Boussinesq approximation which accounts for the bouyancy forces through a source term added to the gas phase momentum equations i.e.:

$$S_{p,z} = -\rho_o \beta_b (T - T_o) g \tag{10-2}$$

For the current problem Crowe et al[152] have shown that the source of momentum added to the gas phase by the particles is:

$$S_{p,z} = \frac{m_p n}{\tau_p} (u_p - u) \tag{10-3}$$

But according to Equation (9-26) this can be re-written as:

$$S_{p,z} = \left(\frac{\rho_p - \rho}{\rho_p} \right) m_p n g - m_p n \frac{du_p}{dt} \tag{10-4}$$

The gravitational term in Equation (10-4) is similar to the source term that arises from the Boussinesq approximation. Hence te momentum source due to the presence of the particles introduces a term similar to a bouyancy source. However, it is the change in discrete phase concentration ($m_p n$) rather than gas phase density differences that drive the flow. By assuming that the particle/gas mixture is a single phase, a Rayleigh (or Grashof) number based on the total mixture density (i.e. gas plus particles) can be defined to account for the natural convection phenomenon. This explains why the Rayleigh number defined in Section 8.2.2 can be used to correlate the cloud heat transfer data.

Figure 10-2 shows the discrete phase concentration field within the reactor. This together with the analysis given above can help explain the presence of the recirculation zones predicted by the model.

8.0e-01	3.0e+00	2.0e-01	5.0e+00
7.2e-01	2.7e+00	1.8e-01	4.5e+00
6.4e-01	2.4e+00	1.6e-01	4.0e+00
5.6e-01	2.1e+00	1.4e-01	3.5e+00
4.8e-01	1.8e+00	1.2e-01	3.0e+00
4.0e-01	1.5e+00	1.0e-01	2.5e+00
3.2e-01	1.2e+00	8.0e-02	2.0e+00
2.4e-01	9.0e-01	6.0e-02	1.5e+00
1.6e-01	6.0e-01	4.0e-02	1.0e+00
8.0e-02	3.0e-01	2.0e-02	5.0e-01
0.0e+00	0.0e+00	0.0e+00	0.0e+00

a) Straight-tube burner   b) Straight-tube burner   c) Swirl burner   d) Swirl burner
Run 1   Run 9   Run 1   Run 9
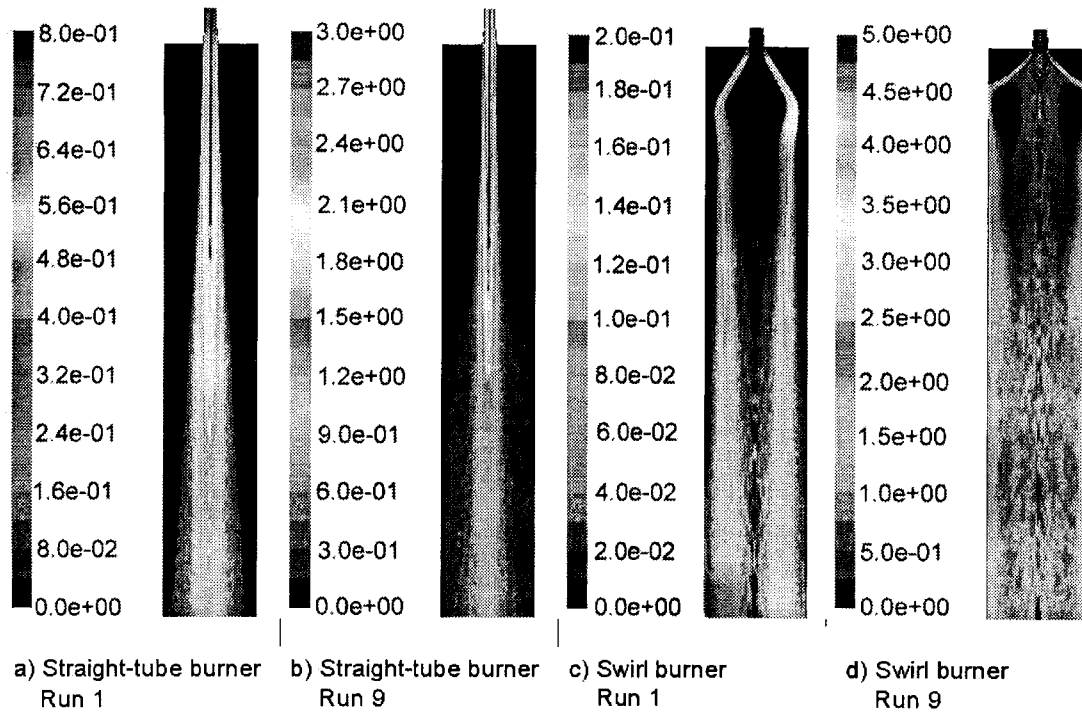
Figure 10-2: Furnace Discrete Phase Concentration Field (kg/m^3) for Run 1 and Run 9 Listed in Table 10-2.

For the straight-tube burner the discrete phase particles produce a dense stream along the furnace centreline which drives the external recirculation zone. On the other hand, the swirl burner ejects the particles radially outward forming a dense stream offset from the furnace centreline, resulting in the observed internal and external recirculation zones.

Figure 10-3 shows the effect of the burner type and discrete phase concentration on the computed temperature field within the reactor.

| a) Straight-tube burner Run 1 | b) Straight-tube burner Run 9 | c) Swirl burner Run 1 | d) Swirl burner Run 9 |
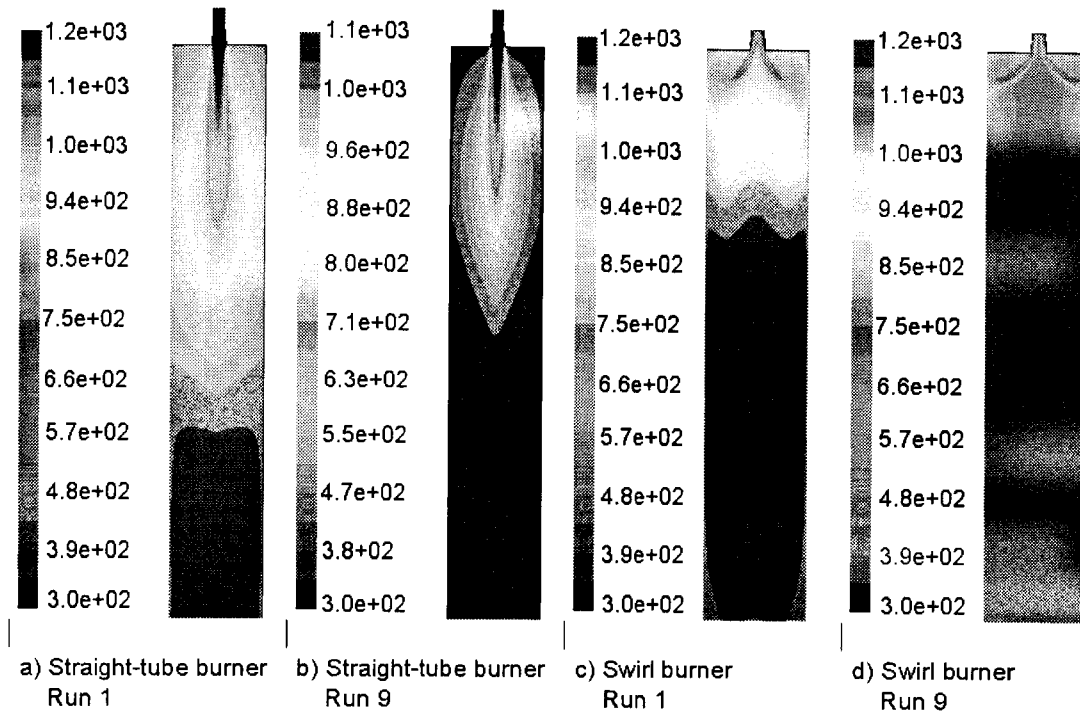
Figure 10-3: Furnace Temperature Field (K) for Run 1 and Run 9 Listed in Table 10-2.

The straight-tube burner produces a central jet resulting in a cold stream extending downward along the furance centreline. The swirl burner, on the other hand, produces a jet with a significant radial velocity component resulting in a cold stream that is offset from the furnace centreline.

The discrete phase concentration also influences the temperature field within the reactor through its influence on the strength of the recirculation zone. For run 1 the discrete concentration approximately 15 times lower compared to run 9. Lower discrete

222

phase concentrations reduce the recirculating mass flowrate (due to the natural convection phenomenon described by Equation (10-4)) for both the swirl and straight-tube burners. Because of the strong recirculation zone, more heat is carried from the combustion zone back to the furnace entrance, resulting in a more uniform temperature field at higher particle loadings.

10.1.1.3 Cloud Burning Rate

Figure 10-4 shows the burning rate of the cloud and indicates that the small particles burn faster than large particles. In addition, the swirl burner produces a higher burning rate than the straight tube burner. The cloud burning rate is calculated from the mass source terms that are added to the continuity equation due to particle combustion. These source terms are defined in Equation (9-40).

| a) Straight-tube burner | b) Straight-tube burner | c) Swirl burner | d) Swirl burner |
| Run 1 | Run 9 | Run 1 | Run 9 |
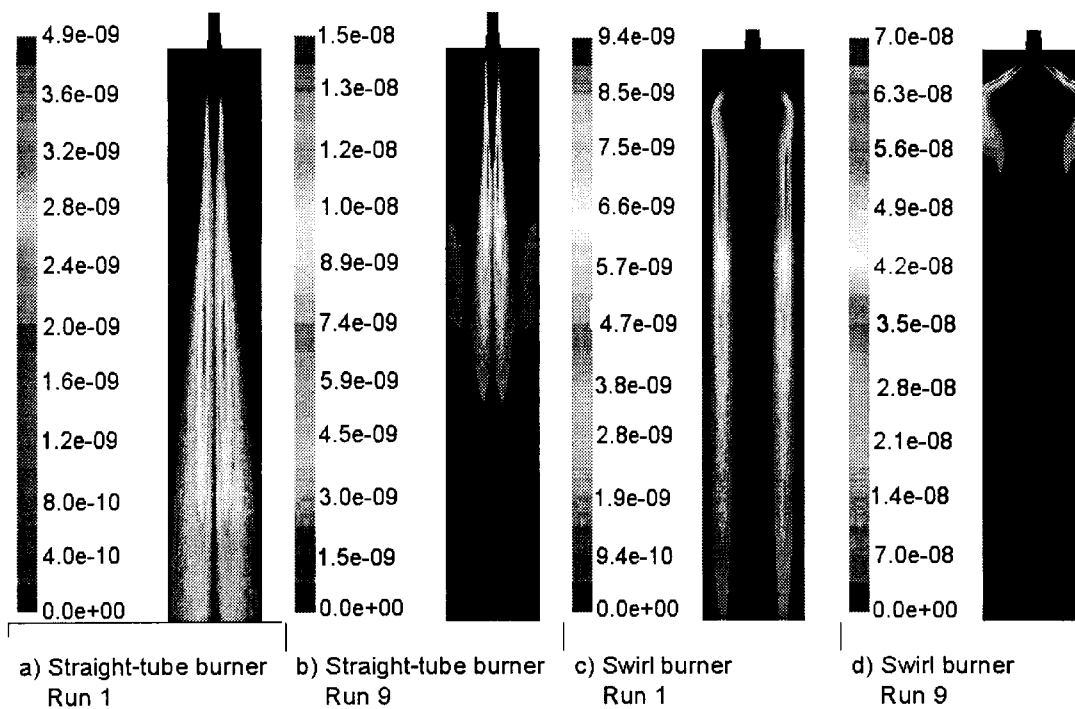
Figure 10-4: Cloud Burning Rate (kg/s) for Run 1 and Run 9 Listed in Table 10-2.

10.1.2 Particle Age Distribution Analysis

Figures 10-1 to 10-4 show the predicted flow, temperature, discrete phase concentration and discrete phase burning fields within the flash reactor. The particle residence time distribution can be applied to explain the experimentally-observed superior performance of the swirl burner. Figures 10-5 and 10-6 show the predicted particle age distributions for both the straight tube and swirl burner for runs 1 and 9 in Table 10-1. In conjunction with the particle age distributions predicted by the CFD model Figures 10-5 and 10-6 show a fitted age distributions for a non-ideal flow reactor. These are discussed below.

The particle age distributions[58] were determined from the particle trajectory calculations used by Fluent during the solution process. Particles were released from the furnace inlet with a velocity equal to the gas phase velocity. The particle trajectory equations were then solved (See Section 9.2.4) and the time taken for the particle to reach the outlet recorded. A total of 5000 particle trajectories were calculated to give the particle age distributions shown in Figures 10-5 and 10-6.
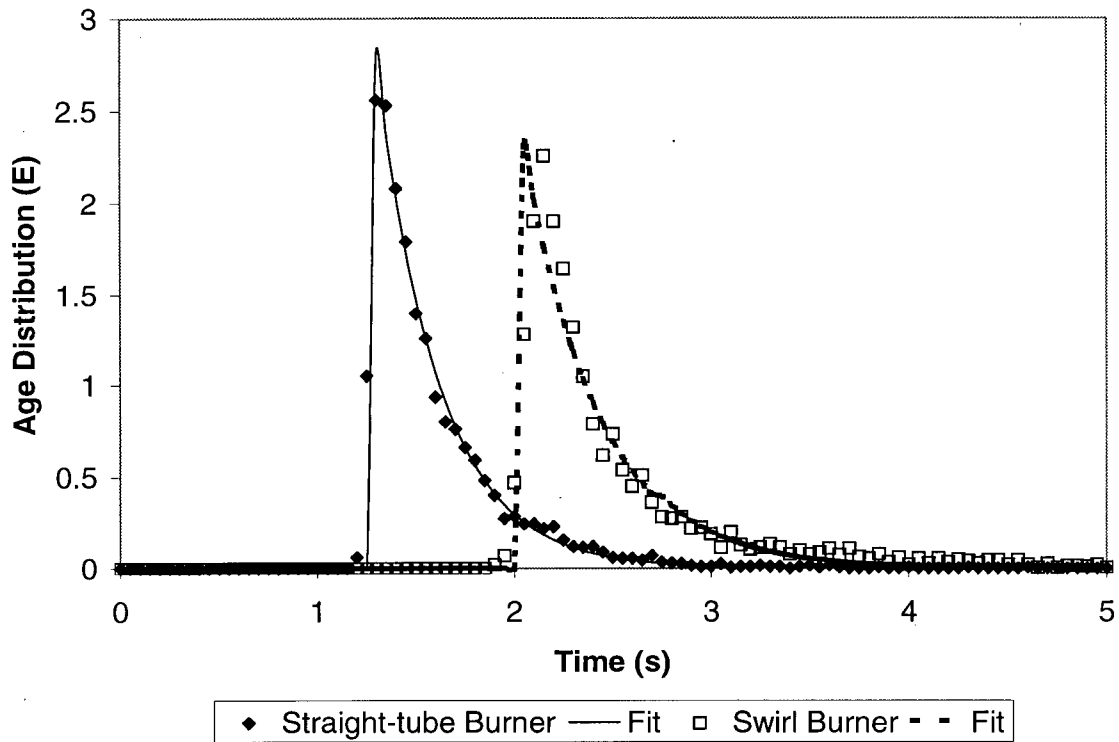
Figure 10-5: Particle Age Distribution Predicted From the CFD Model for Run 1 (Listed in Table 10-2) with the Straight-tube and Swirl burners.
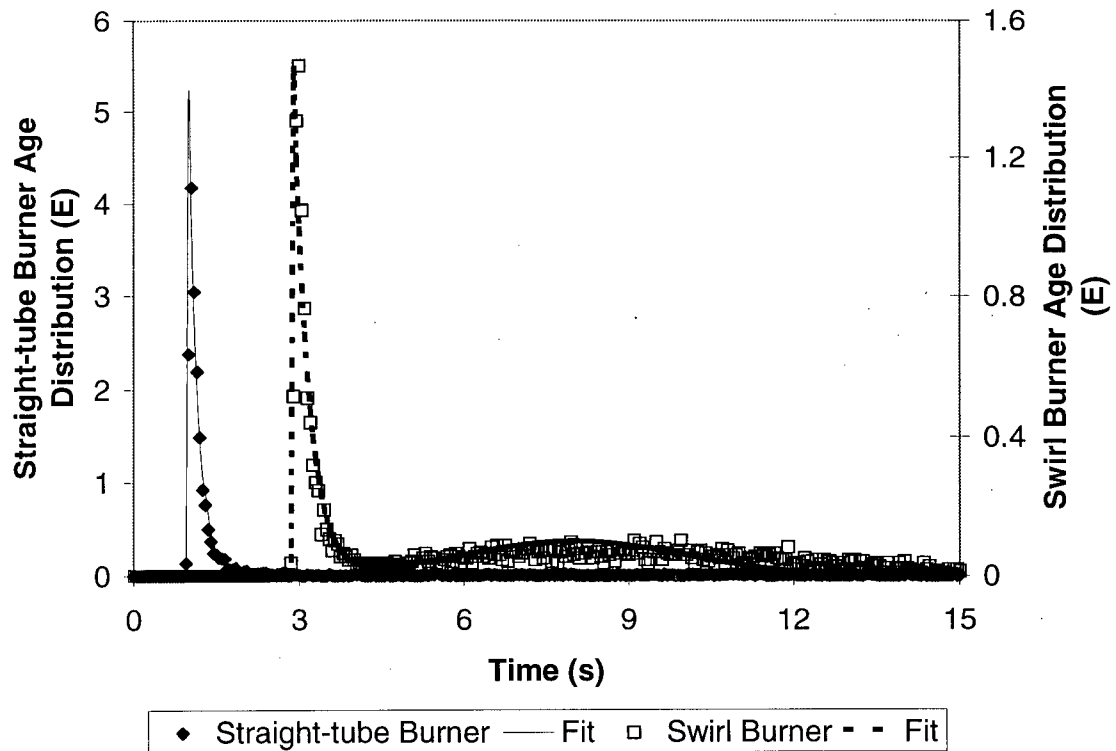
Figure 10-6: Particle Age Distribution Predicted From the CFD Model for Run 9 (Listed in Table 10-2) with the Straight-tube and Swirl Burner.

Table 10-3 lists the predicted particle average residence time and its variance, together with the time associated with the peak of the age distribution, for the runs corresponding to Figures 10-5 and 10-6.

Table 10-3: Age Distribution Characteristics for Run 1 and Run 9 Listed in Table 10-2.

Run	Mode of the Age Distribution (s)	Average Residence Time (s)	Variance (s^2)
Run 1 Straight-tube burner	1.33	1.59	0.12
Run 1 Swirl burner	2.23	2.56	0.37
Run 9 Straight-tube burner	2.27	3.53	14.6
Run 9 Swirl burner	3.15	7.39	23.8

The model suggests that the reactor does not behave as an ideal plug flow reactor, but rather can be described by a reactor consisting of plug flow, well mixed and stagnant regions, together with a recirculating mass flow rate, as shown schematically in Figure 10-7.
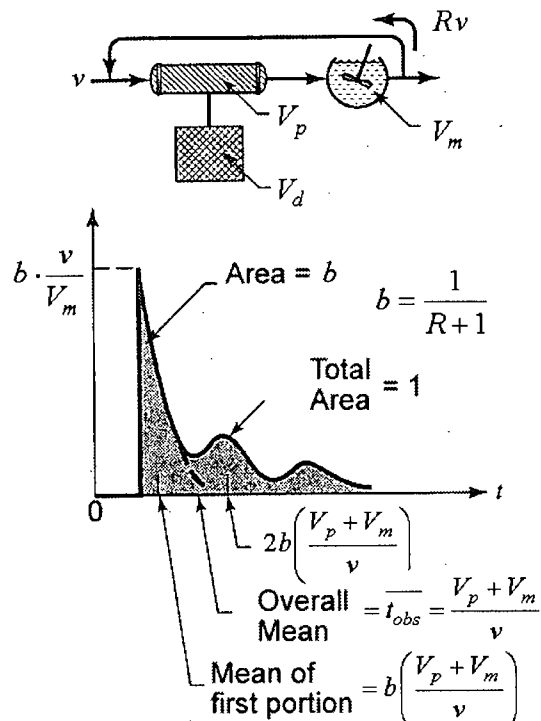
Figure 10-7: Non-ideal Flow Reactor Model[58]

226

By assuming the furnace behaved according to the non-ideal reactor model shown above, a least squares regression fit was conducted to determine the fraction of the plug flow, well-mixed and stagnant regions within the furnace, together with the reciculating mass flow. Because the model fits four parameters the absolute value of the volume fractions for each flow zone and the size of the reciruclating mass flow should not be taken literally. However the analysis is still useful as it offers a relatively simple way of describe the furnace operation in broad terms. It also allows the influence of the different burner designs on furnace operation to be easily identified.

Table 10-4 Non-ideal Flow Characteristics for the Straight-tube and Swirl Burners for Runs 1 and 9 Listed in Table 10-2.

Run	Plug Flow Volume (vol %)	Well Mixed Volume (vol %)	Stagnant Volume (vol %)	Recirculating Volumetric Flow rate (% of input flow rate)
Run 1 straight-tube burner	37.7	15.7	46.6	8.4
Run 1 swirl burner	62.8	17.6	19.6	9.4
Run 9 straight-tube	46.6	13.2	40.2	15.3
Run 9 swirl	55.9	14.7	29.4	32.6

This table shows that the stagnant volume is significantly lower for the swirl burner than for the straight-tube burner due to the increased entrainment rate of the swirling jet relative to that of the straight jet. This higher entrainent rate leads to an increased rate of velocity decay in the swirled jet, which in turn is reflected in the increased shaft residence time of the particles. Therefore the superior performance of the swirl burner appears to result from the reduction in apparent stagnant volume within the reactor which increases the particle residence time and hence increases the smelting intensity of the shaft.

The group combustion model developed in Chapter 7 assumes plug flow conditions within the reactor. The non-ideal nature of the flow affects the predicted heat transfer and combustion effectiveness factors. To gain an improved estimate of these parameters requires that the non-ideal nature of the flow be incorporated into the group combustion model.

Table 10-4 indicates that the well-mixed region of the furnace remains essentially constant at approximately 15% of the reactor volume, or 25% to 50% of the volume of the plug flow region. However, when considering small particles in combination with the swirl burner, the recirculating mass flow rate can be as high as 33% of the input flow, suggesting that it is this recirculating flow which causes the deviation from the ideal plug flow reactor model.

In the experiments presented in Chapter 8, both "once through" and "recirculated" particles are collected by the sampling technique. As a sample constituent, the recirculated particles have had a much longer residence time and so may be more completely desulfurised than other particles which have just emerged from the burner tip. As a result, the apparent desulfurisation rate based on the assumption of plug flow will be higher than the true cloud desulfurisation rate. To obtain the true heat transfer and combustion effectiveness factors requires the influence of the recirculating mass flow to be included in the group combustion model.

10.1.2.1.1 Recommended Implementation Procedure of a Recirculating Mass Flow-Rate in the Group Combustion Model

The influence of the recirculating mass flow has not yet been incorporated into the model. However, the influence of the recirculating mass must be accounted for in order to determine the true combustion effectiveness factor of the cloud.

To fully incorporate the influence of the recirculating mass flow rate into the group combustion model would require the trajectory of the particles within the recycle loop to be known. This is beyond the scope of the mathematical model. However, by applying some simplfing assumptions, the effects of mass recirculation can be estimated. These assumptions are:

1) the particles within the reactor are divided into input, reacting and recirculating streams;

2) the recirculating stream is assumed to be inert; and

3) upon recycle, the particles in the recirculating loop are assumed to join the input stream to form the reacting stream.

Assumption (2) can be justified as the recirculating stream is located in a region of the furnace where the oxygen concentration is negligble. These three assumptions reduce the problem to one of solving for the heat-up and combustion times of the reaction stream.
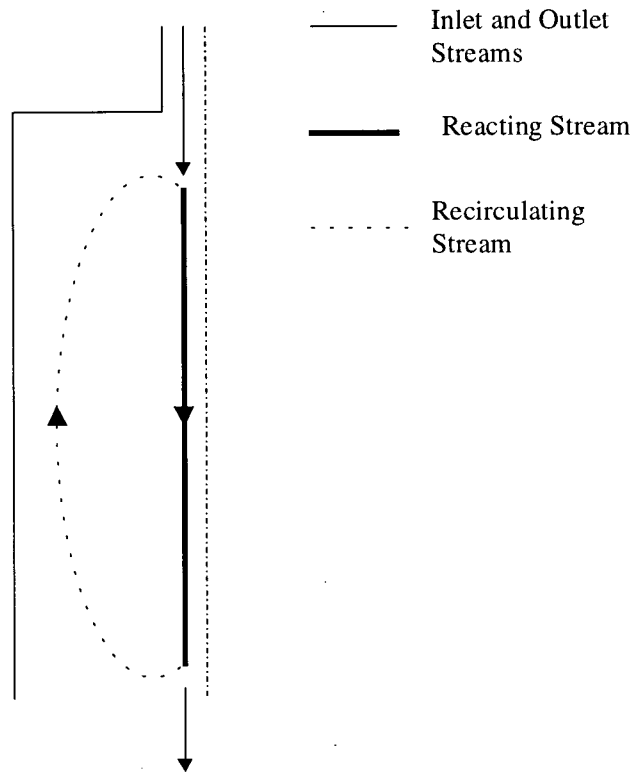
Figure 10-8: Schematic of Input, Reacting and Recirculating Streams

The recirculating stream consists of particles that may have undergone any number of recycle loops. The reacting stream can be considered to consist of a series of sub-streams, with each sub-stream representing particles that have undergone a different number of recycle loops. Simultaneously determining the heat-up and combustion histories of these sub-streams and summing over all streams allows the average cloud combustion rate to be estimated. This procedure is shown in Figure 10-9 and Equation (10-5).

230

Stream Number

| 1 | 2 | 3 | • • • | $n-1$ | n |

$m_{1,0}, T = 300$ $m_{2,0}, T = T_f$ $m_{3,0}, T = T_f$ • • • $m_{n-1,0}, T = T_f$ $m_{n,0}, T = T_f$

$m_{1,1}, T_{1,1}$ $m_{2,1}, T_{2,1}$ $m_{3,1}, T_{3,1}$ • • • $m_{n-1,1}, T_{n-1,1}$ $m_{n,1}, T_{n,1}$

Time Step

$m_{1,m}, T_{1,m}$ $m_{2,m}, T_{2,m}$ $m_{3,m}, T_{3,m}$ • • • $m_{n-1,m}, T_{n-1,m}$ $m_{n,m}, T_{n,m}$
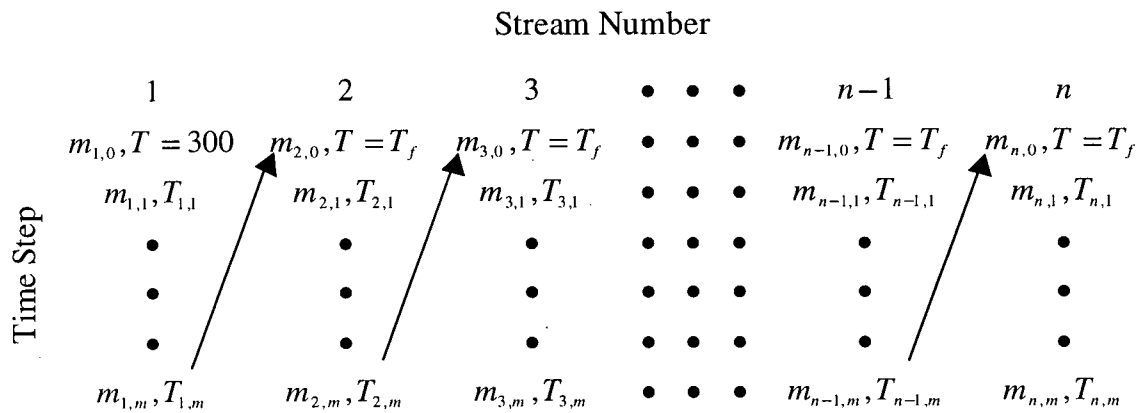
Figure 10-9: Solution Algorithm for the Recirculating Mass Flow Rate

$$m_{ave} = \frac{1}{\sum\limits_{i=1}^{i=n} r_m^{i-1}} \sum\limits_{i=1}^{i=n} m_i r_m^{i-1} \tag{10-5}$$

In Equation (10-5) r is the ratio of recirculating mass flow rate to the total flow rate, and i is the sub-stream number. Because 0<r<1, the number of particles that have undergone a large number of recycles (ie with large values of i) will be low. Therefore only a limited number of recycle loops needs to be considered.

As shown in Figure 10-9, the initial temperature and mass of the input stream (stream 1) are taken as 300K and the initial particle mass respectively. While the initial temperature and mass of the other sub-streams are taken as the ambient furnace temperature and the final mass of the previous sub-stream respectively. Because the initial mass of each sub-stream depends on the final mass of the previous sub-stream and because all sub-streams are solved simultaneously, an iterative approach is required to obtain a solution.

The technique described above provides a method of improving the estimate of the true heat transfer and combustion effectiveness factors by accounting for the recirulating flow on the observed cloud desulfurisation rate. However, to predict furnace performance using these parameters requires the recirculating mass flowrate to be known so that its influence can be incorporated into the cloud desulfurisation calculations.

On the other hand, the heat transfer and combustion effectiveness factors calculated by ignoring the recirculating mass flow rate have the influence of the recirculating mass flow rate already incorporated into their proportionality constants. This means that these effectiveness factors can be used to determine the cloud desulfurisation rate without consideration of the recirculating flow. However, they can only used if the recirculating mass flow rate does not change.

10.1.3 Combustion Effectiveness Factor

The validated CFD model can be used to provide improved estimates for the combustion and heat transfer effectiveness factors with respect to the experimentally determined relationships.

Figure 10-10 shows the combustion effectiveness factor determined from the CFD study, with the recirculation flow ignored, for both the straight-tube and swirl burners.
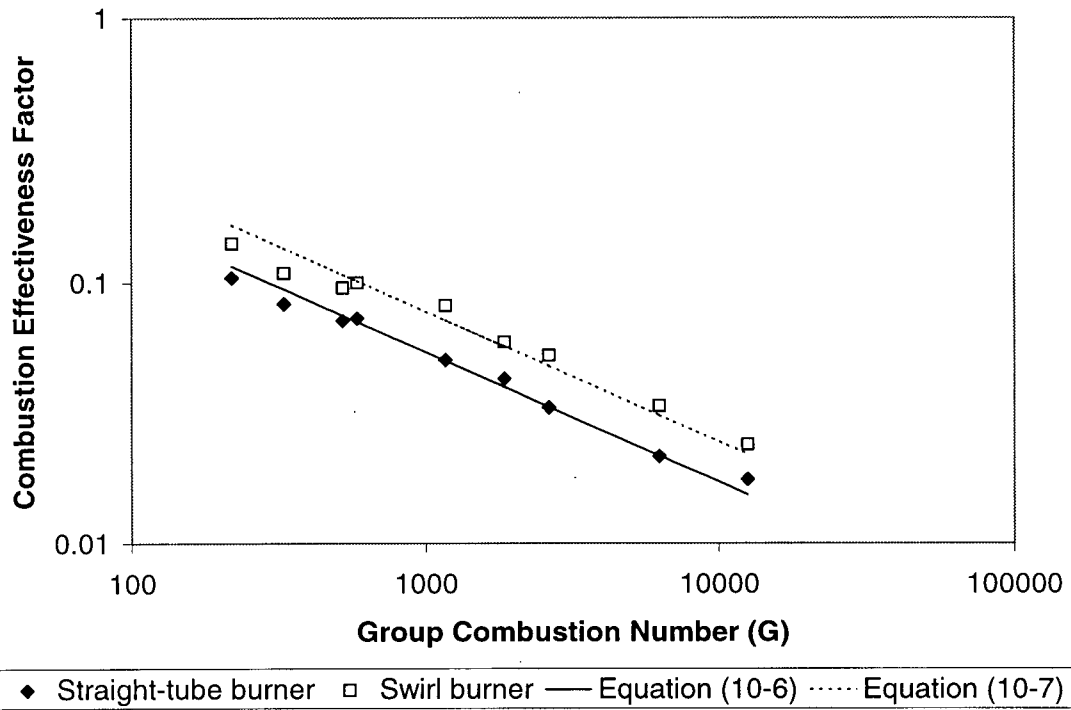
Figure 10-10: Combustion Effectiveness Factor v's Group Combustion Number Based on CFD Model Predictions

The least squares fits together with their 90% confidence intervals for the combustion effectiveness factors calculated for the straight-tube and swirl burner, respectively, are given by:

$$\eta_c = \frac{(1.80 \pm 0.08)}{G^{1/2}} \qquad (10\text{-}6)$$

$$\eta_c = \frac{(2.50 \pm 0.16)}{G^{1/2}} \qquad (10\text{-}7)$$

These fitted values can be compared to the experimentally determined values. For the straight-tube burner the ratio of the CFD-to-experimental proportionality constant is 1.25 ± 0.24 while for the swirl burner the ratio of the CFD-to-experimental

proportionality constants is 0.81 ± 0.41. The large error associated with ratio of proportionality constants for the swirl burner arises because the experimentally determined proportionality constant was only based on four runs. Hence it value had a large confidence interval.

This shows that the proportionality constant predicted from the CFD study compare reasonably well with those determined from the experimental study. However, much less scatter is present in the computational results, allowing a better fit to be obtained.

10.1.3.1 Influence of Recirculating Flow Rate

Figure 10-10 shows that for small group combustion numbers the measured combustion effectiveness factor is lower than the values predicted from Equations (10-6) and (10-7). This deviation results from the lower recirculating mass flow rate associated with small group combustion numbers. For the conditions studied here, as shown in Table 10-4, small group combustion numbers corresponding to large particle sizes and therefore reduces the recirculating mass flow rates. Lower recirculating mass flow rates imply fewer over-oxidised particles within the cloud, increasing its overall sulfur content, reducing the reaction rate and the combustion effectiveness factor predicted by the group combustion model.

Both the experimental and CFD results suggest that the exponent of the group combustion number can be taken as 0.5, with the deviation from this theoretical value resulting from the presence of a recirculating flow within the reactor and sampler bias.

However, because the cloud residence time used to determine the combustion effectiveness factor was estimated from Equation (8-2), the proportionality constant is essentially a lumped parameter that accounts for the difference between the jet velocity decay and that predicted by equation (8-9a). Hence the high proportionality constant for the swirl burner results from the higher decay rate of a swirling jet, not to an increase in the burning rate of the particles. This becomes evident when the ratio of the swirl to the straight-tube burner proportionality constants is compared to the ratio of the times associated with the peaks of the age distributions (a measure of the once-through particle residence time) for runs 1 and run 9. These ratios are shown in Table 10-5. Note that it is the ratio of the swirl to straight tube values reported in Table 10-5.

**Table 10-5: Comparison of Ratios of Combustion Effectiveness Factors
Proportionality Constants and Particle Residence Times**

Ratio of Proportionality Constants	Ratio Once-through Particle Residence Times for Run 1	Ratio Once-through Particle Residence Times for Run 9
1.39 ± 0.15	1.67	1.39

In order to calculate the true proportionality constant, the cloud residence time must be known, but this is beyond the capabilities of the group combustion model. Hence the combustion effectiveness factors in Equations (10-6) and (10-7) are semi-empirical correlations that can only be used for the burner for which they were derived.

235

10.1.4 Cloud Nusselt Number

A plot of cloud Nusselt number against the cloud Rayleigh number is given in Figure 10-11. It shows that the difference between the straight-tube and swirl burner heat transfer is statistically insignificant.
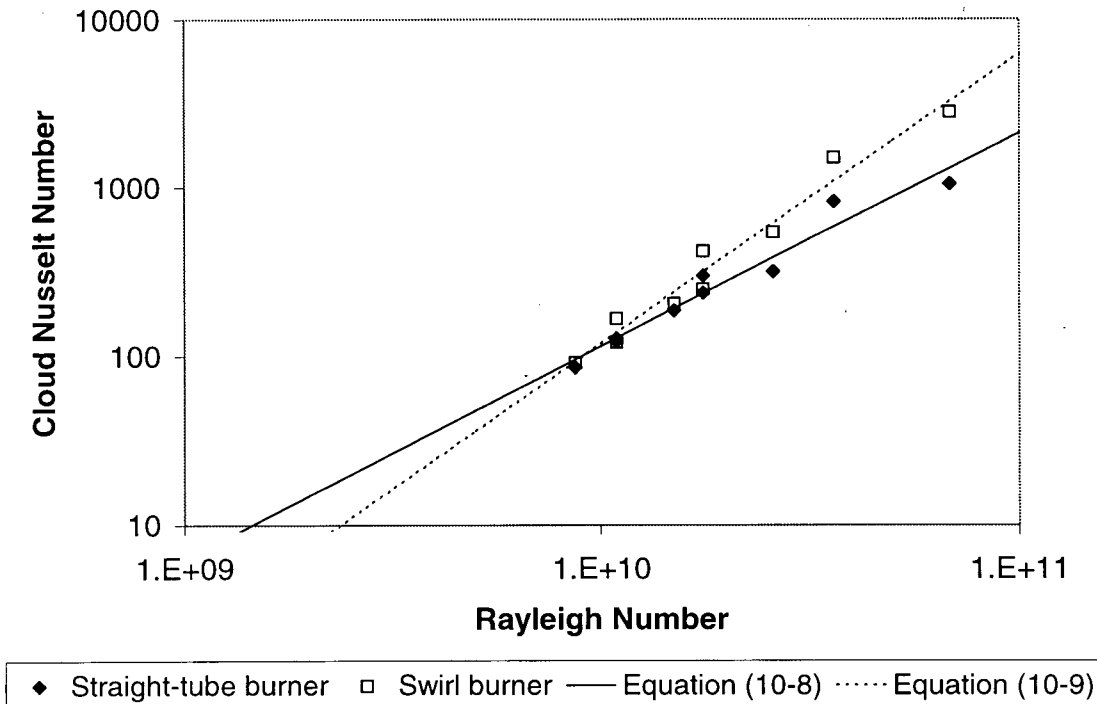
Figure 10-11: Cloud Nusselt Number v's Cloud Rayleigh Number Based on CFD Predictions

The least squares regression fit for the above data together with their 90% confidence intervals, are:

Bluff-body burner:

$$Nu_{cl} = \exp\left(-23.8 \pm 3.2\right) Ra^{1.26 \pm 0.26} \qquad (10\text{-}8)$$

Swirl burner:

$$Nu_{cl} = \exp(-23.3 \pm 4.5) Ra^{1.71 \pm 0.28} \tag{10-9}$$

Recalling from Chapter 3 and Chapter 8 that the cloud Nusselt number describes the rate of heat transfer through the separated boundary layer between the jet issuing from the burner and the surroundings. Hence its characteristic length is based on the burner diameter. With respect to the Rayleigh number the characteristic length is the shaft length and the density is taken as the effective mixture density, which assumes the particle and gas phases to be a single phase (See equations (8-9a) and (8-9b) and Appendix A3).

It is worth noting that while there is significant difference in the data at a 90% confidence interval, the difference becomes insignificant at a 95% confidence interval.

10.1.5 Scatter in Computational Results

Because of the reduced scatter present within the computational results, an improved regression fit has been determined for both the combustion effectiveness factor and cloud Nusselt number with respect to the experimentally determined relationships given in Chapter 8. However, some scatter still exists due to the finite sample size of the discrete phase and the difficulty in obtaining a converged solution.

The scatter caused by the finite sample size results from the turbulent nature of the flow. Because of turbulent dispersion, particles at the same location within the furnace have different trajectory histories, resulting in different degrees of desulfurisation

for different particles. Hence a large number of particle trajectories were required to adequately represent the true particle desulfurisation distribution. For this study 5000 trajectories were calculated. Sampling theory[153] shows that 5000 particle trajectories gives a maximum error between the predicted and true gas phase source terms, that arise due to the presence of the dispersed phase, of ± 5%. While this is acceptable some scatter in the computational results was introduced by this finite sample size.

A second reason for the scatter is due to the difficulty in obtaining a converged solution. Because of the high solids mass loading, the discrete phase source terms added to the continuous phase equations were heavily under-relaxed. As a result the gas phase equations tended to converge to a partially converged discrete phase solution. While every effort was made to ensure that the discrete phase equations had converged to the final solution, it is possible that the discrete phase equations had not completely converged, producing some of the observed scatter.

10.2 Industrial Burner Design

A study was conducted to compare the performance of an industrial scale swirl burner to a bluff-body burner, with the aim of suggesting an improved burner design. The bluff-body burner approximates the burner design used by industrial flash furnaces. However, it is important to note that the are some significant differences between the bluff body burner modelled here and the burner design used in industrial flash furnaces:

1) The distribution cone has not been modelled and has been set level with the shaft roof. For concentrate burners the distribution cone extends into the shaft

(as shown in Figure 4-4). This may cause signficant differences in the calculated flow field close to the burner tip; and

2) The distribution air has not been modelled.

These two factors may cause significant differences in the calculated flow, species and temperature fields close to the burner tip. Hence the bluff-body style burner modelled here should not be considered fully equivalent to the typical concentrate burner used in industry. However, useful insight into the performance characteristics of different burner types can still be inferred from the current study.

Also As shown by Sato et al [74] and Shook et al,[37] the flow within the reaction shaft of an industrial furnace is inherently three-dimensional and transient. Therefore, to accurately predict its performance requires a large, complex model. However, because the aim of this study was not to determine the detailed operation of an industrial reaction shaft, but rather to compare the performance of different burner types under well-defined conditions, a two dimensional, axisymmetric, steady-state model was developed.

As with the reactor study, combustion and heat transfer effectiveness factors were determined, and the model output was investigated to gain insight into the important phenomena occurring within the shaft. Using the combustion effectiveness factor and cloud Nusselt number, the stable operating region of the furnace was calculated for both burner designs.

This model is based on, and incorporates the same physical sub-models turbulence intensity, turbulent Prandtl number and particle integral time scale constant as the UBC flash reactor model. The values used for the turbulence intensity, turbulent

239

Prandtl number and particle integral time constant have not been validated for an industrial furnace, and therefore their applicability is discussed below.

Industrial flash smelting burners are usually fed via a windbox[1,37,154] which, in order to achieve a uniform flow to the burner, is generally designed to produce a flow inside the windbox that has strong streamline curvature and high shear stresses. As a result, the turbulence intensity of the inlet flow to an industrial burner is expected to be higher than that for the UBC flash reactor. As shown in Figures 9-5 and 9-6, the influence of the assumed turbulence intensity on the predicted velocity field for the UBC flash reactor is negligible. If this is true for an industrial furnace, then an assumed turbulence intensity of 30% should be adequate to predict the furnace flow field.

Model results for the turbulence field within the furnace shows that the turbulent Peclet number and particle Stokes number vary from 100 to 100000 and 20 to 200, respectively. These values are similar to those present within the UBC flash reactor. Therefore the values for the turbulent Prandtl number and particle integral time scale constant should be adequate to give reliable predictions for the furnace temperature and discrete phase concentration fields.

Because the model has not been validated, caution should be exercised when using its results to infer the performance of different burner types. However, as shown above the assumed values for the turbulence intensity, turbulent Prandtl number and particle integral time scale constant should give satisfactory results.

10.2.1 Burner and Shaft Designs

The shaft geometry is based on the San Manuel furnace, which has a diameter of 6.5 m and a length of 7 m. The swirl burner is based on the design discussed in Section 4.2.2; the bluff body burner is similar to the San Manuel burner used by Adams et al[36]. However as mentioned caution should be used when attempting to compare model results to the actual burner design. The model boundary conditions are shown below in Figure 10-12 and are identical to those used for the UBC reactor model (See Section 9.2.1).
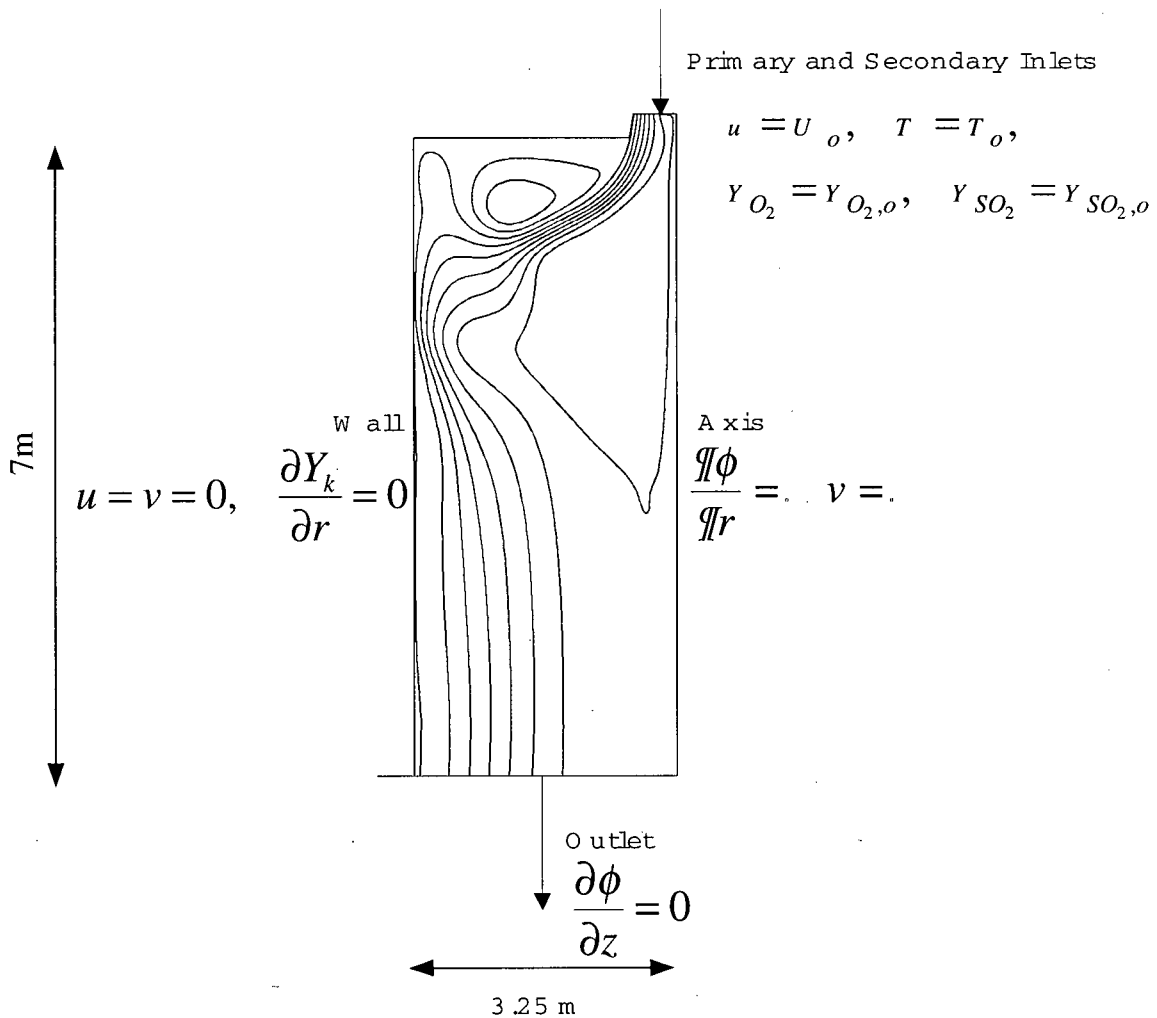
Figure 10-12: Industrial Shaft CFD Model Geometry and Boundary Conditions

The swirl burner used in these calculations is shown in Figure 4-7 while the bluff-body burner is shown in Figure 10-13.
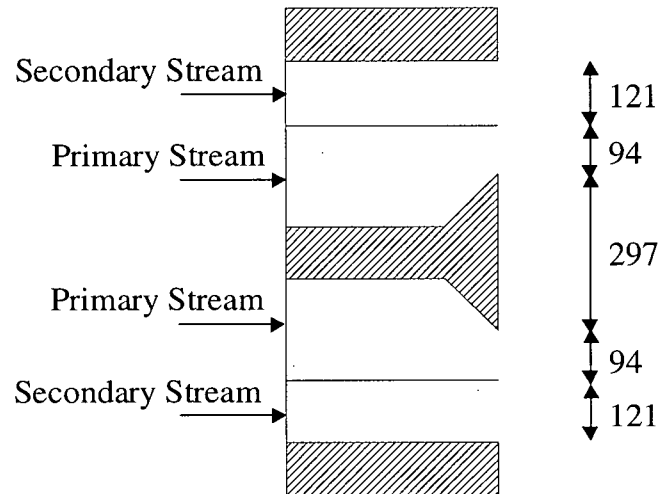
Figure 10-13: Bluff-body Burner Dimensions (All Dimensions in mm)

Both burners had a primary and secondary air stream, and it was assumed that 20% of the gas flow was associated with the primary air stream in each case. For the bluff-body burner the primary air velocity was set to 20% of the secondary air gas velocity, while for the swirl burner the primary air velocity was set to 60% of the secondary air velocity. For the bluff-body burner a primary air velocity of 20% of the secondary air velocity was used as this is typical of industrial practice[3,154], whereas a value of 60% was used for the swirl burner as this is a design value suggested by Basu et al[75].

For the swirl burner, the tangential velocity of both the primary and secondary streams was taken to be equal to the axial velocity of each stream, respectively. This essentially assumes that the swirl vanes were set to an angle of 45°, which is slightly

242

higher than that the 25° to 35° suggested by Basu et al[75]. However an angle of 45° was used as it corresponds to the swirl vane angle used in the experimental and CFD studies of the UBC flash reactor. For the bluff body burner the primary stream was assumed to have a radial velocity component equal to its axial velocity, essentially assuming that the dispersion cone (which was not explicitly modelled) had a vertical half angle of 45°. This value was chosen arbitrarily. However, the study conducted by Adams et al[36] suggests that the inlet conditions of the primary stream have little effect on the global features of the flow field.

This was a scoping study aimed at determining the advantages of replacing the existing bluff-body burner used by industrial flash smelters with a swirl burner, with the objective being to investigate the global influence of the different burner types on shaft operation. Hence the burner inlet conditions were set arbitrarily. Before a final design can be determined, further CFD studies should be conducted to investigate the sensitivity of the flow features close to the burner tip to the assumed burner inlet conditions. This would allow the optimum burner design to be suggested. Plant trials should then be conducted to examine the accuracy of the CFD predictions and recommend changes to the proposed design.

10.2.2 Run Matrix

Five runs were conducted for both burner designs, with the conditions of each run listed in Table 10-6. These runs covered the range of Escondida loadings capable of being treated by the San Manuel furnace at an aim matte production rate of 110 tph and

an aim matte grade of 63 wt%. For all runs the particles were assumed to be spherical with a uniform diameter of 30 μm.

Table 10-6: Industrial Burner CFD Runs

Escondida Loading	Concentrate Feed rate (tph)	Oxygen Flow rate (tph)	Oxygen Enrichment (vol %)	Group Combustion Number	Exit Velocity for Bluff-body Burner (m/s))	Exit Velocity for Swirl Burner (m/s)
0	200	0.285	47	32539	80	34.1
0.1	192	0.265	53	39119	64.3	27.4
0.2	184	0.246	61	48386	49.8	21.2
0.3	177	0.227	73	63534	36.5	15.5
0.4	171	0.207	98	93523	23.9	10.2

Table 10-6 shows that the exit velocity of the bluff-body burner is 2.34 times greater than for the swirl burner. These velocities were chosen because a value of 80 m/s is typical for the bluff-body burner used by most flash smelting furnaces, while a value of 20 m/s was suggested by Basu et al[75] as the design velocity of a swirl burner.

10.2.3 Combustion Effectiveness Factor

Figure 10-14 shows the combustion effectiveness factors, while Equations (10-10) and (10-11) are the least squares regression fits for the bluff-body and swirl burner, respectively.
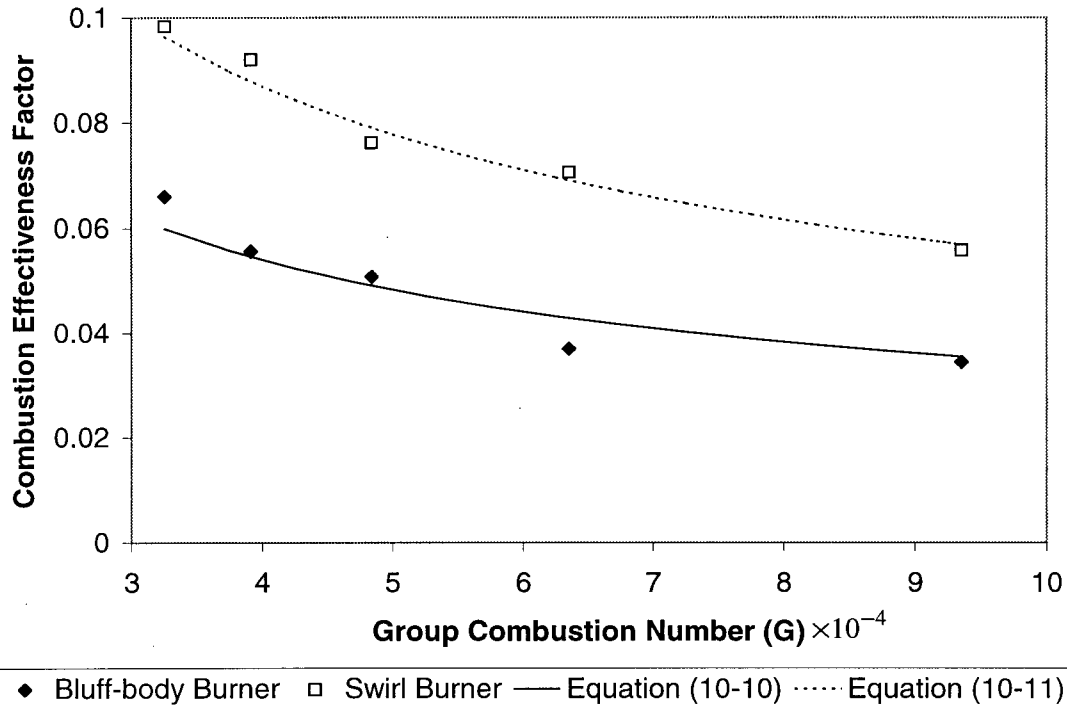
Figure 10-14: Combustion Effectiveness Factor Determined for the Industrial Scale Burners Based on CFD Predictions

Bluff-body burner:

$$\eta_c = \frac{(1.37 \pm 0.10)}{G^{1/2}}$$

(10-10)

Swirl burner:

$$\eta_c = \frac{(2.27 \pm 0.15)}{G^{1/2}}$$

(10-11)

These equations show that the combustion effectiveness factor for the swirl burner is higher than that of the bluff-body burner. As for the UBC reactor, this difference is not caused by enhanced combustion, but rather by the increased rate of velocity decay of a swirling jet. The proportionality constants are essentially lumped

parameters, and therefore the relationships determined here are only valid for the given burner designs. While this lack of generality restricts the application of the results to an individual furnace, it is still possible to use them to gain insight into the performance of industrial burners.

10.2.4 Cloud Nusselt Number

Figure 10-15 shows the relationship between the cloud Nusselt and Reynolds numbers. Recall that the characteristic length for the cloud Nusselt number is the burner diameter. In this figure the cloud Reynolds number is given by Equation (8-29). It uses the burner exit velocity as the characteristic velocity, burner diameter as the characteristic length and the effective mixture density (Equation (8-9a)) as the characteristic density. This definition of the density includes the influence of the solid particles.
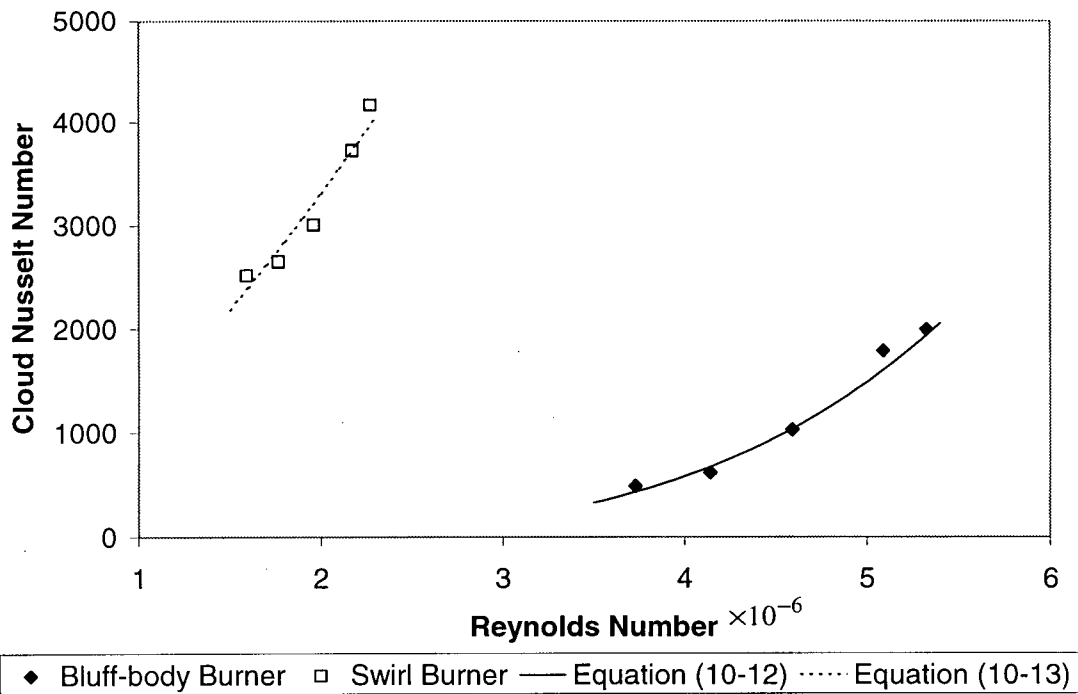
Figure 10-15: Cloud Nusselt Number for the Industrial Burners Based on CFD Predictions

246

The relationship between the cloud Nusselt and Reynolds numbers for the two burner types can be fitted by:

Bluff-body burner:

$$Nu_{cl} = 3 \times 10^{-6} \, Re_{cl}^{1.4} \tag{10-12}$$

Swirl burner:

$$Nu_{cl} = 5 \times 10^{-26} \, Re_{cl}^{4.2} \tag{10-13}$$

Note that in Equations (10-12) and (10-13) the influence of the Prandtl number has been ignored with its influence being accounted for in the proportionality constant. This is justifiable because the Prandtl number is typically close to unity and usually raised to the 1/3 power.

Because Equations (10-12) and (10-13) are based on data from only five runs, with the Reynolds number varying over a narrow range (less than one order of magnitude), the applicability of the correlations outside this range is unknown. However, Figure 10-15 clearly show that, for the conditions studied here, the swirl burner has heat transfer characteristics superior to those of the bluff-body burner.

Of some concern is the exponent in Equation (10-13) which is higher than any reference value found for the heat transfer between a separated flow and its surroundings, casting doubt on its validity. However, two factors suggest that the exponent may be reasonable.

247

Firstly, a similar relationship is implied from the work of Ricou and Spalding[151] on the entrainment and recirculating mass flow rate of an enclosed jet. They showed that the entrainment and recirculating mass flow rate (and therefore the rate of heat transfer) decreased as the total mass flow rate to the furnace decreased and the jet density increased relative to that of the surroundings. Applying these findings to the current study, as Escondida concentrate is added to the blend, the total mass flow to the furnace decreases and the cloud density increases. Both of these contribute to the decrease in the heat transfer to the cloud.

Secondly, none of the studies on the heat transfer between a separated flow and its surroundings included a second phase. Dirix and Van der Wiele[51] studied the mass transfer from a two phase plunging jet and showed that the mass transfer coefficient was proportional to the square of the jet velocity. If similarity is assumed to exist between the heat and mass transfer phenomena, then the exponent is again higher than expected. This suggests that the presence of a second phase affects the heat transfer to a separated flow. Further work is required to determine the heat transfer relationship between a particle-laden jet and its surroundings.

10.2.5 Furnace Analysis

Figures 10-16 to 10-19 show the predicted flow, temperature, discrete phase concentration and burning rate fields for Runs 1 and 5. Table 10-7 shows the important flow conditions and model parameters used to determine the predictions for Runs 1 and 5.

Table 10-7: Flow Conditions and Model Parameters Used to Generate Model Predictions for Runs 1 and 5 in Table 10-5

Parameter	Run 1	Run 5
Bluff-body burner superficial exit velocity (m/s)	80	23.9
Swirl burner superficial exit velocity (m/s)	34.1	10.2
Inlet temperature (°C)	25	25
Furnace wall temperature (°C)	1400	1400
Inlet flow turbulence intensity (-)	30	30
Turbulent Prandtl number (-)	0.65	0.65
Particle diameter (μm)	30	30
Inlet flow oxygen partial pressure (atm)	0.47	0.98
Inlet flow oxygen-to-concentrate ratio (-)	0.285	0.207
Particle integral time scale constant (-)	0.05	0.05

10.2.5.1 Furnace Flow Field

a) Bluff-body burner
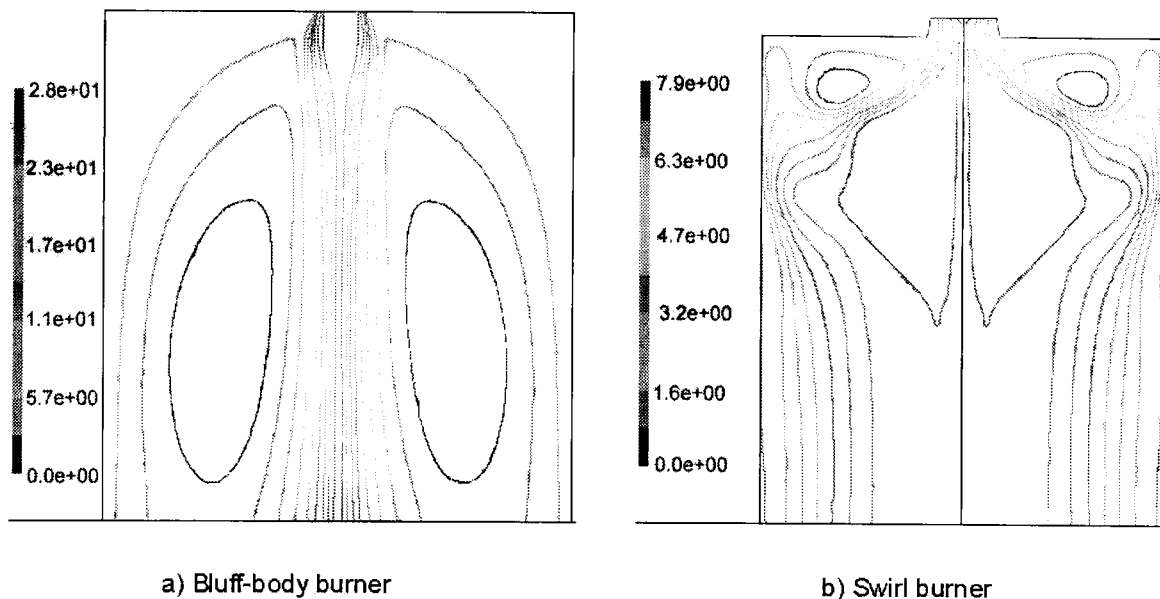
b) Swirl burner

Figure 10-16: Furnace Stream Function (kg/s) for Runs 1 and 5 in Table 10-7.

Figure 10-16 shows that an external recirculation zone is formed by the bluff-body burner, while the swirl burner produces an internal recirculation zone. As discussed below, it is the formation of this internal recirculation zone and its influence on the

249

temperature and dispersed phase concentration field that produces the superior performance of the swirl burner.

10.2.5.2 Furnace Temperature Field

a) Bluff-body burner

b) Swirl burner
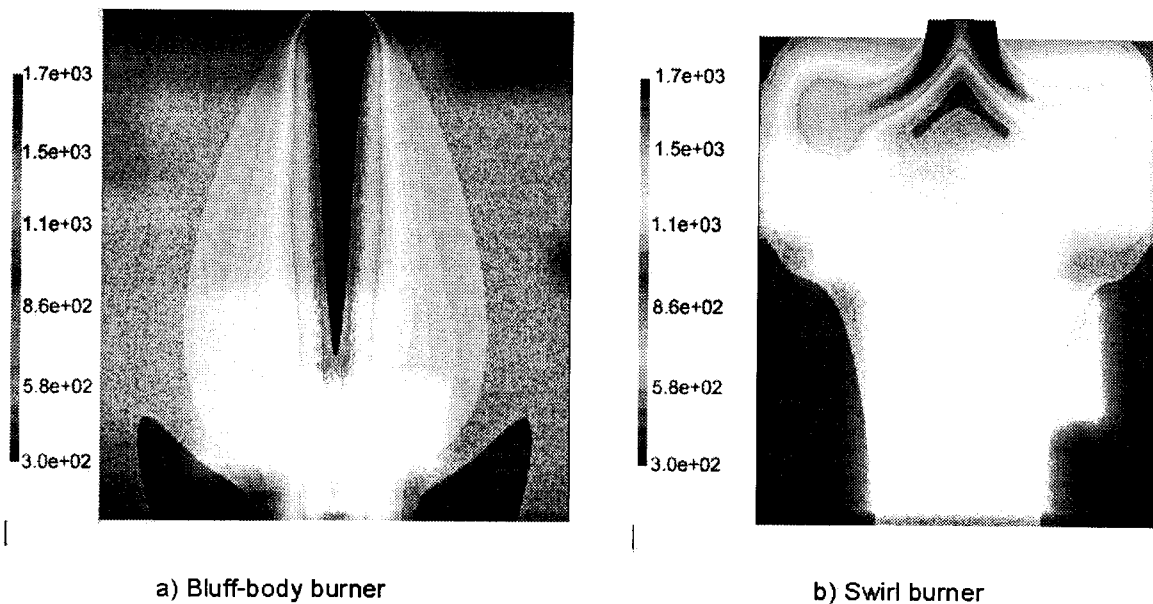
Figure 10-17: Furnace Temperature Field (K) for Runs 1 and 5 in Table 10-7.

Figure 10-17 shows the temperature field within the furnace and shows that a cold stream extends down the furnace centerline for the bluff-body burner. On the other hand, for the swirl burner, the inlet stream is divided into streams (in the 2D representation) with a hot zone forming in the internal recirculation zone. The formation of the hot zone within the internal recirculation zone increases the rate of heat transfer to the cold cloud, thereby improving the heat transfer characteristics of the swirl burner.

a) Bluff-body burner   b) Swirl burner
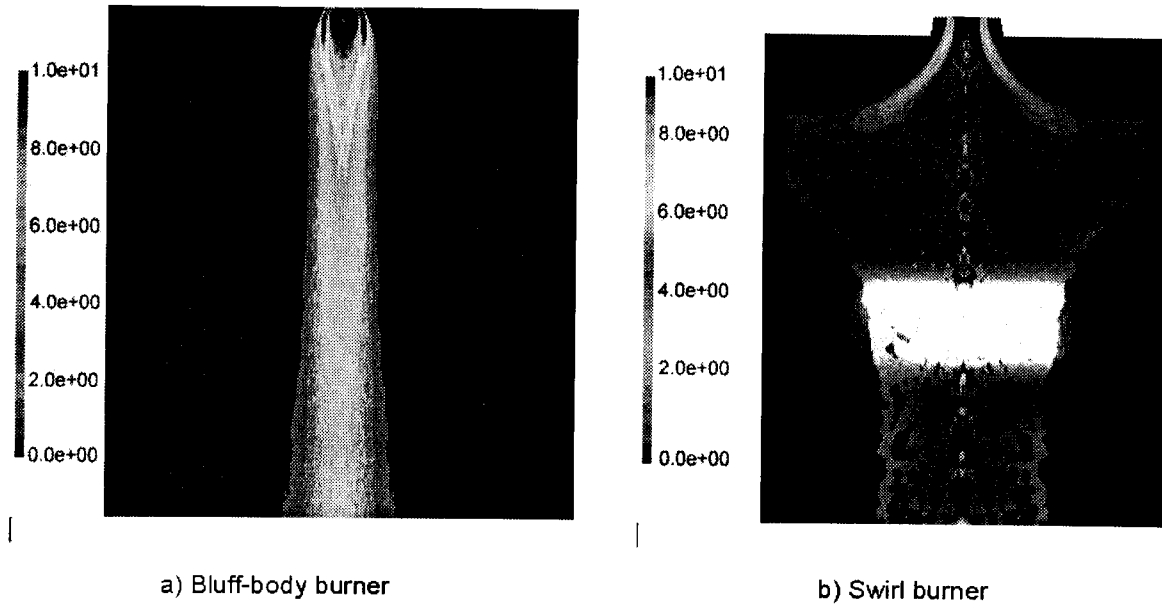
Figure 10-18: Furnace Discrete Phase Concentration Field (kg/m³) for Runs 1 and 5 in Table 10-7.

Figure 10-18 displays the discrete phase concentration and shows that the bluff-body burner produces a dense stream along the furnace centerline, whereas the swirl burner ejects the discrete phase radially outward, improving its distribution within the shaft. As discussed in Section 10.2.6, this increases the particle residence time within the shaft, aiding in improving the performance of the swirl burner.

a) Bluff-body burner   b) Swirl burner
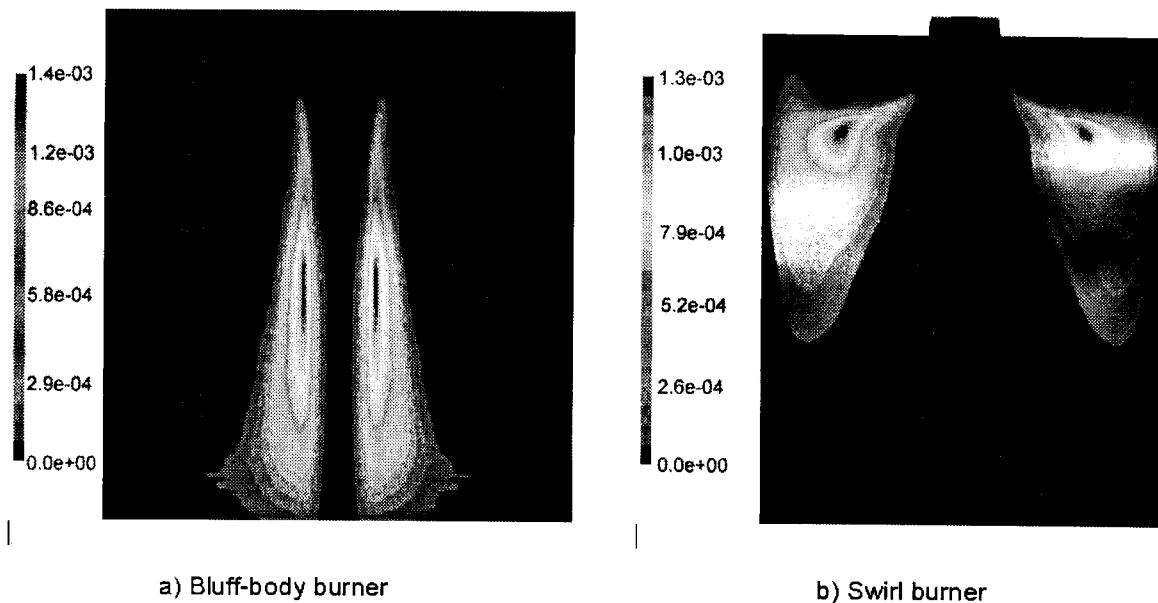
Figure 10-19: Discrete Phase Burning Rate (kg/s) for Runs 1 and 5 in Table 10-7.

Figure 10-19 portrays the predicted burning rate field and shows that, for the swirl burner, burning is complete high in the shaft, while the burning zone extends far downward along the shaft for the bluff-body burner.

10.2.6 Particle Age Distribution

Inspection of the age distribution of the particles within the shaft provides insight into some of the major flow features within the furnace. However, because the flow in an industrial furnace is transient and three-dimensional, some features cannot be captured by the model. Figures 10-20 and 10-21 show the exit age distribution of the particles for both burners for runs 1 and 5 respectively. Fitted non-ideal particle age distributions are shown in Figure 10-20 and 10-21 in conjunction with the CFD model predictions. The values for the plug flow, well-mixed and stagnant regions used to generate the fitted age distributions appear in Table 10-9.
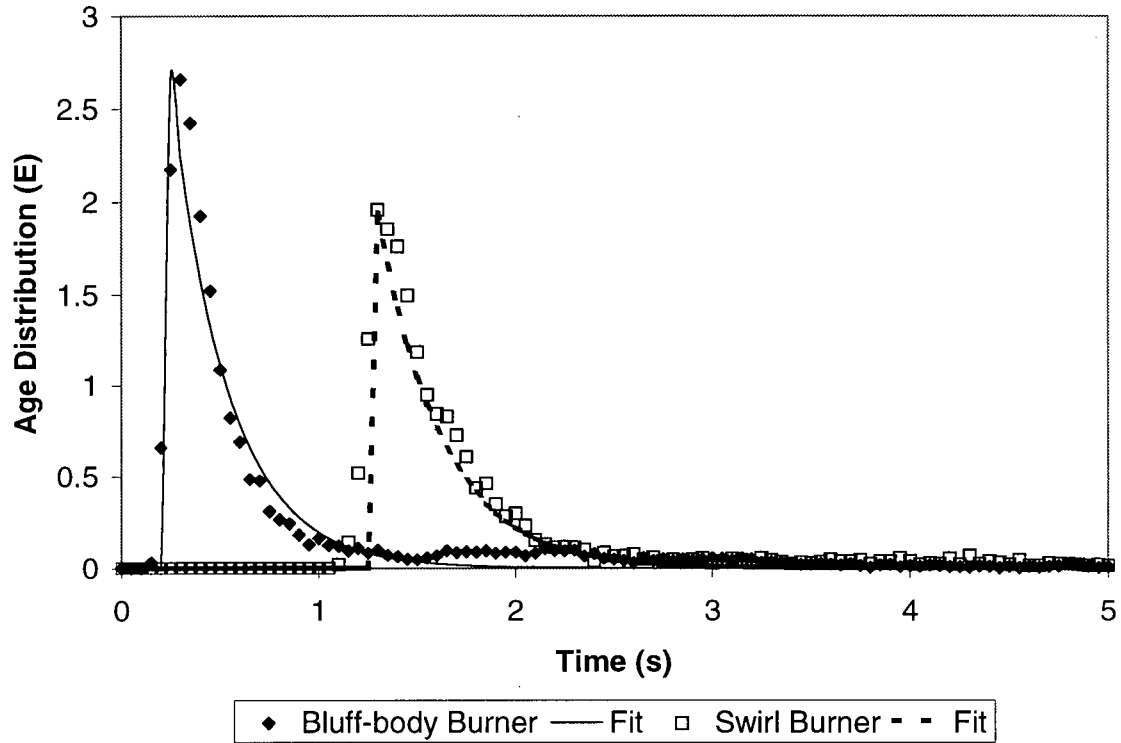
Figure 10-20: Predicted Particle Age Distribution from CFD Model for Run 1 (Listed in Table 10-7) with Bluff-body and Swirl Burners.
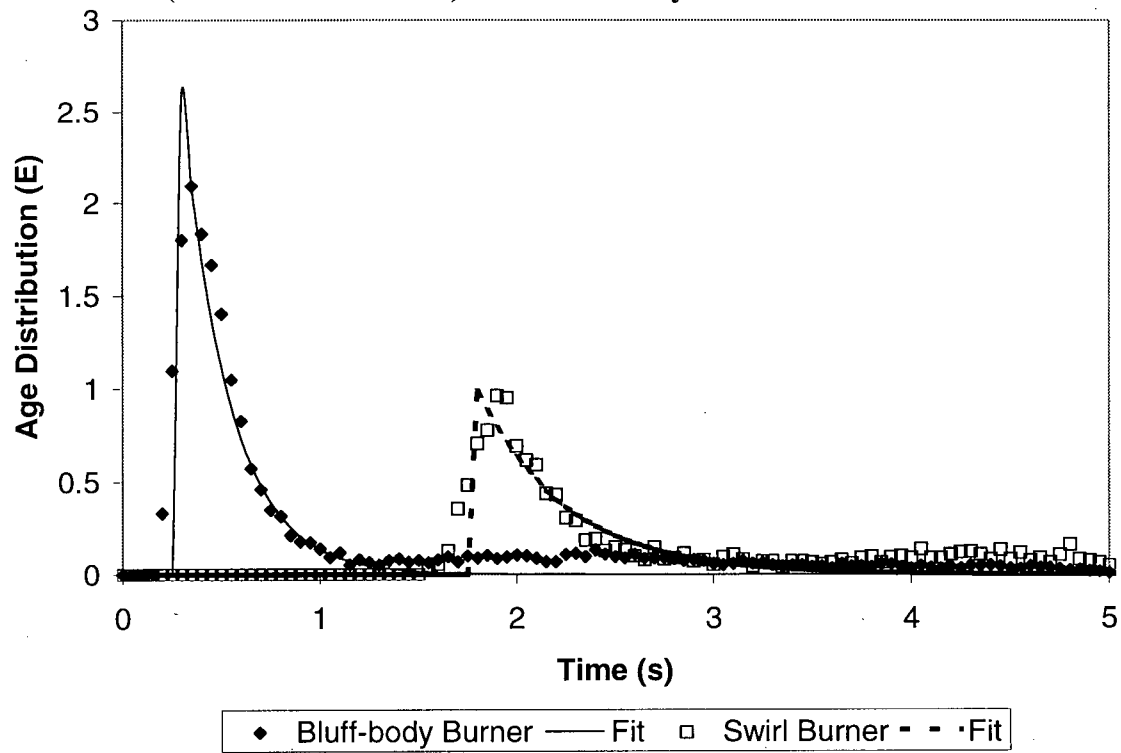
Figure 10-21: Predicted Particle Age Distribution from CFD Model for Run 5 (Listed in Table 10-7) with Bluff-body and Swirl Burners.

Table 10-8 shows the particles average residence time and its variance, together with the time associated with the peak in the age distribution.

Table 10-8: Age Distribution Characteristics for the Bluff-body and Swirl Burners for Runs 1 and 5 Listed in Table 10-7.

| Run	Mode of Age Distribution (s)	Average Residence Time (s)	Variance (s^2)
Run 1 Bluff-body burner	0.33	0.78	0.59
Run 1 Swirl burner	1.35	1.97	3.59
Run 5 Bluff-body burner	0.38	1.12	1.72
Run 5 Swirl burner	1.93	4.73	28.8

As with the UBC reactor, the flash furnace can be considered as having plug flow, well-mixed and stagnant regions together with a recirculating mass flow rate. The size of each of these regions was determined by conducting a least squares regression fit, assuming that the furnace behaved according to the non-ideal flow model described by Figure (10-7). Again, because four parameters are fitted, the absolute value of each of the volume fractions cannot be taken literally. However, the results highlight the influence of the different burner designs on the global operation of the furnace.

Table 10-9 shows the fraction of the shaft volume associated with each of these mixing regions and the recirculating mass flow rate.

Table 10-9: Non-ideal Flow Characteristics for the Bluff-body and Swirl Burners for Runs 1 and Runs 5 (See Table 10-7 for Details)

Run	Plug Flow Volume (vol%)	Well Mixed Volume (vol%)	Stagnant Volume (vol%)	Recirculating Volumetric Flow rate (% of input flow rate)
Bluff-body burner run 1	8.6	16.7	74.7	12.5
Bluff-body burner run 5	3.5	15.6	80.7	19.0
Swirl burner run 1	22.0	18.3	59.7	16.3
Swirl burner run 5	20.1	16.5	63.3	19.0

A number of inferences may be drawn from the results presented in Table 10-9:

1) The volume of the well-mixed region remains relatively constant over the range of conditions considered;

2) The volume of the plug flow region is higher for the swirl burner than for the bluff-body burner, with this increase being at the expense of the stagnant volume. The reduction of the stagnant volume increases the particle residence time within the furnace, resulting in improved performance of the swirl burner.

3) The plug flow volume is lower for Run 5 than for Run 1 due to the lower gas velocity associated with run 5. This reduces the momentum flow rate to the furnace, lowering the driving force for the flow, and resulting in the observed increase in the volume of the stagnant region. For the swirl burner, this effect can be offset to some degree by increasing the swirl intensity of the inlet flow.

4) The stagnant volume of the furnace is large, suggesting that the burner design can be further improved to increase the working volume of the shaft. Therefore further work is required to develop the optimum shaft/burner arrangement.

Taken together, Figures 10-16 to 10-19 and Table 10-9 show that the improved performance of the swirl burner relative to the bluff-body burner is due to its better heat transfer characteristics. This enhances ignition, and its ability to disperse the particles radially, thereby increasing the particle residence time within the shaft.

10.2.7 Furnace Stability Diagram

Based on the relationships developed for the combustion effectiveness factor and the cloud Nusselt number, a furnace stability diagram, similar to Figure 8-11 has been developed and is shown in Figure 10-22. It is worth recalling that the Shaft Smelting Index used to describe the furnace/shaft performance is given by $\left(\dfrac{d_p}{L}\right)\left(\dfrac{\eta}{\sigma}\right)^{3/2}$, where d_p is the particle diameter, L is the shaft length, η is the oxygen-to-concentrate ratio and σ is the oxygen enrichment. For the conditions of this study, Table 10-5 shows that the Shaft Smelting Index varies from 0.4 to 2×10^{-6}.

Because of the empirical nature of the combustion effectiveness factor and cloud Nusselt number, this diagram is only valid for the furnace geometry and burners investigated in this project. However, the general shape and relative size of the operating windows should allow the performance of different burners to be compared.
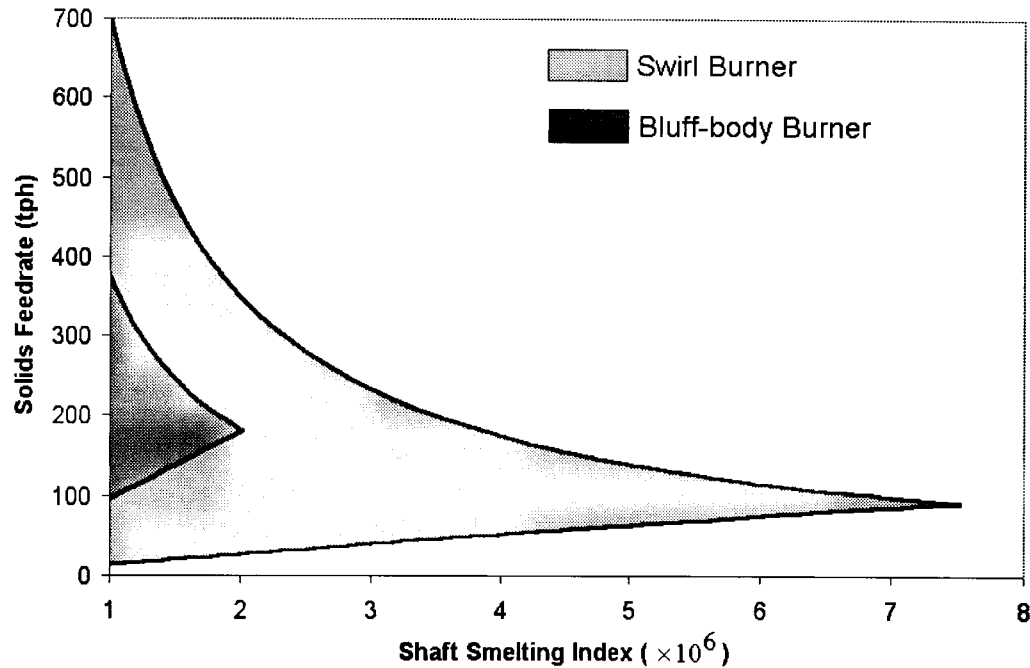
Figure 10-22: Burner Stability Diagram for the Bluff-body and Swirl Burners Based on CFD Predictions

This diagram clearly shows that the swirl burner offers a superior stability envelope compared to the bluff-body burner, as it is capable of smelting both higher and lower solids feedrates for any given shaft smelting index. The superior performance at the high solids feedrates results from the influence of the swirl burners on the particle residence time within the shaft. As Section 8.2.5 shows, the upper limit for the solids feedrate is determined by the particle residence time. Figures 10-20 and 10-21 indicate that the swirl burner increases the particle residence time, therefore allowing higher solids feedrates to be treated. At lower solids feedrates the superior performance of the swirl burner is due to its better heat transfer charactersitics. Again, from Section 8.2.5 the lower limit of the solids feedrate results from the low heat transfer rate to the cloud. The

swirl burner is capable of treating lower solids feed rates due to its improved heat transfer at low gas velocities.

The superior performance of the swirl burner promises greater operational flexibility which, as discussed in Section 8.2.5, should permit larger quantities of high-grade concentrate to be treated for a given matte grade and production rate as compared to the bluff-body burner.

Because the bluff-body burner modelled here is not an exact replica of the concentrate burner used in industry, plant trials should be conducted to confirm these findings and to determine the optimum burner design for the treatment of high-grade concentrates.

10.3 Chapter Summary

Results from the CFD study have provided useful insights into the performance of the UBC flash reactor and of two industrial burner designs.

With respect to the UBC flash reactor the CFD study:

1) Has provided improved estimates of the combustion effectiveness factors and cloud Nusselt number;

2) Has shown that natural convection dominates the flow patterns within the furnace; and

3) Has shown that the superior performance of the swirl burner is due to its influence on the particle residence time within the shaft.

The CFD study of the different burner designs has shown that the swirl burner has a wider operating window than the bluff-body burner investigated, thereby improving the operational flexibility and allowing blends with higher Escondida loadings to be treated. This superior performance results from increased particle residence time within the shaft and improved heat transfer between the cloud and its surroundings.

11 Conclusions

The aim of this project was to develop fundamental understanding of the problems associated with the flash smelting of high-grade concentrate with the ultimate goal being to suggest operational improvements to maximise the throughput of Escondida concentrate in industrial flash smelters. To achieve this goal required the results from the experimental and CFD studies to be analysed using group combustion theory. Key findings are as follows.

Sulfide flash smelting can be described using group combustion theory, which allows the reaction time of the particles to be estimated as a function of furnace operating conditions by accounting for interaction effects during particle heat-up and combustion. Equating the particle reaction time to the shaft residence time showed that the shaft smelting index, $\left(\dfrac{d_p}{L}\right)\left(\dfrac{\eta}{\sigma}\right)^{3/2}$, is an important quantity in describing the operating window of both the UBC flash reactor and an industrial flash smelter. This quantity leads to several insights into the operation of both the UBC flash reactor and an industrial flash furnace and helped identify the problems associated with the flash smelting of Escondida concentrate.

For the UBC flash reactor the maximum solids feed rate that could be smelted by the shaft was found to be inversely proportional to the shaft smelting index. This can be explained by considering the influence of small shaft smelting indices on the particle reaction and residence times. Small values of the shaft smelting index are associated

with small particle diameters, low oxygen-to-concentrate ratios, long shaft lengths and high oxygen enrichments. Small particle diameters, low oxygen-to-concentrate ratios and high oxygen enrichments all cause reductions in the particle reaction time, while low oxygen-to-concentrate ratios, long shaft lengths and high oxygen enrichments all increase the particle residence time. Hence the combination of short reaction times and long residence times at small values of the shaft smelting index, increasing the maximum feedrate that can be treated by the furnace.

For an industrial flash furnace, a parallel analysis showed that for a given shaft smelting index there are maximum and minimum solids feedrates that can be treated. Feedrates in excess of the maximum feed rate cannot be treated because there is insufficient residence time for the cloud of particles to reach the ignition temperature and react with the available oxygen. Feedrates lower than the minimum feed rate cannot be treated because the burner exit velocity is too low, reducing the heat transfer rate between the particle cloud and surroundings. This increases the time required for the cloud to reach ignition, again resulting in insufficient shaft residence time to complete the reaction.

An analysis of the furnace heat and mass balances shows that as Escondida is added to a blend of concentrates the total solids feedrate and oxygen-to-concentrate ratio decrease while the oxygen enrichment increases. These three effects combine to lower the burner exit velocity, reducing the heat transfer to the cloud, until at some Escondida loading the minimum furnace limit is reached. Hence it can be concluded that the

problems associated with the flash smelting of Escondida concentrate arise from the low heat transfer rate between the particle cloud and its surroundings.

Increasing the proportion of Escondida concentrate in the blend to be smelted therefore requires that the heat transfer characteristics of the concentrate burner be improved. Experimental and CFD studies were conducted to compare the performance of a swirl burner to a bluff-body burner. The bluff-body burner was used to approximate the concentrate burner used in industry. Some differences between the bluff-body and concentrate burner may cause the observed results for the bluff-body burner to differ from those of industrial concentrate burners. The results show that the swirl burner gives superior stability to the bluff body burner investigated due to two effects. Firstly, the swirl burner produces an internal recirculation zone that is capable of carrying heat from the combustion zone to the fresh mixture, increasing the heat transfer rate to the cloud. Secondly, the swirl burner reduces the volume of the stagnant zone within the shaft, thereby increasing the mean residence time of particles within the shaft. These two effects broaden the operating window of the shaft, allowing more Escondida concentrate to be smelted. Hence a swirl burner appears to be very promising as a means of increasing the Escondida loading that can be treated by a given furnace.

This study shows that the problems associated with flash smelting of Escondida concentrate are caused by reduced heat transfer to the particles at high Escondida loadings. The results suggest that the problems can be overcome by the use of a swirl burner, increasing both the rate of heat transfer to the particle cloud and the mean particle residence time within the shaft.

References

[1]   Davenport W.G., Partelpoeg E.H., "Flash Smelting – Analysis, Control and Optimisation", Pergamon Press, 1987.

[2]   Eltringham G.A., Personal Communication, BHP, 550 California Street, San Francisco, California, USA, 94104-1020, Tel. 1-415-7825731

[3]   Shook A.A., Personal Communication, BHP, P.O. Box 188, Wallsend, NSW, Australia, 2287, Tel. 61-2-49792550

[4]   BHP, "BHP-Fast Facts-Escondida, Chile",
        http://www.bhp.com.au/aboutbhp/fastfacts/escondida.htm

[5]   Biswas A.K., Davenport W.G., "Extractive Metallurgy of Copper", 2nd Edition, Pergamon, New York, 1980

[6]   Chaubal P.C., Sohn H.Y., "Intrinsic Kinetics of the Oxidation of Chalcopyrite Particles Under Isothermal and Nonisothermal Conditions", Metallurgical Transactions B, Vol. 17B, 1986, pp 51-60

[7]   Pignolet-Brandom S., Hagni R.D., Munroe N.D.H., "Reflected Light Microscope and Electron Probe Analysis of Flash Smelting Products of a Copper Sulfide Concentrate" Process Metallurgy VI SME-AIME Annual Meeting, New York, New York, 1985, pp 579-595

[8]   Asaki Z., Ueguchi A., Tanabe T., Kondo Y., "Oxidation of Cu_2S Pellet", Transactions of the Japan Institute of Metals, Vol. 27, 1986, pp. 361-371

[9]   Kim Y.H., Themelis N.J., "Rate Phenomena in the Oxidation of Zinc, Iron and Copper Sulfide Pellets", Canadian Metallurgy Quarterly, Vol. 26, 1987, pp. 341-349

[10]   Ramakrishna Rao V.V.V.N.S., Abraham K.P., "Kinetics of Oxidation of Copper Sulfide", Metallurgical Transactions, Vol. 2, 1971, 2463-2470

[11]   Qingshuang, Ningyuan L., "Oxidation Kinetics of Cuprous Sulfide in a Fluidised Bed", Trans. Instn. Min. Metall. (Sect. C: Mineral Process. Extr. Metall.), Vol. 95, 1986, C139-C148

[12]   Henderson T.A., "The Oxidation of Powder Compacts of Copper Iron Sulfides" Bull. Inst. Mining and Met. No. 619, 1958, pp. 437-62

[13]   Asaki Z., Tosa M., Tanabe T., Kondo Y., "Oxidation Kinetics of Mixed Copper Iron Sulfides at 1173K", Transactions of the Japan Institute of Metals, Vol. 25, 1984, pp. 487-496

[14]   Asaki Z., Kondo Y., "Oxidation Kinetics of Iron Sulfide in the Form of Dense Plate, Pellet and Single Particles" Journal of Thermal Analysis, Vol 35, 1989, pp171-1759

[15]   Tanabe T., Nishiura M., Asaki Z., "Oxidation Kinetics of Dense $Cu5Fe_{1-x}S_{4-y}$ with wide Non Stoichiometry" Materials Transactions, Vol 33, 1992, pp1155-1162

[16]   Asaki Z., Matsumoto, Tanabe T., Kondo Y., "Oxidation of Mixed Copper Iron Sulfides", Metallurgical Transactions B, Vol. 14B, 1983, pp. 109-116

[17]   Tsukada H., Asaki Z., Tanabe T., Kondo Y., "Oxidation of Mixed Copper Iron Sulfide", Metallurgical Transactions B, Vol. 12B, 1981, pp. 603-609

[18]   Jorgensen F.R.A., Segnit E.R., "Copper Flash Smelting Simulation Experiments", Proc. Australas. Inst. Min. Metall. No. 261, 1977, pp39-46

[19]   Jorgensen F.R.A., "Single Particle Combustion of Chalcopyrite", Proc. Australas. Inst. Min. Metall. No. 288, 1983, pp. 37-46

[20]   Tuffrey N.E., Richards G.G., Brimacombe J.K., "Two-Wavelength Pyrometry Study of the Combustion of Sulfide Minerals: Part I. Apparatus and General Observations" Metallurgical Transactions B, Vol. 26B, 1995, pp929-942

[21]   Tuffrey N.E., Richards G.G., Brimacombe J.K., "Two-Wavelength Pyrometry Study of the Combustion of Sulfide Minerals: Part II. Galena and Commercial Lead Concentrates" Metallurgical Transactions B, Vol. 26B, 1995, pp943-958

[22]   Tuffrey N.E., Richards G.G., Brimacombe J.K., "Two-Wavelength Pyrometry Study of the Combustion of Sulfide Minerals: Part III. The Influence of Oxygen Concentration on Pyrite Combustion" Metallurgical Transactions B, Vol. 26B, 1995, pp959-970

[23]   Hahn Y.B., Sohn H.Y., "Mathematical Modeling of Sulfide Flash Smelting Process: Part I Model Development and Verification with Laboratory and Pilot Plant Measurements for Chalcopyrite Concentrate Smelting" Metallurgical Transactions B, Vol. 21B, 1990, pp945-958.

[24]   Suominen R., Jokilaakso A., Taskinen P., Lilius K., "Morphology and Mineralogy of Copper Matte Particles Reacted in Simulated Flash Converting Conditions", Scandinavian Journal of Metallurgy, Vol 23, 1994, pp 30-36.

[25]   Jyrkonen S., Jokilaakso A., Nopanen M., Peuraniemi E., Stromberg S., "Oxidation of Synthetic Nickel Matte Under Simulated Flash Smelting Conditions", EPD Congress 1996, Proceedings of a Symposium held at the TMS Annual Meeting, Anaheim, TMS, Warrendale, pp 53-61.

[26]   Stromberg S., Jokilaakso A., Jokinen T., Jyrkonen S., "Microscopical Study of Roasted Nickel Concentrates Produced in Simulated Flash Smelting Conditions", Extraction and Processing Division, TMS Annual Meeting, 1997, TMS, Warrendale, p271-291

[27]   Jyrkonen S., "Oxidation of Solid Particles of Synthetic Nickel Mattes in Simulated Flash Smelting Conditions", Acta Polytechnica Scandinavica Chemical Technology Series, No. 265, 1999, p 1-70

[28]   Shook A.A., Richards G.G., Brimacombe J.K., "Mathematical Model of Chalcocite Particle Combustion", Metallurgical Transactions B, Vol. 26B, 1995, pp719-729

[29]   Shook A.A., "Flash Converting of Chalcocite Concentrate: A Study of the Flame", PhD Thesis, The University of British Columbia, 1992

[30]   Munroe N.D.H., "Simulation of Flash Smelting Phenomena in a Laboratory Reactor", PhD Thesis, Columbia University, 1987

[31]   Hahn Y.B., Sohn H.Y., "Mathematical Modeling of Sulfide Flash Smelting Process: Part II Quantitative Analysis of Radiative Heat Transfer" Metallurgical Transactions B, Vol. 21B, 1990, pp959-966.

[32]   Koh P.T.L., "Simulating Flow in a Flash Smelting Burner", The Nineteenth Australasian Chemical Engineering Conference, Chemeca 91, 1991, pp616-623

[33]   Nuguyen T.V., Taylor R.N., Hall T.P., "Fluid Flow in a Nickel Flash Smelter – A Simulation Study", International Conference on Extractive Metallurgy of Gold and Base Metals, Australasian Institute of Mining and Metallurgy, Kalgoorlie, 1992, pp 401-406

[34]   Koh P.T.L., Taylor R.N., "Mathematical Modelling of Heat Transfer in Flash-Smelting Burners", International Conference on Extractive Metallurgy of Gold and Base Metals, Australasian Institute of Mining and Metallurgy, Kalgoorlie, 1992, pp 407-411

[35]   Ahokainen T., Jokilaakso A., "Numerical Simulation of the Outokumpu Flash Smelting Furnace Reaction Shaft", Canadian Metallurgical Quarterly, Vol 37, 1998, pp275-283

[36]   B.R. Adams, K.A. Davis, M.P. Heap, A.F. Sarofim, G.A. Eltringham and A.A. Shook, "Application of a Reacting CFD Model to Drop Tube Kinetics and Flash Smelter Combustion" Copper 99/Cobre 99 Vol. 6, The Mineral, Metals and Materials Society (TMS), pp. 389-402

[37]   Shook A.A., Eltringham G.A., Adams B.R., Davis K.A., Caffery G.A., "Mathematical Modelling of Copper Flash Smelting Process", Brimacombe Memorial Symposium, 2000, pp 349-362

265

[38] Annamalai K., Ryan W., Dhanapalan S., "Interactive Processes in Gasification and Combustion-Part III: Coal/Char Particle Arrays, Streams and Clouds", Prog. Energy and Combustion Science, Vol. 20, 1994, pp. 487-618

[39] Gieras M., Klemens R., Wolanski P., Wojcicki S., "Experimental and Theoretical Investigation into the Ignition and Combustion Processes of Single Coal Particles Under Zero and Normal Gravity Conditions", 21st Symposium (International) on Combustion, The Combustion Institute, Pittsburgh, 1986, pp 315-323

[40] Ryan W., Annamalai K., "Group Ignition of a Cloud of Coal Particles", Journal of Heat Transfer, 1991, Vol 113, pp. 677-687

[41] Essenhigh R.H., Misra M.K., Shaw D.W., "Ignition of Coal Particles: A Review", Combustion and Flame, Vol. 77, 1989, pp. 3-30

[42] Krishna C.R., Berlad A.L., "A Model of Dust Cloud Auto-ignition", Combustion and Flame, Vol. 37, 1980, pp 207-210

[43] Annamalai K., Ramalingam S., "Group Combustion of Char/Carbon Particles", Combustion and Flame, Vol 70, 1987, pp307-332

[44] Sotirchos S.V., Amundson N.R., "Dynamic Behaviour of porous char particle burning in an Oxygen Containing Environment Part I: Constant Particle Radius" A.I.Ch.E. Journal, Vol 30, 1984, pp537-549

[45] Sotirchos S.V., Amundson N.R., "Dynamic Behaviour of porous char particle burning in an Oxygen Containing Environment Part II: Transient Analysis of a Shrinking Particle" A.I.Ch.E. Journal , Vol 30, 1984, pp550-556

[46] Satterfield C.N., Sherwood T.K., "The Role of Diffusion in Catalysis", Addison-Wesley Publishing Co., Reading, MA, 1963

[47] Arise R., "A Mathematical Theory of Diffusion and Reaction in a Permeable Catalyst: Vol I, The Theory of the Steady State", Clarendon Press, Oxford, 1975

[48] Cussler E.L., "Diffusion, Mass Transfer in Fluid System", Cambridge University Press, New York, 1984

[49] Frank-Kamentskii D.A., " Ignition of Coal and High Speed Gasification", J. Tech. Phys. USSR, Vol. 9, 1939, 1457-64

[50] Beer J.M., Chigier N.A., "Combustion Aerodynamics", Applied Science Publishers LTD, London, 1972

[51] Dirix C.A.M.C., Van Der Wiele K., "Mass Transfer in Jet Loop Reactors", Chemical Engineering Science, Vol. 45, 1990, pp 2333-2340

[52] Vaitiekunas P., Zukauskas A., Ziugzda J., "Numerical Modeling of Separated Flow Over and Heat Transfer from a Circular Cylinder or a Plate in Longitudinal Flow of Air", Heat Transfer – Soviet Research, Vol. 23, 1991, pp 291-305

[53] Avramenk A.A., "Heat Transfer in the Zone of Boundary Layer Separation", Heat Transfer - Research, Vol. 29, 1998, pp 391-396

[54] Scherer V., Wittig S., "The Influence of the Recirculation Region: A Comparison of the Convective Heat Transfer Downstream of a Backward-Facing Step and Behind a Jet in Crossflow", Journal of Engineering of Gas Turbines and Power, Vol. 113, 1991, pp 127-134

[55] Shula S.Z., Habib M.A., "Fluid Flow and Heat Transfer Characteristics in Axisymmetric Annular Diffusers", Computers and Fluids, Vol. 25, 1996, pp 133-150

[56] Festschrift A., Eckert E.R.G., Kang Y., Suzuki K., Sato T., "Studies in Heat Transfer", Hemisphere Publishing Corporation, New York, 1979, pp 103-125

[57] Libby P.A., Blake T.R., "Theoretical Study of Burning Carbon Particles", Combustion and Flame, Vol 36, 1979, pp139-169

[58] Levenspiel O., "Chemical Reaction Engineering", 2nd Edition, John Wiley and Sons, New York, 1972

[59] Wheeler A., "Advances in Catalysis Vol III", Academic Press Inc., New York, 1951

[60] Caffery G.A., Shook A.A., Grace J.R., Samarasekera I.V.; Meadowcroft T.R., "Comparisons Between Sulfide Flash smelting and Coal Combustion - With Implications for the Flash Smelting of High-Grade Concentrate", Metallurgical and Materials Transactions B, Vol 31, 2000, pp 1005-1012

[61] Glassman I., "Combustion", 3rd Edition, Academic Press, San Diego, 1996

[62] Zeldovich Y.B., "A Theory of the Limit of Slow Flame Propagation", J. Exptl. Theoret. Phys. USSR, Vol 11, 1941, pp 133-139

[63] Damkohler G., "Influence of Turbulence on the Velocity of Flame in Gas Mixtures" Z. Electrochem, Vol 46, 1940, pp601-626

[64] Shchelkin K.I., "Combustion in a Turbulent Stream", J. Tech. Phys. USSR, Vol 18, 1943, pp 520-530

[65] Scurlock A.C., "Experimental Studies on Turbulent Flames", Selected Combustion Problems: Combustion Colloquium, Cambridge University, Cambridge, 1953, pp 215-247

[66] Lewis B., von Elbe G., "Combustion, Flames and Explosions of Gases", Academic Press, New York, 1951

[67] Edelman R.B., Harsha P.T., "Laminar and Turbulent Gas Dynamics in Combustors: Current Status", Prog. Energ. Combust. Sci., Vol 4, 1978, pp 1-62

[68] Thring M.W., Newby M.P., "Combustion Length of Enclosed Turbulent Gas Jets", 4th Symposium (International) on Combustion, The Combustion Institute, Pittsburgh, 1953, pp789-96

[69] Davies T.W., Beer J.M., "The Turbulence Characteristics of Annular Wake Flows", International Seminar on Heat and Mass Transfer in Flows with Separated Regions, International Centre for Heat and Mass Transfer, Beograd, 1969, 200-209

[70] Bespalov I.V., 'Physical Principles of the Working process in Combustion Chambers of Jet Engines", Clearinghouse for Federal Scientific and Technical Information, USA AD 658 372, 1967, pp 366-378

[71] Beer J.M., Lee K.B., "The Effect of Residence Time Distribution on the Performance and Efficiency of Combustors", 10th Symposium (International) on Combustion, The Combustion Institute, Pittsburgh, 1965, 1187-1202

[72] Inami T., Baba K., Kurokawa H., Nagai K., Kondo Y., "Modification of the Concentrate Burner for a Copper Flash Smelting Furnace", Copper 91/Cobre 91, The Minerals, Metals and Materials Society (TMS), 1991, pp 49-63

[73] Yasuda Y., Sohn H.Y., "Experimental and Theoretical Study of Particle Dispersion Phenomena in a Turbulent Gas Jet of the Flash Smelting Process by Image Analysis Technique", Metallurgical and Materials Transactions B, Vol 26B, 1995, pp 637-646

[74] Sutalo I.D., Jorgensen F.R.A., Gray N.B., "Experimental and Mathematical Investigation of the Fluid Flow Inside and Below a ¼ Scale Air Model of a Flash Smelting Burner", Metallurgical Transactions B, Vol 29B, 1998, pp 993-1006

[75] Basu P., Kefa C., Jestin L., "Boilers and Burners: Design and Theory", Springer, New York, 2000

[76] Mclean W.J., Hardesty D.R., Poul J.H., "Direct Observation of Devolatilising Pulverised Coal in a Combustion Environment", 18th Symposium (International) on Combustion, The Combustion Institute, Pittsburgh, 1981, pp 1239-1248

[77] Kharbat E., Annamalai K., Gopalakrishinan C., "Ignition and Combustion of Isolated and Binary Arrays of Coal Particles" Combustion and Flame, Vol. 100, 1995, pp 413-421

268

[78]   Sergeant G.D., Smith I.W., "Combustion Rate of Bituminous Coal Char in the Temperature Range 800 to 1700 K", Fuel, Vol 52, 1973, pp52-57

[79]   Saito M., Sadakata M., Sakai T., "Measurement of Surface Combustion Rate of Single Coal Particles in a Laminar Flow Furnace", Combustion Science and Technology, Vol 51, 1987, pp 109-128

[80]   Lester T.W., Seeker W.R., Merkin J., "The Influence of Oxygen and Total Pressure on the Surface Oxidation of Bituminous Coal", 18th Symposium (International) on Combustion, The Combustion Institute, Pittsburgh, 1981, pp 1257-1265

[81]   Dutta S., Wen C.Y., Belt R.J., "Reactivity of Coal Char 1. In Carbon Dioxide Atmosphere", Ind. Eng. Chem. Proc. Des. Dev. Vol 16, 1977, pp 20-30

[82]   Dutta S., Wen C.Y., "Reactivity of Coal Char 2. In Oxygen-Nitrogen Atmosphere", Ind. Eng. Chem. Proc. Des. Dev. Vol 16, 1977, pp 31-40

[83]   Jenkins R.G., Nandi S.P., Walker P.L., "Reactivity of Heat-Treated Coals in Air at $500^{\circ}C$", Fuel, Vol 52, 1973, pp 288-93

[84]   Hippo E., Walker P.L., "Reactivity of Heat-Treated Coals in Carbon Dioxide at $900^{\circ}C$", Fuel, Vol 54, 1975, p 245-252

[85]   Gilot P., Bonnefoy F., Marcuccilli F., Prado G., "Determination of Kinetic Data for Soot Oxidation. Modelling of Competition Between Oxygen Diffusion and Reaction During Thermogravimetric Analysis", Combustion and Flame Vol 95, 1993, pp 87-100

[86]   Farzan H., Essenhigh R.H., "High Intensity Combustion of Coal", 19th Symposium (International) on Combustion, The Combustion Institute, Pittsburgh, 1982, pp 1105-1111

[87]   Cashdollar K.L., Hertzberg M., "Infrared Temperatures of Coal Dust Explosions", Combustion and Flame, Vol 51, 1983, pp23-35

[88]   HSC Chemistry Outokumpu Research Oy, Pori, Finland

[89]   Ladner W.R., Pnakhurst K.S., "Mechanisms of Corrosion by Fuel Impurities", Butterworths London, 1963, pp195

[90]   Dunn J.P., Stenger H.G., Wachs I.E., "Molecular Structure-Reactivity Relationships for the Oxidation of Sulfur Dioxide Over Supported Metal Oxide Catalysts", Catalysis Today, Vol 53, 1999, pp 543-556

[91]   Doering F.J., Lunland M.L., Berkel D.A., "Modelling of SO_2 Oxidation Rates Based on Kinetic Data of a Cs/V Catalyst at High Pressures and Conversions", Chemical Engineering Science, Vol 43, 1988, pp221-226

269

[92] Perry R.H., Green D., "Perry's Chemical Engineers Handbook", 6th Edition, McGraw Hill Book Co., New York, 1984, pp 20-81 to 20-84

[93] Nelder, J. A. and R. Mead, "A Simplex Method for Function Minimization," Computer Journal, Vol. 7, pp 308-313.

[94] Lagarias, Jeffrey C., James A. Reeds, Margaret H. Wright, and Paul E. Wright, "Convergence Properties of the Nelder-Mead Simplex Algorithm in Low Dimensions", May 1, 1997.

[95] Clift R., Grace J.R., Weber M.E., "Bubbles, Drops, and Particles", Academic Press, New York, 1978

[96] Srinivasachar S., Boni A.A., "A Kinetic Model for Pyrite Transformations in a Combustion Environment", Fuel, Vol 69, July, 1989, pp 829-836

[97] Taylor E.S., "Dimensional Analysis for Engineers", Clarendon Press, Oxford,1974

[98] Becker H.A., "Dimensionless Parameters: Theory and Methodology", Applied Science Publishers LTD, London, 1976

[99] Delichatsios M.A., "Transition from Momentum to Buoyancy-Controlled Turbulent Jet Diffusion Flames and Flame Height Relationships", Combustion and Flame, Vol 92, 1993, pp 349-364

[100] Fluent Incoporated, "Fluent User's Guide", Fluent Inc., Lebanon New Hampshire, 1997.

[101] AEA Technology, "CFX Technical Update", AEA Technology, Oxfordshire, England, 2001

[102] Eastwick C.N., Pickering S.J., Aroussi A., "Comparisons of Two Commercial Computational Fluid Dynamics Codes in Modelling Pulverised Coal Combustion for a 2.5MW Burner", Applied Mathematical Modelling, Vol. 23, 1999, 437-446

[103] Launder B.E., Spalding D.B., "The Numerical Computation of Turbulent Flows", Computer Methods in Applied Mechanics and Engineering, Vol. 3, 1974, pp 269-289

[104] Wolfstein M., "The Velocity and Temperature Distribution of One-Dimensional Flow with Turbulence Augmentation and Pressure Gradient", International Journal of Heat and Mass Transfer, Vol 12, 1969, pp 301-318

[105] Crowe C.T., "On the Relative Importance of Particle Particle Collisions in Gas Particle Flows", Proceedings from Conference on Gas Borne Particles, 1981, pp135-137

[106] Gouesbet G., Berlemont A., "Eulerian and Lagrangian Approaches for Predicting the Behaviour of Discrete Particles in Turbulent Flows", Progress in Energy and Combustion Science, Vol. 25, 1999, pp 133-159

[107] Bird R.B., Stewart W.E., Lightfoot E.N., "Transport Phenomena", John Wiley and Sons, New York, 1960

[108] Nallasamy M., "Turbulence Models and Their Applications to the Prediction of Internal Flow: A Review", Computers and Fluids, Vol. 15, 1987, pp 151-194

[109] Hanjalic K., "Advanced Turbulence Closure Models: A View of Current Status and Future Prospects", International Journal of Heat and Fluid Flow, Vol. 15, 1994, pp 178-203

[110] Lakshminarayana B., "Turbulence Modeling for Complex Shear Flows", AIAA Journal, Vol 24, 1986, pp 1900-1917

[111] Qin H., "The Flow Characteristics of a Sudden Axisymmetric Expansion", PDR/CPDU IC/4, Imperial College of Science and Technology, Lodon, 1984

[112] Amano R.S. Goel P., "A Numerical Study of a Separated and Reattached Flow by Using Reynolds Stress Turbulence Closure", Numerical Heat Transfer, Vol. 7, 1984, pp 343-357

[113] Launder B.E., Reece G.J., Rodi W., "Progress in the Development of a Reynolds Stress Turbulence Closure", Journal of Fluid Mechanics, Vol 68, 1975, pp 537-566

[114] Schlichting H., "Boundary-Layer Theory", McGraw-Hill, New York, 1955

[115] Antoine Y., Lemoine F., Lebouche M., "Turbulent Transport of a Passive Scalar in a Round Jet Discharging into a Co-Flowing Stream", European Journal of Mechanics B: Fluids, Vol 20, 2001, pp 275-301

[116] Chevray R., Tutu N.K., "Intermittency and Prefential Transport of Heat in a Round Jet", Journal of Fluid Mechanics, Vol 88, 1977, pp 133-160

[117] Chua L.P., Antonia R.A., "Turbulent Prandtl Number in a Circular Jet", International Journal of Heat and Mass Transfer", Vol 33, 1990, pp331-339

[118] Fletcher C.A.J. "Computational Techniques for Fluid Dynamics: Volume I", 2nd Edition, Springer-Verlag, New York, 1991

[119] Fletcher C.A.J. "Computational Techniques for Fluid Dynamics: Volume II", 2nd Edition, Springer-Verlag, New York, 1991

[120] Patankar S.V., "Numerical Heat Transfer and Fluid Flow", McGraw Hill, NewYork, 1980

[121] Leonard B.P., "A Stable and Accurate Convective Modelling Procedure Based on Quadratic Upstream Interpolation", Comput. Methods Appl. Mech. Eng., Vol 19, 1979, pp59-98

[122] Hottel H.C., Sarofim A.F., "Raditive Transfer", McGraw-Hill Book Company, New York, 1967

[123] Viskanta R., "Radiation Transfer and Interaction of Convection with Radiation Heat Transfer", Advances in Heat transfer, Irvine and Hartnett (Eds), Vol 3, pp 175-251

[124] Howell J.R., "Thermal Radiation in Participating Media: The Past, the Present, and Some Possible Futures", Journal of Heat Transfer, Vol 110, 1988, pp1221-1229

[125] Viskanta R., Menguc M.P., "Radiation Heat Transfer in Combustion Systems", Prog. Energy Combust. Sci., Vol 13, 1987, pp 97-160

[126] Carvalho M.G., Farias T.L., "Modelling of Heat Transfer in Radiating and Combustion Systems", Trans IchemE, Vol 76, Part A, 1998, pp 175-184

[127] Chandrasekhar S., Radiative Transfer, Dover Publications, New York, 1960

[128] Cheng P., "Two Dimensional Radiating Gas Flow by a Moment Method", AIAA Journal, Vol. 2, 1964, pp 1662-1664

[129] Raithby G.D., Chui E.H., "A Finite-Volume Method for Predicting a Radiant Heat Transfer in Enclosures With Participating Media", Journal of Heat Transfer, Vol 112, 1990, pp 415-423

[130] Chai J.C., Lee H.S., Patankar S.V., "Finite Volume Method for Radiation Heat Transfer", Journal of Thermophysics and Heat Transfer, Vol. 8, 1994, pp 419-425

[131] Higenyl J., Bayazitoglu Y., "Differential Approximation of Radiative Heat Transfer in a Gray Medium: Axially Symmetric Radiation Field", Journal of Heat Transfer, Vol. 102, 1980, pp 719-723

[132] Whitacre G.R., McCann R.A., "Comparison of Methods for the Prediction of Radiant Heat Flux Distrbution and Temperature", ASME Paper, 75-HT-9, 1975

[133] Lewis E.E., Miller W.F., "Computational Methods of Neutron Transport", Wiley, New York, 1984

[134] Fiveland W.A., "Discrete-Ordinates Solutions of the Radiative Transport Equation for Rectangular Enclosures", Journal of Heat Transfer, Vol. 106, 1984, pp 699-706

[135] Lathrop K.D., "Ray Effects in the Discrete Ordinates Equations", Nuclear Science and Engineering, Vol 32, 1968, pp 357-369

[136] Lathrop K.D., "Remedies for Ray Effects", Nuclear Science and Engineering, Vol 45, 1971, pp 255

[137] Shirolkar J.S., Coimbra C.F.M., McQuay M.Q., "Fundamental Aspects of Modelling Turbulent Particle Dispersion in Dilute Flows", Prog. Energy Combust. Sci., Vol 22, 1996 pp 363-399

[138] Durbin P.A., "A Stochastic Model of Two Particle Dispersion and Concentration Fluctations in Homogeneous Turbulence", Journal of Fluid Mechanics, Vol 100, 1980, pp 279-302

[139] Durbin P.A., "A Random Flight Model of Inhomogeneous Turbulent Dispersion", Physics of Fluids, Vol 23, 1980, pp 2151-2153

[140] Daly B.J., Harlow F.H., "Transport Equations in Turbulence", The Physics of Fluids, Vol. 13, 1970, pp 2634-2649

[141] Ranz W.E., Marshal W.R., "Evaporation from Drops, Part I", Chemical Engineering Progress, Vol. 48(3), 1952, pp. 141-146

[142] Ranz W.E., Marshal W.R., "Evaporation from Drops, Part II", Chemical Engineering Progress, Vol. 48(4), 1952, pp. 173-180

[143] Hinze J.O., "Turbulence", McGraw-Hill, New York, 1975

[144] Reynolds A.J., "Turbulent Flows in Engineering", Wiley and Sons, London,1974

[145] Kenning V.M., Crowe C.T., "On the Effect of Particles on Carrier Phase Turbulence in Gas-Particle Flows", International Journal of Multiphase Flow. Vol. 23, 1997, pp 403-408

[146] Poirier D.R., Geiger G.H., "Transport Phenomena in Materials Processing", The Minerals Metals and Materials Society, Warrendale, 1994

[147] Kays W.M., "Turbulent Prandtl Number – Where are We?", Journal of Heat Transfer, Vol 116, 1994, pp. 284-295

[148] Kawamura H., Kurihara Y., "Modelling of Turbulent Scalar Transport in Homogeneous Turbulence"" International Journal of Heat and Mass Transfer, Vol. 43, 2000, pp. 1935-1945

[149] Yu B., Ozoe H., Churchill S.W., "The Charactersitics of Fully Developed Turbulent Convection in a Round Pipe", Chemical Engineering Science, Vol 56, 2001, 1781-1800

[150] Klose G., Rembold B., Koch R., Wittig S., "Comparison of State-of-the-Art Turbulence Interaction Models for Jet Engine Combustor Conditions", International Journal of Heat and Fluid Flow, Vol. 22, 2001, pp 343-349

[151] Ricou F.P., Spalding D.B., "Measurements of Entrainment by Axi-Symmetric Turbulent Jets", Journal of Fluid Mechanics, Vol. 11, 1961, pp 21-32

[152] Crowe C.T., Sharma M.P., Stock D.E., "The Particle Source in Cell (PSI-CELL) Model for Gas-Droplet Flows", Journal of Fluids Engineering, Vol. 99, 1977, pp 325-332

[153] ASTM Committee E-11, "E 122 – 89: Standard Practice for Choice of Sample Size to Estimate a Measure of Quality for a Lot or Process", ASTM Standards, 1989

[154] Kemori N., Ojima Y., Mori Y., Kondo Y., "Development of New Flash Smelting Technology for High-Grade Copper Matte Production", Proceedings of the Nickel-Cobalt International Symposium, 1997, pp 539-549

[155] Krieth F., Bohn M.S., "Principles of Heat Transfer", 6th Edition, Brooks/Coles, Pacific Grove California, 2001

Appendix A1: Rotameter and Orifice Plate Calibration Curves

The two rotameters and orifice plate were calibrated using a dry positive displacement flow meter. The temperature was recorded and atmospheric pressure was assumed to be 101.3 kPa allowing the flows to be converted to flows at normal temperature and pressure.


$$Q = 0.1427r + 0.00061r^2 - 5 \times 10^{-5} r^3 + 2 \times 10^{-7} r^4$$

Q = Air Flow Rate (l/min)
r = Rotameter Reading
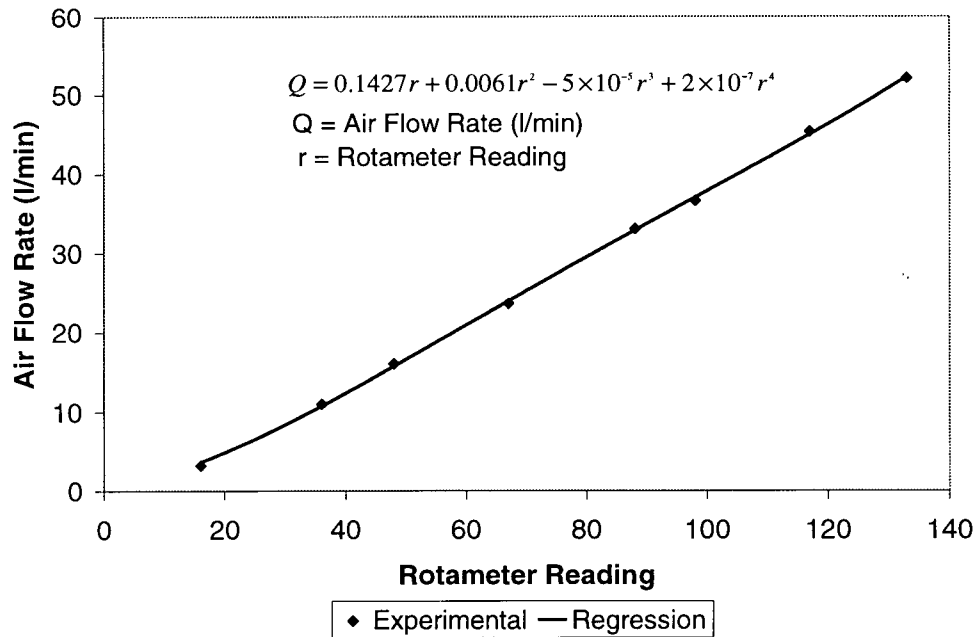
Figure A1-1: Air Rotameter Calibration Curve (Flowrates are at NTP)

$$Q = 0.0426r + 0.0088r^2 - 8\times10^{-5}r^3 + 3\times10^{-7}r^4$$

Q = Oxygen Flow Rate (l/min)

r = Rotameter Reading
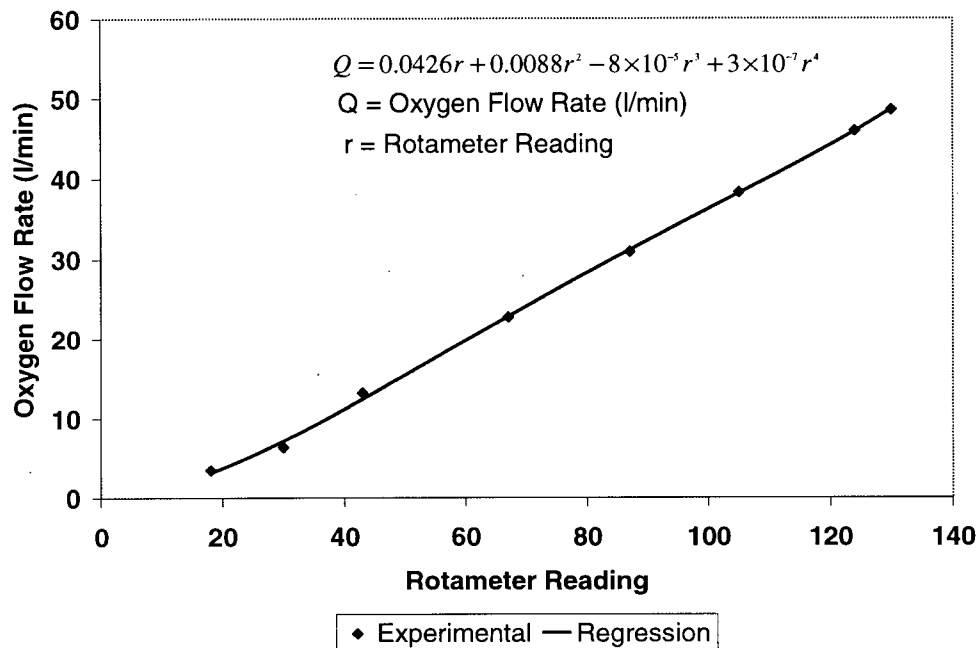
Figure A1-2: Oxygen Rotameter Calibration Curve (Flowrates are at NTP)


$$Q = 3.79(\Delta P)^{0.501}$$
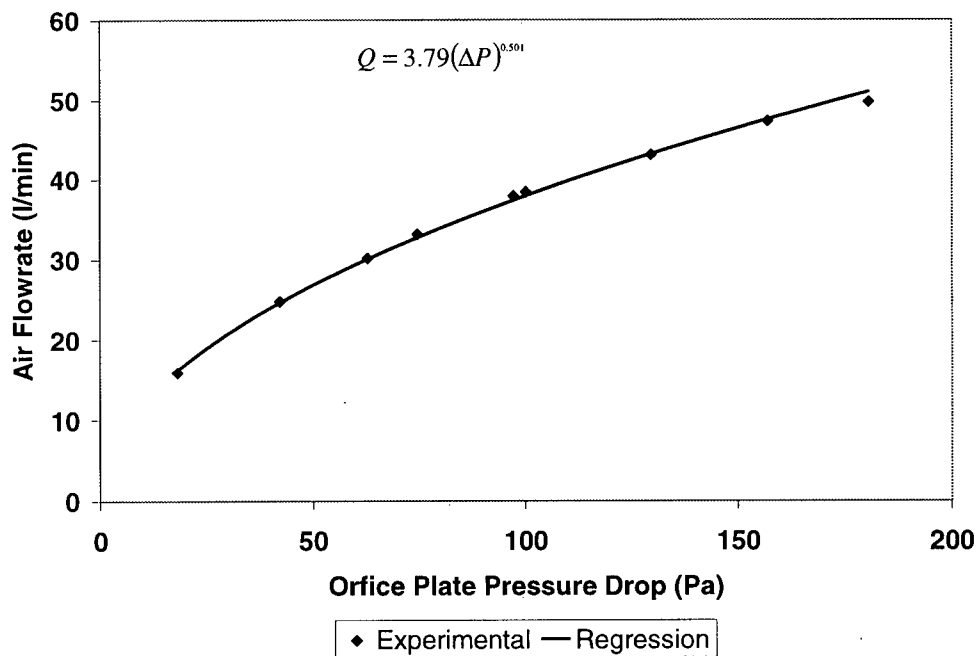
Figure A1-3: Orifice Plate Calibration Curve (Flowrates are at NTP)

276

Appendix A2: Group Combustion Model Code

A2.1   Group Combustion Code

```
function
[devaim,tp,time]=temp(tinf,ea,a,thiheat,thireac,po2,o2tocon,dp,maxtime)

% tinf is furnace temperature (K)
% ea is the reaction activation energy (j/mol)
% a is the reaction pre-exponential factor (m/s)
% thiheat and thireac are the heat transfer and combistion effectivness
% facotr
% po2 is the oxygen partial pressure (atm)
% o2tocon is the oxygen to concentrate ratio(-)
% dp is the particle diameter (m)
% maxtime is time to solve the equations over

%  Set up Initial Conditions

rho = 1.17;
ap = 3.4159*dp^2;
mp = 3.14159*4500./6*dp^3;
tp(1) = 300.;
time(1) = 0.;
no2 = mp*o2tocon/32;
no2int = no2;
volgas = no2*8.314*tinf/101.325/po2;
co2 = no2/volgas;
devaim(1) = 1;
deltah = 32*8.8e6;

dt = maxtime/1000;

%  This solves for the particle mass particle temperature and oxygen
concentration


for i = 2:2000;

%  calvulate the heat transfer rate

    h = 2*0.04/dp/thiheat;

%  update time step

    time(i) = time(i-1)+dt;

%  calculate the beta term in Equation (7-11)

    beta = 6*h/4500/dp/1000.;
```

277

```
%  calculate the reaction rate constant

   kmass = 1.2e-5*((tinf+tp(i-1))/2/298)^1.5*2/dp;
   kr = a*exp(-ea/8.314/tp(i-1));
   kov = kr*kmass/(kr+kmass);

%  calvulate the reaction rate

   r = ap*kov*co2/thireac;

%  update the oxygen concentration and particle mass

   no2 = no2 - r*dt;
   mp = mp - 8.42*r*dt
   devaim(i) = no2/no2int;
   newvol = 0.5*(tp(i-1)+tinf)*volgas/tinf;
   co2 = no2/newvol;
   if (co2<0)
      co2=0;
   end

%  update the particle temperature


   alpha = tinf+r*deltah/h/ap;
   tp(i) = (tp(i-1)-alpha)*exp(-beta*dt)+alpha;
end
```

A2.2 Minimisation Algorithm

```
function
[thiheat,thireac]=plotfit(yact,tact,tinf,po2,o2tocon,dp,iheat,icomb)

% yact is the experimental particle conversions
% tact is the experimental particle residence times
% tinf is furnace temperature (K)
% po2 is the oxygen partial pressure (atm)
% o2tocon is the oxygen to concentrate ratio(-)
% dp is the particle diameter (m)
% iheat and icomb are the intial guesses for heat transfer and
combsiton effective factors

% fmin minimises the function errorfuc


xact = fmins('errorfuc',[2.37e5,3.7e12,iheat,icomb],[1,1e20,5e-
5,10],[],yact,tact,tinf,po2,o2tocon,dp)
thiheat = xact(1);
thireac = xact(2);
```

```matlab
function err = errorfuc(x,ea,a,yact,tact,tinf,po2,o2tocon,dp)

% x is an array containing the current values for the heat transfer and
combustion effectiveness factors
% yact is the experimental particle conversions
% tact is the experimental particle residence times
% tinf is furnace temperature (K)
% po2 is the oxygen partial pressure (atm)
% o2tocon is the oxygen to concentrate ratio(-)
% dp is the particle diameter (m)


% this calculates the particle conversion v's time for the current
values for the heat transfer and combustion effectiveness factors

[devaim,tp,time] =
temp(tinf,ea,a,x(1),x(2),po2,o2tocon,dp,tact(length(tact)));

% this determines the error between the model output and exprimental
values


err=0;
i=1;
for j = 1:length(tact)
    while (time(i)<tact(j))
            i=i+1;
    end
 err = err+(devaim(i)-yact(j))^2;
```

Appendix A3: Effective Mixture and Furnace Atmosphere Densities

A3.1 Effective Mixture Density

Take 1 kilogram of solids as basis. The oxygen-to-concentrate mass ratio, η, defines the kilograms of oxygen present in the reaction gas. The oxygen enrichment, σ, which is volume or mole percent of oxygen in the reaction gas, allows the total moles of gas associated with the reaction gas to be given by $\dfrac{\eta}{32\sigma}$. The kilograms of nitrogen in the reaction gas can then be given by $\dfrac{28}{32}\eta\left(\dfrac{1-\sigma}{\sigma}\right)$.

The volume of the reaction gas can be calculated from the ideal gas law as:

$$V = \frac{nRT_o}{P} = \frac{\dfrac{\eta}{32\sigma}RT_o}{P} \tag{A3-1}$$

If the volume associated with the solids is assumed negligible (as the density of the solids is approximately 1000 times greater than that of the gas). The density of the mixture can be calculated as:

$$\rho_o = \frac{1+\eta+\dfrac{28}{32}\eta\left(\dfrac{1-\sigma}{\sigma}\right)}{V} = \frac{P}{RT_o}\cdot\frac{1+\eta+\dfrac{28}{32}\eta\left(\dfrac{1-\sigma}{\sigma}\right)}{\dfrac{\eta}{32\sigma}} \tag{A3-2}$$

This can be rearranged to give:

$$\rho_o = \frac{P}{RT_o}\left(32\frac{\sigma}{\eta}+4\sigma+28\right) \tag{A3-3}$$

A3.2 Furnace Atmosphere Density

The density of the furnace atmosphere can be estimated in a similar manner. If it is assumed that no particles are present in the ambiance and that all of the oxygen reacts to SO_2 (this is not the case and therefore the predicted density will be higher than the actual density) the following can be calculated.

Take as a basis 1 mole of oxygen in the reaction gas. The moles of nitrogen associated with the 1 mole of oxygen is $\left(\dfrac{1-\sigma}{\sigma}\right)$. If it is assumed that all of the oxygen reacts to SO_2 then we have 1 mole of SO_2 in the furnace ambiance and therefore the volume of the gas is:

$$V = \frac{RT_\infty}{P} \cdot \frac{1}{\sigma}$$

(A3-4)

and the density can be given by:

$$\rho_a \approx \frac{P}{RT_\infty} \cdot \frac{64 + 28\left(\dfrac{1-\sigma}{\sigma}\right)}{\dfrac{1}{\sigma}}$$

(A3-5)

This can be rearranged to give:

$$\rho_a \approx \frac{P}{RT_\infty}(36\sigma + 28)$$

(A3-6)

Appendix A4: Single Particle Burning Time

The following analysis allows the combustion time of a particle to be predicted providing the following assumptions are valid:

1) insufficient oxygen available to achieve complete combustion;

2) the rate of combustion is controlled by gas phase diffusion;

3) the combustion process proceeds via the shrinking core model; and

4) the volume of gas remains constant throughout the combustion process.

Consider the reaction:

$$\text{Solid} + \eta O_2 \rightarrow \text{Products} \qquad\qquad (A4\text{-}1)$$

Here η represents the mass of oxygen available for reaction per kilogram of solid and hence is the same as the oxygen-to-concentrate ratio already defined

Given a particle with an initial diameter d_p and molar density ρ_s, the initial moles of oxygen available for reaction is:

$$m_{O_2,0} = \eta \rho_p \frac{\pi d_p^3}{6} \qquad\qquad (A4\text{-}2)$$

If the initial oxygen concentration $C_{O_2,0}$ is known, then the volume of gas that participates in the combustion process is:

$$V = \frac{m_{O_2,0}}{MW_{O_2}C_{O_2,0}} = \frac{\eta\rho_p}{MW_{O_2}C_{O_2,0}}\frac{\pi d_p^3}{6} \tag{A4-3}$$

Because the volume of gas is assumed to remain constant throughout the reaction then:

$$C_{O_2} = \frac{m_{O_2}}{MW_{O_2}V} = \frac{6C_{O_2,0}m_{O_2}}{\pi\eta\rho_p d_p^3} \tag{A4-4}$$

According to Levenspiel the combustion process can be described by:

$$\frac{dm_{O_2}}{dt} = -\pi d_p^2 k_m C_{O_2} MW_{O_2} \tag{A4-5}$$

Combining Equations (A4-4) and (A4-5) gives:

$$\frac{\pi\eta\rho_p d_p^3}{6C_{O_2,0}}\frac{dC_{O_2}}{dt} = -\pi d_p^2 k_m C_{O_2} MW_{O_2} \tag{A4-6}$$

Which can be simplified to:

$$\frac{dC_{O_2}}{dt} = -\frac{6k_m C_{O_2,0}}{\eta\rho_p d_p}C_{O_2} MW_{O_2} \tag{A4-7}$$

This equation can be solved to give:

$$C_{O_2} = C_{O_2,0}\exp\left(-\frac{6MW_{O_2}k_m C_{O_2,0}}{\eta\rho_p d_p}t\right) \tag{A4-8}$$

Therefore the combustion time is given by:

$$\tau_c = -\frac{\eta \rho_p d_p}{6 MW_{O_2} k_m C_{O_2,0}} \ln\left(\frac{C_{O_2}}{C_{O_2,0}}\right) \qquad (A4\text{-}9)$$

If the Sherwood number is assumed to be 2 (i.e. negligible slip between the particle and surrounding gas) then Equation (A4-9) can be simplified to:

$$\tau_c = -\frac{\eta \rho_p d_p^2}{12 MW_{O_2} D C_{O_2,0}} \ln\left(\frac{C_{O_2}}{C_{O_2,0}}\right) \qquad (A4\text{-}10)$$

Clearly a value of $C_{O_2} = 0$ in Equation (A4-10) is meaningless. However, if the combustion process is assumed to be complete when the oxygen concentration falls to 1% of its initial value, then the combustion time can be estimated by:

$$\tau_c = 0.3838 \frac{\eta \rho_p d_p^2}{MW_{O_2} D C_{O_2,0}} \qquad (A4\text{-}11)$$

Equation (A4-11) shows that the combustion time is proportional to the square of the particle diameter and the oxygen-to-concentrate ratio and inversely proportional to the combustion effectiveness factor and oxygen concentration.

Appendix A5: Cloud Biot Number Analysis

The objective of this Appendix is to develop an analysis to allow the heat-up time of the cloud to be determined when thermal gradients exist within the cloud. This is achieved by solving a modified form of the transient heat conduction equation to determine the gas phase temperature as a function of radial position and time. The modified form of the heat conduction equation accounted for the presence of the particles by suitably increasing the thermal mass of the gas phase. This then allowed the particle temperatures within the cloud to be determined as a function of radial position and time. Then by defining an average particle temperature within the cloud the time required for this particle to heat to its ignition temperature was determined. Figure 8-9 was obtained using this analysis and shows that the effect of thermal gradients within the cloud is to increase the time required for the cloud to reach ignition.

A5.1 Problem Definition

Consider a cylindrical particle cloud as shown in Figure A5-1.

$$q = k_{h,cl}(T_\infty - T)$$
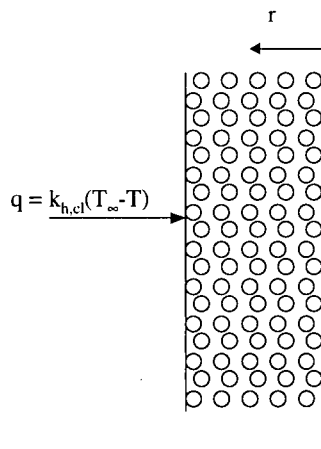
Figure A5-1: Cloud Geometry and Boundary Conditions

285

A5.2 Problem Formulation

If conduction is assumed to be the dominant mode of heat transfer within the gas phase then the gas and particle temperatures can be calculated from:

$$\rho C_p \frac{\partial T}{\partial t} = \frac{\lambda}{r} \frac{\partial}{\partial r}\left(r \frac{\partial T}{\partial r}\right) - n k_h A_p \left(T - T_p\right) \qquad \text{(A5-1)}$$

and

$$m_p C_{p,p} \frac{dT_p}{dt} = k_h A_p \left(T - T_p\right) \qquad \text{(A5-2)}$$

In these equations the gas (T) and particle (T_p) temperatures, are functions of time and radial position.

A numerical approach is required to obtain the exact solution to these equations. However if it is assumed that the gas and particle temperatures increase at the same rate (i.e. $\dfrac{dT}{dt} = \dfrac{dT_p}{dt}$) then Equations (A5-1) and (A5-2) can be simplified to the one dimensional heat conduction equation.

$$\left(\rho C_p + n m_p C_{p,p}\right)\frac{\partial T}{\partial t} = \frac{\lambda}{r} \frac{\partial}{\partial r}\left(r \frac{\partial T}{\partial r}\right) \qquad \text{(A5-3)}$$

Here the volume fraction of the particle is assumed negligible compared to the volume fraction of the gas. This is reasonable as the volume fraction of the particle is in the order of 1×10^{-3}. Equation (A5-3) shows that the influence of the particles on the gas phase temperature can be accounted for by adding the thermal mass of the particles

$\left(nm_pC_{p,p}\right)$ to the gas phase thermal mass $\left(\rho C_p\right)$. Hence Equation (A5-3) can be used to predict the gas phase temperature.

A5.3 Solution

Figures A5-2 and A5-3 show the graphical solution to Equation (A5-3) for the boundary conditions described in Figure A5-1. These graphs are discussed in detail by Kreith and Bohn.[155]
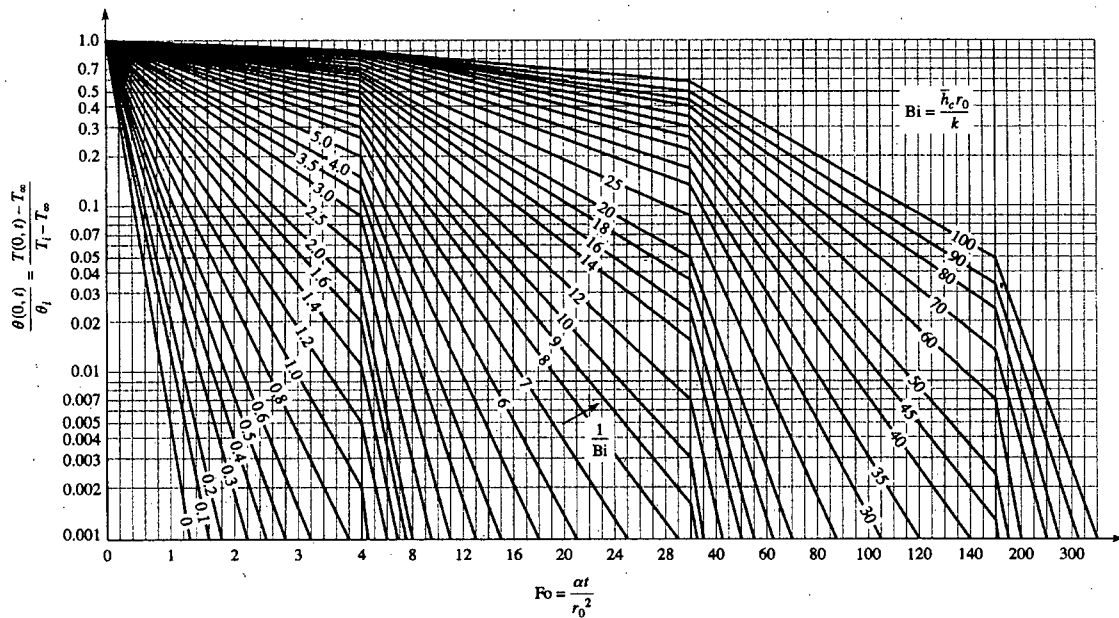

Figure A5-2: Dimensionless Centerline Temperature for a Long Cylinder[155]
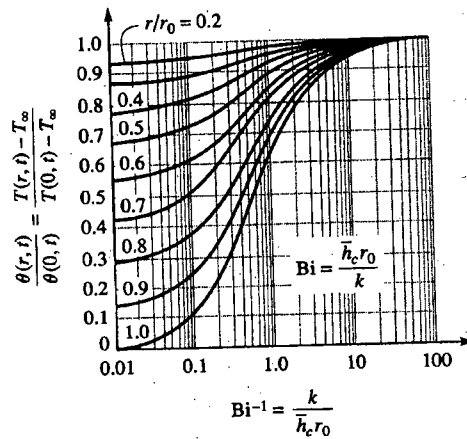
Figure A5-3: Dimensionless Radial Temperature for a Long Cylinder[155]

In Figure A5-2 the heating time of the cloud is defined in terms of the Fourier number, which contains the gas phase thermal diffusivity. For this case, Equation (A5-3) shows that the thermal diffusivity used to calculate the Fourier number is:

$$\alpha_t = \frac{\lambda}{\rho C_p + n m_p C_{p,p}} \tag{A5-4}$$

A5.3.1 Gas Phase Temperature

Using Equation (A5-4) together with Figure A5-2 and A5-3 allows the gas phase temperature to be estimated. Figure A5-4 shows an example of the radial temperature distribution within the cloud at different times. The temperature profiles described here were calculated for a cloud having a diameter of 0.0254 m and a Biot number of 0.2, while the particle number density of the cloud was 4.5×10^{10} m^{-3}, with the particles having a diameter of 50 μm.
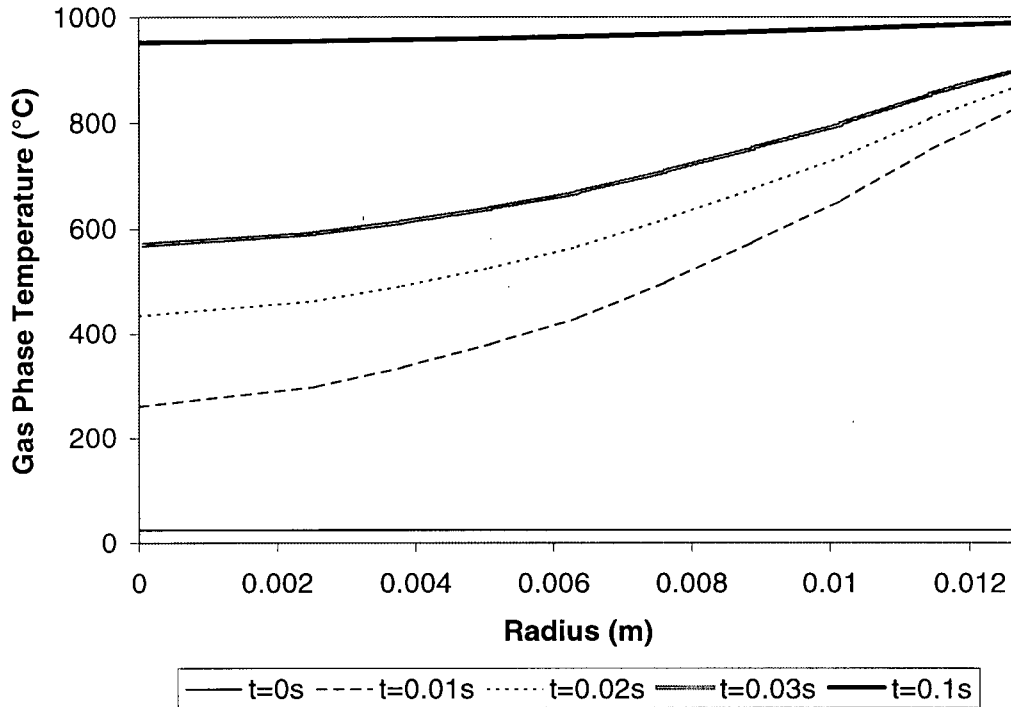
Figure A5-4: Example of Gas Phase Radial Temperature Distribution at Different Times

A5.3.2 Particle Temperature

Once the gas phase temperature is known Equation (A5-2) can be integrated to give the particle temperature at the different radial positions within the cloud as a function of time. Know we are capable of determining the time required for the cloud to reach ignition. However it is difficult to determine this time because the particles close to the outer edge of the cloud will heat-up and reach ignition before particles close to the cloud centre. But some fraction of the particles must ignite before we can consider that the entire cloud has ignited. Therefore the average particle temperature defined below was used to determine when cloud ignition had occurred.

$$\overline{T}_p(t) = \frac{8}{d_c^2} \int_0^{d_c/2} r T_{p,r}(t) dr \qquad\qquad (A5\text{-}5)$$

Note that the particle temperature given by this equation does weight the temperature towards those close to the outer edge of the cloud. Once Equation (A5-5) has been calculated, the time required for the average particle to reach its ignition temperature could be determined by developing curves similar to Figure A5-4. Results from Equation (A5-5) were used to develop Figure 8-9.

A5.3 Investigation of Particle Heating Rate

The heat-up time that was determined from this analysis is only valid if the particle and gas heating rates are approximately equal. Figure A5-5 shows the ratio of the gas and particle heating rates for different particle sizes.
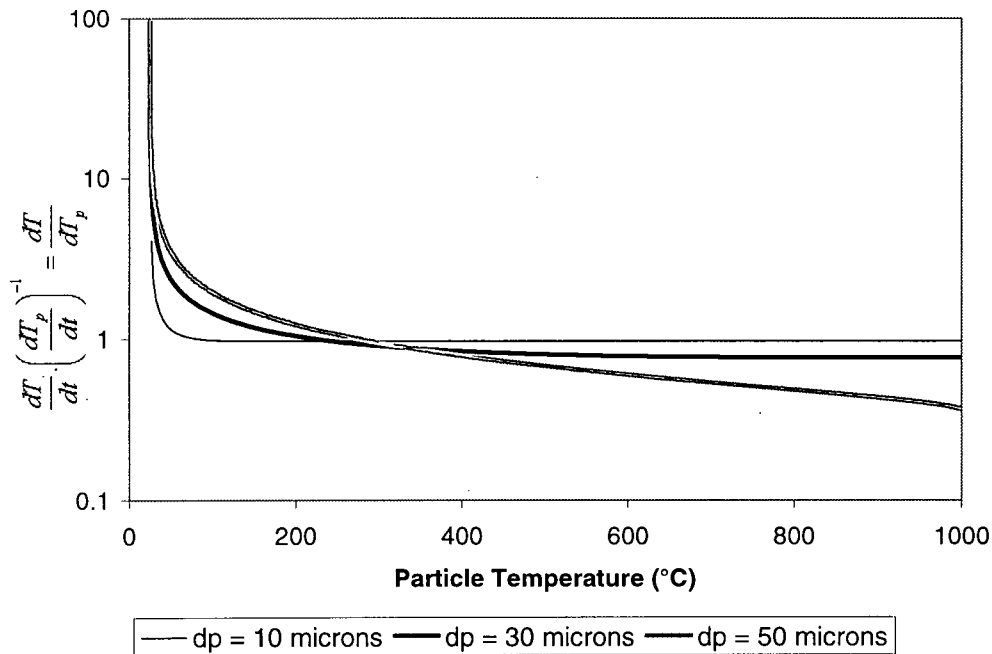

Figure A5-5: Ratio of Rate of Gas-to-Particle Temperature Increase for Different Particle Sizes

Initially the rate of increase in the gas phase temperature is higher than that for the particles, for all particle sizes. However, as time proceeds the rate of increase in the gas particle temperature increases towards that of the gas phase. Figure A5-5 shows that small particles quickly reach the gas phase heating rate, while the temperature of a relatively large particle tends to lag behind that of the gas. Hence the assumption of equal rates of particle and gas phase temperature increases is reasonable for small particle (less than approximately 30μm in diameter) but less valid for large particles (larger than approximately 50μm). Consequently, the analysis developed here can only be used for particles smaller than approximately50 μm. As this is the approximate size range used in the experiments, the technique described here to determine the time required for the cloud to reach ignition when temperature gradients exit within the cloud, should provide an acceptable estimate of the particle heat-up time.

Appendix A6: Reynolds Stress Model Terms[100,109-110]

A6.1 Diffusive Transport Terms

$$D_{zr} = \frac{\partial}{\partial z}\left(\frac{\nu_t}{\Pr_k}\frac{\partial \overline{u'v'}}{\partial z}\right) + \frac{1}{r}\frac{\partial}{\partial r}\left(r\frac{\nu_t}{\Pr_k}\frac{\partial \overline{u'v'}}{\partial r}\right) \qquad (A6\text{-}1)$$

$$D_{zz} = \frac{\partial}{\partial z}\left(\frac{\nu_t}{\Pr_k}\frac{\partial \overline{u'u'}}{\partial z}\right) + \frac{1}{r}\frac{\partial}{\partial r}\left(r\frac{\nu_t}{\Pr_k}\frac{\partial \overline{u'u'}}{\partial r}\right) \qquad (A6\text{-}2)$$

$$D_{rr} = \frac{\partial}{\partial z}\left(\frac{\nu_t}{\Pr_k}\frac{\partial \overline{v'v'}}{\partial z}\right) + \frac{1}{r}\frac{\partial}{\partial r}\left(r\frac{\nu_t}{\Pr_k}\frac{\partial \overline{v'v'}}{\partial r}\right) \qquad (A6\text{-}3)$$

A6.2 Production Terms

$$P_{zr} = -\left(\overline{u'v'}\frac{\partial v}{\partial r} + \overline{v'v'}\frac{\partial u}{\partial r} + \overline{u'v'}\frac{\partial u}{\partial z} + \overline{u'u'}\frac{\partial v}{\partial z}\right) \qquad (A6\text{-}4)$$

$$P_{zz} = -\left(2\overline{u'v'}\frac{\partial u}{\partial r} + 2\overline{u'u'}\frac{\partial u}{\partial z}\right) \qquad (A6\text{-}5)$$

$$P_{rr} = -\left(2\overline{v'v'}\frac{\partial v}{\partial r} + 2\overline{u'v'}\frac{\partial v}{\partial z}\right) \qquad (A6\text{-}6)$$

A6.3 Pressure Strain Terms

$$\phi_{zr} = -C_1\frac{\varepsilon}{k}\left(\overline{u'v'}\right) - C_2\left(P_{zr} - S_{zr}\right) \qquad (A6\text{-}7)$$

$$\phi_{zz} = -C_1 \frac{\varepsilon}{k}\left(\overline{u'u'} - \frac{2}{3}k\right) - C_2\left(\frac{2}{3}P_{zz} - S_{zz}\right)$$ (A6-8)

$$\phi_{rr} = -C_1 \frac{\varepsilon}{k}\left(\overline{v'v'} - \frac{2}{3}k\right) - C_2\left(\frac{2}{3}P_{rr} - S_{rr}\right)$$ (A6-9)

Here C_1 and C_2 are empirical constants with values of 1.8 and 0.6 respectively. These values are discussed by Launder et al.[112]

A6.4 Dissipation Terms

Fluent assumes the dissipation as isotropic and equal to the scalar dissipation rate.

$$\varepsilon_{zr} = 0$$ (A6-10)

$$\varepsilon_{zz} = \frac{2}{3}\varepsilon$$ (A6-11)

$$\varepsilon_{rr} = \frac{2}{3}\varepsilon$$ (A6-12)

A6.5 Curvature Terms

$$S_{zr} = \rho\frac{w}{r}\overline{u'v'}$$ (A6-14)

$$S_{zz} = 0$$ (A6-15)

$$S_{rr} = 2\rho\frac{w}{r}\overline{v'w'}$$ (A6-16)

$$E_{zr} = -\overline{u'v'}\frac{\mu_t}{r^2} \tag{A6-17}$$

$$E_{zz} = 0 \tag{A6-18}$$

$$E_{rr} = -2\left(\overline{v'v'} - \overline{w'w'}\right)\frac{\mu_t}{r^2} \tag{A6-19}$$